

**Flux Directed Branched Nanowire Growth via VLS-GLAD**

by

Allan Leo Beaudry

A thesis submitted in partial fulfillment of the requirements for the degree of

Doctor of Philosophy

in

Microsystems and Nanodevices

Department of Electrical and Computer Engineering  
University of Alberta

©Allan Leo Beaudry, 2014

# Abstract

---

In this thesis, a new technique named vapour-liquid-solid glancing angle deposition (VLS-GLAD) will be used to enhance structural control over branched nanowire (NW) arrays. NWs are 1D crystals that have been extensively applied in sensors, photovoltaic devices, and transistors. The functional properties of NWs have been thoroughly investigated over the past two decades, however, producing 3D architectures using NW building blocks via bottom-up fabrication remains challenging.

VLS-GLAD uses glancing angle deposition (GLAD) to deposit a collimated vapour flux to direct the vapour-liquid-solid (VLS) growth of NWs. Branched NWs, also known as “nanotrees”, are formed by growing secondary NWs (branches) epitaxially on the sidewall of another NW (trunk). In this thesis, control over morphology, branching and alignment in indium tin oxide (ITO) NW arrays will be demonstrated.

VLS-GLAD will be used to fabricate structures with unique morphological anisotropy by exploiting vapour flux shadowing. For instance, branches will be shown to grow preferentially on the side of trunks facing the collimated flux, enabling anisotropic branch growth that can be controlled along the height of NWs. Flux shadowing will also be used to enable the fabrication of azimuthally aligned nanotrees without requiring epitaxy at the substrate. Aperiodic signals will be encoded into diameter oscillations along the length of branches by engineering their

local shadowing environment using dynamic substrate motion during growth. Such signals enable morphological time-stamps to be controllably inserted in the structures, providing insight into the VLS-GLAD process. Further, facet selective branch growth on epitaxially aligned nanotrees will be shown to enable the fabrication of precisely aligned arrays of self-similar L-, T-, or X-branched nanotrees. Using this control, VLS-GLAD may unlock access to previously unachievable 3D architectures using bottom-up fabrication.

Extensive characterization of the branched NW arrays using a wide variety of nanomaterial characterization techniques will be presented, including: X-ray diffraction, transmission electron microscopy, and scanning helium ion microscopy. In addition, VLS-GLAD will be used to fabricate transparent branched ITO NW electrodes for organic solar cell applications. Sheet resistance and optical transmission will be optimized by tuning the deposition parameters and post-growth annealing procedures.

“Talent wins games, but teamwork and intelligence wins championships.”  
– Michael Jordan

# Preface

---

The work described in Chapters 3, 4, 5, and 6 were published in *Nanotechnology*<sup>a</sup>, *Applied Physics Letters*<sup>b</sup>, *Crystal Growth and Design*<sup>c</sup>, and *Nano Letters*<sup>d</sup>, respectively. The work in Chapter 7 is primarily unpublished, however, some of the data was published in two papers in *Nanotechnology*<sup>a,c</sup>. See the following page for bibliographic details for each publication.

The work in this thesis was the result of a collaborative effort under the supervision of Dr. Michael Brett. Ryan Tucker was the first member in our lab to achieve nanotree growth. He also led the development of the numerical model described in Chapter 4, and developed the annealing procedures used in Chapter 7. Tucker also used his graphic design expertise to produce many of the schematics throughout this thesis. Joshua LaForge performed X-ray diffraction, led collaborations that helped elucidate the electrical properties of our structures, and provided his crystal growth expertise to develop a deep understanding of competitive growth described in Chapter 5. Michael Taschuk provided invaluable input drawing from his expertise gained from many years of materials science and optics research. Taschuk and Tucker led the development of simulation software that guided our understanding of the growth process as published in *The Journal of Applied Physics*<sup>f</sup>. The aforementioned collaborators and I were the core team of the VLS-GLAD project that were deeply involved at every level. I performed the majority of the experimental work, led interpretation of the data, prepared numerous manuscripts, and led the overall direction of the VLS-GLAD project.

Jason Sorge assisted me in installing and calibrating the second iteration of the VLS-GLAD experimental apparatus. Sorge also helped design substrate motion algorithms for the work in Chapter 6. Nicholas Adamski assisted in data analysis and experimental work for the work in Chapter 6. Peng Li obtained and analyzed TEM data in Chapter 5 and 6. Helium ion microscope images in Chapter 6 were obtained by Chuong Huynh from Carl Zeiss Microscopy. HAADF-STEM data in

Chapter 6 was obtained by Akira Yasuhara from the EM Business Unit and TEM applications group in JEOL Ltd. The template used for this thesis was generously provided by Steven Jim.

## Thesis Publications

---

<sup>a</sup>Beaudry, A. L., Tucker, R. T., LaForge, J. M., Taschuk, M. T., and Brett, M. J. *Nanotechnology* **2012**, *23*, 105608. **(Chapters 3 and 7)**

<sup>b</sup>Tucker, R. T., Beaudry A. L., LaForge, J. M., Taschuk, M. T., and Brett M. J. *Applied Physics Letters* **2012**, *101*, 193101. **(Chapter 4)**

<sup>c</sup>Beaudry, A. L., LaForge, J. M., Tucker, R. T., Li, P., Taschuk, M. T., and Brett, M. J. *Crystal Growth and Design* **2013**, *13*, 212. **(Chapter 5)**

<sup>d</sup>Beaudry, A. L., LaForge, J. M., Tucker, R. T., Sorge J. B., Adamski, N. L., Li, P., Taschuk, M. T., and Brett, M. J. *Nano Letters* **2014**, *14*, 1797. **(Chapter 6)**

<sup>e</sup>LaForge, J. M., Cocker, T. L., Beaudry, A. L., Cui, K., Tucker, R. T., Taschuk, M. T., Hegmann, F. A., and Brett, M. J. *Nanotechnology* **2014**, *25*, 035701. **(Partially included in Chapter 7)**

<sup>f</sup>Taschuk, M. T., Tucker, R. T., LaForge, J. M., Beaudry, A. L., Kupsta, M. R., and Brett, M. J. *Journal of Applied Physics*. **2013**, *114*, 244304. (Not described in thesis, however, simulation software within was used to interpret results.)

# Acknowledgements

---

I have many to thank for making graduate school a phenomenal experience. First, I'd like to thank Dr. Michael Brett for building a research environment filled with talented and driven people. You gave us the freedom to pursue our vision while accepting nothing less than excellence. The cooperative culture established under your leadership in the GLAD lab over the years has continuously enabled students to be successful. It was an honor and a privilege to work for you.

I'd like to thank the VLS-GLAD team, Joshua LaForge, Ryan Tucker, and Michael Taschuk, for sharing my enthusiasm and for shaping me into the engineer I am today. I'll try to spare the hockey analogies. LaForge, thanks for pushing me to be better. Your constructive criticism allowed me to avoid settling for less. I look forward to working with you again very soon! Tucker, thanks for showing me science could have style, and for listening to me speak before I think. It was quite a humbling experience working with someone as talented as you. Taschuk, my Inbox currently has 833 unread messages. I flinched while typing that. In all seriousness, thanks for showing us how to get the job done. Your ability to lead by example is what keeps the lab working hard. Couldn't have done it without you guys. I can only hope I am lucky enough to work with such a motivated and productive team again.

Thank you to the NINT Electron Microscopy team for providing access to their world-class facilities. In particular, thank you to Peng Li, Kai Cui and Martin Kupsta for their invaluable expertise. Also, thank you to the University of Alberta nanoFAB staff for their dedication and excellent training. Thank you to the director of the nanoFAB, Dr. Eric Flaim, and Peng Li for taking our samples around the globe to get characterized at cutting edge facilities. A big thank you to Chuong Huynh from Carl Zeiss Microscopy for beautiful helium ion microscopy imaging and Akira Yasuhara from the EM Business Unit and TEM applications group in JEOL Ltd. for obtaining outstanding HAADF-STEM images. Each of your input was of utmost importance to the success of this project.

Thank you to my supervisory committee, Dr. Karthik Shankar and Dr. Ken Cadien, for their invaluable input to this thesis. Thank you Dr. Robert Fedosejevs, Dr. David Mitlin, and Dr. Ken Westra for the supervision and guidance each of you gave me during my undergraduate research. Thanks to Chris Holt and Hal Friesen for being outstanding graduate student mentors early in my development as an experimentalist. Thanks to Jeffrey Tait for being a tireless colleague and a great friend during our Engineering Physics years. I am extremely grateful to have had the opportunity to work with each of you.

I am tremendously appreciative to have met so many marvellous people in the GLAD Lab, ENL Lab, and Buriak Group. I'd like to thank you all for not only making graduate school tolerable, but downright fun. Steve Jim, thanks for rewarding good behavior with chocolate, and for having a contagious positive attitude. Your thoughtfulness and genuine character made the lab a pleasant place to work. Graham Hunt, thanks for introducing me to some awesome music and enforcing a strict gym regimen. I have no doubt we will be lifelong friends. Abeed (Al) Lalany, thanks for the camaraderie, the endless ITO discussions, and for attempting to give me a sense of style, but red pants, seriously? Jason Sorge, a big thank you for the countless hours spent tinkering around on Dagda and for showing me the GLAD ropes. How 'bout them Oilers? Brian Worfolk, thanks for being the life of the party and for bringing people together. You were truly missed when you left, cheers. Ryan Shewchuk, thanks for sharing my appreciation for the Sugar Bowl. Jocelyn Westwood, Eng Phys fo' life. Also, thanks for keeping me in line throughout the undergrad years! Matthew Hawkeye, thanks for living up to your legendary reputation. Joshua Siewert, thanks for the laughs! Your wit can't be matched. Ben Bathgate, thanks for not letting me electrocute myself. Audrey Lin, thank you for being so kind, patient, and efficient. The lab could not function without you. Michael Fleischauer, thanks but Robot Chicken isn't really my thing. Nicholas Adamski, it was a blast working with you! I look forward to hearing about your future endeavours, enjoy California! Salma Elmallah, your hard working nature can't be taught, we're all expecting big things from you. Henry Brausen, I'm almost certain you are related to Gene Principe. I'd also like to thank Jillian Buriak,

Jeremy Sit, Bing Cao, Jon Kwan, Katie Krause, Viktor Leontyev, Michael Thomas, Grayson Ingram, Tate Hauger, Jennifer Bruce, Jeremy Bau, Anthony Oko, Jaron Van Dijken, Daniel Smetaniuk, Balázs Gyenes, and Zhen Wang for making graduate school enjoyable every single day.

Thank you to my parents for providing me a space where I could focus and still eat like a king. Thanks for showing me that hard work pays off. Most of all, thank you for giving me the confidence to pursue my dreams. Words truly cannot express my gratitude for having such patient, understanding, and loving parents. Ryan, I love you brother. Couldn't ask for a better older bro. The resilience I gained from growing up with a bigger and stronger brother made the trials of graduate school endurable, for that I can't thank you enough. Rebecca, thanks for taking Ryan off our hands and welcome to the family sis!

A big thank you to the funding agencies who make research possible in the GLAD Lab: Natural Sciences and Engineering Research Council of Canada, Alberta Innovates: Technology Futures, and Micralyne Inc. I owe many thanks to the NSERC Photovoltaic Innovation Network, and the Society of Vacuum Coaters for generously sponsoring my attendance to numerous international conferences.

# Contents

---

1. Introduction .....	1
1.1 Motivation.....	1
1.2 Outline.....	4
2. Background .....	6
2.1 Focus .....	6
2.2 Nanowires (NWs) .....	6
2.2.1 Properties .....	6
2.2.2 1D Crystal Growth.....	8
2.2.3 Vapour-Liquid-Solid (VLS) Growth .....	9
2.2.4 NW Applications .....	10
2.2.5 Branched NWs.....	12
2.2.6 Interconnected Nanotree Architectures.....	13
2.3 Glancing Angle Deposition (GLAD).....	15
2.3.1 Introduction.....	15
2.3.2 Nanostructured Thin Films .....	17
2.3.3 Seeding.....	18
2.3.4 Crystal texture in GLAD films .....	20
2.4 Indium Tin Oxide (ITO) .....	23
2.4.1 Electrical and Optical Properties .....	23
2.4.2 ITO Crystal Structure.....	24
2.4.3 Self-catalyzed VLS of ITO NWs.....	25
2.4.4 Nanostructured electrodes for organic photovoltaics .....	26
2.5 Nanomaterial characterization techniques .....	28
2.5.1 Scanning Electron Microscopy (SEM) .....	28
2.5.2 Energy-dispersive X-ray spectroscopy (EDX) .....	29
2.5.3 Scanning Helium Ion Microscopy (SHIM).....	29
2.5.4 X-ray Diffraction (XRD) .....	30
2.5.5 Transmission Electron Microscopy (TEM) .....	33
3. VLS-GLAD .....	35
3.1 Introduction.....	36
3.1.1 Introduction.....	36

3.1.2 Early VLS-GLAD .....	36
3.1.3 VLS-GLAD of branched ITO NWs.....	40
3.2 Experimental .....	42
3.2.1 VLS-GLAD growth of ITO NWs .....	42
3.2.2 Characterization .....	43
3.3 Results and Discussion .....	45
3.3.1 Deposition angle ( $\alpha$ ) .....	45
3.3.2 Deposition rate .....	49
3.3.3 Temperature .....	54
3.3.4 Substrate rotation .....	54
3.3.5 Branch-trunk diameter relationship .....	55
3.3.6 Crystal structure .....	56
3.3.7 Composition.....	59
3.3.8 Height dependent morphology.....	60
3.4 Conclusions.....	62
<b>4. Branch Rippling .....</b>	<b>63</b>
4.1 Introduction.....	64
4.2 Model .....	66
4.3 Complex ripple control .....	70
4.4 Conclusions.....	72
<b>5. Branch Placement and Nanotree Alignment.....</b>	<b>74</b>
5.1 Introduction.....	75
5.1.1 Introduction.....	75
5.1.2 Contributions.....	76
5.2 Experimental .....	77
5.2.1 Film Fabrication.....	77
5.2.2 Film characterization .....	79
5.3 Results and Discussion .....	80
5.3.1 Height dependent branch placement.....	80
5.3.2 Azimuthal branch alignment.....	83
5.3.3 Individual nanotree morphology.....	87
5.3.4 Crystal structure .....	89
5.3.5 Crystal texture .....	93
5.3.6 Branch alignment and crystal texture relationship.....	97

5.3.7 Competitive alignment.....	98
5.4 Conclusions.....	103
<b>6. Epitaxially Aligned Nanotrees .....</b>	<b>104</b>
6.1 Introduction.....	105
6.1.1 Introduction.....	105
6.1.2 Contributions.....	106
6.2 Experimental.....	108
6.2.1 Nanotree growth.....	108
6.2.2 Characterization.....	110
6.3 Results and Discussion .....	112
6.3.1 Nanotrees .....	112
6.3.2 Nanotree alignment.....	115
6.3.3 Epitaxy .....	118
6.3.4 L-, T-, and X-shaped nanotrees.....	121
6.3.5 Mechanism.....	123
6.3.6 Non-idealities.....	124
6.3.7 Uniaxial branch elongation.....	125
6.4 Conclusions.....	128
<b>7. Transparent Electrode Optimization .....</b>	<b>129</b>
7.1 Introduction.....	129
7.1.1 Introduction.....	129
7.1.2 ITO transparent electrode optimization .....	130
7.2 Experimental.....	131
7.2.1 Annealing procedure.....	131
7.2.2 Characterization.....	131
7.3 Results.....	132
7.3.1 Sheet resistance – four-point-probe .....	132
7.3.2 Sheet resistance – $\alpha$ .....	133
7.3.3 Sheet resistance – deposition rate .....	134
7.3.4 Sheet resistance – temperature.....	139
7.3.5 Optical transmittance – annealing.....	141
7.3.6 Optical transmittance - $\alpha$ .....	141
7.3.7 Optical transmittance – deposition rate.....	144
7.3.8 Optical transmittance - temperature.....	144

7.3.9 Haacke's Figure of Merit .....	147
7.4 Conclusions.....	149
<b>8. Conclusions .....</b>	<b>150</b>
8.1 Summary of Thesis Results .....	150
8.1.1 Summary .....	150
8.1.2 VLS-GLAD capabilities .....	151
8.1.3 Morphological control .....	152
8.1.4 Engineered branch oscillations .....	152
8.1.5 Height dependent branch orientation control.....	152
8.1.6 Epitaxy-free competitive nanotree alignment.....	152
8.1.7 L-, T-, and X-branched nanotrees .....	153
8.1.8 Transparent electrodes .....	154
8.2 Future Work .....	154
8.2.1 Looking forward .....	154
8.2.2 Directional branch interconnectivity.....	154
8.2.3 Enhanced branch placement – new material systems .....	155
8.2.4 Further transparent electrode optimization .....	155
8.3 Reflection .....	156
<b>References .....</b>	<b>157</b>

# List of tables

---

<b>Table 3.1:</b> Morphological parameters as a function of deposition angle. Measured for ITO NW arrays grown at a temperature of 240 °C, rate of 0.2 nm/s and various $\alpha$ . .....	47
<b>Table 3.2:</b> Morphological parameters as a function of deposition rate. NW arrays grown at a temperature of 240 °C. ....	51
<b>Table 5.1:</b> Deposition conditions and properties of nanotree films deposited at 2 nm/s to a nominal thickness of 1200 nm. Reproduced with permission from <i>Crystal Growth and Design</i> . <sup>307</sup> Copyright 2013, American Chemical Society. ....	81
<b>Table 7.1:</b> Sheet resistance, average visible transmission ( $400 < \lambda < 780$ nm) and Haacke's figure of merit measured before and after each annealing stage for ITO NW films grown at a temperature of 240 °C, rate of 0.2 nm/s, and at various $\alpha$ . ....	135
<b>Table 7.2</b> Sheet resistance, average visible transmission ( $400 < \lambda < 780$ nm) and Haacke's figure of merit measured before and after each annealing stage for ITO NW films grown at a temperature of 240 °C. ....	136

# List of figures

---

**Figure 1.1:** Tree-shaping – guiding the growth of a tree into a designed shape. Reproduced with permission from <http://pooktre.com/photos/living-chair/>. ... 2

**Figure 2.1:** (a) Si NWs grown using Al catalyst, Reprinted by permission from Macmillan Publishers Ltd: *Nature Nanotechnology*<sup>62</sup>, copyright 2003. (b) Si wires grown using Cu catalyst, reprinted with permission from Kayes, B. et al.'s work.<sup>63</sup> Copyright 2007, AIP Publishing LLC. .... 7

**Figure 2.2:** Schematic for screw driven 1D crystal growth. (A) a step on a dislocation free surface, depicting conventional layer by layer crystal growth. (B) Depicts a screw dislocation that has a self-perpetuating step. (C) Depicts preferential adsorption of adatoms at tip of growing crystal, leading to 1D crystal growth along the screw dislocation. Adapted with permission from *The Journal of Physical Chemistry Letters*.<sup>71</sup> Copyright 2010 American Chemical Society..... 9

**Figure 2.3:** Schematic of Au-catalyzed Si VLS growth. (a) Vapour deposition on Au-Si liquid alloy droplet. (b) Crystalline Si-NW with Au-Si alloy at the tip. Reprinted with permission from Wagner and Ellis' work.<sup>13</sup> Copyright 1964, AIP Publishing LLC. .... 9

**Figure 2.4:** (a-b) SEMs of GaP nanotrees, (c) TEM image of trunk with five branches, (d) HRTEM image indicating epitaxial growth of branch on trunk (image taken from region indicated by arrow in (c)). Reprinted by permission from Macmillan Publishers Ltd: *Nature Materials*, copyright 2004.<sup>83</sup> ..... 12

**Figure 2.5:** (a-f) Schematic for the fabrication of position controlled, interconnected branched InAs NWs epitaxially grown on InP substrate. Gold seeds are placed on NW sidewalls in (d) for epitaxial branch growth. (g) SEM image of the resulting NW network. Adapted with permission from *Nano Letters*.<sup>84</sup> Copyright 2006 American Chemical Society. .... 14

**Figure 2.6:** Schematic of e-beam evaporated ITO deposited using GLAD.  $\alpha$  and  $\phi$  are controlled by stepper motors during deposition. Adapted with permission from *Nanotechnology*.<sup>122</sup> Copyright 2011 Institute of Physics..... 16

**Figure 2.7:** Schematic of shadowing in GLAD leading to slanted post films. (a) Formation of nuclei on substrate surface. (b) Nuclei begin to cast shadows. (c) Columnar growth begins, smaller structures are starved from flux. (d) Columns grow inclined at an angle  $\beta$ . Adapted with permission from *Handbook of Deposition Technologies for Films and Coatings*.<sup>138</sup> Copyright 2010 Elsevier. .... 17

- Figure 2.8:** Various GLAD morphologies: (a) slanted post, (b) zig-zag posts, (c) helical posts, and (d) vertical post. Adapted with permission from *Journal of Materials Science: Materials in Electronics*.<sup>141</sup> Copyright 2006 Springer..... 18
- Figure 2.9:** Illustration of (a) stochastic or random nucleation versus (b) periodic nucleation on pre-patterned seeds. Taken with permission from *Journal of Materials Science: Materials in Electronics*.<sup>141</sup> Copyright 2006 Springer..... 19
- Figure 2.10:** Highly ordered square spiral GLAD film grown on top of pre-positioned seeds. Taken with permission from *Science*.<sup>107</sup> ..... 19
- Figure 2.11:** Schematic illustrating texture evolution mechanisms in crystalline W films at (a) normal deposition, and (b) oblique angle deposition. Taken with permission from *Applied Physics Letters*.<sup>150</sup> Copyright 2003, AIP Publishing LLC. .... 21
- Figure 2.12:** Schematic of azimuthal flux configurations and resulting crystallite alignment. (a) substrate rotation led to randomly oriented crystallites. (b) Symmetric 3-fold azimuthal flux configuration led to aligned crystallites, and biaxial film texture. Adapted with Permission from *Crystal Growth and Design*.<sup>170</sup> Copyright 2012 American Chemical Society. .... 22
- Figure 2.13:** Schematic of the self-catalyzed VLS growth of branched ITO NWs. (a) In-Sn liquid droplets form on substrate early in ITO deposition. (b) Liquid droplets catalyze growth of NWs, liquid droplets form on sidewall of trunk. (c) Liquid droplets catalyze epitaxial branch growth on sidewall of NWs, trunks and branches grow along  $\langle 400 \rangle$  directions. (d) SEM image of VLS grown branched ITO NWs. .... 26
- Figure 2.14:** Schematic of BHJ OPV device with branched ITO NW transparent electrode designed for enhanced charge extraction. .... 28
- Figure 2.15:** Schematic of Bragg diffraction condition for X-rays incident at an angle  $\theta$  on a crystal lattice with spacing  $d_{hkl}$ . .... 30
- Figure 2.16:** Schematic of Miller indices in a simple cubic system. Planes are listed in the order: blue, green, red. (a) (004), (002), (001); (b) (022), (011), (022); (c) (444), (222), (111). Purple arrows correspond to (a) [001], (b) [011], and (c) [111]. .... 31
- Figure 2.17:** (a) Schematic of X-ray scattering process, where  $\mathbf{K}$ ,  $\mathbf{K}_\theta$ , and  $\mathbf{Q}$  refer to the incident and scattered X-rays, and scattering vector, respectively.  $\mathbf{K}$ ,  $\mathbf{K}_\theta$ , and  $\mathbf{Q}$  are all in the scattering plane. The sample coordinates are  $s_1$ ,  $s_2$ , and  $s_3$ . (b) XRD pole figure collection schematic in an Euler cradle configuration. The orientation of the scattering plane is controlled by substrate tilt angle  $\psi$  and azimuthal angle  $\phi$ . (c) X-ray scattering intensity is measured for each  $\mathbf{Q}$  vector that intersects with a hemisphere above the sample for a fixed Bragg angle  $\theta$ . Reproduced from “Thin Film Analysis by X-Ray Scattering” by Mario Birkholz with permission from John Wiley and Sons. Copyright 2006.<sup>172</sup> ..... 32

- Figure 2.18:** Conceptual (222) XRD pole figures for arrays of cubic crystals that are (a) randomly aligned, (b) vertically aligned but randomly aligned azimuthally, and (c) aligned vertically and azimuthally.  $\psi$  and  $\phi$  correspond to the orientation of a particular scattering vector  $\mathbf{Q}$  and the red represents the detected X-ray intensity. .... 33
- Figure 3.1:** This figure depicts height dependent control over branch density and trunk diameter achieved by modulating flux rate during VLS-GLAD growth of branched ITO NWs. Portions of this chapter were published in *Nanotechnology*<sup>271</sup>, and this figure was featured in a news article entitled, “Nanotree structures shaped with an arborist’s precision” on Nanotechweb.org (<http://nanotechweb.org/cws/article/lab/48939>). .... 35
- Figure 3.2:** (a) Ge deposited without Au seeds ( $\alpha = 85^\circ$ ), Ge deposited on Au seeds for (b)  $\alpha = 85^\circ$ , (c)  $\alpha = 73^\circ$ , and (d)  $\alpha = 58^\circ$ . Adapted from the work by Suzuki et al. with permission from *Applied Physics Letters*.<sup>273</sup> Copyright 2011, AIP Publishing LLC. .... 39
- Figure 3.3:** (a) cross-sectional and (b) top-down SEM images of Ge NWs grown on Au seeds using VLS-GLAD at  $\alpha = 85^\circ$ . (c) and (d) are grown without Au seeds. Adapted from the work by Alagoz et al. with permission from *MRS Proceedings*.<sup>272</sup> .... 39
- Figure 3.4:** (a) Qualitative parameter space for ITO planar, glancing angle deposition (GLAD), and vapour-liquid-solid (VLS) grown films. Combining high substrate temperature and high deposition angles produces unique morphologies in a process we call VLS-GLAD. (b) Schematic definition of deposition angle ( $\alpha$ ) and the angle of rotation about substrate normal ( $\phi$ ). Typical NWs are characterized as having a trunk, droplet, and numerous branches. Reproduced with permission from *Nanotechnology*.<sup>271</sup> Copyright 2012 Institute of Physics. .... 41
- Figure 3.5:** Two halogen bulbs are directed at the center of the chuck using aluminum reflectors. The heating assembly rotates in  $\alpha$  with the substrate. This photo was adapted with permission from Graham Hunt’s thesis<sup>282</sup> ..... 43
- Figure 3.6:** Temperature measured by TC fixed to substrate, and TC elevated 1 cm above substrate versus time. The elevated TC set point temperature was 240 °C, resulting in a measured temperature of about 270 °C at the surface of the substrate. .... 44
- Figure 3.7:** VLS-GLAD ITO NW films deposited with varying deposition angle  $\alpha = 50^\circ, 70^\circ, 80^\circ, 85^\circ,$  and  $87^\circ$  (temperature = 240 °C, flux rate = 0.2 nm/s, pitch = 10 nm nominal). Reproduced with permission from *Nanotechnology*.<sup>271</sup> Copyright 2012 Institute of Physics. .... 46
- Figure 3.8:** Gaussian fits from frequency versus nearest neighbour spacing between trunks measured from top-down SEM images (see **Figure 3.7**) for ITO

NW arrays grown at various $\alpha$ , (a) $50^\circ$ , (b) $70^\circ$ , (c) $87^\circ$ , and (d) is $90^\circ$ . This data is used in <b>Figure 3.9a</b> .....	47
<b>Figure 3.9:</b> Measured parameters for VLS-GLAD NWs deposited at various deposition angles (a) trunk density per unit area and nearest neighbour distance (see <b>Figure 3.8</b> ), and (b) average branches per unit trunk length and trunk diameter. Error bars indicate standard deviation (nearest neighbour distance, trunk diameter) or propagated counting error (trunk density, branches per trunk length). Reproduced with permission from <i>Nanotechnology</i> . <sup>271</sup> Copyright 2012 Institute of Physics.....	48
<b>Figure 3.10:</b> VLS-GLAD NWs growth with high deposition angle and varying deposition rate of 0.05 nm/s, 0.1 nm/s, 0.5 nm/s, 1 nm/s, and 2 nm/s (temperature = $240^\circ\text{C}$ , deposition angle = $85^\circ$ , pitch = 10 nm nominal). Reproduced with permission from <i>Nanotechnology</i> . <sup>271</sup> Copyright 2012 Institute of Physics.....	50
<b>Figure 3.11:</b> Average number of branches per unit trunk length and trunk diameter measured for VLS-GLAD NWs grown at $\alpha = 85^\circ$ and varying flux rate. Reproduced with permission from <i>Nanotechnology</i> . <sup>271</sup> Copyright 2012 Institute of Physics.....	51
<b>Figure 3.12:</b> Images of VLS-GLAD NWs at various flux rates of 0.05 nm/s, 0.5 nm/s, and 2 nm/s for deposition temperature of $240^\circ\text{C}$ , and deposition angle of $\alpha = 50^\circ$ . Reproduced with permission from <i>Nanotechnology</i> . <sup>271</sup> Copyright 2012 Institute of Physics.....	52
<b>Figure 3.13:</b> VLS-GLAD NWs grown at various substrate temperatures and at deposition angles of $\alpha = 50^\circ$ and $85^\circ$ . Reproduced with permission from <i>Nanotechnology</i> . <sup>271</sup> Copyright 2012 Institute of Physics. ....	53
<b>Figure 3.14:</b> Images of VLS-GLAD NWs at various flux rates of 0.05 nm/s, 0.5 nm/s, and 2 nm/s for deposition temperature of $165^\circ\text{C}$ , and deposition angle of $85^\circ$ . Reproduced with permission from <i>Nanotechnology</i> . <sup>271</sup> Copyright 2012 Institute of Physics.....	54
<b>Figure 3.15:</b> For all deposited films, branch diameter has an upper limit of $1/2$ of the trunk diameter. The dotted line represents the side length of the inscribed square of the trunk's circular cross-section, as illustrated in the inset figure. Reproduced with permission from <i>Nanotechnology</i> . <sup>271</sup> Copyright 2012 Institute of Physics.....	55
<b>Figure 3.16:</b> X-ray diffraction patterns of select samples deposited on Si substrates at a pitch of 10 nm, with variation in deposition angle, substrate temperature and nominal deposition rate. Powder diffraction pattern file for ITO (01-089-4597) is shown for comparison. Reproduced with permission from <i>Nanotechnology</i> . <sup>271</sup> Copyright 2012 Institute of Physics. ....	57

- Figure 3.17:** TEM images of an ITO NW deposited with the following deposition conditions:  $\alpha = 85^\circ$ ,  $T = 240^\circ\text{C}$ , flux rate = 0.1 nm/s and pitch = 10 nm nominal. (a) TEM image of an ITO NW, and SAED data in the inset. (b) HRTEM image at a selected trunk-branch interface. To guide the eye, we have added the dark lines to mark the crystal planes in the branch and trunk of the ITO NW. Reproduced with permission from *Nanotechnology*.<sup>271</sup> Copyright 2012 Institute of Physics. .... 58
- Figure 3.18:** (a) and (c) TEM images, white arrows indicate region where EDX line-scans were performed, and correspond to position axis in (b) and (d), respectively. .... 59
- Figure 3.19:** Side and plan view SEM images of: (a,b) flux rate modulated VLS-GLAD NWs with high deposition angle ( $85^\circ$ ) and flux rate switching from 1 nm/s to 0.05 nm/s; (c,d) flux rate modulated VLS-GLAD NWs with high deposition angle ( $85^\circ$ ) and flux rate switching between 1 nm/s, 0.05 nm/s, 1 nm/s; and (e,f) deposition angle modulated VLS-GLAD NWs with deposition angle switching from  $\alpha = 30^\circ$  to  $\alpha = 85^\circ$  during deposition. Reproduced with permission from *Nanotechnology*.<sup>271</sup> Copyright 2012 Institute of Physics. ... 61
- Figure 4.1:** The work in this chapter was featured on the cover of the November 2012 issue of *Applied Physics Letters*.<sup>285</sup> ..... 63
- Figure 4.2:** SEM images of VLS-GLAD ITO nanotrees exhibiting rippled branch features deposited with the parameters (a)  $\alpha = 87^\circ$ ,  $T = 240^\circ\text{C}$ ,  $R = 2 \text{ \AA/s}$ ,  $\tau_{rot} = 50 \text{ s}$ ; (b) magnified edge and (c) plan view of  $\alpha = 85^\circ$ ,  $T = 240^\circ\text{C}$ ,  $R = 10 \text{ \AA/s}$ ,  $\tau_{rot} = 10 \text{ s}$ . Reproduced with permission from *Applied Physics Letters*.<sup>285</sup> Copyright 2012, AIP Publishing LLC. .... 65
- Figure 4.3:** Schematic of VLS-GLAD rippling phenomenon. Side view (a) shows glancing angle ( $\alpha$ ) and flux shadowing region. Darker droplets are receiving incoming flux and lighter droplet occluded; b) plan view shows rotation of substrate by the angle  $\phi$ , and flux modulation ( $\gamma$ ) at a droplet from shadowing by the attached trunk; (c) droplet radius ( $r$ ) and volume ( $V$ ), branch length ( $L$ ) and monolayer thickness ( $d$ ), flux rate ( $R$ ) and capture area ( $A$ ), and incoming/outgoing volume rates ( $V_{in}/V_{out}$ ) as used in the model. Reproduced with permission from *Applied Physics Letters*.<sup>285</sup> Copyright 2012, AIP Publishing LLC. .... 67
- Figure 4.4:** Branch simulation (a) input volume rate ( $V_{in}$ ) to droplet for  $\tau_{rot} = 10 \text{ s}$  and volume rate out ( $V_{out}$ ) of the droplet as calculated in each time-step; (b) enlarged SEM image of a branch deposited at  $\tau_{rot} = 10 \text{ s}$ ; (c) branch edge profile (open circles) and simulated branch morphology (red line) for  $\tau_{rot} = 10 \text{ s}$ ; (d) simulated branch profile for  $\tau_{rot} = 1 \text{ s}$  (blue),  $\tau_{rot} = 100 \text{ s}$  (green), and  $\tau_{rot} = 1000 \text{ s}$  (magenta); y-axis of inset is 1 nm range. Reproduced with permission from *Applied Physics Letters*.<sup>285</sup> Copyright 2012, AIP Publishing LLC. .... 69

**Figure 4.5:** Complex VLS-GLAD ITO branch growth by shutter-modulated flux according to the pattern shown in (a), where 1 is shutter open and 0 is shutter closed; (b) SEM image of resulting NW with unique branching morphology; (c) magnified key branch region, with (d), (e), and (f) displaying the flux modulation due to shuttering, due to rotation-induced shadowing, and the combined shutter-rotation effect on the flux profile, respectively, for the magnified branch. Reproduced with permission from *Applied Physics Letters*.<sup>285</sup> Copyright 2012, AIP Publishing LLC. .... 71

**Figure 4.6:** Complex VLS-GLAD ITO branch growth by changing the rotation rates according to the following program (rotations @  $\tau_{rot}$ ): 10 @ 10 s, 2 @ 25 s, 10 @ 5 s, 1 @ 50 s, ~17 @ 3 s, as shown in (a) as flux attenuation due to the rotational shadowing (1 is flux, 0 is shadowed); (b) SEM image of resulting NW morphology, and magnified branches (c, e) along with the approximate sections of rotational shadowing from (a) that contributed to each branch morphology (d, f, respectively). Reproduced with permission from *Applied Physics Letters*.<sup>285</sup> Copyright 2012, AIP Publishing LLC. .... 73

**Figure 5.1:** Table of Contents figure published in *Crystal Growth and Design*.<sup>307</sup> This figure schematically depicts in-plane nanotree alignment and height dependent branch placement using by engineering the azimuthal flux distribution as presented in this chapter. The arrows represent the azimuthal flux positions. Discretized flux position (left) result in aligned nanotrees, isotropic flux distribution (right) results in random nanotree alignment. .... 74

**Figure 5.2:** Illustration of VLS-GLAD growth of ITO nanotrees. Deposition angle ( $\alpha$ ) and angle of flux rotation ( $\phi$ ) are shown.  $\phi_0$  indicates the initial azimuthal position of the flux. Reproduced with permission from *Crystal Growth and Design*.<sup>307</sup> Copyright 2013, American Chemical Society. .... 77

**Figure 5.3:** Top-down schematic of VLS-GLAD azimuthal modulation schemes for (a) unidirectional, (b) periodic, and (c) chiral (one continuous rotation) and isotropic ( $p = 10$  nm) ITO nanotree structures. Reproduced with permission from *Crystal Growth and Design*.<sup>307</sup> Copyright 2013, American Chemical Society. .... 78

**Figure 5.4:** Cross-sectional SEM images of ITO nanotrees grown with  $\alpha = 85^\circ$ ,  $T = 240$  °C, and flux rate = 0.2 nm/s (top) or 2 nm/s (bottom). Scale bars are all 500 nm in length. The initial azimuthal vapour flux angle ( $\phi_0$ ) is oriented from the right to left in each image. The nominal thickness of the films are 300 nm (top) and 1200 nm (bottom). Reproduced with permission from *Crystal Growth and Design*.<sup>307</sup> Copyright 2013, American Chemical Society. .... 82

**Figure 5.5:** Cross-sectional SEM images of ITO nanotrees ( $\alpha = 85^\circ$ ,  $T = 240$  °C, and flux rate = 0.2 nm/s). Scale bars are all 100 nm in length. The ITO nanotrees are named: (a) unidirectional, (b) periodic, (c) chiral and (d) isotropic, based on the azimuthal modulation configuration used during growth, shown in **Figure 5.3**. The initial azimuthal vapor flux angle ( $\phi_0$ ) is oriented from the right to left

- as indicated by the arrow in each image. The nominal thicknesses (CTM) of the films were 300 nm for (a), (b) and (c), and 450 nm for (d). Reproduced with permission from *Crystal Growth and Design*.<sup>307</sup> Copyright 2013, American Chemical Society. .... 82
- Figure 5.6:** Top-SEMs of (a) unidirectional, (b) periodic, (c) chiral and (d) isotropic films. The top and bottom rows show structures grown at 0.2 nm/s and 2 nm/s, respectively. Initial flux position is from left to right in each case. Reproduced with permission from *Crystal Growth and Design*.<sup>307</sup> Copyright 2013, American Chemical Society. .... 83
- Figure 5.7:** Sample measurements taken from top-down SEM images using ImageJ software for (a) unidirectional, (b) periodic, (c) chiral and (d) isotropic films. Five images (same as shown above) were measured for each array. One branch measured for each growth direction on a trunk, with a maximum of four measurements per trunk. Lines were drawn from trunk-branch interface to branch tip. Reproduced with permission from *Crystal Growth and Design*.<sup>307</sup> Copyright 2013, American Chemical Society. .... 84
- Figure 5.8:** Normalized radial histograms illustrating the number of branches counted at azimuthal orientations from  $\phi_0$  are shown for (a) unidirectional, (b) periodic, (c) chiral, and (d) isotropic ITO nanotree films grown at 2 nm/s. Integrated intensity from (440) XRD pole figures are illustrated by dotted black lines in the histograms. Solid black lines illustrate the integrated intensity from (440) XRD pole figures with isotropic ITO nanotree background signal subtracted. The initial flux direction ( $\phi_0 = 0^\circ$ ) is oriented from right to left as indicated by the horizontal dashed black line and arrow in each figure. Rotation of the flux is counter clockwise in (c) and (d). Bin size is  $10^\circ$ , and the outer ring corresponds to a maximum of (a) 99, (b) 111, (c) 75, and (d) 154 counts for each histogram. Reproduced with permission from *Crystal Growth and Design*.<sup>307</sup> Copyright 2013, American Chemical Society. .... 85
- Figure 5.9:** Histogram density plots of the branch orientation and length for (a) unidirectional, (b) periodic, (c) chiral, and (d) isotropic films. Bin color code indicates the number of counts at a particular orientation and length. Dotted blue lines indicate  $\phi_0$ , dotted red lines indicate  $\pm 45^\circ$  from  $\phi_0$ , and dotted green lines indicate  $\pm 135^\circ$  from  $\phi_0$ . .... 86
- Figure 5.10:** Typical BF-TEM images within a tilt series of an isotropic nanotree: (A) tilted at  $-65^\circ$ ; (B)  $0^\circ$  degree with red arrow indicating tilt axis; (C)  $+65^\circ$ . Reproduced with permission from *Crystal Growth and Design*.<sup>307</sup> Copyright 2013, American Chemical Society. .... 88
- Figure 5.11:** A volumetric rendering of an isotropic nanotree obtained from TEM tomography shown tilted at an arbitrary angle in (a), and sliced along its cross-section in (b). The red, blue and green arrows are used to identify axes between images. Reproduced with permission from *Crystal Growth and Design*.<sup>307</sup> Copyright 2013, American Chemical Society. .... 88

- Figure 5.12:** Diffraction line profiles for the 2.0 nm/s films that were used for pole-figures. Diffraction peaks in the profiles correspond to the expected peak positions for ITO (PDF: 01-089-4597) shown at the bottom of the figure. Reproduced with permission from *Crystal Growth and Design*.<sup>307</sup> Copyright 2013, American Chemical Society. .... 90
- Figure 5.13:** A TEM image of a nanotree cross-section at a branch-trunk interface is shown in (a). Electron diffraction patterns were taken at locations indicated by the white circles: (b) trunk, (c) trunk-branch interface and (d) branch. Reproduced with permission from *Crystal Growth and Design*.<sup>307</sup> Copyright 2013, American Chemical Society. .... 91
- Figure 5.14:** A projection view of a nanotree along its trunk obtained from a volumetric rendering is shown in (a). Diffraction analysis of a single nanotree with the electron beam perpendicular to the trunk was taken across a full 180°, at locations indicated by the white arrows, as shown from b to h. Diffraction patterns taken along branch axes (b, e, h) have a zone axis of [001], [0-10] and [00-1]. Reproduced with permission from *Crystal Growth and Design*.<sup>307</sup> Copyright 2013, American Chemical Society. .... 92
- Figure 5.15:** Pole figures for each films taken of the (222), (400), (440), and (622) diffraction peaks. The dashed circles indicate the expected radial positions for X-ray diffraction around a single crystal nanotree oriented [100] normal to the substrate and are located at 54.7° for (222), 45° for (440), and 25.2° (inner circle) and 72.5° for (622). The flat dashed line indicates the initial flux axis ( $\phi_0$ ), and the flux rotates counter clockwise in the chiral and isotropic films. Reproduced with permission from *Crystal Growth and Design*.<sup>307</sup> Copyright 2013, American Chemical Society. .... 94
- Figure 5.16:** XRD pole figures obtained from a periodic ITO nanotree film are shown for (a) (400), (b) (222), (c) (440) and (d) (622) planes. The initial flux direction ( $\phi_0 = 0^\circ$ ) is oriented from right to left as indicated by the horizontal dashed black line and arrow for each pole figure. The dashed circles indicate the expected radial positions for X-ray diffraction around a single crystal nanotree oriented [100] normal to the substrate. A schematic illustrating the crystal structure and facets of a single crystal ITO nanotree trunk growing in the [100] direction are shown from (e) cross-sectional and (f) top-down perspectives. Branch growth occurs in the four {100} directions normal to the trunk. Reproduced with permission from *Crystal Growth and Design*.<sup>307</sup> Copyright 2013, American Chemical Society. .... 96
- Figure 5.17:** Plan view schematic of competitive growth mechanism. Shown are two different azimuthal trunk orientations that have flux capture cross-sections of  $d$  (left) and  $2d$  (right)..... 98
- Figure 5.18:** (222) pole figure for a unidirectional nanotree grown to a nominal thickness of 150 nm. The dashed circle indicates the expected radial position (54.7°) for X-ray diffraction around single crystal nanotrees oriented [100]

normal to the substrate. The flat dashed line indicates the flux axis ( $\phi_0$ ). Reproduced with permission from *Crystal Growth and Design*.<sup>307</sup> Copyright 2013, American Chemical Society. .... 99

**Figure 5.19:** Sample measurements taken from top-down SEM images using ImageJ software for (a) unidirectional, (b) periodic, (c) chiral and (d) isotropic NW films. Five images (same as shown above) were measured for each array. One branch measured for per trunk. Lines were drawn from trunk-branch interface to branch tip. .... 101

**Figure 5.20:** Normalized radial histograms illustrating the number of **trunks** oriented with a certain angle from  $\phi_0$  for (a) unidirectional, (b) periodic, (c) chiral and (d) isotropic ITO nanotree films grown at 2 nm/s. The colored regions between  $0^\circ$  and  $90^\circ$  provide all the unique trunk orientations due to the four fold symmetry of the square cross-section of an ITO nanotree trunk. The data was mirrored around the origin for clarity, indicated by the grey bars. Symmetrized pole figure data was radially integrated and plotted over the histograms, as shown by the solid black (isotropic background subtracted) and dotted black (with isotropic background) lines. The initial flux direction ( $\phi_0 = 0^\circ$ ) is oriented from right to left as indicated by the horizontal dashed black line and arrow in each figure. Bin size is  $10^\circ$ , and the outer ring corresponds to a maximum of (a) 186, (b) 219, (c) 144, and (d) 281 counts for each histogram. Reproduced with permission from *Crystal Growth and Design*.<sup>307</sup> Copyright 2013, American Chemical Society. .... 102

**Figure 6.1:** Table of Contents figure published in *Nano Letters*.<sup>317</sup> This figure schematically depicts directed branch growth in epitaxially aligned nanotree arrays, enabling the fabrication of self-similar L-, T-, and X-shaped ITO nanotrees. .... 104

**Figure 6.2:** (a) Oblique view SEM of a nanotree film grown on YSZ. Region in the white box of (a) is shown magnified below in (b), with a schematic representation of epitaxial VLS-GLAD ITO nanotree growth. The vapor flux is deposited at oblique angles ( $\alpha$ ) relative to substrate normal, offset by an angle ( $\phi$ ) from the [100] direction of the single cubic crystal YSZ substrate. The inset depicts various surface diffusion processes that occur once the flux deposits material on the trunk sidewall. Growth conditions for nanotree array shown here are substrate temperature =  $300^\circ\text{C}$ , flux rate =  $0.1\text{ nm/s}$ ,  $\alpha = 85^\circ$  and  $\phi = 45^\circ$ . .... 107

**Figure 6.3:** (a) New heating set-up used for epitaxial nanotree growth, with a reduced size 4" chuck. (b) two 300 W halogen bulbs in each casing, four bulbs total. (c) Heating set-up installed in GLAD system, oriented with the flux  $85^\circ$  to substrate normal. QCM behind sample monitors deposition rate. (d) Macor head piece, and (e) ITO source material. .... 109

**Figure 6.4:** (a) Temperature measured by TC directly attached to Si substrate, and TC 1 cm above center of chuck as the variac controlling power to the lamps is

- incrementally increased. (b) Difference in temperature between the two TCs. .... 110
- Figure 6.5:** Cross-sectional SEM images of ITO NW films grown on Si substrates placed from one edge (a) to the other (f), through the center of the 4" chuck to test uniformity in the following order: (b), (c), (d) and (e)..... 111
- Figure 6.6:** Nanotrees grown on YSZ substrates at a variety of temperatures at 1 nm/s and  $\alpha = 85^\circ$ . Red arrows indicate in-plane flux direction..... 113
- Figure 6.7:** Nanotrees grown on YSZ substrates at a variety of deposition rates at 300 °C and  $\alpha = 85^\circ$ . Red arrows indicate in-plane flux direction. .... 113
- Figure 6.8:** The vapor flux is deposited at oblique angles ( $\alpha$ ) relative to the substrate normal, offset by an angle ( $\phi$ ) from the [100] direction of the single cubic crystal YSZ substrate. SHIM images of ITO nanotrees grown on YSZ with  $\alpha = 85^\circ$ , and (a-d)  $\phi = 45^\circ$  (resulting in L-shaped nanotrees), and (e-h)  $\phi = 0^\circ$  (resulting in T-shaped nanotrees). (a) and (e) are oblique images. (b), (c), (f) and (g) are plan view images. (d) and (h) are cross-sectional images. Red arrows depict vapor flux orientation, and black arrows indicate crystal directions of the YSZ substrate. All scale bars are 200 nm. Reproduced with permission from *Nano Letters*.<sup>317</sup> Copyright 2014, American Chemical Society. .... 114
- Figure 6.9:** Overlain XRD  $2\theta$  plots taken detected from a variety of positions above the sample. Red and green lines in (a) and (b) indicate boundaries for ITO peaks used in pole figure generation. Grey lines indicate background regions used for pole figure analysis. .... 116
- Figure 6.10:** XRD pole figures for (a) (400), (b) (222), (c) (440), and (d) (622) planes for an ITO nanotree array grown epitaxially on a YSZ substrate with 1 nm/s,  $\phi = 45^\circ$  and  $\alpha = 85^\circ$ . The red arrows correspond to the flux direction, and the black dotted lines in (b), (c) and (d) correspond to the expected radial positions for the diffraction peaks. The region with missing peaks at the outer radial ring in (d) was not measured. Reproduced with permission from *Nano Letters*.<sup>317</sup> Copyright 2014, American Chemical Society. .... 117
- Figure 6.11:** (a, b) HRTEM images of ITO NW-YSZ substrate interface. (b) white lines indicate stacking of lattice planes from substrate into NW trunk. (c, d) STEM images of the interface between the YSZ substrate and an ITO nanotree early in the growth process. Red lines in (d) indicate 0.26 nm measured in ITO trunk. Dashed white circle indicates edge dislocation at interface. Green lines indicate imperfect stacking of horizontal atomic columns in YSZ substrate. Reproduced with permission from *Nano Letters*.<sup>317</sup> Copyright 2014, American Chemical Society. .... 119
- Figure 6.12:** (a) HAADF-STEM image with electron beam oriented along [110] direction of ITO NW trunk. Bright spots indicate In or Sn atomic columns. Schematics of  $\text{In}_2\text{O}_3$  unit cells viewed along (b) [110], (c) [100], and (d) [111]

directions. Red and blue balls correspond to In and O atoms, respectively. (b), (c), and (d) were reproduced with permission from Rauf, I. A. *Appl. Phys. Lett.* **2008**, *93*, 143101.<sup>323</sup> Copyright 2008, AIP Publishing LLC. .... 120

**Figure 6.13:** One fifth of total branch orientation and length measurements taken from top-down SEM images for each of (a)  $\phi$  continuously rotated on Si, and (b)  $\phi$  continuously rotated, (c)  $\phi = 0^\circ$ , and (d)  $\phi = 45^\circ$  on YSZ. Reproduced with permission from *Nano Letters*.<sup>317</sup> Copyright 2014, American Chemical Society. .... 121

**Figure 6.14:** Plan view SEM images of nanotrees grown on YSZ substrates with (a)  $\phi = 45^\circ$ , (c)  $\phi = 0^\circ$ , and (e)  $\phi$  rotated. (g) Plan view SEM image of nanotrees grown on a Si substrate with  $\phi$  rotated. Radial density scatter plots shown in (b), (d), (f), and (h) depict 1892, 2552, 1866, and 1919 branch length and orientation measurements taken across  $140 \mu\text{m}^2$  of plan view SEM images of nanotree arrays in (a), (c), (e), and (g), respectively. Radial rings represent 100 nm length increments. Red arrows indicate flux direction. The in-plane [100] and [010] directions shown in (a) are the same for (a-f). All data in figure corresponds to growth conditions of rate = 1 nm/s, T = 300 °C and  $\alpha = 85^\circ$ . Reproduced with permission from *Nano Letters*.<sup>317</sup> Copyright 2014, American Chemical Society. .... 122

**Figure 6.15:** Plan view schematic of direct branch growth on select NW facets. (a)  $\phi = 45^\circ$  leads to L-shaped nanotrees, (b)  $\phi = 0^\circ$  leads to T-shaped nanotrees, and (c)  $\phi$  rotated leads to X-shaped nanotrees. Red arrows illustrate flux direction and the red lines along the surface indicate where the nanotree's cross-section is directly exposed to flux. Reproduced with permission from *Nano Letters*.<sup>317</sup> Copyright 2014, American Chemical Society. .... 124

**Figure 6.16:** (a) Plan view schematic of a nanotree grown with serial bi-deposition motion where the azimuthal flux position is periodically alternated between two positions separated by  $180^\circ$ . (b) Plan view SEM image, and (c) oblique SHIM image showing nanotrees grown using a SBD process, the alternated flux positions are indicated by the red arrows. The white dotted line circle in (b) indicates a possible interconnection between two nanotrees. (d) Radial density scatter plot of 1437 branch length and orientation measurements taken across an area of  $140 \mu\text{m}^2$  where each ring corresponds to 200 nm length. Reproduced with permission from *Nano Letters*.<sup>317</sup> Copyright 2014, American Chemical Society. .... 127

**Figure 7.1:** Sheet resistance for ITO NW films grown at different deposition angles ( $\alpha$ ), measured for as-grown, after annealing in air (anneal 1), and after H<sub>2</sub> anneal (anneal 2). .... 134

**Figure 7.2:** Sheet resistance for ITO NW films grown at (a)  $\alpha = 85^\circ$  and (b)  $\alpha = 50^\circ$ , and different deposition rates. Measured for as-grown, after annealing in air (anneal 1), and after H<sub>2</sub> anneal (anneal 2). .... 137

<b>Figure 7.3:</b> Comparison of the nucleation layer of NW arrays grown at various deposition rates. Figure reproduced with permission from <i>Nanotechnology</i> . <sup>326</sup> Copyright 2014, Institute of Physics.....	138
<b>Figure 7.4:</b> The Sn/In ratio of the nanowires as a function of flux rate. Composition was estimated by (a) XPS and by EDS through comparison of the (b) K- $\alpha$ lines of Sn and In and (c) the L- $\beta$ Sn lines to the L- $\alpha$ In lines. The dashed horizontal lines represent the average value for each set of data. Figure reproduced with permission from <i>Nanotechnology</i> . <sup>326</sup> Copyright 2014, Institute of Physics. 139	139
<b>Figure 7.5:</b> Sheet resistance for ITO NW films grown at $\alpha = 50^\circ$ , 0.2 nm/s, different deposition temperatures. Measured for as-grown, after annealing in air (anneal 1), and after H <sub>2</sub> anneal (anneal 2). .....	140
<b>Figure 7.6:</b> Photograph of various ITO NW films (a) as-grown, and (b) after first stage air anneal. (c) Transmission spectra for an ITO NW film grown at 1 nm/s, $\alpha = 50^\circ$ , and 240 °C, as-grown, after annealing in air, and after H <sub>2</sub> anneal. 142	142
<b>Figure 7.7:</b> (a) Transmission spectra for ITO NW films grown at 0.2 nm/s, 240 °C and different $\alpha$ , after annealing. (b) Average visible transmission (400 < $\lambda$ < 780 nm) for ITO NW films grown at 0.2 nm/s, 240 °C and different $\alpha$ . Measured for as-grown, after annealing in air (Anneal 1), and after H <sub>2</sub> anneal (Anneal 2). (a) Reproduced with permission from <i>Nanotechnology</i> . <sup>271</sup> Copyright 2012 Institute of Physics.....	143
<b>Figure 7.8:</b> (a) Optical transmission of ITO NW films deposited at $\alpha = 50^\circ$ , 240 °C and various flux rates, after annealing. (b) Average visible transmission (400 < $\lambda$ < 780 nm) for ITO NW films grown at $\alpha = 50^\circ$ , 240 °C and various deposition rates. Measured for as-grown, after annealing in air (anneal 1), and after H <sub>2</sub> anneal (anneal 2). (a) Reproduced with permission from <i>Nanotechnology</i> . <sup>271</sup> Copyright 2012 Institute of Physics.....	145
<b>Figure 7.9:</b> Average visible transmission for ITO NW films grown at 0.2 nm/s, and various deposition temperatures, for (a) $\alpha = 85^\circ$ and (b) $\alpha = 50^\circ$ . Measured for as-grown, after annealing in air (anneal 1), and after H <sub>2</sub> anneal (anneal 2). 146	146
<b>Figure 7.10:</b> Haacke's FOM ( $F_H$ ) for ITO NW films grown at (a) 0.2 nm/s, and 240 °C, at various $\alpha$ , and (b) $\alpha = 50^\circ$ , and 240 °C, at various deposition rates. 30/85° label in (a) refers to NW film grown with $\alpha$ changed midway through growth as shown in <b>Figure 3.19e</b> . .....	148
<b>Figure 8.1:</b> Summary of notable achievements in this thesis using VLS-GLAD. ....	151

# Symbols and nomenclature

---

$a$	Envelope function constant for branch growth extinction due to shadowing
$a_{ITO}$	Lattice constant of ITO
$a_{YSZ}$	Lattice constant of YSZ
$\alpha$	Vapour flux deposition angle relative to substrate normal
$A$	Flux capture area
BHJ	Bulk heterojunction
CVD	Chemical vapour deposition
$d$	Monolayer thickness
$dhkl$	Lattice spacing between (hkl) planes
$D$	Diffusion coefficient
GLAD	Glancing angle deposition
HAADF	High angle annular dark field
$e$	Elementary charge
EBE	Electron beam evaporation
EDS	Energy-dispersive X-ray spectroscopy (see EDX)
EDX	Energy-dispersive X-ray spectroscopy (see EDS)
$F_H$	Haacke's figure of merit
FIB	Focussed ion beam
$\gamma$	Flux modulation parameter due to rotation-induced shadowing or flux shuttering
$hkl$	Miller indices
HRTEM	High-resolution transmission electron microscopy
ICSD	Inorganic Crystal Structure Database

ITO	Indium tin oxide, or tin-doped indium oxide
$\mathbf{K}_0$	Incident X-ray wave vector
$\mathbf{K}$	Scattered X-ray wave vector
$L$	Branch length grown after time $t_{max}$
$\lambda$	Wavelength
NW	Nanowire
$O_0$	Lattice oxygen
OPV	Organic photovoltaics
$\phi$	Azimuthal substrate rotation angle
$\psi$	Tilt angle between substrate normal and X-ray scattering plane during pole figure measurement
PVD	Physical vapour deposition
$\theta$	Bragg angle
$r$	Instantaneous branch droplet radius
$R$	Flux rate
$R_s$	Sheet resistance
$\mathbf{Q}$	X-ray scattering vector
SAED	Selected area electron diffraction
SBD	Serial bi-deposition
sccm	Standard cubic centimeters per minute
SEM	Scanning electron microscopy
SHIM	Scanning helium ion microscopy
STEM	Scanning transmission electron microscopy
$T$	Temperature
$T_0$	Optical transparency

$\tau_{LS}$	Liquid-to-solid crystallization time
$\tau_{rot}$	Rotation period
TCO	Transparent conductive oxide
TEM	Transmission electron microscopy
THz	Terahertz
THz-TDS	Terahertz time-domain spectroscopy
$t_{max}$	Length of time required for a branch to grow
$\dot{V}_{in}$	Rate of incoming volume to branch droplet
$\dot{V}_{out}$	Rate of outgoing volume from branch droplet
VLS	Vapour-liquid-solid
VLS-GLAD	Vapour-liquid-solid glancing angle deposition
$V_O^{\bullet\bullet}$	Oxygen vacancy
XPS	X-ray photoelectron spectroscopy
XRD	X-ray diffraction
YSZ	Yttria-stabilized zirconia

# 1. Introduction

---

## 1.1 Motivation

Nanotechnology has forever changed the way humans live, think, and interact by enabling rapid advances in computational power, and expanding our knowledge of fundamental physical phenomena such as electrical conductivity, quantum mechanics, and the relationship between light and matter. Significant advances in energy generation and storage, lighting, catalysis, and sensing are a result of improved control over nanoscale processes. Nanofabrication methods need to be developed and improved upon as design targets for nanodevices become more intricate, and the required feature sizes continue to plummet. In this thesis, a bottom-up fabrication technique capable of producing arrays of 3D crystalline nanostructures with controlled alignment and structural anisotropy will be presented.

## ***1. Introduction***

---

There are two nanofabrication approaches: top-down fabrication, and bottom-up assembly. The top-down approach typically involves nanostructuring a planar thin film using lithography. It is currently the standard mass manufacturing method used for nanodevices due to its incredibly high yield and throughput. In contrast, bottom-up assembly relies on allowing matter to arrange itself into ordered nanostructures with a predictable shape, morphology, and crystal structure.<sup>1,2</sup> While the top-down approach is comparable to carving a large piece of lumber into the shape of a chair, the bottom-up approach is comparable to tree-shaping; the art of guiding the growth of a tree into the shape of a chair (Pooktre method, as shown in **Figure 1.1**). A deep understanding of the tree's growth mechanism is required to guide its growth into a chair with a desired shape. In principle, a bottom-up approach should reduce fabrication steps, and enable device architectures that would be highly challenging to achieve using a conventional top-down approach. In practice, however, it is also highly challenging to reliably guide materials into useful device architectures from the bottom-up.

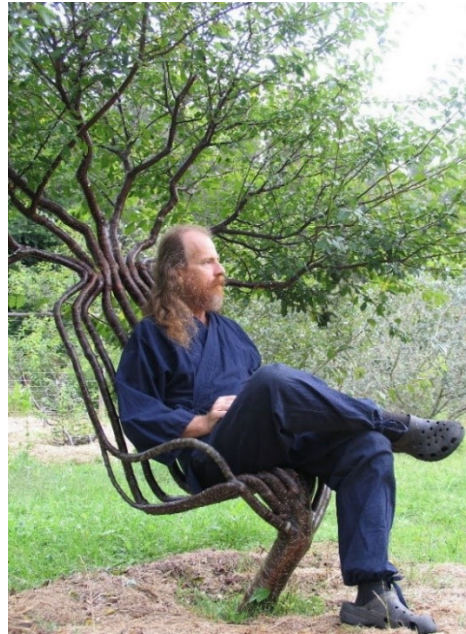


**Figure 1.1:** Tree-shaping – guiding the growth of a tree into a designed shape. Reproduced with permission from <http://pooktre.com/photos/living-chair/>.

## ***1. Introduction***

---

In bottom-up fabrication, the self-assembly of matter is guided to produce ordered architectures. Self-assembly was defined as “the autonomous organization of components into patterns or structures without human intervention” by Whitesides and Grzybowski.<sup>2</sup> Self-assembly can be guided using top-down fabricated templates or by engineering the growth conditions, such as temperature, pressure, and the concentration of material at the growth site. The resulting morphology of the nanostructures produced by bottom-up processes strongly depends on properties of the growth material, including composition, and crystal structure. In a paper from 2003 titled, “Nanoscale Science and Technology: Building a Big Future from Small Things”<sup>1</sup>, Lieber states:

*Central to my vision for nanotechnology is the idea that by developing and following a common intellectual path—the bottom-up paradigm of nanoscale science and technology it will be possible in the future to build (or more correctly, assemble) virtually any kind of device or functional system, ranging from ultra-sensitive medical sensors to nanocomputers. Underpinning this bottom-up paradigm is the controlled growth of nanoscale materials—the building blocks of the bottom-up approach—pursued within the disciplines of materials science and chemistry. Specifically, our goal is to control with atomic precision the morphology, structure, composition, and size of nanoscale materials, since these will define and enable our control over the physical properties of the resulting materials.*

While the synthesis of individual nanostructures with highly tunable functionality has been achieved, guiding the arrangement of nanostructures into ordered 3D architectures using bottom-up fabrication remains challenging. In this thesis, arrays of self-similar and preferentially aligned 3D nanostructures with controlled morphological anisotropy are produced by depositing material on select regions of structures to guide their self-assembly. The technique relies on depositing material on regions where growth is desired, and preventing material from reaching other regions. The technique is an additive fabrication approach, similar to 3D printing. Such control may be a powerful tool for achieving control over nanostructured architectures called for by Lieber.

### 1.2 Outline

Nanowires (NWs) are high aspect ratio crystalline nanomaterials that are often produced using a bottom-up process named vapour-liquid-solid (VLS) growth. NWs have enticing properties for applications in transistors, solar cells, and sensors. In this thesis, a technique named vapour-liquid-solid glancing angle deposition (VLS-GLAD) is shown to significantly enhance structural control in 3D branched NW architectures. The control offered by VLS-GLAD may enable the design of directional conductive pathways between adjacent NWs, and may lead to the growth of intricate interconnected 3D NW networks across large substrate areas.

VLS-GLAD is used to provide a collimated vapour flux to guide the growth of branched indium tin oxide (ITO) NWs. Enhanced control over morphology, branching and crystal texture will be presented. The collimated flux is deposited at oblique angles with respect to substrate normal, causing flux shadowing to prevent material from reaching directly behind growing structures. Asymmetric vapour deposition enables controlled anisotropic branching in nanotree arrays. Using substrate motion, the flux can be placed on select sides and heights of the growing NWs, significantly enhancing branch placement. The arrangement of these branched NWs into architectures for device applications are discussed. Properties of both individual and the ensemble of branched NWs are thoroughly investigated using a number of nanomaterial characterization techniques. In addition, branched ITO NW transparent electrodes are optimized for organic photovoltaic device applications.

The main capabilities achieved using VLS-GLAD presented in this thesis include:

1. Highly tunable height dependent morphological control.
2. Height controlled anisotropic branch growth.
3. Preferential azimuthal branch and nanotree crystal alignment without requiring epitaxial growth on a lattice matched substrate.

4. Fabrication of precisely aligned self-similar L-, T-, and X-branched NWs via epitaxial trunk growth on lattice matched substrates.
5. Arbitrary signals encoded into the diameter of branches along their length.
6. Tuning optical and electrical properties of nanostructured ITO transparent electrodes by optimizing deposition conditions and post-growth annealing procedures.

Chapter 2 will present the required concepts, techniques, and mechanisms to provide a background for the reader. The growth and applications of nanowires will be discussed, followed by an outline of the glancing angle deposition principles. Chapter 2 concludes with a brief description of nanomaterial characterization techniques used throughout this thesis. Chapter 3 will introduce the VLS-GLAD technique, provide an overview of work by previous groups, and will show significantly enhanced morphological control over branched ITO NW networks grown by self-catalyzed VLS. Chapter 4 will present how self-shadowing effects can be exploited to encode arbitrary oscillations along the diameter of a nanowire branch. Enhanced branch placement using a directional vapour flux to grow branches on select facets of NW will be demonstrated in Chapter 5, followed by a discussion of a shadow mediated competitive growth mechanism that allows nanotrees to be azimuthally aligned without requiring epitaxy at the substrate. In Chapter 6, branch placement is decoupled from competitive alignment by growing nanowires epitaxially on a lattice match substrate. Directed branch growth on these epitaxially aligned nanotrees resulting in arrays of self-similar L-, T-, and X-branched nanotrees. Conductivity optimization and the preliminary fabrication of electrodes will be presented in Chapter 7. Finally, the thesis will be summarized and directions for future work proposed in Chapter 8.

# 2. Background

---

## 2.1 Focus

This thesis involves a technique that uses glancing angle deposition (GLAD) to control the vapour-liquid-solid (VLS) growth of crystalline branched nanowires. Therefore, NW growth and properties will be described first, followed by a discussion of GLAD principles. The intersection between crystal growth and ballistic vapour deposition will then be presented. The chapter will conclude with a brief description of essential techniques used to characterize the morphology, crystallinity, and composition of the nanostructures in this thesis.

## 2.2 Nanowires (NWs)

### *2.2.1 Properties*

NWs are 1D crystalline nanostructures with enticing properties for nanoelectronic applications. NWs have been the subject of intensive research over the past twenty years, and a number of excellent review papers regarding the growth, properties and applications of NWs are available.<sup>3-11</sup> NWs are typically produced by vapour-liquid-solid (VLS) growth<sup>12-15</sup>, or by high-aspect ratio etching of crystalline substrates<sup>16,17</sup>. NWs are crystals with two dimensions confined between 1 to 100

## 2. Background

---

nm, and the third dimension typically extends to microns, but has been grown to lengths upward of millimeters.<sup>18,19</sup> The crystalline structure and smooth faceted surfaces of VLS grown NWs ensure high quality 1D charge transport properties as compared to amorphous or polycrystalline materials shaped at a similar size scale.<sup>10,20</sup> As a result, NWs exhibit excellent electrical properties for applications in transistors<sup>20–30</sup>, and solar cells<sup>31–42</sup>. In addition, NWs are applicable as biological sensors<sup>43–52</sup> due to their diameter being on the order of many biological processes, and their high surface to volume ratio. NW surfaces can be functionalized to interact strongly with certain analytes. The smooth faceted surfaces of NWs enable epitaxial growth on their outer walls, allowing for the fabrication of core-shell p-n junctions.<sup>53–55</sup> Extremely sharp doping profiles can also be formed along the length of a NW simply by changing the precursor gas during growth.<sup>56,57</sup> In addition, epitaxy between materials with relatively large lattice mismatches due to strain relaxation on a NW's surface is achievable, enabling the fabrication of devices with previously incompatible materials.<sup>58–61</sup> The functional properties and growth of NWs have been well developed, however, new approaches to arrangement of these 1D building blocks into device architectures still need to be developed. Examples of vertically aligned Si NWs fabricated by Wang et al., and microwires grown by Kayes et al. via VLS growth are shown in **Figure 2.1 a** and **b**, respectively.

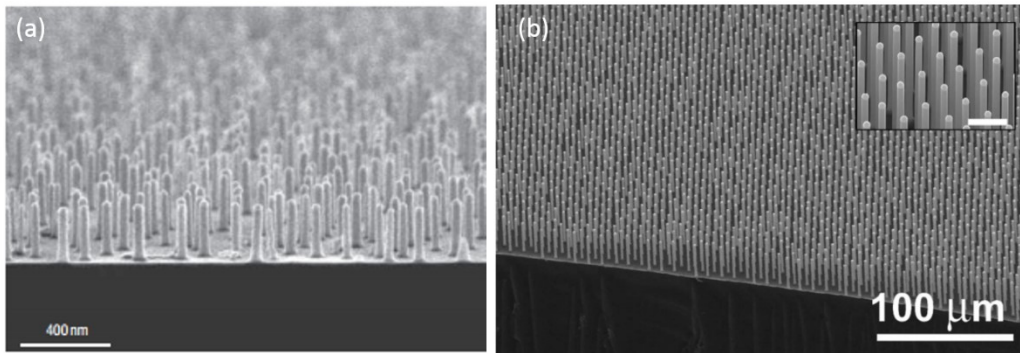


**Figure 2.1:** (a) Si NWs grown using Al catalyst, Reprinted by permission from Macmillan Publishers Ltd: *Nature Nanotechnology*<sup>62</sup>, copyright 2003. (b) Si wires grown using Cu catalyst, reprinted with permission from Kayes, B. et al.'s work.<sup>63</sup> Copyright 2007, AIP Publishing LLC.

### ***2.2.2 1D Crystal Growth***

An excellent source describing the basics of crystal growth is available from Markov.<sup>64</sup> 1D crystal growth refers to a crystal growing rapidly in one direction, requiring a feature that preferentially collects adatoms on one side of the crystal's surface to favour anisotropic growth. Prior to 1964, a screw-dislocation driven growth mechanism proposed by Frank was the dominant theory used to explain the growth of 1D crystals.<sup>65</sup> Frank suggested that unidirectional crystal growth was a result of energetically favorable accommodation of adatoms on a self-perpetuating step created by a screw dislocation at the tip of the growing crystal.<sup>66-70</sup> A schematic adapted from the work by Jin et al. illustrating screw dislocation driven 1D crystal growth, is shown in **Figure 2.2**.<sup>71</sup> The high surface energy provided by the dangling bonds at a step results in the preferential adsorption of adatoms. The incorporation of adatoms along the step will lead to continued propagation of the screw dislocation, leading to continuous anisotropic growth. Therefore, the nucleation rate is higher at the tip of the crystal compared to at the crystal's sidewalls or at the substrate surface due to the high concentration of adatoms. As a result, crystal growth is faster in the direction orthogonal to the screw dislocation, leading to 1D crystal growth.

However, three key observations made in numerous 1D crystal growth studies suggested a different mechanism was at play: many were found to be dislocation free, the presence of certain impurities was necessary for unidirectional growth, and "small globules" observed on the tips of the crystals were found to have a higher concentration of impurities than the rest of the structure.<sup>12-14</sup>

## 2. Background

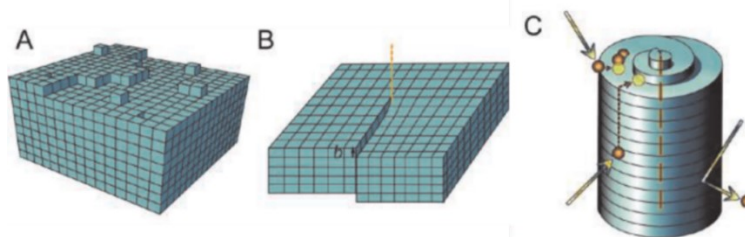


**Figure 2.2:** Schematic for screw driven 1D crystal growth. (A) a step on a dislocation free surface, depicting conventional layer by layer crystal growth. (B) Depicts a screw dislocation that has a self-perpetuating step. (C) Depicts preferential adsorption of adatoms at tip of growing crystal, leading to 1D crystal growth along the screw dislocation. Adapted with permission from *The Journal of Physical Chemistry Letters*.<sup>71</sup> Copyright 2010 American Chemical Society.

### 2.2.3 Vapour-Liquid-Solid (VLS) Growth

The aforementioned observations led Wagner and Ellis to intentionally include Au as an impurity on the substrate prior to Si vapour deposition, leading to their seminal VLS growth paper in 1964, which has been cited over 3000 times.<sup>13</sup> First, a thin film of gold deposited onto a  $\langle 111 \rangle$  Si substrate, and then the temperature was elevated to 950 °C.  $\text{SiCl}_4$  and  $\text{H}_2$  was then flown over the molten film of Au, resulting in the growth of 1D Si crystals with hemispherical tips composed of an Au-Si alloy. The VLS process is depicted in the classic schematic adapted from Wagner and Ellis's work in **Figure 2.3**.

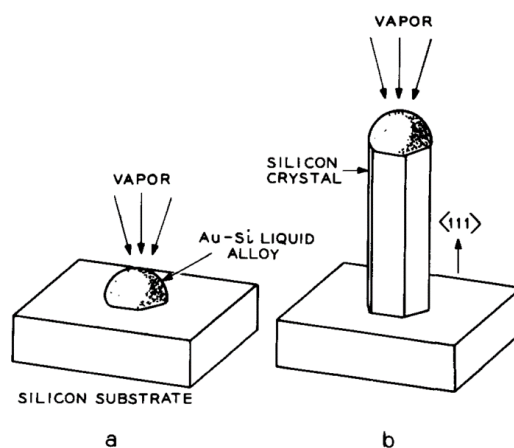


**Figure 2.3:** Schematic of Au-catalyzed Si VLS growth. (a) Vapour deposition on Au-Si liquid alloy droplet. (b) Crystalline Si-NW with Au-Si alloy at the tip. Reprinted with permission from Wagner and Ellis' work.<sup>13</sup> Copyright 1964, AIP Publishing LLC.

## ***2. Background***

---

It was postulated that the Au must have somehow been lifted on top of the growing crystals. Wagner and Ellis reached the conclusion that liquid Au droplets form early in growth and play a similar role to the screw dislocation in the mechanism proposed by Frank. Si vapour is preferentially adsorbed to the liquid droplets due to their high sticking coefficient; meaning once adsorbed, adatoms have a much lower probability of escaping the droplet surface compared to adatoms on the bare substrate. Adatoms on the substrate surface are highly mobile in comparison, and therefore, liquid droplets serve as “sinks” for adatoms migrating on the surface; resulting in a large proportion of the deposited Si becoming stuck to the surface of the droplets.

The Au droplets become Au-Si alloys as Si diffuses into the droplet. Recently, in-situ transmission electron microscopy was used to image the early stages of Au-catalyzed VLS Si NW growth in real-time, providing insight into the alloy formation and nucleation stages.<sup>72–74</sup> The alloy becomes supersaturated as the Si concentration in the droplet continues to rise, driving the precipitation of solid Si onto the substrate surface underneath the liquid droplet. As a result, Si crystals grow layer-by-layer underneath the droplets, and the droplets are lifted on the tip of the crystals, sustaining growth as long as the droplets remains sufficiently concentrated with Si. The term VLS growth was used to describe this crystal growth process, and has been studied extensively for the past 50 years.

### ***2.2.4 NW Applications***

NWs are ideal structures for transistors due to their attractive properties: width can be controlled below size-scales achievable by conventional lithography; scattering of charge carriers is reduced due to their crystalline structure and smooth surfaces; and high yield fabrication of NWs with uniform electrical performance is readily achievable.<sup>20,25,55</sup> Using core-shell epitaxy, gate oxides and metal gates can be grown on the sidewall of NW channels, enabling the fabrication of cylindrical wrap-gated transistors that enhance electrostatic control over the channel compared to conventional single sided gate configurations.<sup>20,23,28,30,75</sup> In some cases, the electrostatic control is sufficient to deplete the channel of the charge carriers upon

## ***2. Background***

---

the application of an “off” gate voltage.<sup>20,27,30,76,77</sup> Therefore device fabrication is simplified due to the elimination for the need of abrupt dopant concentration gradients to be formed between the channel, and the source and drain. Recently, the highest reported device density for any reported nanoelectronic system was fabricated using NW components.<sup>78</sup> This result suggests NWs may play a role in maintaining the rapid pace of Moore’s Law of increasingly miniaturized computation architectures.

NWs with core-shell p-n junctions along their length may improve performance in solar cells by reducing the distances generated minority charge carriers need to travel to reach their majority carrier region.<sup>34,35,40</sup> NW solar cells have been shown to increase defect tolerances, easing fabrication requirements.<sup>42</sup> High efficiencies attained in vertically oriented NW arrays have been achieved due to their excellent light absorption and trapping properties.<sup>16,41,79,80</sup> NWs also make excellent materials for sensors due to their high surface to volume ratio and the ability to controllably functionalize their smooth surfaces. For example, a pH sensor can be fabricated simply by functionalizing a p-type Si NW’s surface to interact strongly with H<sup>+</sup> ions.<sup>50</sup> Therefore, the H<sup>+</sup> concentration determines the NW’s surface charge, behaving much like a gate voltage, and the pH can be determined by measuring the conductivity of the wire. Biological sensors designed to interact with more sophisticated molecules have been fabricated using a very similar approach.<sup>43</sup>

## 2. Background

### 2.2.5 Branched NWs

Branched NWs, also known as “nanotrees”, are 3D nanostructures composed of NW trunks and branches.<sup>32,71,81–94</sup> Branches are grown by epitaxial VLS on the faceted sidewall of a NW trunk, and offer the unique capability of arranging NWs in three-dimensions which may enable access to new NW device architectures. 3D nanotree electrodes have been shown to enhance charge collection from the surrounding photoactive material in an organic solar cell device, mimicking the evolved solution of trees for efficiently capturing light and transporting nutrients.<sup>95</sup> Branched NWs increase the surface area above that of 1D NWs, which may enable improved sensing, and catalysis.

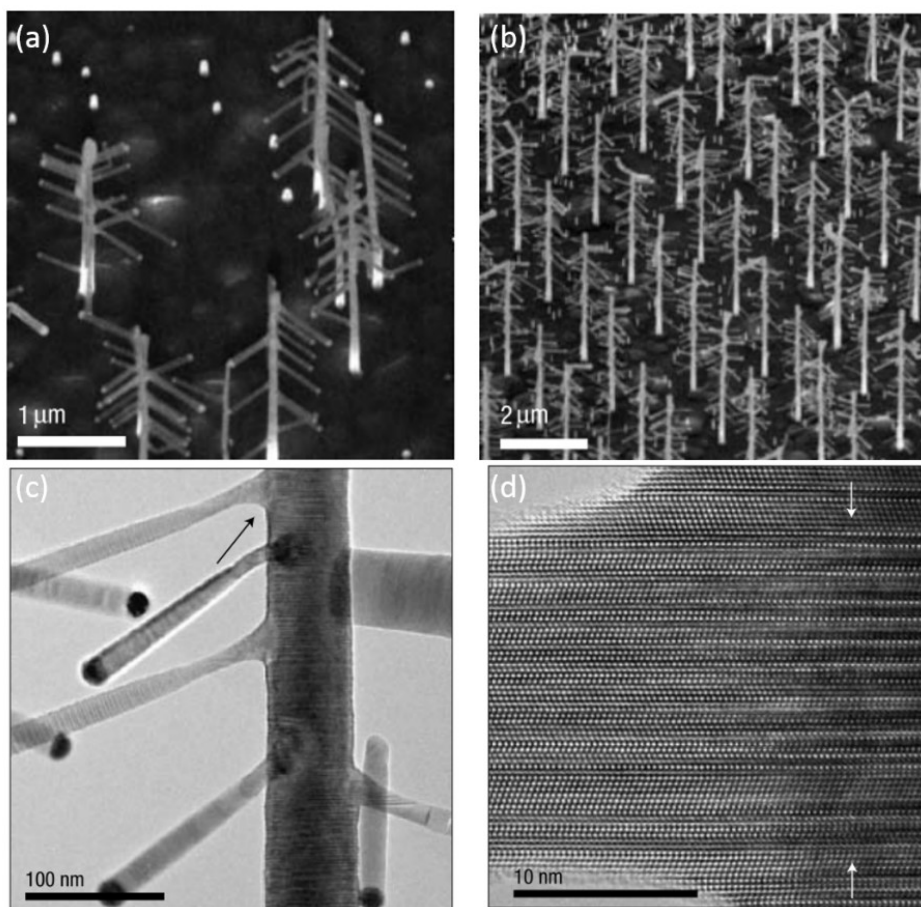


**Figure 2.4:** (a-b) SEMs of GaP nanotrees, (c) TEM image of trunk with five branches, (d) HRTEM image indicating epitaxial growth of branch on trunk (image taken from region indicated by arrow in (c)). Reprinted by permission from Macmillan Publishers Ltd: *Nature Materials*, copyright 2004.<sup>83</sup>

## ***2. Background***

---

Liquid droplets can be deposited on the trunk sidewall to catalyze branch growth by a variety of methods, including: a separate catalyst deposition step<sup>83,84,86</sup>; surface migration from primary growth droplet<sup>96</sup>; self-catalyzed placement<sup>97-99</sup>; in-situ catalyst formation<sup>88</sup>; or co-evaporation of catalysts<sup>100</sup>. Branches with different compositions as the trunk have been grown, such as Ge NW branches grown epitaxially on Si NWs.<sup>101</sup> In addition, screw dislocation driven trunk growth followed by secondary VLS growth of branches has resulted in unique helical branched structures.<sup>71,89</sup> Epitaxially grown and aligned GaP nanotrees from the work by Dick et al. are shown in **Figure 2.4**. Aerosol Au particles were deposited on the trunks to subsequently catalyze branch growth. Branch growth was shown to be epitaxial on the sidewall of the trunk using high-resolution transmission electron microscopy imaging (**Figure 2.4d**). In this thesis, significantly enhanced control over branch placement will be demonstrated.

### ***2.2.6 Interconnected Nanotree Architectures***

Branched NWs are building blocks for the bottom-up fabrication of interconnected 3D NW networks, and offer a new approach to constructing nanoscale architectures for device applications.<sup>84,87,93,100,102-105</sup> To fabricate NW networks, the trunks are periodically arranged on a substrate using electron beam or nanoimprint lithography to pattern seeds that will alloy with the vapour, and catalyze VLS growth. NW branches are grown epitaxially on the sidewall of the trunk, therefore, if the trunks are grown epitaxially on a lattice matched substrate, their facets will be azimuthally aligned, resulting in branches growing along a discrete number of in-plane directions determined by the substrate crystal orientation. If the seed pattern is strategically designed to reflect the crystal symmetry of the substrate and NW material, branch growth can be directed toward adjacent trunks to form connections.

## 2. Background

A schematic adapted from Dick et al. depicting the fabrication of interconnected NW networks using epitaxial growth and pre-patterned seeding is shown in **Figure 2.5**.<sup>84</sup> **Figure 2.5g** shows an SEM image of the resulting NW network. In the work by Dick et al., isotropic interconnectivity had been achieved, however, height dependent anisotropic interconnectivity throughout NW networks has yet to be achieved. Improved control over positioning branches on select sides and select heights of NWs would enable the fabrication of NW networks with complex conductive pathways. Precise branch positioning is a capability currently lacking in the NW community<sup>81,90,106</sup>. The improved control over branch placement demonstrated in this thesis may enable design of conductive pathways throughout NW networks.

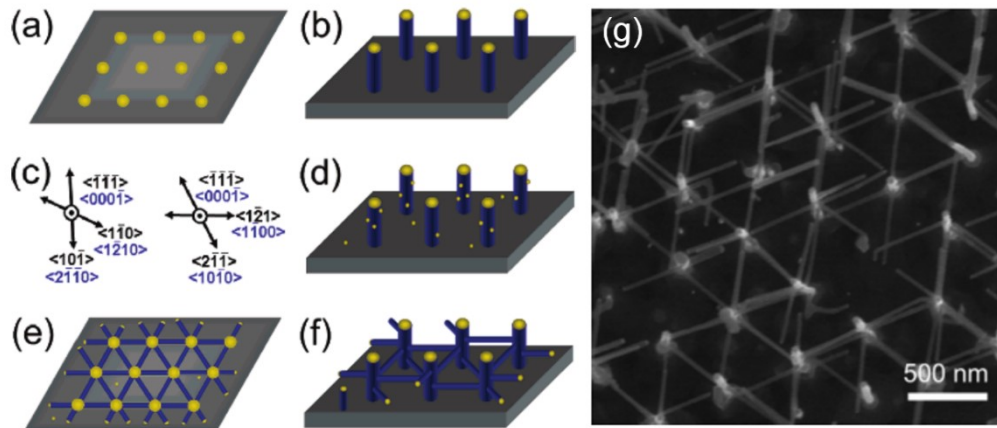


**Figure 2.5:** (a-f) Schematic for the fabrication of position controlled, interconnected branched InAs NWs epitaxially grown on InP substrate. Gold seeds are placed on NW sidewalls in (d) for epitaxial branch growth. (g) SEM image of the resulting NW network. Adapted with permission from *Nano Letters*.<sup>84</sup> Copyright 2006 American Chemical Society.

## 2.3 Glancing Angle Deposition (GLAD)

### *2.3.1 Introduction*

Glancing angle deposition (GLAD) is a physical vapour deposition (PVD) technique used to fabricate nanostructured thin films.<sup>107–113</sup> During GLAD, a collimated vapour flux is directed onto a steeply tilted substrate that can be rotated around two axes (**Figure 2.6**). The angle between the flux and substrate normal is referred to as the deposition angle ( $\alpha$ ), and is controlled by tilting the substrate. The azimuthal angle ( $\phi$ ) can also be controlled independently by rotation about substrate normal, enabling the position of the vapour source to be changed from the perspective of the developing film. At oblique deposition angles ( $\alpha > \sim 70^\circ$ ) shadowing of the flux between adjacent nuclei results in the evolution of separated columns (**Figure 2.7**). The growth direction of columns can be guided during deposition using substrate motion, enabling a high degree of morphological control over nanostructured thin films. GLAD films are applicable as humidity sensors<sup>114–116</sup>, nanostructured solar cells<sup>117–124</sup>, ultrathin layer chromatography<sup>125–132</sup>, and liquid crystal alignment<sup>133–136</sup>.

A highly collimated flux is required to control geometric shadowing between adjacent structures. Electron beam evaporation (EBE) is the preferred PVD method to achieve good flux collimation due to lower deposition pressures compared to sputtering, and smaller source size compared to thermal evaporation. In addition, a large source to substrate distance is used to further collimate the flux. EBE will be used to deposit ITO throughout this thesis as shown schematically in **Figure 2.6**.

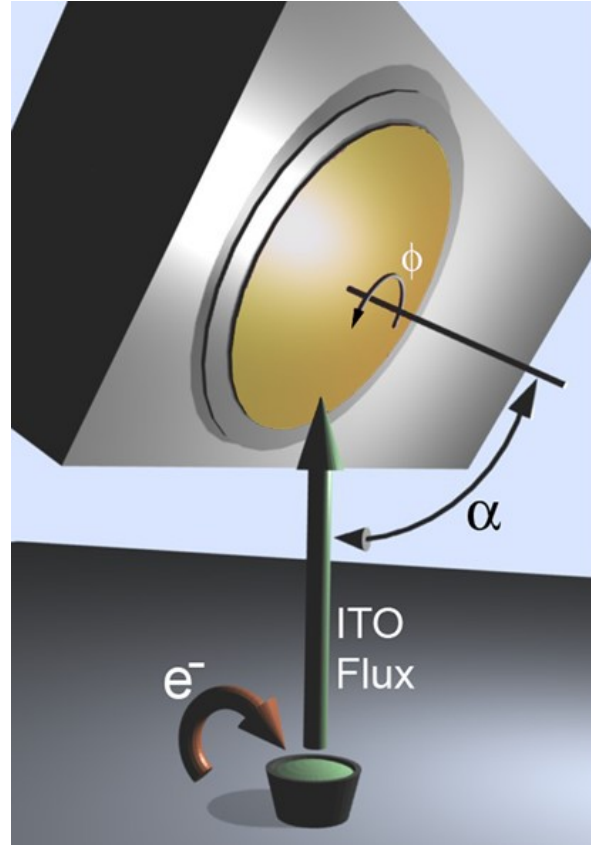


**Figure 2.6:** Schematic of e-beam evaporated ITO deposited using GLAD.  $\alpha$  and  $\phi$  are controlled by stepper motors during deposition. Adapted with permission from *Nanotechnology*.<sup>122</sup> Copyright 2011 Institute of Physics.

During GLAD, shadowing of the collimated flux prevents material from reaching regions behind nuclei that form on the substrate as adatoms begin to agglomerate and form raised islands on the substrate (**Figure 2.7b**).<sup>137</sup> Nucleation is inhibited in regions shadowed from flux in conditions of limited adatom mobility on the substrate (ie low temperature). As nuclei increase in size, ballistic deposition eventually results in growth material accumulating solely on top of the separated nuclei, leading to growth of structures toward the incoming vapour flux. This process leads to the growth of separated nanocolumns inclined at an angle  $\beta$  with respect to substrate normal (**Figure 2.7c**).

## 2. Background

$\beta \neq \alpha$  in general, instead  $\beta$  depends on  $\alpha$ , substrate temperature, pressure, crystal structure, growth mechanism, and surface diffusion. As will be seen in this thesis, the growth direction of VLS grown ITO NW structures appear to be independent of  $\alpha$ , which deviates from what is typically observed in conventional GLAD. Smaller nuclei and columns stop growing as they become increasingly shadowed from flux by larger structures as depicted in **Figure 2.7d**. Shadow mediated competitive growth is inherent to GLAD, and will be investigated in detail in this thesis.

### 2.3.2 Nanostructured Thin Films

Structures cast longer shadows as  $\alpha$  is increased, enabling control over spacing between adjacent structures. The azimuthal orientation of the collimated flux with respect to the growing columns can be controlled by rotating the substrate in  $\phi$ . Columns grow toward the flux, therefore, substrate rotation can be used to guide the growth of columns into more complex nanostructures (**Figure 2.8**), including: helices, vertical posts, and chevrons.<sup>108,110–112</sup>

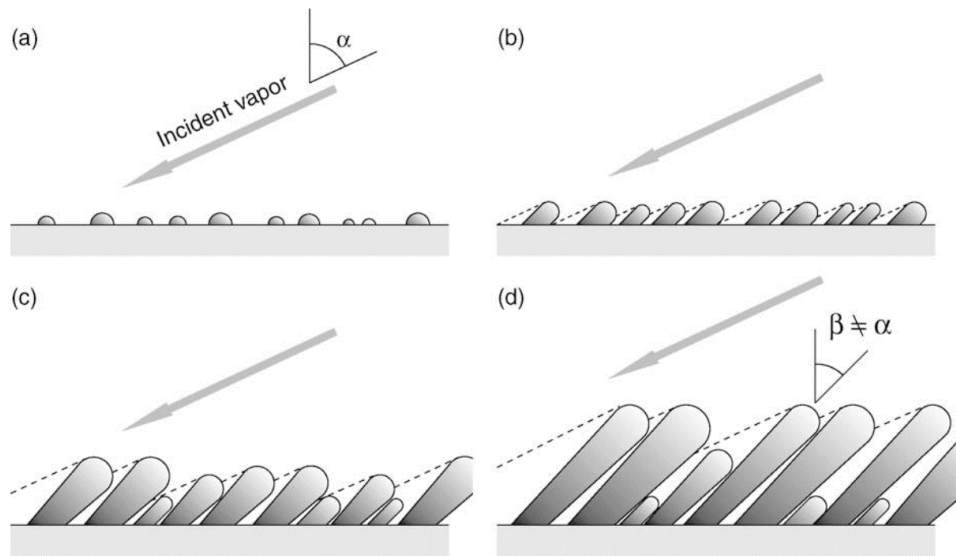


**Figure 2.7:** Schematic of shadowing in GLAD leading to slanted post films. (a) Formation of nuclei on substrate surface. (b) Nuclei begin to cast shadows. (c) Columnar growth begins, smaller structures are starved from flux. (d) Columns grow inclined at an angle  $\beta$ . Adapted with permission from *Handbook of Deposition Technologies for Films and Coatings*.<sup>138</sup> Copyright 2010 Elsevier.

## 2. Background

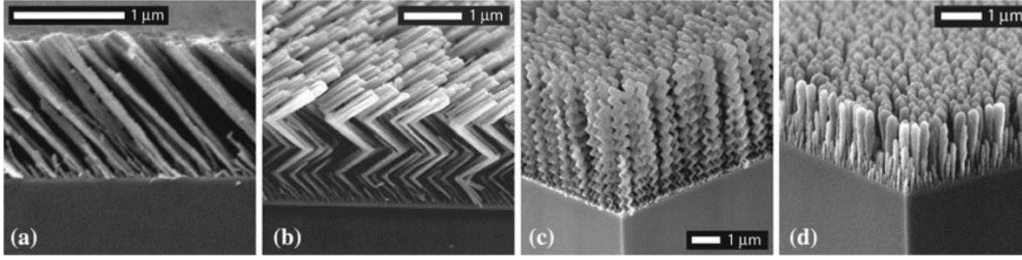


**Figure 2.8:** Various GLAD morphologies: (a) slanted post, (b) zig-zag posts, (c) helical posts, and (d) vertical post. Adapted with permission from *Journal of Materials Science: Materials in Electronics*.<sup>141</sup> Copyright 2006 Springer.

Alternating  $\phi$  between  $0^\circ$  and  $180^\circ$  results in columns slanting back and forth as they follow the apparent position of the flux, leading to chevron structures shown in **Figure 2.8b**. Slow rotation about  $\phi$  causes the growth direction of the column to slowly rotate, leading to the growth of helical structures shown in **Figure 2.8c**. The helical morphology is lost when  $\phi$  is rapidly rotated since the apparent vapour source essentially becomes isotropic azimuthally, leading to the growth of vertically oriented columns (**Figure 2.8d**). More complex substrate motion algorithms can be designed to achieve further control over film morphology.<sup>139,140</sup> The morphology of GLAD films is primarily determined by geometrical features of the vapour flux, and surface diffusion properties of the material. In contrast, the shape of VLS grown crystals is largely dependent on the crystal properties of the material.<sup>10</sup>

### 2.3.3 Seeding

In VLS growth lithographically patterned seeds can be liquefied to collect adatoms from an isotropic vapour flux, due to their high sticking coefficient, leading to the growth of periodically arranged arrays of NWs, as previously discussed. In contrast, seeding in GLAD relies on ballistic flux deposition solely onto pre-patterned seeds on the substrate to grow ordered columnar films (**Figure 2.9**). Seed spacing must be designed for a particular  $\alpha$  to ensure shadowing is sufficient between seeds to prevent deposition on the substrate, and that seeds do not shadow adjacent seeds from receiving flux. Seeding in GLAD eliminates stochastic nucleation, leading to a uniform local shadowing environment for the growing

## 2. Background

columns which significantly enhances morphological control.<sup>142–147</sup> Physical seeding during GLAD enables the fabrication of 3D architectures composed of periodically arranged nanocolumns with highly uniform shape and morphology (Figure 2.10).

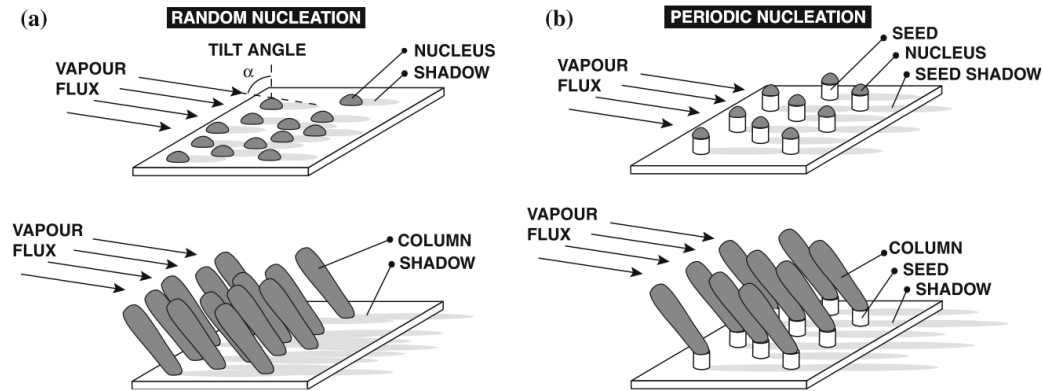


**Figure 2.9:** Illustration of (a) stochastic or random nucleation versus (b) periodic nucleation on pre-patterned seeds. Taken with permission from *Journal of Materials Science: Materials in Electronics*.<sup>141</sup> Copyright 2006 Springer.

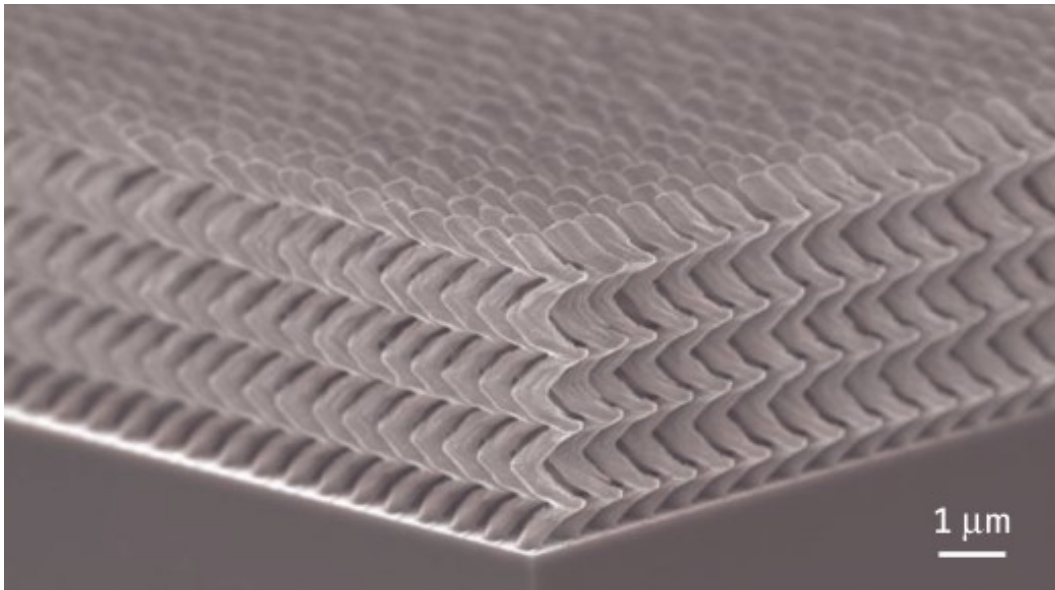


**Figure 2.10:** Highly ordered square spiral GLAD film grown on top of pre-positioned seeds. Taken with permission from *Science*.<sup>107</sup>

### 2.3.4 Crystal texture in GLAD films

GLAD nanostructures are typically polycrystalline or amorphous unlike crystalline structures obtained through VLS growth.<sup>140</sup> In this thesis, the intersection between VLS crystal growth and GLAD will be explored. This section presents a discussion regarding the atypical case of crystalline growth using GLAD, and how ballistic vapour deposition can lead to the evolution of crystal texture through shadow mediated competitive growth mechanisms.

During GLAD processes, crystalline column growth is occasionally achieved at lower temperatures than typically required for crystal growth ( $T_{Growth} < \sim 0.3T_{Melting}$ )<sup>137</sup> due to reduced adatom mobility requirements for posts with nanoscale dimensions.<sup>148</sup> Following initial observations of preferred crystalline orientations in GLAD posts<sup>147-149</sup>, numerous studies regarding the GLAD growth of crystalline and polycrystalline nanorods composed of a variety of material systems have been reported.<sup>124,150-171</sup>

Crystal texture refers to the degree of alignment of crystallites in a polycrystalline sample.<sup>172</sup> Fiber texture is used to describe the case where crystallites in a thin film have a preferred orientation in the axial direction (typically pointing vertically on the substrate), and a random azimuthal orientation. Biaxial texture is used to describe the case where crystallites are preferentially aligned both in- and out-of-plane of the substrate.

GLAD can be used to selectively grow crystallites oriented with high surface energy facets pointing vertically, enabling fiber texture to be achieved even in the case of random crystallite nucleation on a non-lattice matched substrate.<sup>150</sup> High surface energy facets exhibit faster vertical growth rates due to low adatom mobility; adatoms stick to high energy facets, leading to enhanced vertical growth rates.<sup>110</sup> Karabacak et al. used GLAD to selectively grow  $\beta$ -W or  $\alpha$ -W crystals in a film that nucleates with a mixture of crystal phases.<sup>150</sup>  $\beta$ -W posts have high surface energies, and therefore a high vertical growth rate.  $\alpha$ -W crystals have higher adatom mobility, and therefore, adatoms diffuse to column sidewalls and contribute

## 2. Background

to lateral growth, slowing vertical growth. During GLAD growth, the  $\alpha$ -W phase goes extinct due to increased shadowing from the enhanced vertical growth rate of  $\beta$ -W crystallites (**Figure 2.11b**). Conversely, in an isotropic deposition geometry (non-GLAD)  $\alpha$ -W oriented films result (**Figure 2.11a**). The enhanced lateral  $\alpha$ -W phase growth rate results in burying of the  $\beta$ -W phase. Therefore, the orientation of the crystallites in the film depends strongly on the geometry of the vapour flux.

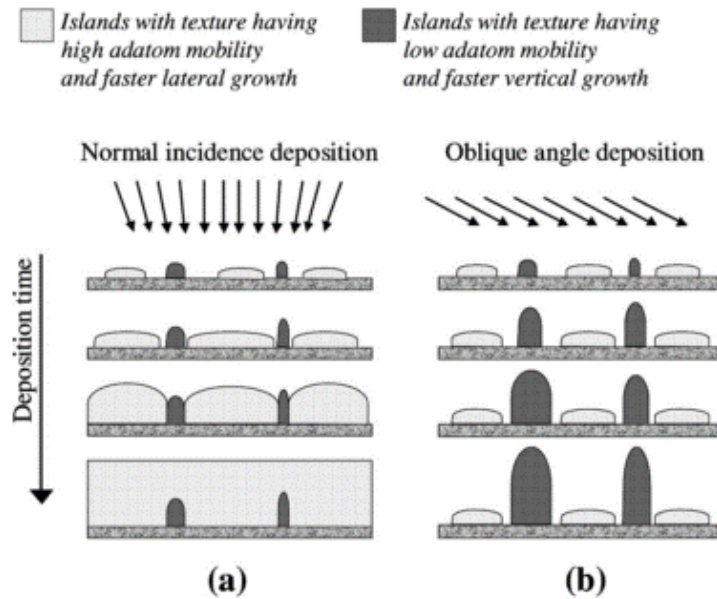


**Figure 2.11:** Schematic illustrating texture evolution mechanisms in crystalline W films at (a) normal deposition, and (b) oblique angle deposition. Taken with permission from *Applied Physics Letters*.<sup>150</sup> Copyright 2003, AIP Publishing LLC.

GLAD can also be used to engineer the azimuthal flux distribution to grow crystallites with a select in-plane orientation, resulting in biaxially textured films.<sup>159,161,166–168,170,171</sup> One application of biaxially textured GLAD films is to act as a buffer layer on amorphous substrates to enable subsequent epitaxial thin film growth.<sup>161,167</sup> LaForge et al. demonstrated a flux engineering methodology capable of growing films composed of crystalline Fe nanocolumns with their triangular cross-sections preferentially aligned in-plane.<sup>170</sup>  $\phi$  was alternated between three positions separated by  $120^\circ$ , resembling a three-fold symmetric flux distribution. A large number of nanocolumns oriented with their triangular cross-section such that each of the three flux positions was normal to each sidewall were observed

## 2. Background

---

following growth. It was postulated that evenly distributing the flux on the facets of the growing crystallites gave crystallites with the preferred orientation a competitive advantage during deposition. Conversely, an isotropic azimuthal flux configuration (achieved by rotating  $\phi$  continuously) resulted in random alignment of the crystallites' triangular cross-sections. The flux engineering technique developed by LaForge et al. is used extensively in this thesis.

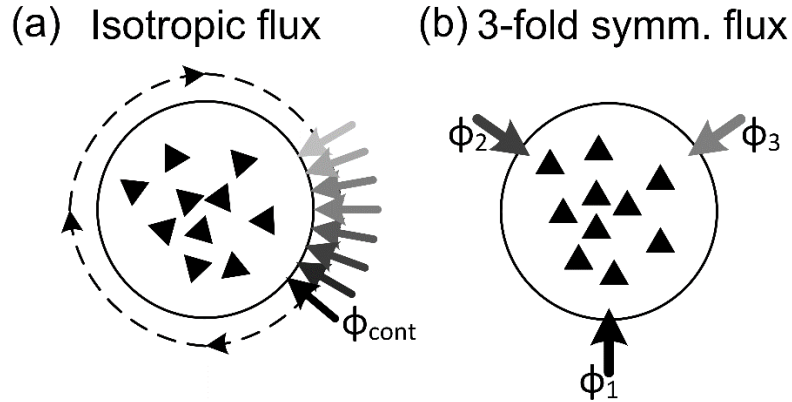


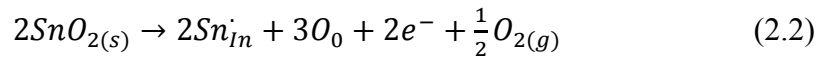
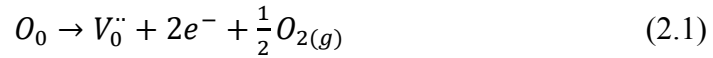
**Figure 2.12:** Schematic of azimuthal flux configurations and resulting crystallite alignment. (a) substrate rotation led to randomly oriented crystallites. (b) Symmetric 3-fold azimuthal flux configuration led to aligned crystallites, and biaxial film texture. Adapted with Permission from *Crystal Growth and Design*.<sup>170</sup> Copyright 2012 American Chemical Society.

### 2.4 Indium Tin Oxide (ITO)

ITO is the primary material used throughout this thesis. ITO has many useful properties, including: (i) ITO is a transparent conductive oxide (TCO)<sup>173–193</sup>, and (ii) branched ITO NWs are produced through a low temperature self-catalyzed VLS growth process<sup>97–99,194–202</sup>.

#### 2.4.1 Electrical and Optical Properties

ITO is the standard transparent electrode used in organic devices, including: organic light emitting diodes (OLEDs), and organic solar cells.<sup>183,203–213</sup> ITO is a wide bandgap ( $\sim 4$  eV), degenerately doped n-type semiconductor. Therefore, ITO has the unique property of being simultaneously transparent to visible light and conductive. Sn and O-vacancies act as electron donors in an  $\text{In}_2\text{O}_3$  lattice.  $\text{Sn}^{4+}$  substitutes  $\text{In}^{3+}$  in the  $\text{In}_2\text{O}_3$  lattice, donating an electron. The following equations describe how electrons are introduced into the lattice via incorporation of Sn and O:<sup>174</sup>



O-vacancies donate two electrons to the conduction band ( $\text{O}^{2-}$  is removed from lattice). Due to the highly doped nature of ITO, the bandgap is wider than  $\text{In}_2\text{O}_3$  (3.75 eV to 4 eV) since the low energy bands in the conduction band are occupied (Burstein-Moss shift).<sup>181,186,207,214–219</sup> ITO has a relatively high work function, reported between 4.1 eV<sup>220</sup> to 5.3 eV<sup>187</sup>, although, is generally assumed to be 4.7 eV<sup>221,222</sup>.

ITO was first recognized as a transparent conductive material in 1971, where a low sheet resistance of 15  $\Omega/\text{sq}$  and a high transmissivity of 80% were reported.<sup>178</sup> Shortly after in 1972, a significantly improved sheet resistance of 1.6  $\Omega/\text{sq}$  (with 73% optical transmission) for ITO was obtained via sputtering in a slightly oxygen

## ***2. Background***

---

deficient environment.<sup>184</sup> In 1975, Molzen determined low sheet resistances of 2-3  $\Omega/\text{sq}$  achieved 95% transmittance in the visible region by annealing ITO films in argon.<sup>175</sup> The effect of annealing has on the optical and electrical properties of ITO will be discussed further in Chapter 7.

The variance in ITO properties between research groups is a result of a complex balance between stoichiometry, and crystallinity. An excellent review describing the dependence of ITO's electrical and optical properties on growth and annealing conditions was written by Bel Hadj Tahar et al.<sup>177</sup> ITO is a material with highly tunable properties where the optimal balance between transmittance and sheet resistance can be achieved depending on the requirements of the desired application.

### ***2.4.2 ITO Crystal Structure***

ITO has a complex cubic bixbyite crystal structure composed of 80 atoms per unit cell.<sup>215,223–225</sup> As a result, the properties of ITO can vary strongly with changing stoichiometry, doping, impurities, and phase-segregation, placing stringent requirements on the growth conditions. The preferred crystallographic growth direction depends on the O-content in the chamber. In an oxygen deficient environment, ITO films grow along the [004] direction, and have a high oxygen vacancy concentration leading to high carrier concentration, poor mobility, and poor light transmission.<sup>218,226,227</sup> Meanwhile, in an O-rich growth environment, ITO grows preferentially along the [222] direction, and has enhanced  $\text{Sn}^{4+}$  doping, leading to higher carrier mobility.<sup>218,226</sup> The change in growth direction is a result of the (004) surface being higher energy than (222) in an O-rich environment, and vice versa. The effect of oxygen concentration during growth not only effects carrier concentration, it also impacts the preferred crystallographic growth direction, increasing the complexity when determining optimal ITO growth conditions.

The lattice constant of  $\text{In}_2\text{O}_3$  increases upon Sn doping. This increased lattice constant violates Vegard's law, which predicts a reduced lattice constant upon Sn

## 2. Background

---

doping due to the smaller radius of  $\text{Sn}^{4+}$  compared to  $\text{In}^{3+}$ . The lattice constant increase is attributed to amplified electrostatic repulsion caused by the incorporation of increased positive charges from  $\text{Sn}^{4+}$ .<sup>228–232</sup>

### 2.4.3 Self-catalyzed VLS of ITO NWs

ITO undergoes self-catalyzed VLS growth when deposited by PVD onto a sufficiently heated substrate.<sup>97–99,194–202,233–242</sup> **Figure 2.13** shows a schematic for self-catalyzed growth of branched ITO NWs. Early in deposition, In and Sn form liquid alloy droplets on the substrate at relatively low temperatures (under 150 °C) as shown in **Figure 2.13a**.<sup>243</sup> These molten alloys collect material and catalyze the VLS growth of crystalline ITO NWs (**Figure 2.13b**). A detailed description regarding the precipitation of Sn-doped  $\text{In}_2\text{O}_3$  crystals from In-Sn melts was reported by Frank et al.<sup>244</sup> As a result of this nucleation process, a very thin (~ 5 nm) solid film layer remains on the surface of the substrate (**Figure 7.3**). In some cases, In-Sn liquid droplets form on the sidewall of the initial NWs. These droplets collect growth material, and catalyze epitaxial growth of NW branches on the sidewall of the NW trunk (**Figure 2.13c**).<sup>241</sup> Separate catalysts, such as Au, are sometimes used to catalyze ITO NW growth, however, higher temperatures are required to form a liquid alloy.<sup>198,229,245–255</sup>

The structure of ITO NWs is strongly effected by growth conditions. A similar effect as observed in planar films<sup>226</sup>, Takaki et al. reported that ITO NW crystallographic growth direction and resulting morphology was a function of sputtering power and oxygen partial pressure.<sup>98</sup> Both  $\langle 400 \rangle$ <sup>98,196–198,234,235,245,249,250,253</sup> and  $\langle 222 \rangle$ <sup>98,99,254</sup> oriented ITO NW growth has been reported in literature. The catalytic droplets have been found to have a higher Sn composition than the NW, supporting the proposed self-catalyzed VLS mechanism.<sup>99,195,197,199,242</sup>

ITO is an excellent material system to study the combination of GLAD with VLS growth because it is self-catalyzed, grown through simple PVD processes, and occurs at low temperatures (~ 150°C). These features reduce fabrication steps and

## 2. Background

ease equipment requirements. The self-catalyzed mechanism of ITO will be studied extensively throughout this thesis.

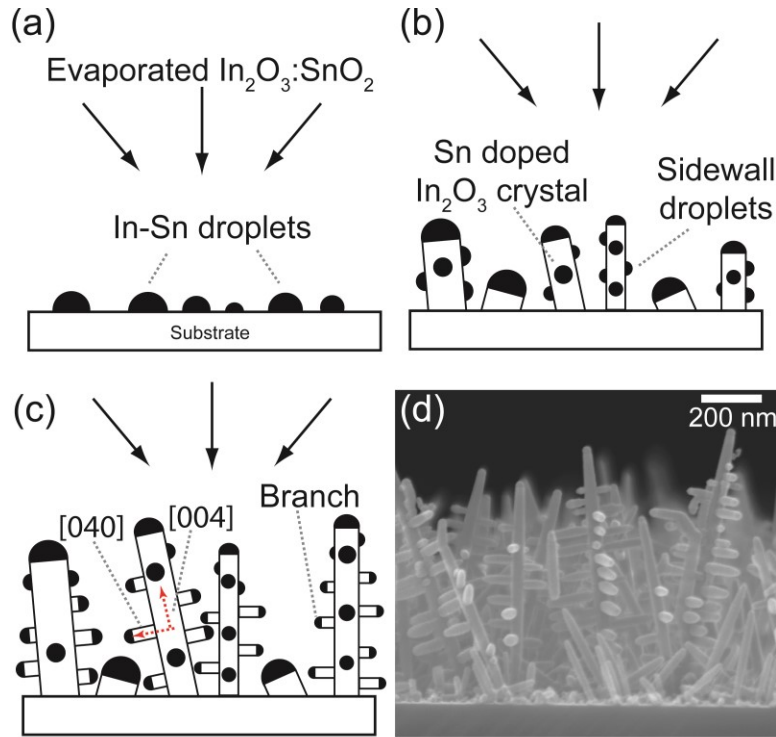


**Figure 2.13:** Schematic of the self-catalyzed VLS growth of branched ITO NWs. (a) In-Sn liquid droplets form on substrate early in ITO deposition. (b) Liquid droplets catalyze growth of NWs, liquid droplets form on sidewall of trunk. (c) Liquid droplets catalyze epitaxial branch growth on sidewall of NWs, trunks and branches grow along  $\langle 400 \rangle$  directions. (d) SEM image of VLS grown branched ITO NWs.

### 2.4.4 Nanostructured electrodes for organic photovoltaics

OPV devices use organic photoactive materials to absorb light and produce electricity.<sup>203,204,209,211,256–260</sup> OPVs offer potential solutions to cheap power generation and flexible devices. However, low efficiency and short device lifetimes have prevented OPV from becoming a contender in the solar energy market. Nanostructured electrodes have been used to extract charges in OPV devices, leading to enhanced performance and lifetimes. In this thesis, 3D branched ITO NW transparent electrode architectures will be optimized for OPV applications. This section will briefly describe the operation of OPV devices, and provide a background of nanostructured ITO electrodes.

## ***2. Background***

---

Upon absorption of light in an organic photoactive layer, an electron-hole pair is created as a bound exciton. Unlike inorganic semiconductors, the exciton has a significant binding energy that must be overcome to separate the generated electron-hole pair. An interface between an acceptor and donor provides offset energy levels that enable the separation of an exciton into an electron and hole. However, excitons often decay prior to reaching the interface in a planar device due to their extremely short diffusion length, typically on the order of  $\sim 10$  nm in polymeric materials. The bulk heterojunction (BHJ) architecture is composed of a mixture of donor and acceptor materials, enabling the generated excitations to be within a diffusion length of an interface at all times, ensuring efficient charge separation.<sup>259</sup> The separated free charge carriers must travel to their respective electrodes, however, charge transport in polymeric materials is also extremely limited. Therefore, the thickness of the BHJ is limited by the distance charge carriers can travel prior to decaying, which limits light absorption, and as a result, places limitations on the amount of charges generated in an OPV device.

A limiting factor in the performance of OPV devices are the long conduction pathways separating the generated charge carriers from their respective electrodes. As a result, the generated charge carriers often undergo recombination or are trapped prior to collection at an electrode. Embedded nanostructured electrodes have potential to improve OPV performance by shortening the distance a charge carrier must travel prior to being collected by their respective electrode (**Figure 2.14**).<sup>33,123,201,261</sup> This can enhance the efficiency of an OPV device by improving charge collection of a low mobility charge carrier. By enhancing conductive pathways, nanostructured electrodes may remove the need to compromise between increased optical absorption and efficient charge collection. In Chapter 7, branched ITO NW architectures will be fabricated and optimized for applications as nanostructured transparent electrodes in OPV devices.

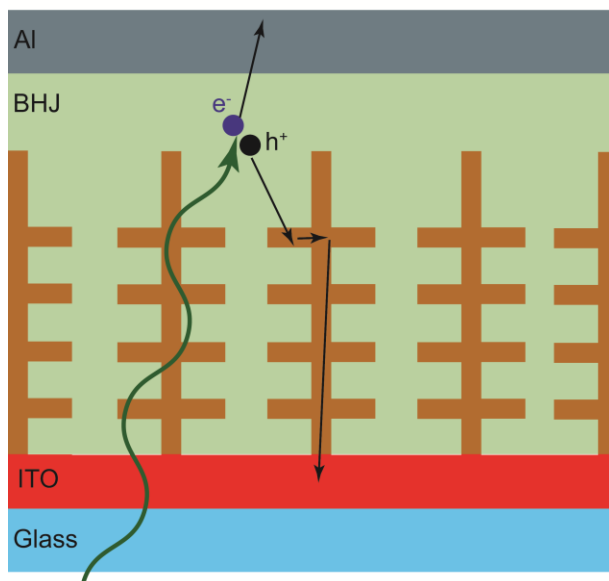


**Figure 2.14:** Schematic of BHJ OPV device with branched ITO NW transparent electrode designed for enhanced charge extraction.

## 2.5 Nanomaterial characterization techniques

Numerous characterization techniques are used throughout this thesis to assess the structure, composition, conductivity, and crystallinity of NWs. This section will provide a brief discussion of the relevant characterization techniques.

### 2.5.1 Scanning Electron Microscopy (SEM)

Scanning electron microscopy (SEM) is used to analyze the morphology, topography, and to a lesser extent composition of a sample.<sup>262</sup> Electrons produced by field-emission or thermionic-emission are scanned across a sample of interest. Backscattered electrons and secondary electron emission result from interaction between the electrons and the sample. The emitted electrons are detected and used to reproduce highly magnified images of the samples. Backscattered electrons are a result of Rutherford scattering, and their intensity increases with atomic number. Therefore, backscattered electron imaging can provide compositional contrast. Secondary electrons are ejected from the core of an atom. Due to their relatively low energy, secondary electrons escape from a shallow distance below the surface

## ***2. Background***

---

of the sample (~ 5 nm). As a result, secondary electrons imaging provides information about the topography and morphology of a sample. SEM imaging requires conductive samples, otherwise charging may obscure the image. Coating with Cr or Au or low voltage imaging are often performed on insulating samples to prevent charging.

### ***2.5.2 Energy-dispersive X-ray spectroscopy (EDX)***

Electrons from higher energy orbitals fall to fill the vacancy left behind when a secondary electron is emitted from a core energy level. A photon (X-ray) is released when electrons fall from higher energy levels. The energy of the emitted X-ray is equal to the difference in energy levels involved in the transition (ie  $K\alpha$  refers to X-rays emitted when an electron falls from the L-shell to the K-shell). The X-rays are detected in a technique named energy-dispersive X-ray spectroscopy (EDX, or EDS) where elemental fingerprints are obtained and used to identify the composition of a sample.

### ***2.5.3 Scanning Helium Ion Microscopy (SHIM)***

Scanning helium ion microscopy (SHIM) is a recently developed technique that improves upon the resolution of an SEM. SHIM bombards the sample with helium ions, which results in the ejection of secondary electrons from the sample.  $He^+$  ions are produced by flowing He through an intense electric field generated by a positively charged metal needle. He atoms are polarized by the needle, and are pulled towards it. Near the tip of the needle, electrons tunnel from the He atoms into the tip, forming  $He^+$  ions which are accelerated toward a negatively charged anode, and focussed into a beam directed toward the sample.<sup>263–265</sup>

The helium ion beam is scanned across the sample and the secondary electrons are detected to produce a highly magnified image of the sample. An advantage of SHIM is the small interaction volume in the sample compared to SEM. Secondary electrons are produced within a few nanometers of the surface providing high resolution imaging of the topography of the sample. In addition, the yield of

## 2. Background

---

secondary electrons is very high, allowing very low ion currents to be used for imaging, reducing charging effects on insulative or semiconducting samples that limit resolution in SEM images. Helium ions are noble gas atoms, and therefore, have very little chemical reactivity with the sample. Helium ions do not sputter or implant into the sample to a significant extent due to their low mass compared to gallium ion beams.

### 2.5.4 X-ray Diffraction (XRD)

X-ray diffraction (XRD) is used to determine the crystal structure and texture in thin films.<sup>172</sup> In this thesis, XRD will provide insight into the internal structure and composition of the NWs, and will also be used to characterize the alignment of the nanostructure arrays. X-rays diffract from adjacent lattice planes and undergo constructive or destructive interference as defined by Bragg's law (**Figure 2.15**):

$$n\lambda = 2d_{hkl} \sin(\theta) \quad (2.3)$$

$n$  is an integer,  $d_{hkl}$  is the distance between lattice planes, and  $\theta$  is the angle between the X-rays and substrate plane.

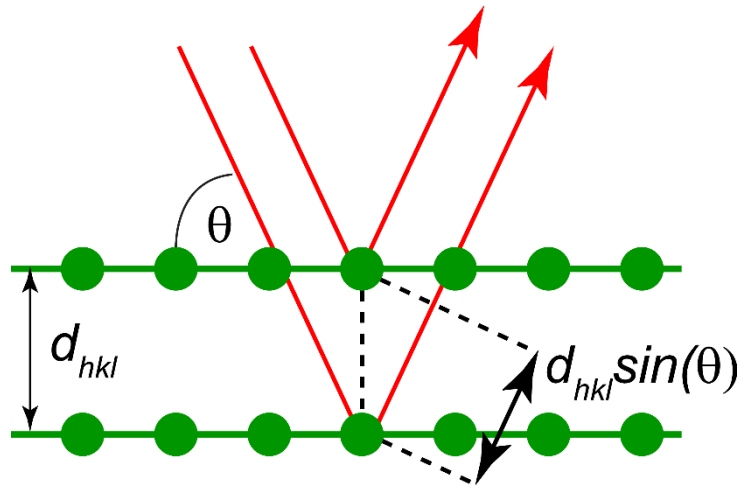


**Figure 2.15:** Schematic of Bragg diffraction condition for X-rays incident at an angle  $\theta$  on a crystal lattice with spacing  $d_{hkl}$ .

## 2. Background

The spacing between lattice planes in a cubic crystal with lattice constant  $a$  can be determined using the following equation:

$$d_{hkl} = \frac{a}{\sqrt{h^2+k^2+l^2}} \quad (2.4)$$

Where  $h$ ,  $k$ , and  $l$  are integers known as the Miller indices that define the orientation of the crystal plane with respect to the unit cell.  $[hkl]$  denotes a direction orthogonal to the  $(hkl)$  plane.  $\{hkl\}$  refers to the family of equivalent  $(hkl)$  planes.  $\langle hkl \rangle$  refers to the family of equivalent  $[hkl]$  directions. The  $h$ ,  $k$ , and  $l$  values are obtained by taking the reciprocal of the three points that the  $(hkl)$  plane intersects with the unit cell. Miller indices of a cubic crystal are depicted in **Figure 2.16**.

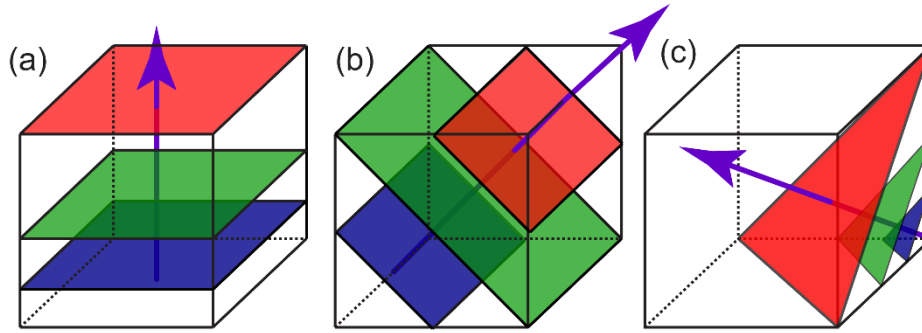


**Figure 2.16:** Schematic of Miller indices in a simple cubic system. Planes are listed in the order: blue, green, red. (a) (004), (002), (001); (b) (022), (011),  $(0\bar{2}\bar{2})$ ; (c)  $(\bar{4}44)$ ,  $(\bar{2}22)$ , (111). Purple arrows correspond to (a) [001], (b) [011], and (c)  $[\bar{1}11]$ .

Crystal texture refers to the degree of alignments of crystallites in a film; a textured film describes the scenario where crystal planes preferentially point in a certain direction. XRD pole figures provide spatial insight into preferential orientations of crystallites both vertically and azimuthally. The scattering vector,  $\mathbf{Q}$ , is defined as:

$$\mathbf{Q} = \mathbf{K} - \mathbf{K}_0 \quad (2.5)$$

Where  $\mathbf{K}$  and  $\mathbf{K}_0$  are the wave vectors for the incident and scattered X-rays, respectively (**Figure 2.17a**). In a conventional XRD line scan,  $\mathbf{Q}$  is typically oriented along substrate normal, and therefore, if a film is textured, lattice planes oriented such that they are stacked vertically on the substrate will scatter X-rays with a higher intensity compared to an untextured film where their alignment is random. In a pole figure,  $\mathbf{Q}$  is mapped throughout a hemisphere above the sample

## 2. Background

for a certain crystal plane by changing the orientation between the scattering plane and substrate during collection. The source, detector, and sample are motioned in an Euler cradle to measure a single Bragg angle as the substrate is incrementally tilted by an angle  $\psi$  from substrate normal, and rotated azimuthally about  $\phi$  during collection (**Figure 2.17b**). **Figure 2.17c** shows how XRD scans are performed at each  $\mathbf{Q}$  intersecting with the hemisphere above the sample to provide a spatial map of the scattering intensity. Therefore, it is possible to determine the direction crystal planes are pointing in three-dimensions, allowing the alignment of crystallites to be quantified. The pole figure represents the stereographic projection of the detected X-ray intensity for all  $\mathbf{Q}$ .

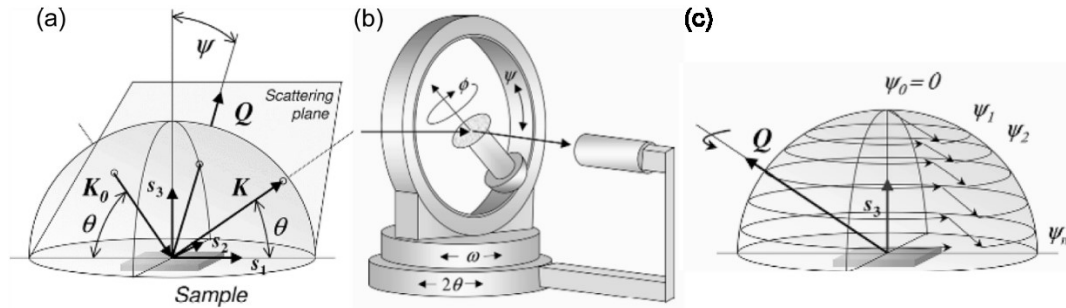


**Figure 2.17:** (a) Schematic of X-ray scattering process, where  $\mathbf{K}$ ,  $\mathbf{K}_\theta$ , and  $\mathbf{Q}$  refer to the incident and scattered X-rays, and scattering vector, respectively.  $\mathbf{K}$ ,  $\mathbf{K}_\theta$ , and  $\mathbf{Q}$  are all in the scattering plane. The sample coordinates are  $s_1$ ,  $s_2$ , and  $s_3$ . (b) XRD pole figure collection schematic in an Euler cradle configuration. The orientation of the scattering plane is controlled by substrate tilt angle  $\psi$  and azimuthal angle  $\phi$ . (c) X-ray scattering intensity is measured for each  $\mathbf{Q}$  vector that intersects with a hemisphere above the sample for a fixed Bragg angle  $\theta$ . Reproduced from “Thin Film Analysis by X-Ray Scattering” by Mario Birkholz with permission from John Wiley and Sons. Copyright 2006.<sup>172</sup>

Conceptual figures for (222) pole figures for an array of unaligned, vertically aligned but azimuthally isotropic, and vertically and azimuthally aligned cubic crystals are shown in **Figure 2.18a, b** and **c**, respectively.  $\psi$  refers to tilt angle of the scattering vector with respect to substrate normal, and  $\phi$  is the azimuthal angle. Randomly aligned cubes have no preferential orientation for (222) planes, and therefore produce equal scattering intensity in all directions, as shown in **Figure 2.18a**. For a vertically aligned array of cubic crystals, the (222) planes point  $55^\circ$  from substrate normal. Therefore, (222) planes will scatter the most intensely when  $\psi \sim 55^\circ$ . Due to random azimuthal alignment, the scattering intensity will be

## 2. Background

uniform about  $\phi$ , resulting in a pole figure with an isotropic ring located at  $55^\circ$  as shown in **Figure 2.18b**. For vertically and azimuthally aligned cubes, the (222) planes only point along four possible directions above the substrate, resulting in four peaks at  $\psi = 55^\circ$ , separated by  $90^\circ$  in  $\phi$  as shown in **Figure 2.18c**. Pole figures provide information regarding the alignment of crystallites over large substrate areas ( $\sim 1 \text{ mm}^2$ ).

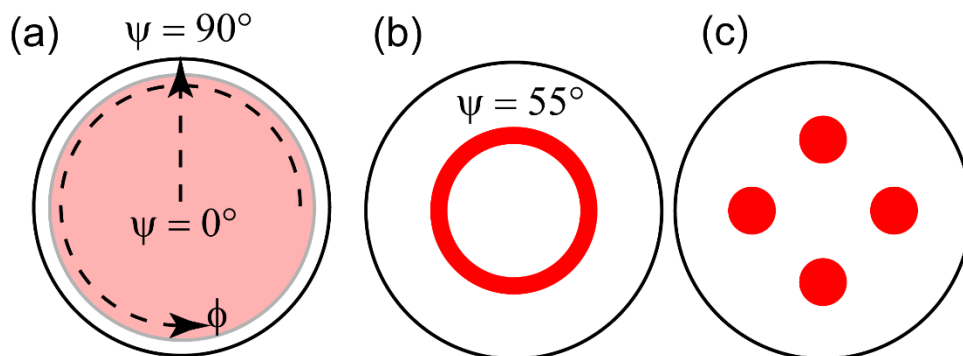


**Figure 2.18:** Conceptual (222) XRD pole figures for arrays of cubic crystals that are (a) randomly aligned, (b) vertically aligned but randomly aligned azimuthally, and (c) aligned vertically and azimuthally.  $\psi$  and  $\phi$  correspond to the orientation of a particular scattering vector  $\mathbf{Q}$  and the red represents the detected X-ray intensity.

### 2.5.5 Transmission Electron Microscopy (TEM)

Transmission electron microscopy (TEM) is used to analyze morphology, composition, and crystallinity of a sample.<sup>266</sup> Unlike XRD, TEM is used to determine local crystallinity rather than crystal properties of the bulk. Electrons are transmitted through a thin sample, and are either unscattered, elastically scattered or inelastically scattered. Unscattered electrons are used for bright field TEM imaging, and provide information regarding thickness and composition of a sample. Regions that undergo Bragg scattering (elastically scattered electrons) will appear dark, because the diffracted beam is blocked from being detected. In addition, thicker areas and areas of the sample with heavy atoms will also appear dark.

Elastically scattered electrons undergo Bragg scattering like in XRD, and provide information regarding the crystal structure of a sample. In selected area electron diffraction (SAED), the beam can be set to interact with select regions of the sample to locally characterize crystallinity in a sample. SAED provides a map of the

## ***2. Background***

---

reciprocal lattice of the crystal. It is possible to determine whether a region is amorphous, polycrystalline, or a single crystal using this technique. In a crystalline sample, which will be what is imaged in this thesis, a series of points will be detected that correspond to planes of the crystal.

High resolution TEM (HRTEM) imaging enables imaging of lattice planes of a crystal.<sup>267</sup> This is done by allowing a selected diffracted beams and the unscattered beams both to pass to the detector unblocked. Interference between the unscattered beam and the diffracted beam enables spatial imaging of the lattice planes, this is often called phase contrast imaging, and can be difficult to interpret. High angle annular dark field (HAADF) imaging involves using a scanning TEM (STEM) to raster a highly focussed beam of electrons across a sample, and detecting incoherently scattered (no interference effects or Bragg scattering) electrons.<sup>268-270</sup> Bright spots correspond directly to the position of atomic columns in the sample when the electron beam is aligned down a zone-axis of a crystalline material. HAADF-STEM images are therefore simpler to interpret compared to HRTEM imaging.

## 3. VLS-GLAD

---

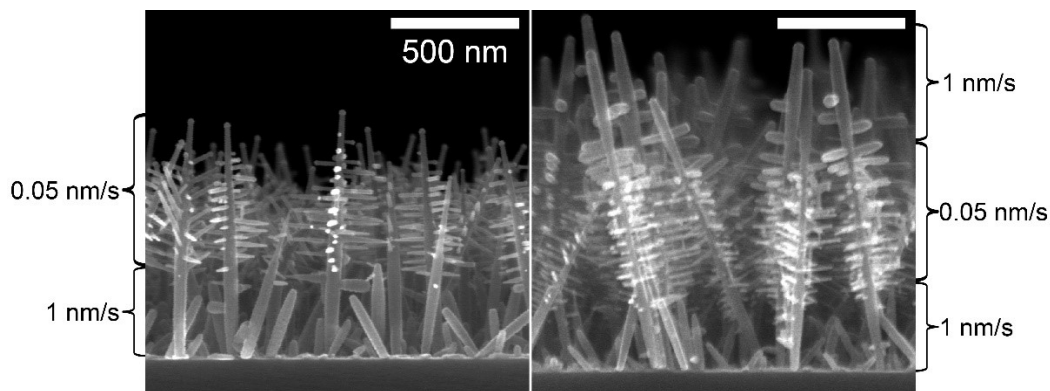


**Figure 3.1:** This figure depicts height dependent control over branch density and trunk diameter achieved by modulating flux rate during VLS-GLAD growth of branched ITO NWs. Portions of this chapter were published in *Nanotechnology*<sup>271</sup>, and this figure was featured in a news article entitled, “Nanotree structures shaped with an arborist’s precision” on Nanotechweb.org (<http://nanotechweb.org/cws/article/lab/48939>).

---

Portions of this chapter were reproduced with permission of The Institute of Physics (IOP) from the following publication:

Beaudry, A. L., Tucker, R. T., LaForge, J. M., Taschuk, M. T., and Brett, M. J. *Nanotechnology* **2012**, *23*, 105608.

## 3.1 Introduction

### *3.1.1 Introduction*

This chapter introduces a technique named VLS-GLAD, where GLAD is used to provide a directable collimated vapour flux to enhance control over VLS growth. First, an overview of other group's early attempts at VLS-GLAD NW growth will be presented. This will be followed by in-depth investigations into the impact of various deposition parameters, including deposition rate,  $\alpha$ , and substrate temperature, on the morphology of branched ITO NW arrays grown by self-catalyzed VLS. Control over NW spacing, branching, and diameter will be demonstrated. The chapter concludes with a demonstration of powerful height-dependent morphological control achieved by modulating deposition parameters during VLS-GLAD growth.

### *3.1.2 Early VLS-GLAD*

During GLAD, low temperatures are usually required to enable a ballistic vapour flux to direct where adatoms are incorporated in a developing columnar film. At high temperatures, adatoms have a much higher mobility on the surface, therefore, adatoms are likely to migrate far from where they land, and the ability to control the structure of a film using ballistic vapour flux deposition would be diminished. Conversely, crystal growth requires high temperatures to give adatoms sufficient mobility to reach their lowest energy configuration. As a result, the intersection between crystal growth and GLAD has remained largely unexplored. Throughout this thesis, the value of placing adatoms on select regions of structures undergoing VLS crystal growth using GLAD will be demonstrated.

Two groups have attempted to use GLAD to enhance control over the VLS growth of Ge NWs.<sup>272,273</sup> The combination of VLS and GLAD was named VLS-GLAD by Alagoz and Karabacak<sup>272</sup>, while Suzuki et al. referred to the process as high-temperature GLAD (HT-GLAD) assisted VLS growth<sup>273</sup>. Throughout this thesis, VLS-GLAD will be used to describe the use of GLAD to guide VLS growth.

Suzuki et al. led early investigations into the impact of elevated substrate temperatures during the deposition of metals using GLAD.<sup>274,275</sup> Early in Suzuki et al.'s HT-GLAD work, they observed that metallic crystalline whiskers would grow on substrates heated to 1/3 the melting point of the respective metal only when deposited at elevated deposition angles ( $\alpha > \sim 80^\circ$ ).<sup>274,275</sup> In contrast, normal deposition (low  $\alpha$ ) resulted in whisker-free planar, granular films. It was postulated that the low temperature crystal growth was enabled by oblique deposition due to favoured nucleation of well separated structures, and increased sidewall deposition on raised structures. Sidewall deposition was thought to significantly reduce adatom mobility requirements to sustain crystal growth. The phrase “efficient deposition” was used to describe the use of GLAD to deposit adatoms near a region where crystal growth was favorable. For instance, material landing on the sidewall of a vertically growing crystal has to travel a much shorter distance to reach the tip of the crystal compared to material landing on the substrate. Material deposited on the substrate would have a much higher likelihood of being incorporated into a planar film, therefore, in normal deposition (low  $\alpha$ ) the planar film would bury the high aspect ratio crystals.

Following this work, Suzuki et al. investigated the use of GLAD during the VLS growth of Ge NWs.<sup>273</sup> A thin layer of Au was deposited onto a Si substrate and heated to 420 °C prior to Ge deposition. It was found that VLS growth of Ge NWs was observed only for deposition angles above 73°, and not below, as shown in **Figure 3.2** (adapted from Suzuki et al.'s work).<sup>273</sup> Once again, Suzuki et al. postulated that oblique vapour deposition increased the amount of Ge deposited on the sidewall of the growing structures, reducing the distance adatoms need to travel to be incorporated into the liquid droplet at the tip of the growing crystal. Suzuki et al. stated that GLAD enables NW growth for conditions (lower temperatures, etc.) that would otherwise not be conducive to NW growth. To support this claim, Suzuki et al. developed a preliminary model that suggests sidewall deposition is essential to VLS growth during HT-GLAD. However, it is clear more studies need to be performed to better understand the relationship between  $\alpha$  and VLS growth.

In a similar work, Alagoz et al. used GLAD to deposit Ge onto Au catalysts patterned by nanosphere lithography.<sup>272</sup> The Ge vapour was deposited using thermal evaporation at  $\alpha = 85^\circ$ , and 400 °C substrate temperature. Crystalline VLS NW growth was achieved, however, an unexplained tilting effect was observed; the NWs were observed to tilt away from the flux. Au-droplets were observed at the tips of the NWs, providing evidence for VLS growth (see **Figure 3.3** adapted from Alagoz et al.'s work). No obvious benefits of VLS-GLAD were presented. It is clear from the work presented in this section that significant work still needs to be done to fully understand the impact of GLAD on VLS growth. The work in this thesis presents a significant advancement in the use of GLAD to enhance control over the VLS growth of NW structures.

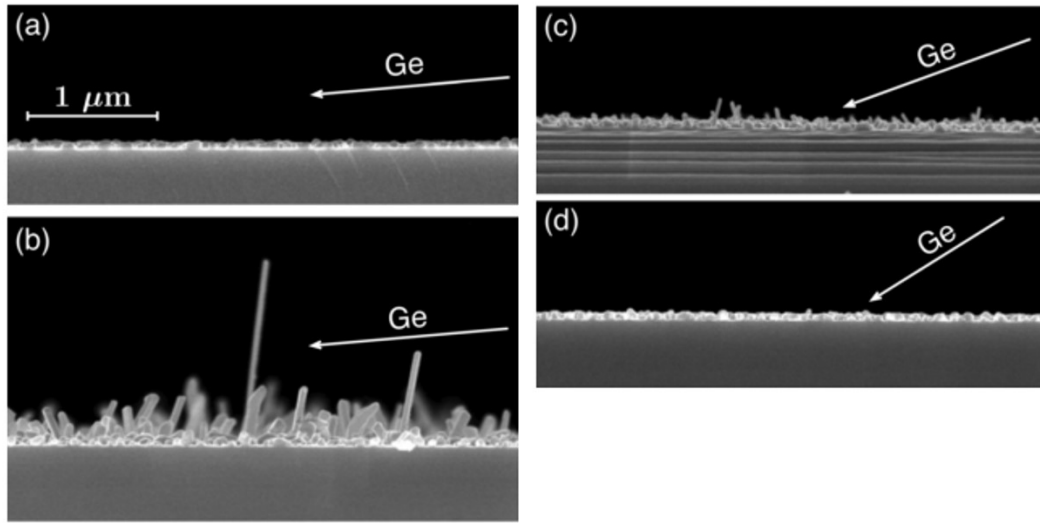


**Figure 3.2:** (a) Ge deposited without Au seeds ( $\alpha = 85^\circ$ ), Ge deposited on Au seeds for (b)  $\alpha = 85^\circ$ , (c)  $\alpha = 73^\circ$ , and (d)  $\alpha = 58^\circ$ . Adapted from the work by Suzuki et al. with permission from *Applied Physics Letters*.<sup>273</sup> Copyright 2011, AIP Publishing LLC.

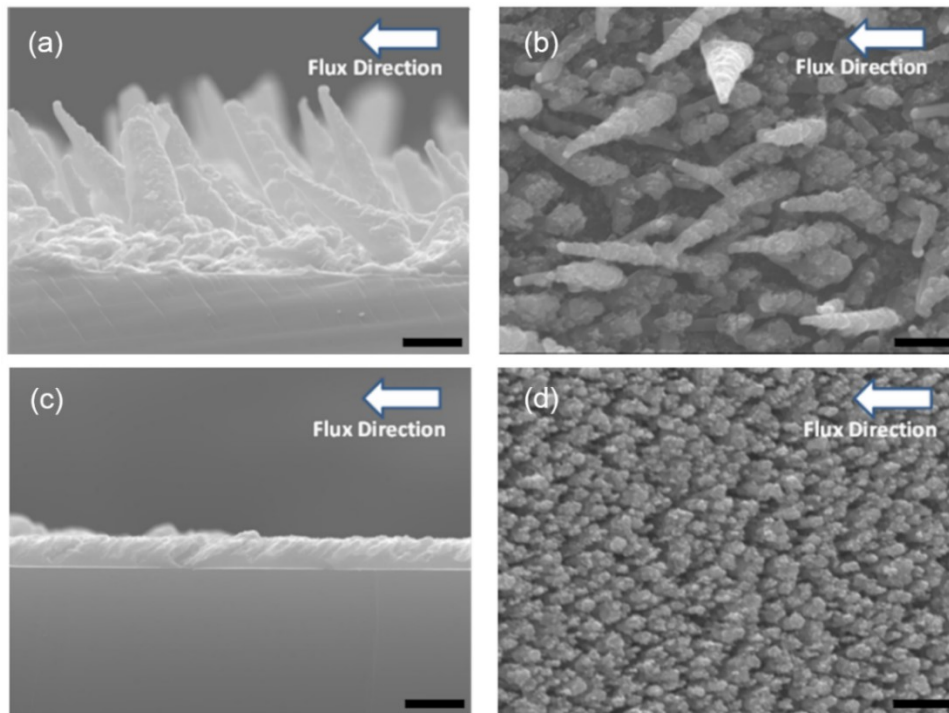


**Figure 3.3:** (a) cross-sectional and (b) top-down SEM images of Ge NWs grown on Au seeds using VLS-GLAD at  $\alpha = 85^\circ$ . (c) and (d) are grown without Au seeds. Adapted from the work by Alagoz et al. with permission from *MRS Proceedings*.<sup>272</sup>

### *3.1.3 VLS-GLAD of branched ITO NWs*

Throughout this thesis, GLAD will be used to guide the self-catalyzed VLS growth mechanism of branched ITO NWs as presented in Section 2.4.3. ITO undergoes self-catalyzed VLS at relatively low temperatures ( $\sim 150$  °C), and is readily achievable using PVD. In addition, the self-catalyzed growth removes the need for pre-deposition of catalysts, and the resulting branches serve as indicators of morphological anisotropy due to asymmetric vapour flux deposition (will be discussed in Chapters 5 and 6). Therefore, ITO is a perfect material system for initial VLS-GLAD studies. In this chapter, precise control over branched ITO NW morphology using VLS-GLAD is presented. The control demonstrated throughout this thesis goes far beyond what has been demonstrated by previous groups using VLS-GLAD, and has led to a new level of structural control in branched NWs.

**Figure 3.4a** depicts the VLS-GLAD parameter space relative to conventional GLAD, VLS and planar deposition of ITO. In this chapter, a systematic characterization of the effects of vapour flux rate,  $\alpha$ , and substrate temperature on ITO NW morphology is reported. The effects of deposition parameters on the NW morphological properties, including trunk diameter, branch diameter and trunk density (defined in **Figure 3.4b**) are examined in detail. In addition, powerful height dependent morphological control is demonstrated in ITO NW arrays via manipulating  $\alpha$  and flux rate during growth. ITO NW growth has been reported with a large range of substrates, flux rates, vapour incidence angles and deposition techniques.<sup>97–99,102,194,197–200,234,235,237,247,254,276–280</sup> However, a systematic study of the effect of highly oblique vapour incidence angle in combination with varied deposition parameters had not been reported previously, and is presented here.

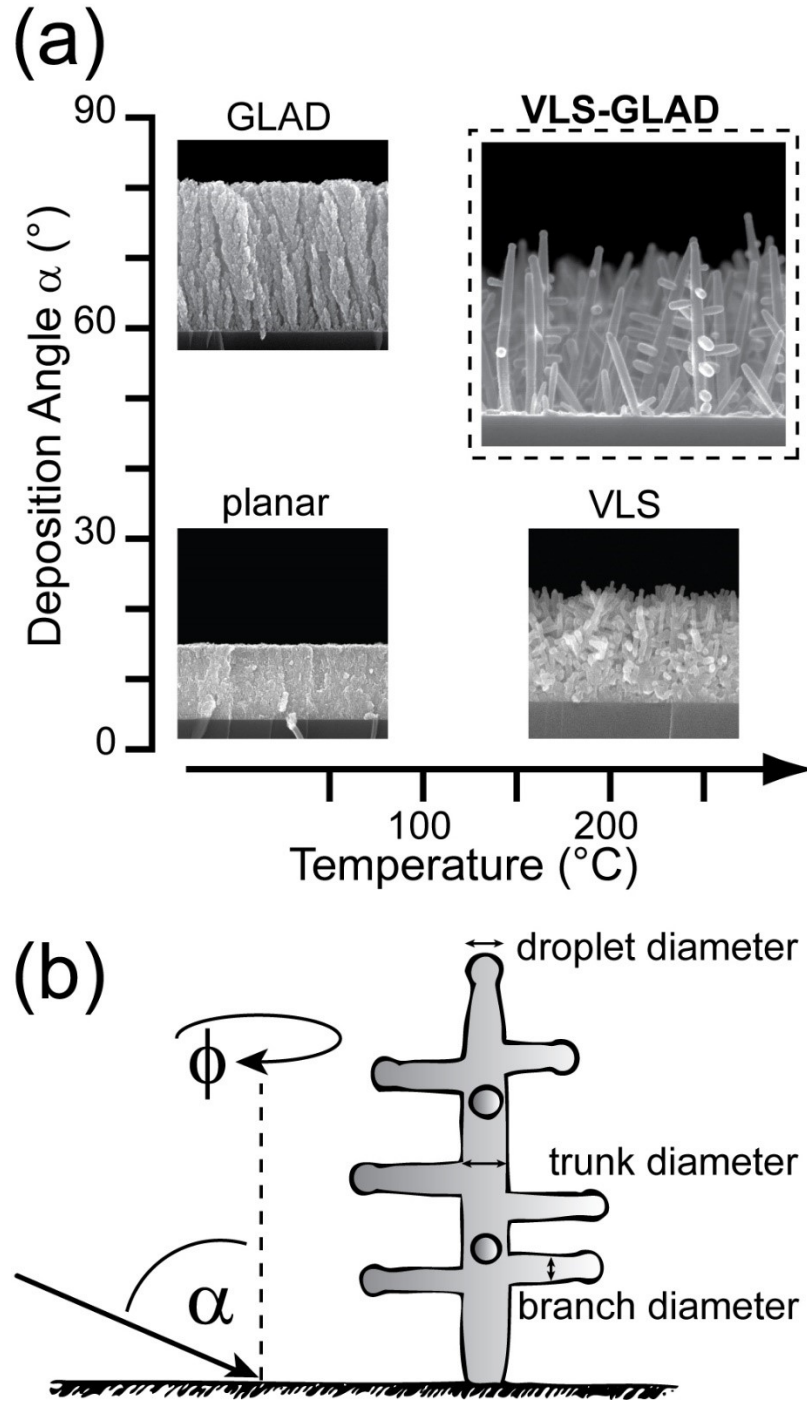


**Figure 3.4:** (a) Qualitative parameter space for ITO planar, glancing angle deposition (GLAD), and vapour-liquid-solid (VLS) grown films. Combining high substrate temperature and high deposition angles produces unique morphologies in a process we call VLS-GLAD. (b) Schematic definition of deposition angle ( $\alpha$ ) and the angle of rotation about substrate normal ( $\phi$ ). Typical NWs are characterized as having a trunk, droplet, and numerous branches. Reproduced with permission from *Nanotechnology*.<sup>271</sup> Copyright 2012 Institute of Physics.

## 3.2 Experimental

### 3.2.1 VLS-GLAD growth of ITO NWs

ITO NW films were deposited using a high vacuum (base pressure below 0.1 mPa) electron beam evaporation system (Kurt J. Lesker, AXXIS) with a custom substrate motion controller capable of precisely controlling  $\alpha$  (angle of vapour incidence) and  $\phi$  (angle of substrate rotation around substrate normal). Substrate temperature was controlled by two halogen lamps illuminating substrates on a copper chuck. Temperature was monitored by a cold-junction corrected (ASTM E2730-10 standard)<sup>281</sup> type T thermocouple (TC) held approximately 1 cm above the substrate holder. This position exposed the TC to the same vapour flux and radiative loading as the substrate, but still allowed for substrate rotation. A photograph of the custom heating assembly is shown in **Figure 3.5**. For further details regarding this heating assembly, see Graham Hunt's thesis.<sup>282</sup> The temperature of the elevated TC was calibrated with respect to a TC fixed to a silicon substrate on the chuck when stationary (**Figure 3.6**). The floating TC consistently reports growth temperatures approximately 30 °C less than the fixed TC. The floating TC temperature was used to monitor temperature during deposition and is the temperature reported in this chapter.

The distance between the source and substrate was 42 cm. The ITO source was composed of pure 3 mm to 12 mm pieces of In<sub>2</sub>O<sub>3</sub> : SnO<sub>2</sub> (91:9 % mol.; 99.99% purity; Cerac, Inc.). No process gas was added during deposition. The films were grown on Si wafers (<100>; p-type; University Wafer), quartz (Quartz Scientific), B270 glass (Howard Glass Co.) and commercial ITO on borofloat glass (Delta Technologies, Ltd.). The films were deposited across a range of deposition angles (30° to 90°), pitch values (1 nm nominal to 1000 nm nominal), flux rates (0.05 nm/s nominal to 2 nm/s nominal) and substrate temperatures (80 °C to 240 °C). Effective source diameter was estimated to be approximately 1 cm. This large source area permits deposition even at a deposition angle of 90°, as the source is not fully occluded by the substrate holder.

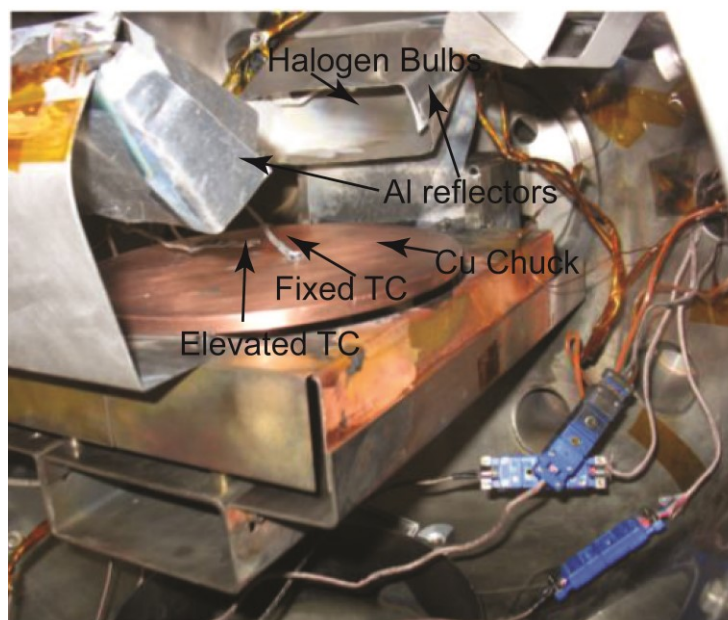


**Figure 3.5:** Two halogen bulbs are directed at the center of the chuck using aluminum reflectors. The heating assembly rotates in  $\alpha$  with the substrate. This photo was adapted with permission from Graham Hunt's thesis<sup>282</sup>

### 3.2.2 Characterization

A SEM (Hitachi S-4800, 15 kV accelerating voltage) was used to image the films. Films deposited on Si substrates were imaged without further coating, whereas films deposited on quartz, B270 glass, or commercial ITO on borofloat glass were coated with approximately 10 nm Cr to reduce charging. Trunk diameter, droplet diameter, branch diameter, trunk density, and nearest neighbour distance were measured by manually analyzing cross-sectional and top-down SEM images of uncoated ITO NWs on Si substrates. Length and diameter values were averaged over five measurements from cross-sectional SEMs using ImageJ image analysis software.<sup>283</sup> Nearest-neighbour distance was estimated as the mean of a gaussian distribution fit to the distances between all unique trunk pairs for each top-down image. XRD (Bruker D8 Discover) patterns were taken on the films deposited on Si substrates using a Cu  $K\alpha$  radiation, a 0.5 mm collimator, and a Bruker HiStar area detector at a distance of 15 cm. TEM was used to image select ITO NWs, and to further analyze the crystal structure (JEOL 2200 FS and Hitachi H9500).

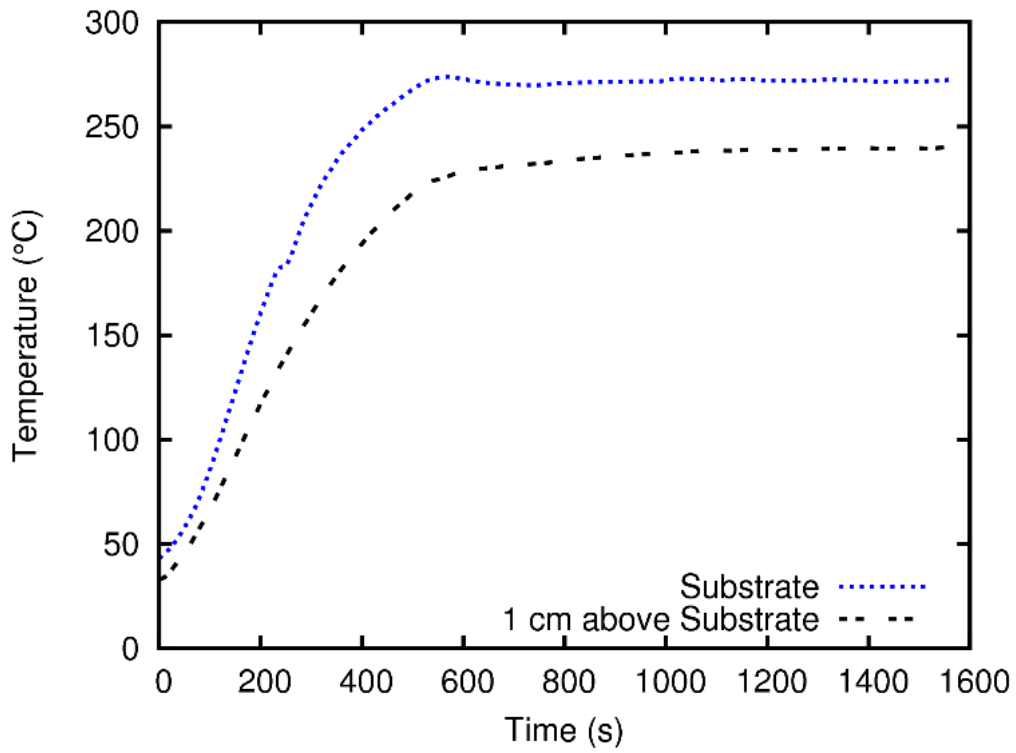


**Figure 3.6:** Temperature measured by TC fixed to substrate, and TC elevated 1 cm above substrate versus time. The elevated TC set point temperature was 240 °C, resulting in a measured temperature of about 270 °C at the surface of the substrate.

## 3.3 Results and Discussion

### 3.3.1 Deposition angle ( $\alpha$ )

Cross-sectional and top-down SEM images of VLS-GLAD ITO NW films deposited with an increasing deposition angle ( $\alpha$ ) are shown in **Figure 3.7**. At elevated  $\alpha$ , larger droplets may starve smaller droplets of flux via an increase in geometric shadowing, leading to a decreased subset of droplets producing trunks. Increasing deposition angle results in increased shadowing length and the growth of fewer NWs over the same substrate area, consistent with the competitive growth model used to describe reduced number density of features in GLAD films.<sup>110</sup> Therefore, the deposition angle can be used to control trunk spacing in ITO NW films. Gaussian fits used to determine the nearest neighbour spacing are shown in **Figure 3.8**.

The relationship between deposition angle and number density of trunks, nearest neighbour distance, number of branches, and trunk diameter is shown in **Table 3.1** and **Figure 3.9**. Interestingly, the trunk diameter also appears to be a function of  $\alpha$ , peaking in width at around  $\alpha = 70^\circ$ . The number of branches per unit trunk length increase rapidly with increasing deposition angle. Branch formation may be dependent on the amount of flux incident on the side of the trunk, which is controlled by geometric shadowing from nearby NWs. With increasing deposition angle, the combination of decreasing trunk diameter and increasing trunk-to-trunk spacing results in decreasing shadowing from neighbouring NWs. These dominant geometric effects appear to increase flux incident on trunk sides and thus increase branching.

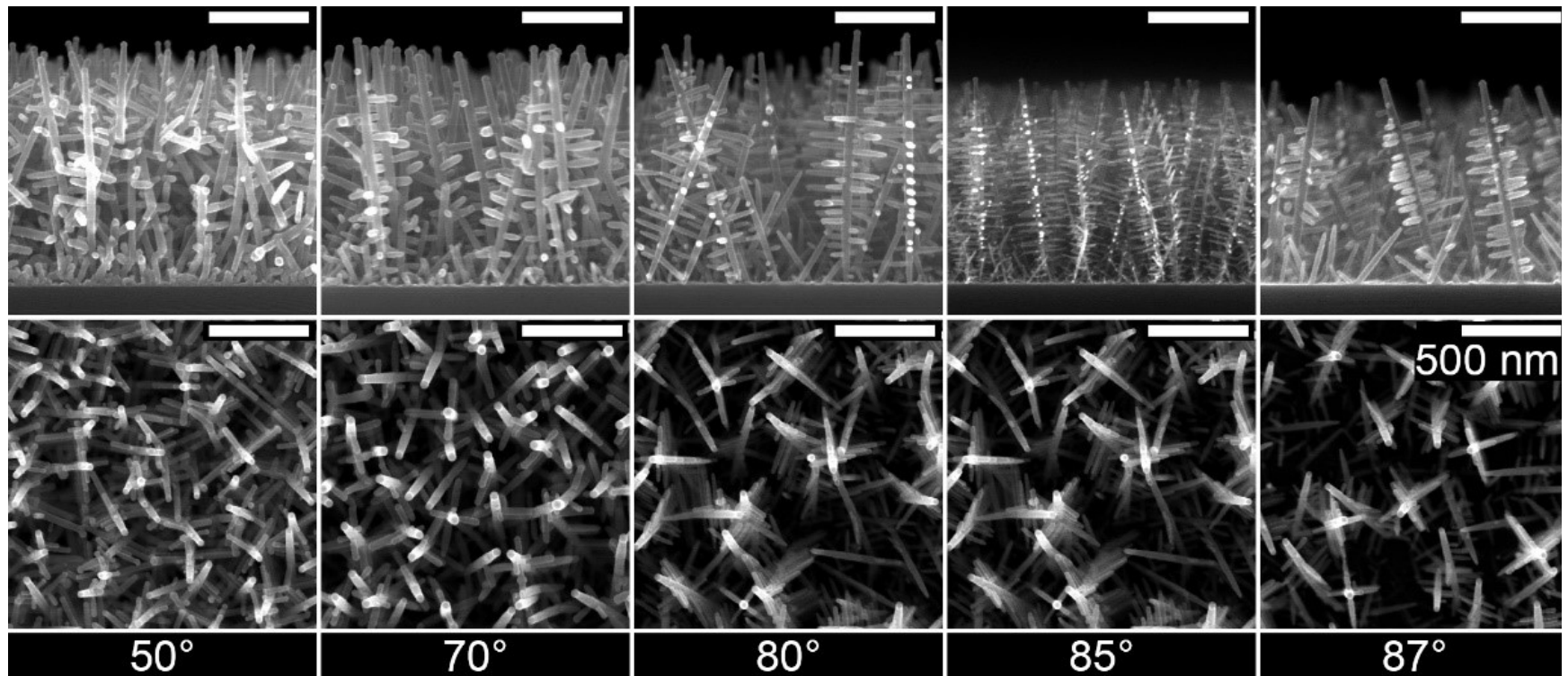


**Figure 3.7:** VLS-GLAD ITO NW films deposited with varying deposition angle  $\alpha = 50^\circ, 70^\circ, 80^\circ, 85^\circ,$  and  $87^\circ$  (temperature = 240 °C, flux rate = 0.2 nm/s, pitch = 10 nm nominal). Reproduced with permission from *Nanotechnology*.<sup>271</sup> Copyright 2012 Institute of Physics.

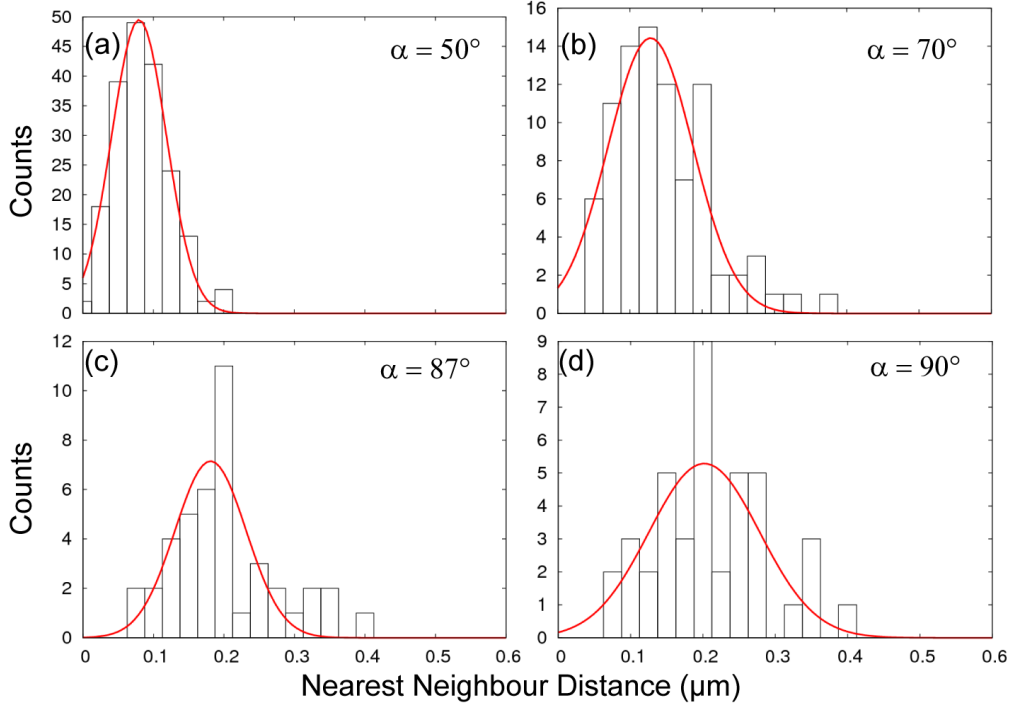


**Figure 3.8:** Gaussian fits from frequency versus nearest neighbour spacing between trunks measured from top-down SEM images (see **Figure 3.7**) for ITO NW arrays grown at various  $\alpha$ , (a)  $50^\circ$ , (b)  $70^\circ$ , (c)  $87^\circ$ , and (d) is  $90^\circ$ . This data is used in **Figure 3.9a**.

$\alpha$ ( $^\circ$ )	Trunk				Branch		# per trunk length (#/µm)
	Diameter (nm)	Height (µm)	Density (µm <sup>-2</sup> )	Nearest Neighbour Distance (nm)	Diameter (nm)	Length (nm)	
50	51 ± 2	1.10 ± 0.06	43 ± 3	80 ± 39	34 ± 4	110 ± 30	19 ± 4
70	55 ± 2	1.19 ± 0.03	20 ± 2	130 ± 60	37 ± 2	102 ± 14	29 ± 4
80	49 ± 1	1.22 ± 0.02	12 ± 2	134 ± 98	30 ± 3	190 ± 60	45 ± 3
85	33 ± 2	0.97 ± 0.01	20 ± 2	122 ± 65	16 ± 3	66 ± 19	97 ± 2
87	48 ± 2	0.97 ± 0.01	9 ± 2	181 ± 51	26 ± 2	125 ± 42	42 ± 3
90	21 ± 2	0.57 ± 0.02	9 ± 1	202 ± 77	11 ± 1	78 ± 7	151 ± 2

**Table 3.1:** Morphological parameters as a function of deposition angle. Measured for ITO NW arrays grown at a temperature of 240 °C, rate of 0.2 nm/s and various  $\alpha$ .

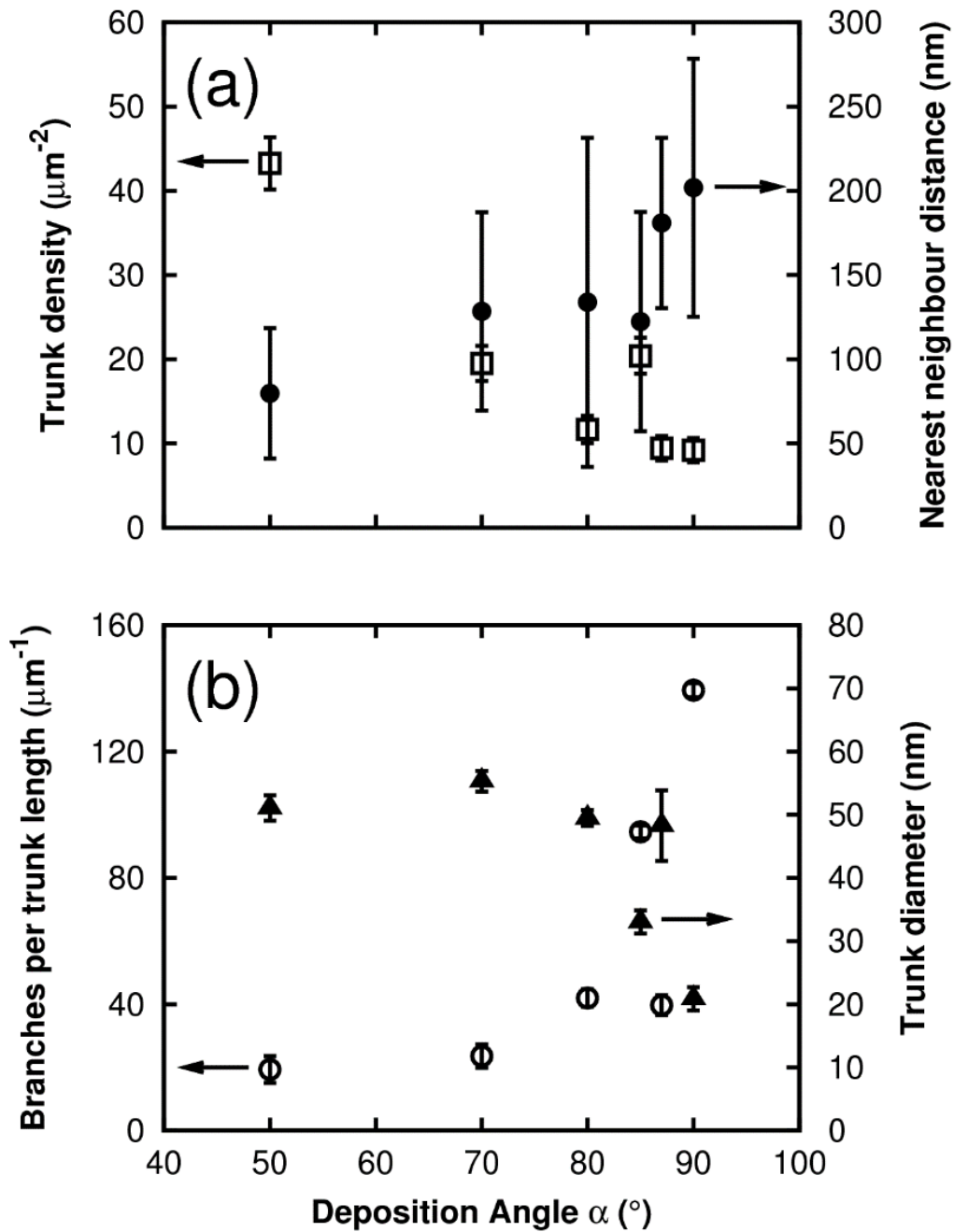


**Figure 3.9:** Measured parameters for VLS-GLAD NWs deposited at various deposition angles (a) trunk density per unit area and nearest neighbour distance (see **Figure 3.8**), and (b) average branches per unit trunk length and trunk diameter. Error bars indicate standard deviation (nearest neighbour distance, trunk diameter) or propagated counting error (trunk density, branches per trunk length). Reproduced with permission from *Nanotechnology*.<sup>271</sup> Copyright 2012 Institute of Physics.

### *3.3.2 Deposition rate*

Nominal flux rate has a strong impact on film morphology, as seen in **Figure 3.10**. For films deposited at large deposition angles, increasing flux rate results in a reduction in the number of branches and an increase in both trunk and branch diameter. Measurements for these parameters are shown in **Table 3.2** and **Figure 3.11**. Similar effects on morphology are observed at low deposition angles (**Figure 3.12**). Typical VLS growth is described as having two transitions: vapour-to-liquid and liquid-to-solid.<sup>284</sup> Increasing the flux rate will proportionally increase the rate of material crossing the vapour-to-liquid interface. The liquid droplet size will hence increase until the rate of liquid-to-solid transition (related to the area of this interface) has increased as well. The increase in size of the liquid droplets thereby increases trunk diameter. A similar effect likely results in the increasing branch diameter observed at high rates. The decrease in branching with increasing rate also appears to be related to geometrical shadowing. As trunk diameter increases with flux rate and trunk-to-trunk spacing remaining relatively constant, the trunk sides are increasingly shadowed from incoming flux. This decrease in flux incident on the trunk sides leads to branching decreasing to nearly zero in the largest flux rate case. The effect may also be due to the large trunk droplets capturing a majority of the adatoms prior to catalyst formation on the sidewall of the trunk.

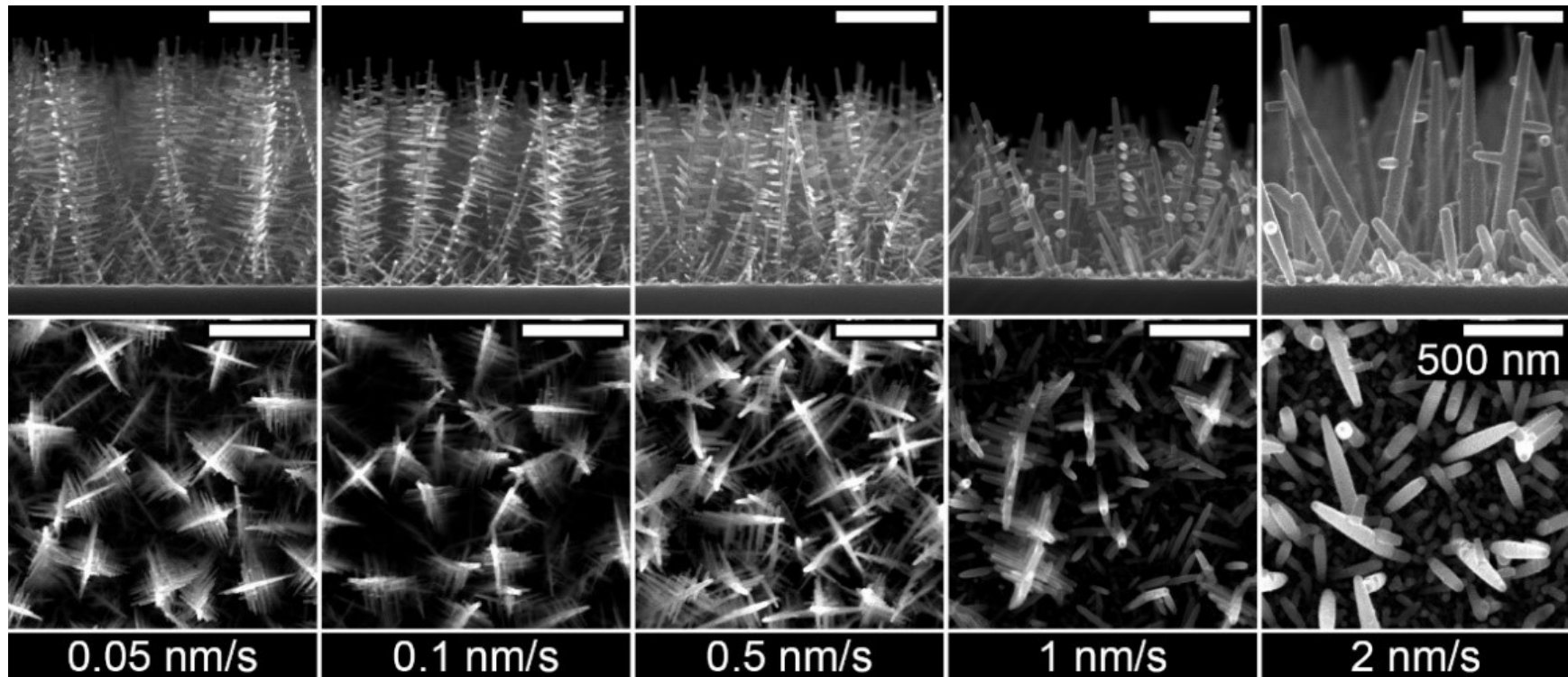


**Figure 3.10:** VLS-GLAD NWs growth with high deposition angle and varying deposition rate of 0.05 nm/s, 0.1 nm/s, 0.5 nm/s, 1 nm/s, and 2 nm/s (temperature = 240 °C, deposition angle = 85°, pitch = 10 nm nominal). Reproduced with permission from *Nanotechnology*.<sup>271</sup> Copyright 2012 Institute of Physics.

$\alpha$ (°)	Rate (nm/s)	Trunk				Branch		# per trunk length (#/μm)
		Diameter (nm)	Height (μm)	Density (μm <sup>-2</sup> )	Nearest Neighbour Distance (nm)	Diameter (nm)	Length (nm)	
50	0.05	36 ± 2	1.21 ± 0.04	37 ± 3	98 ± 35	24 ± 4	87 ± 26	36 ± 3
50	0.1	44 ± 3	1.16 ± 0.06	33 ± 3	107 ± 39	29 ± 5	134 ± 50	38 ± 3
50	0.2	51 ± 2	1.10 ± 0.06	43 ± 3	80 ± 39	34 ± 4	110 ± 30	19 ± 4
50	0.5	55 ± 5	0.98 ± 0.04	27 ± 3	106 ± 56	36 ± 5	101 ± 43	18 ± 5
50	1	55 ± 5	0.93 ± 0.03	24 ± 2	112 ± 52	38 ± 6	108 ± 23	17 ± 4
50	2	78 ± 7	1.04 ± 0.18	14 ± 2	112 ± 51	40 ± 5	112 ± 18	18 ± 5
85	0.05	26 ± 2	1.13 ± 0.02	12 ± 2	181 ± 87	15 ± 1	89 ± 21	106 ± 1
85	0.1	30 ± 3	1.08 ± 0.03	11 ± 2	195 ± 65	16 ± 2	79 ± 28	82 ± 2
85	0.2	33 ± 2	0.97 ± 0.01	20 ± 2	122 ± 65	16 ± 3	66 ± 19	97 ± 2
85	0.5	34 ± 1	1.04 ± 0.01	16 ± 2	127 ± 49	22 ± 3	108 ± 52	58 ± 3
85	1	51 ± 3	0.81 ± 0.05	9 ± 1	180 ± 100	35 ± 5	118 ± 35	33 ± 1
85	2	85 ± 6	1.11 ± 0.08	14 ± 2	155 ± 52	48 ± 8	72 ± 13	4 ± 10

**Table 3.2:** Morphological parameters as a function of deposition rate. NW arrays grown at a temperature of 240 °C.

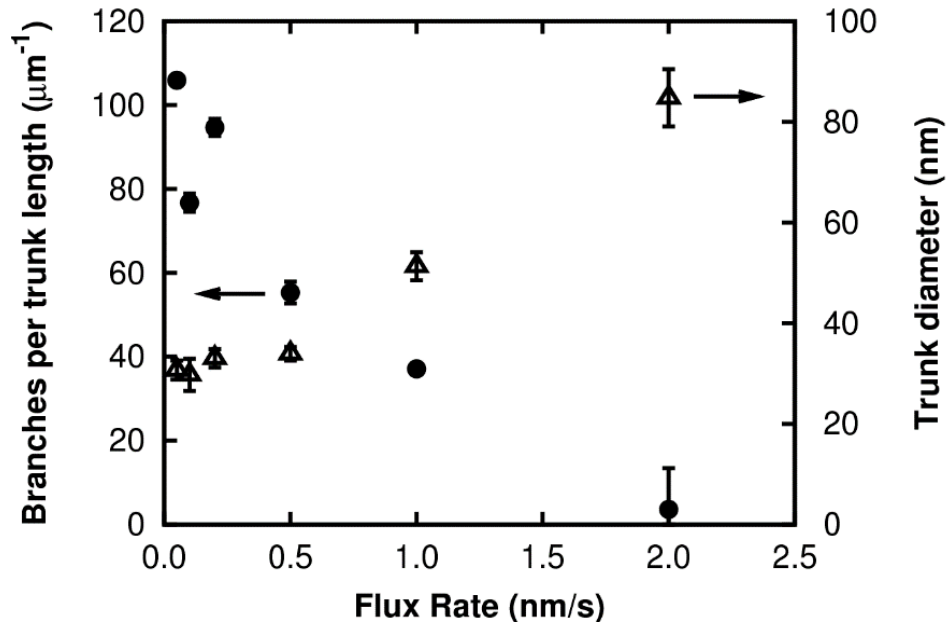


**Figure 3.11:** Average number of branches per unit trunk length and trunk diameter measured for VLS-GLAD NWs grown at  $\alpha = 85^\circ$  and varying flux rate. Reproduced with permission from *Nanotechnology*.<sup>271</sup> Copyright 2012 Institute of Physics.

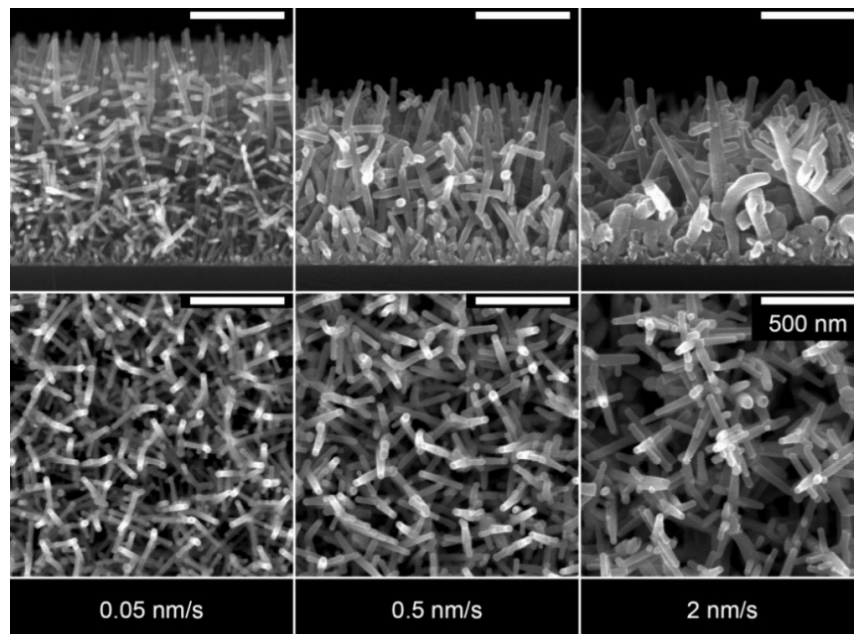


**Figure 3.12:** Images of VLS-GLAD NWs at various flux rates of 0.05 nm/s, 0.5 nm/s, and 2 nm/s for deposition temperature of 240 °C, and deposition angle of  $\alpha = 50^\circ$ . Reproduced with permission from *Nanotechnology*.<sup>271</sup> Copyright 2012 Institute of Physics.

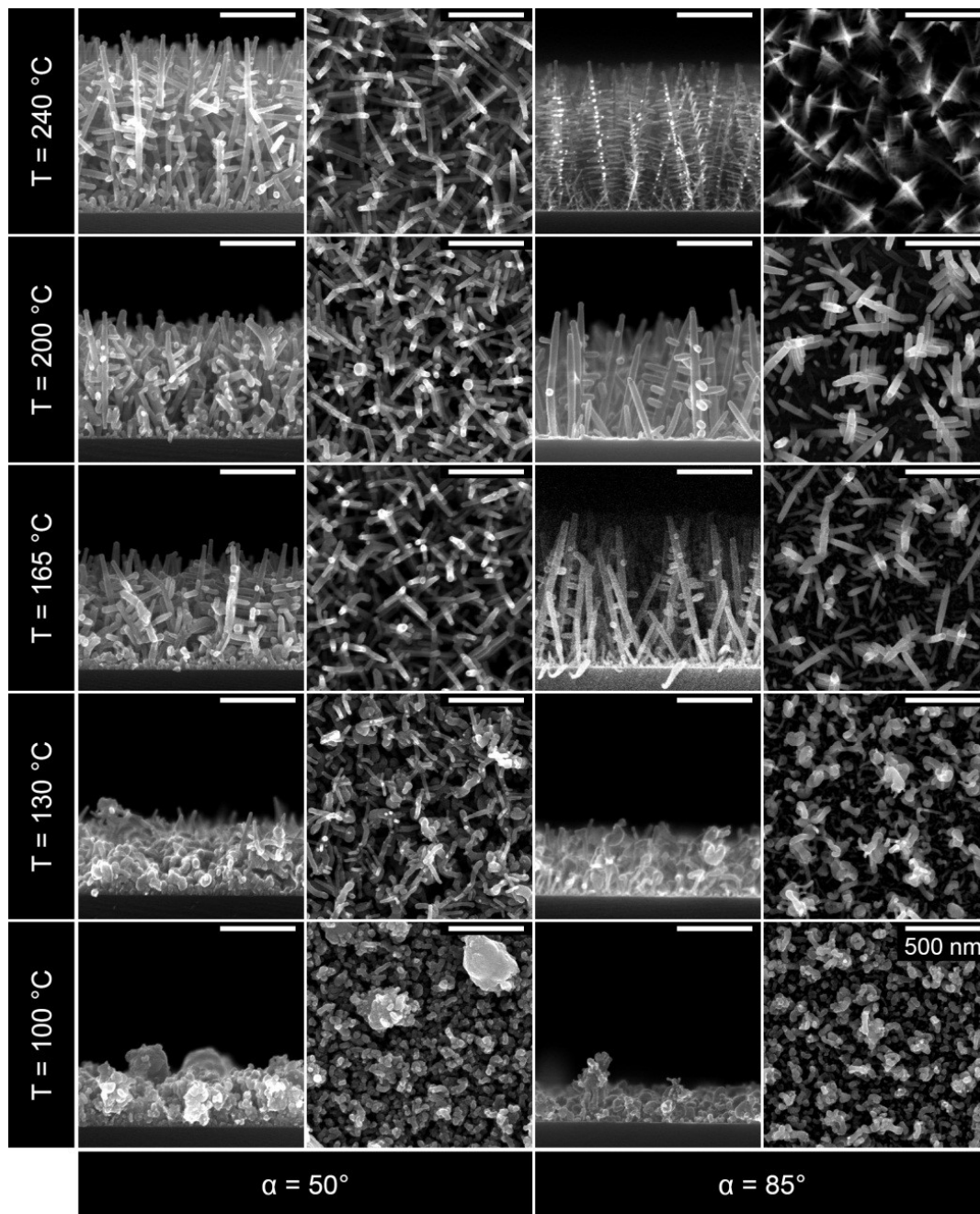


**Figure 3.13:** VLS-GLAD NWs grown at various substrate temperatures and at deposition angles of  $\alpha = 50^{\circ}$  and  $85^{\circ}$ . Reproduced with permission from *Nanotechnology*.<sup>271</sup> Copyright 2012 Institute of Physics.

### 3.3.3 Temperature

It was observed that pronounced NW growth begins at temperatures between 130 °C and 165 °C, for deposition angles of 50° and 85° (see **Figure 3.13**). At a reduced temperature of 165 °C VLS growth is noted for lower flux rates. However, at higher flux rates the NWs begin to appear misshapen or curled (see **Figure 3.14**). It is hypothesized that without sufficient temperature, the rate of crystallization at the liquid-solid interface cannot increase to match higher flux rates, at which point ballistic growth dominates over kinetic growth.

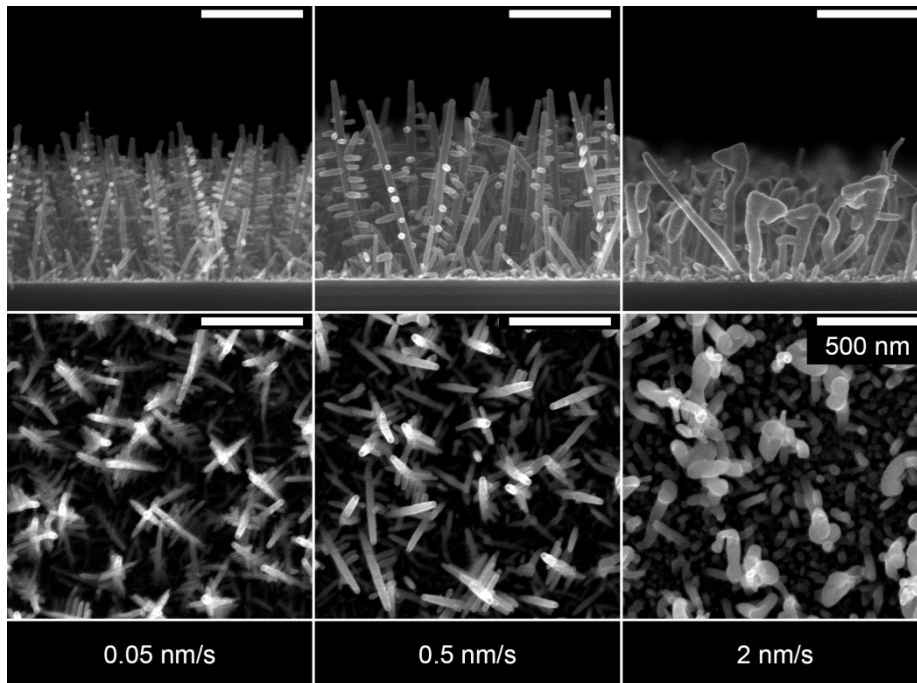


**Figure 3.14:** Images of VLS-GLAD NWs at various flux rates of 0.05 nm/s, 0.5 nm/s, and 2 nm/s for deposition temperature of 165 °C, and deposition angle of 85°. Reproduced with permission from *Nanotechnology*.<sup>271</sup> Copyright 2012 Institute of Physics.

### 3.3.4 Substrate rotation

Pitch (nominal film thickness deposited per substrate rotation) did not appear to have a significant effect on NW morphology. However, as pitch approaches infinity (no rotation), preferential branch formation in the direction of incident vapour flux

was observed as catalytic liquid droplets form favourably on the edge of the NW facing the vapour flux, resulting in branching towards the incident vapour flux. In-depth studies into the effects of substrate rotation and its use to position branches will be discussed in later chapters.

### 3.3.5 Branch-trunk diameter relationship

For all VLS-GLAD films grown across a large range of temperatures, flux rates, deposition angles, and rotation rates, the branch diameter seems to be limited to a portion of trunk diameter. This upper bound is located at a fraction of  $1/\sqrt{2}$  of the trunk diameter, representing the side length of the inscribed square in the trunk's circular cross-section (**Figure 3.15**). The observed geometrical restriction to branch diameter suggests the branches are a continuation of the cubic crystal lattice of the trunk. Therefore, by controlling the initial droplet diameter via the VLS-GLAD mechanism, trunk and branch diameters can be tailored. The control over trunk and branch diameters, as well as the number of branches, is a coupled effect between flux rate and  $\alpha$ .

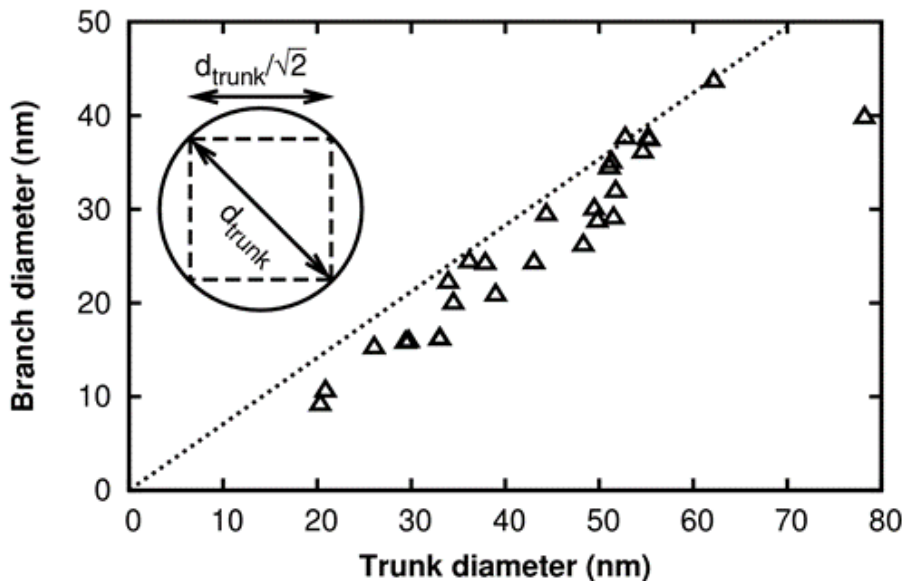


**Figure 3.15:** For all deposited films, branch diameter has an upper limit of  $1/\sqrt{2}$  of the trunk diameter. The dotted line represents the side length of the inscribed square of the trunk's circular cross-section, as illustrated in the inset figure. Reproduced with permission from *Nanotechnology*.<sup>271</sup> Copyright 2012 Institute of Physics.

### *3.3.6 Crystal structure*

Crystal structure of the films was analyzed with XRD. Diffraction patterns for as-deposited samples on Si substrates were taken for all deposition conditions studied. A selection of the diffraction patterns chosen to represent the entire set of data is shown in **Figure 3.16**. Note that the diffraction peaks in samples C ( $\alpha = 85^\circ$ , 100 °C, 0.2 nm/s, 10 nm) and E ( $\alpha = 50^\circ$ , 240 °C, 0.2 nm/s, 10 nm) were textured. Overall these results are consistent with the NW films composed of crystalline ITO, as expected. Of the patterns that matched ITO, the (222) and (400) peaks were present in nearly all cases, which is consistent with previously reported  $\langle 400 \rangle$ <sup>33,102,202,247</sup> and  $\langle 222 \rangle$ <sup>98,99</sup> growth directions, along with lattice matched branches occurring orthogonal to the trunk.

TEM was performed to further analyze crystal structure. **Figure 3.17a** shows an image, obtained through TEM, of a representative ITO NW. SAED (**Figure 3.17a** inset) confirmed that the ITO NWs were single crystal. **Figure 3.17b** shows a HRTEM image of a branch-trunk interface. Aligned crystal lattice planes were observed, with the planes continuing from the trunk into the branch. This supports the geometrical data in **Figure 3.15**, further suggesting that the branches grow as part of the same crystal lattice as the trunk.

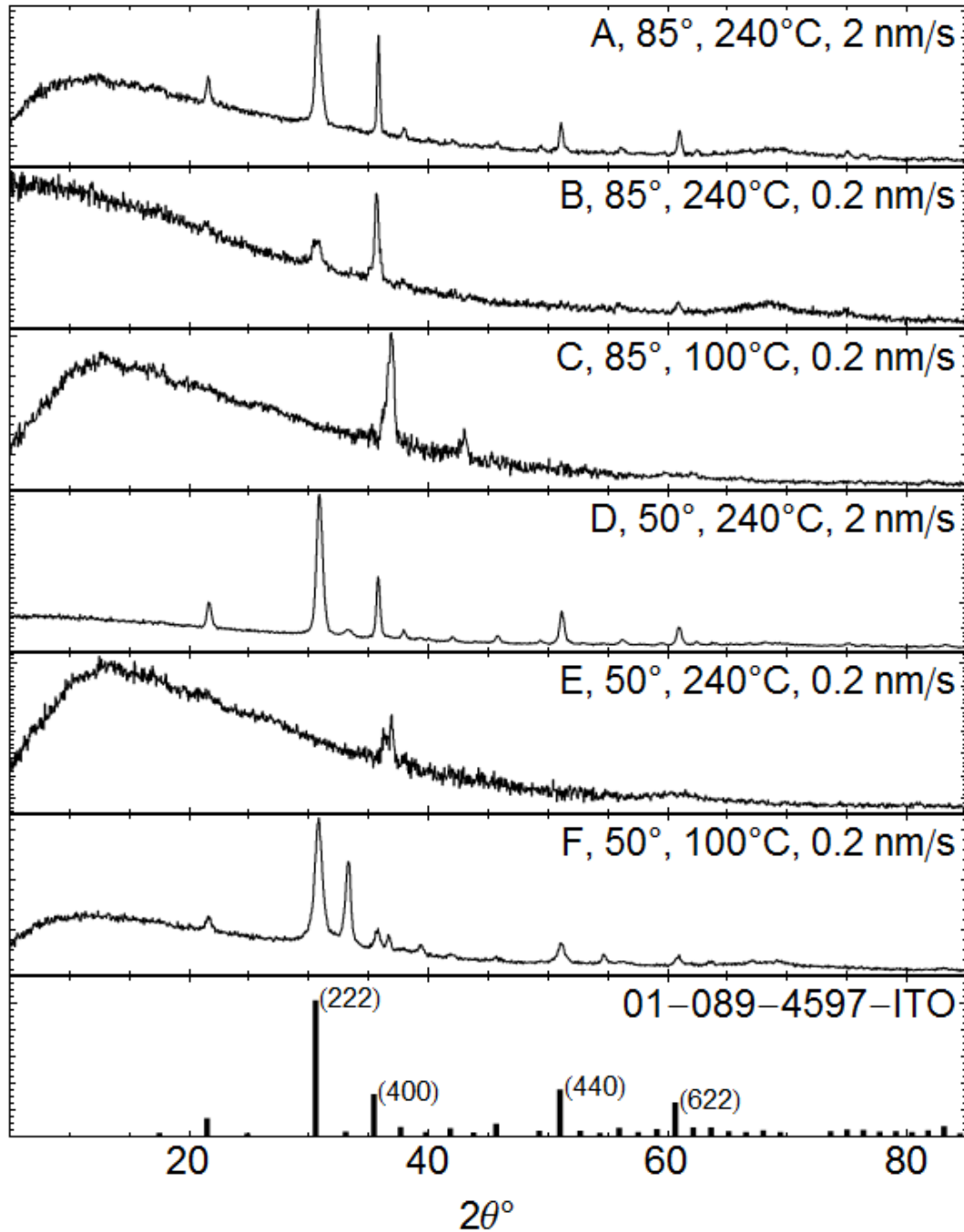


**Figure 3.16:** X-ray diffraction patterns of select samples deposited on Si substrates at a pitch of 10 nm, with variation in deposition angle, substrate temperature and nominal deposition rate. Powder diffraction pattern file for ITO (01-089-4597) is shown for comparison. Reproduced with permission from *Nanotechnology*.<sup>271</sup> Copyright 2012 Institute of Physics.

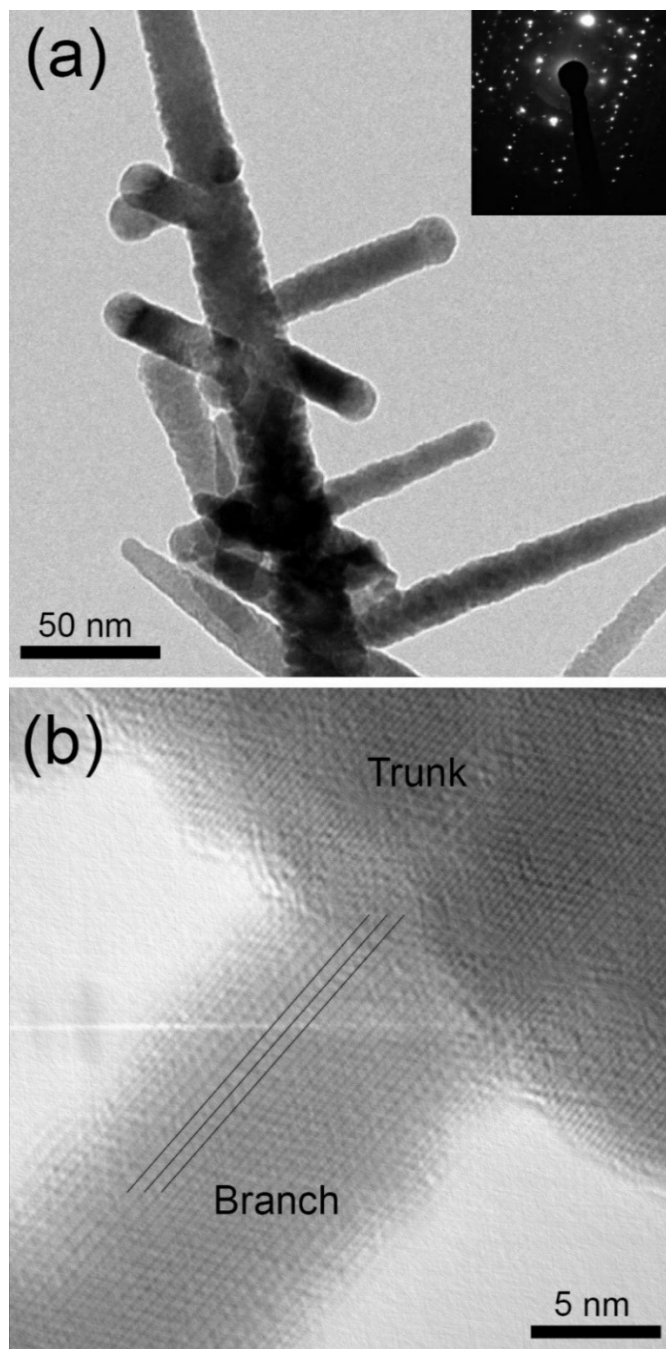


**Figure 3.17:** TEM images of an ITO NW deposited with the following deposition conditions:  $\alpha = 85^\circ$ ,  $T = 240^\circ\text{C}$ , flux rate = 0.1 nm/s and pitch = 10 nm nominal. (a) TEM image of an ITO NW, and SAED data in the inset. (b) HRTEM image at a selected trunk-branch interface. To guide the eye, we have added the dark lines to mark the crystal planes in the branch and trunk of the ITO NW. Reproduced with permission from *Nanotechnology*.<sup>271</sup> Copyright 2012 Institute of Physics.

### 3.3.7 Composition

Composition of individual structures was obtained using EDX taken during TEM. EDX line scans provide information regarding spatial composition locally along a wire. **Figure 3.18a and b** shows an EDX line scan taken along the trunk and droplet. The scan indicates the presence of In, Sn, and O along the wire.

Interestingly, there is a decreased amount of O, and increased amount of In/Sn detected in the droplet, agreeing with the proposed mechanism in which primarily metallic droplets catalyze the VLS growth of NWs. **Figure 3.18c and d** shows an EDX line scan along the length of a branch. O content is lower at the tip of the branch, agreeing with observations of decreased O concentration in the trunk's droplet. Therefore, the EDX data suggests metallic droplets catalyze the growth and that In, Sn, and O are all present in the bulk of the trunk.

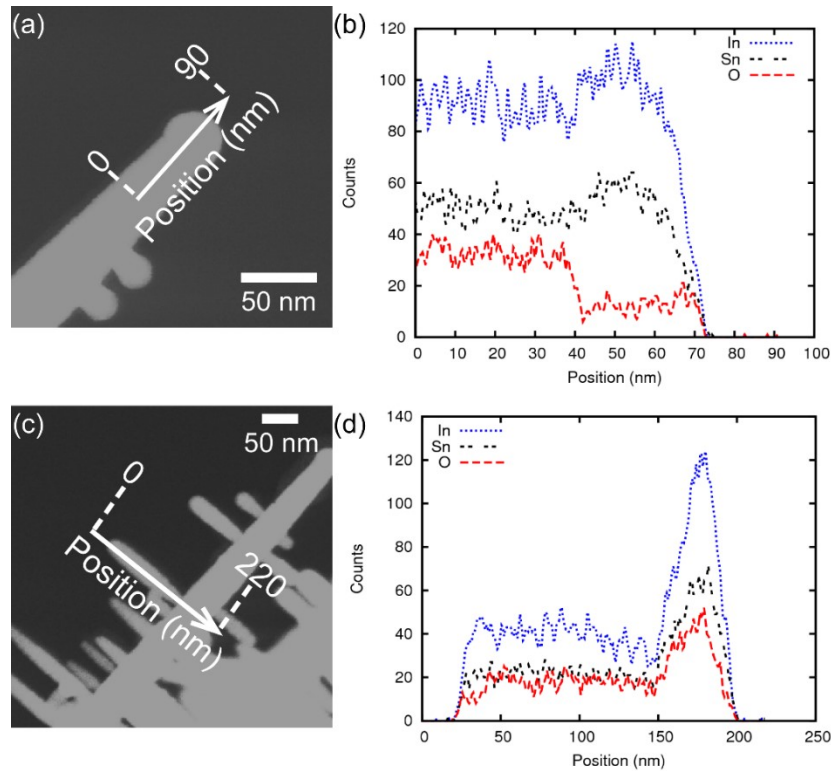


**Figure 3.18:** (a) and (c) TEM images, white arrows indicate region where EDX line-scans were performed, and correspond to position axis in (b) and (d), respectively.

### *3.3.8 Height dependent morphology*

Modulating the flux rate and deposition angle during growth via VLS-GLAD allows for the precise fabrication of unusual hybrid NW structures. These hybrid morphology architectures could provide improved control over the optical and electrical properties of the films. Examples of flux rate modulation and deposition angle modulation are shown in **Figure 3.19**. Modulation of the flux rate (**Figure 3.19 a-d**) can be used to adjust the trunk diameter and branch density during growth. In **Figure 3.19a** the trunk diameter responds to the flux rate by contracting from  $54 \pm 4$  nm to  $23 \pm 1$  nm as the flux rate is modulated from 1 nm/s to 0.05 nm/s. Similarly, in **Figure 3.19c** the trunk diameter responds to the flux rate by contracting from  $53 \pm 6$  nm to  $27 \pm 2$  nm and then expanding back to  $56 \pm 3$  nm as the flux rate is modulated from 1 nm/s to 0.05 nm/s and back to 1 nm/s. The branch diameter and density also respond to the modulation of flux rate. Branching density increases with decreasing flux rate; resulting in a morphology resembling a lobster tree in **Figure 3.19a**, and a trunk with branches only near the center of the trunk in **Figure 3.19c**.

In **Figure 3.19e-f** the effect of modulating the deposition angle can be seen, where a highly interconnected network of NWs grown at  $\alpha = 30^\circ$  is transformed back to a NW forest morphology at  $\alpha = 85^\circ$ . This height dependent density NW film will be revisited in Chapter 7 as an ideal architecture for a transparent electrode in an organic solar cell device. The control provided by VLS-GLAD allows morphologies characteristic to different deposition conditions to be stacked along the height of the film, providing the possibility to optimize the NW properties for a variety of applications.

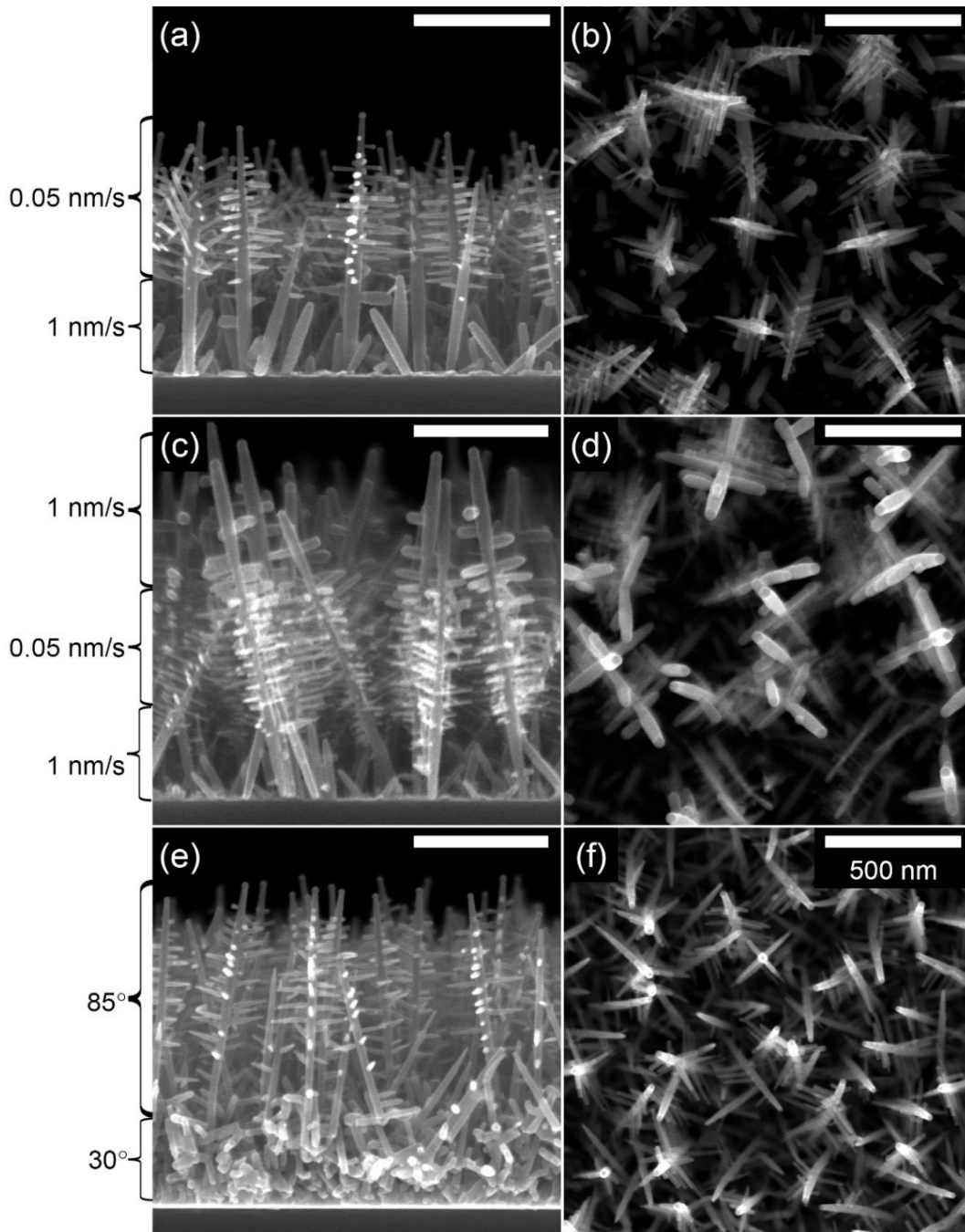


**Figure 3.19:** Side and plan view SEM images of: (a,b) flux rate modulated VLS-GLAD NWs with high deposition angle ( $85^\circ$ ) and flux rate switching from 1 nm/s to 0.05 nm/s; (c,d) flux rate modulated VLS-GLAD NWs with high deposition angle ( $85^\circ$ ) and flux rate switching between 1 nm/s, 0.05 nm/s, 1 nm/s; and (e,f) deposition angle modulated VLS-GLAD NWs with deposition angle switching from  $\alpha = 30^\circ$  to  $\alpha = 85^\circ$  during deposition. Reproduced with permission from *Nanotechnology*.<sup>271</sup> Copyright 2012 Institute of Physics.

## 3.4 Conclusions

This chapter demonstrated that VLS-GLAD has the potential to be a powerful tool in guiding the growth of NW arrays, and its further development will be the focus for the remainder of the thesis. Here, significantly enhanced control over trunk spacing, branch density, and feature size in branched ITO NW networks was readily achieved using VLS-GLAD. ITO readily forms branched NWs using PVD without requiring a separate catalyst deposition step, and occurs at relatively low substrate temperatures. The reduced complexity and technological requirements afforded by the self-catalyzed VLS growth of ITO NWs made it an excellent test material for VLS-GLAD.

VLS-GLAD was also shown to enable powerful height dependent morphological control over branch density and trunk diameter via modulation of the flux rate during growth. Substrate motion during growth, a feature unique to VLS-GLAD, enabled the fabrication of NW arrays with graded density along the height of the film. These density graded NW arrays are of interest for OPV applications, as will be discussed in Chapter 7. The results presented in this chapter form a foundation for the VLS-GLAD technique, and further development of this technique will be demonstrated throughout the remainder of this thesis. Investigations into the impact of flux asymmetry on morphological anisotropy, crystal texture, and branch rippling in branched ITO NW arrays using VLS-GLAD will be presented in the following chapters.

# 4. Branch Rippling

---

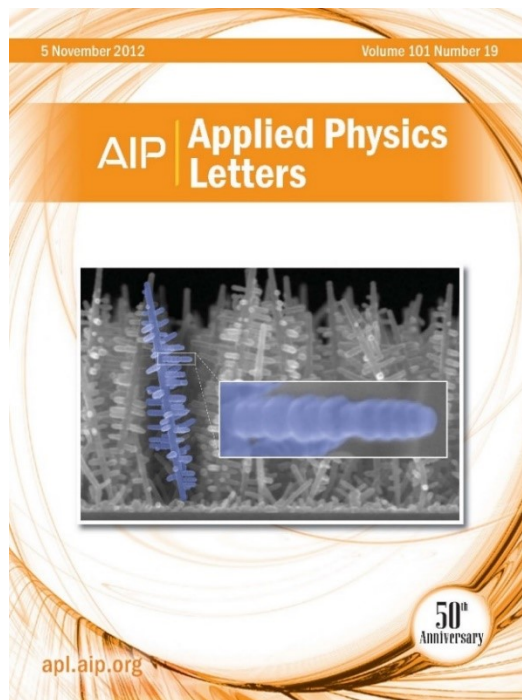


**Figure 4.1:** The work in this chapter was featured on the cover of the November 2012 issue of *Applied Physics Letters*.<sup>285</sup>

---

Portions of this chapter were reproduced with permission of the American Institute of Physics (AIP) from the following publication:  
Tucker, R. T., Beaudry A. L., LaForge, J. M., Taschuk, M. T., and Brett M. J. *Applied Physics Letters* **2012**, *101*, 193101.

## 4.1 Introduction

In this chapter, control over branch diameter oscillations using self-shadowing and macroscopic shuttering of the flux is presented. The experimental portion of this chapter was performed by Allan Beaudry, and the numerical model was developed by Ryan Tucker. Two key features distinguish VLS-GLAD: (i) a collimated (low divergence) flux which breaks flux symmetry at the growth surface, enabling geometrical shadowing effects to mediate the NW growth and (ii) three-dimensional substrate motion to orient the flux during growth. Continuous rotation about substrate normal modulates the incident flux on the branches as they pass through the trunk's shadow. In response, the branch diameter oscillates during growth producing a rippled surface. **Figure 4.2** shows ITO NWs with rippling behaviour grown by VLS-GLAD.

Control over intra-wire morphology has also been investigated, with several groups reporting variations in nanowire diameters<sup>286–297</sup>. Givargizov and others suggest an unstable model of self-oscillations based on droplet contact angle and surface roughness driven by droplet supersaturation<sup>289,291,294,295</sup>. Most of these reports attribute rippled (or bamboo) nanowire structures to this self-oscillatory growth mode<sup>286,291,294–297</sup>. However, others have demonstrated discontinuous diameter changes through annealing-driven catalyst migration<sup>290</sup>, switching between different crystal cross-sections during growth<sup>292</sup>, and segmented nanowire morphologies controlled by carrier gas pulsing<sup>293</sup>.

Observations of branch surface rippling, the derivation of a model linking branch growth physics to experimentally accessible variables in the VLS-GLAD technique, and the engineering of aperiodic ripples into growing branches will be presented in this chapter. As changes in incident flux drive changes in the diameter, this model captures diameter control modulated by both motion-controlled shadowing and flux rate. The VLS-GLAD technique provides an opportunity to study VLS growth kinetics, and produce nanostructures that have been previously unachievable.

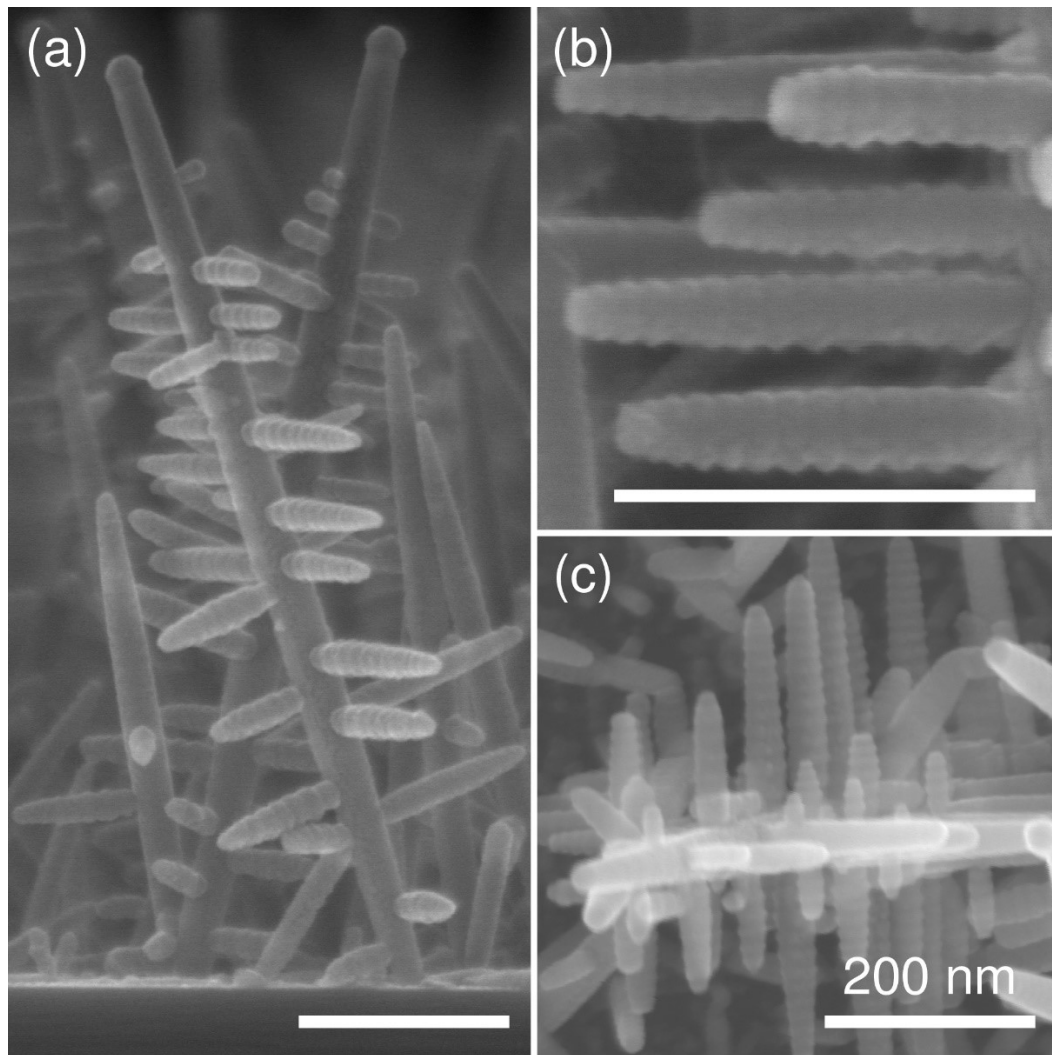


**Figure 4.2:** SEM images of VLS-GLAD ITO nanotrees exhibiting rippled branch features deposited with the parameters (a)  $\alpha = 87^\circ$ ,  $T = 240^\circ\text{C}$ ,  $R = 2 \text{ \AA/s}$ ,  $\tau_{\text{rot}} = 50 \text{ s}$ ; (b) magnified edge and (c) plan view of  $\alpha = 85^\circ$ ,  $T = 240^\circ\text{C}$ ,  $R = 10 \text{ \AA/s}$ ,  $\tau_{\text{rot}} = 10 \text{ s}$ . Reproduced with permission from *Applied Physics Letters*.<sup>285</sup> Copyright 2012, AIP Publishing LLC.

## 4.2 Model

From mass conservation, droplet diameter is controlled by the vapour flux capture rate and the liquid-solid crystallization rate. Vapour flux capture rate is a function of evaporation conditions, adatom diffusivity, and most importantly for the work presented here, the local shadowing environment a growing nanowire experiences. Unlike typical isobaric VLS-growth systems, the collimated vapour approach used here allows for dynamic control over local vapour pressure. For a growing nanowire array, high deposition angles ( $\alpha$ ) produce shadows between adjacent nanowires, as shown in **Figure 4.3a**. When deposition flux is occluded by ‘upstream’ nanowire trunks or branches, the liquid Sn-In(-O) droplet is starved of growth material. Vapour undersupply can lead to droplet decay and subsequently, branch tapering.<sup>298</sup> In some cases, the liquid-solid crystallization process can continue until the droplet is exhausted, resulting in a blunt-ended nanowire.<sup>196</sup>

For a constantly rotating substrate, the incoming flux absorbed by a branch droplet oscillates between minimum and maximum values which depend on the local nanowire environment. A droplet on the side of an isolated nanowire will experience periodic shadowing, resulting in periodic growing and shrinking of the droplet. The growing branch’s diameter follows droplet diameter, as long as the droplet does not become completely depleted. **Figure 4.3b** shows this rotational effect on flux arriving at a droplet and its periodic nature in an ideal case. The correct conditions produce periodic ripples along the branch growth direction. However, the GLAD process is tunable, and can produce complex shadowing environments, providing a route to enhancing control of VLS growth.

The schematic in **Figure 4.3c** shows the parameters used in a model relating volume change to both flux rate and rotation rate. Using MATLAB, a single droplet of hemispherical shape was simulated in a finite time domain for varying incoming flux volume. For simplicity, only single branch growth was considered. One type of particle was used, with properties calculated for an average atom in a cubic 91% In<sub>2</sub>O<sub>3</sub> – 9% SnO<sub>2</sub> lattice:  $\rho = 7.18 \text{ g/cm}^3$ , 55.0 g/mol, and monolayer thickness

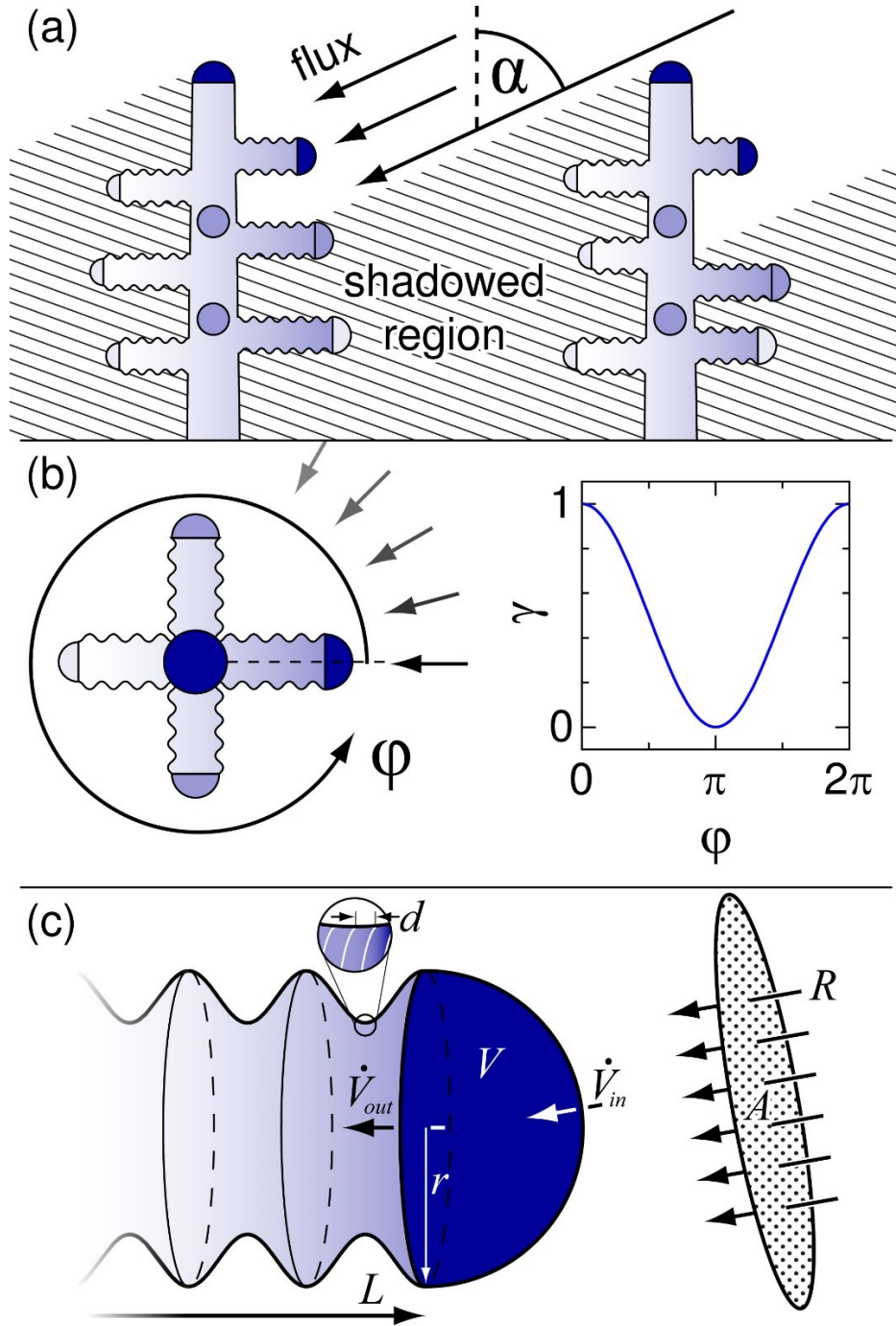


**Figure 4.3:** Schematic of VLS-GLAD rippling phenomenon. Side view (a) shows glancing angle ( $\alpha$ ) and flux shadowing region. Darker droplets are receiving incoming flux and lighter droplet occluded; b) plan view shows rotation of substrate by the angle  $\phi$ , and flux modulation ( $\gamma$ ) at a droplet from shadowing by the attached trunk; (c) droplet radius ( $r$ ) and volume ( $V$ ), branch length ( $L$ ) and monolayer thickness ( $d$ ), flux rate ( $R$ ) and capture area ( $A$ ), and incoming/outgoing volume rates ( $\dot{V}_{in}/\dot{V}_{out}$ ) as used in the model. Reproduced with permission from *Applied Physics Letters*.<sup>285</sup> Copyright 2012, AIP Publishing LLC.

$d = 0.233$  nm. All vapour phase atoms within a certain projected area,  $A$ , were assumed to condense into the liquid droplet (we expect a high probability of adatom diffusion to the liquid droplet within a certain distance<sup>299</sup>). The rate of incoming volume to the droplet ( $\dot{V}_{in}$ ) was calculated:

$$\dot{V}_{in}(t) = RA\gamma(t) \quad (4.1)$$

where  $R$  is the material flux rate as measured at the QCM in nm/s and  $\gamma$  parameterizes the flux modulation due to rotation-induced shadowing or flux shuttering ( $0 \leq \gamma \leq 1$ ). For continuous rotation,  $\gamma(t) = (\sin(2\pi t/\tau_{rot}) + 1)/2$  where  $\tau_{rot}$  is the rotation period in seconds. As neighbouring trunks increase in height, a branch will eventually become completely occluded from the flux. This effect is incorporated as an envelope on  $\dot{V}_{in}$ . For this work, we approximate the envelope as an exponential of the form  $1 - e^{a(t-t_{max})}$ , where  $a$  is a constant and  $t_{max}$  is the time for a certain branch to grow. Detailed studies will be required to elucidate the envelope's functional form.

We assume the branch crystallizes in a layer-by-layer, or birth and spread growth mode<sup>64,284</sup>, with each layer having a circular cross-section of the same radius as the droplet and monolayer thickness of  $d$ . We further assume nucleation time dominates layer crystallization time, such that liquid-solid crystallization time ( $\tau_{LS}$ ) is independent of droplet size and constant for growth of an entire branch. In reality, the growth rate is likely dependent on droplet diameter<sup>300,301</sup>, however, this assumption is tolerable for small changes in droplet diameter. The rate of outgoing volume from the droplet is then:

$$\dot{V}_{out}(t) = d\pi r(t)^2/\tau_{LS} \quad (4.2)$$

where  $r$  is the instantaneous radius of the both the droplet and the branch at the liquid-solid crystallization interface. For a growth of a branch of length  $L$  in time  $t_{max}$ ,  $\tau_{LS} = t_{max}d/L$ . Note that this is not valid at extremely slow rotation rates where the droplet becomes extinct. At each time step  $t_i$  of length  $\Delta t$ , the instantaneous droplet volume and droplet/branch radius were then calculated:

$$V(t_i) = V(t_{i-1}) + \dot{V}_{in}(t_i)\Delta t - \dot{V}_{out}(t_i)\Delta t \quad (4.3)$$

$$r(t_i) = \sqrt[3]{3V(t_i)/2\pi} \quad (4.4)$$

The proposed model reproduces the observed rippling behavior, as shown in **Figure 4.4** for an example case of a branch from **Figure 4.2**. The calculated input and output volume rates ( $\dot{V}_{in}$  and  $\dot{V}_{out}$ , respectively) are shown in **Figure 4.4a** in the case of constant rotation with  $R = 1$  nm/s and  $\tau_{rot} = 10$  s. From the magnified image of the branch (**Figure 4.4b**), we measure  $L = 225$  nm and 13 rippling nodes. Based on the number of nodes and rotation speed, we calculate  $t_{max} = 125$  s, with  $\tau_{LS} = 0.13$  s. We achieved a fit of the extracted branch profile to the simulated

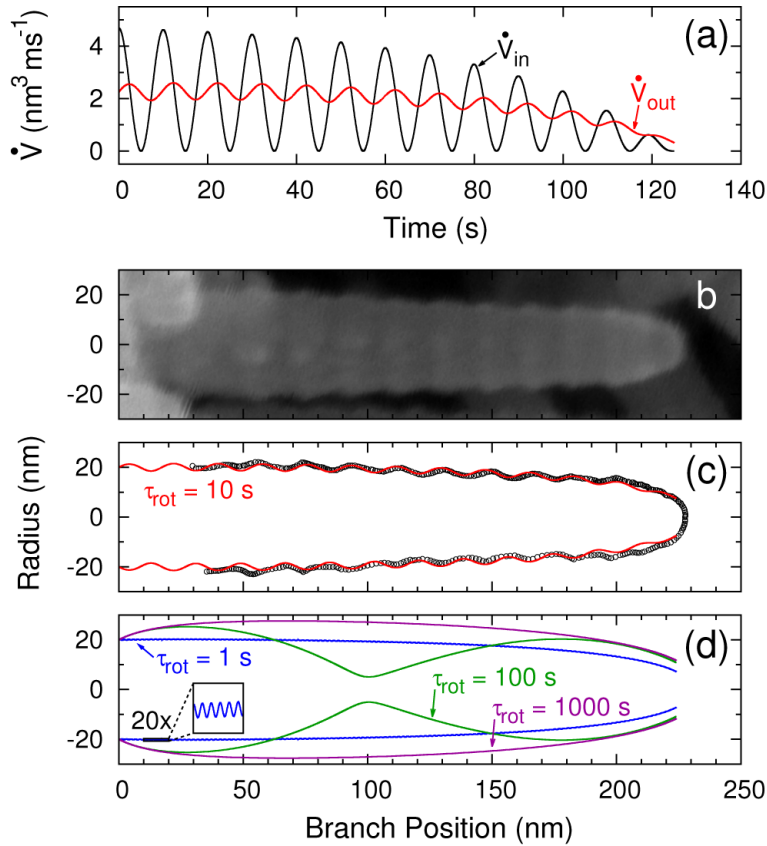


**Figure 4.4:** Branch simulation (a) input volume rate ( $\dot{V}_{in}$ ) to droplet for  $\tau_{rot} = 10$  s and volume rate out ( $\dot{V}_{out}$ ) of the droplet as calculated in each time-step; (b) enlarged SEM image of a branch deposited at  $\tau_{rot} = 10$  s; (c) branch edge profile (open circles) and simulated branch morphology (red line) for  $\tau_{rot} = 10$  s; (d) simulated branch profile for  $\tau_{rot} = 1$  s (blue),  $\tau_{rot} = 100$ s (green), and  $\tau_{rot} = 1000$  s (magenta); y-axis of inset is 1 nm range. Reproduced with permission from *Applied Physics Letters*.<sup>285</sup> Copyright 2012, AIP Publishing LLC.

branch profile by varying the envelope parameter ( $a$ ) and capture area ( $A$ ). A good match is shown in **Figure 4.4c** between the observed and simulated rippling behavior for parameters of  $a = 0.025$  and  $A = 4900 \text{ nm}^2$  (equivalent to a circle with  $\sim 39.5 \text{ nm}$  radius). Several other rippled branches were simulated (not shown) and all showed good fit with the model.

To explore the conditions for which these rippling effects can be observed, the same simulation was run with different rotation speeds. **Figure 4.4d** shows a simulation of the same parameters, but with  $\tau_{rot} = 1 \text{ s}$ ,  $\tau_{rot} = 100 \text{ s}$ , and  $\tau_{rot} = 1000 \text{ s}$ . In the case of  $\tau_{rot} = 1 \text{ s}$ , the rippling effect is still present, however, the amplitude of the rippling is so small it is only visible in the magnified inset. For the case of one and two orders of magnitude increase in rotation time, the length of the rippling events is on the order of the branch length. The rippling is effectively lost as a result of the slower rotation times.

### 4.3 Complex ripple control

To further validate the hypothesis that rippling is a result of flux starvation, more complex structures were grown by two different methods of controlling the incoming flux to the liquid droplet. This was achieved by controlling the local shadowing function (e.g. changing the rotation rate) and by attenuating the vapour flux directly (e.g. rate control or shuttering). The model indicates that both methods should have a similar effect. In the previous chapter, it was shown that rate modulation dynamically controls ITO NW diameter<sup>271</sup>; here we have demonstrated the effect of shuttered flux and the local shadowing environment. ITO NWs grown with shuttered flux are shown in **Figure 4.5**. See **Figure 4.6** for a demonstration of similar rippling control with varying rotation rates.

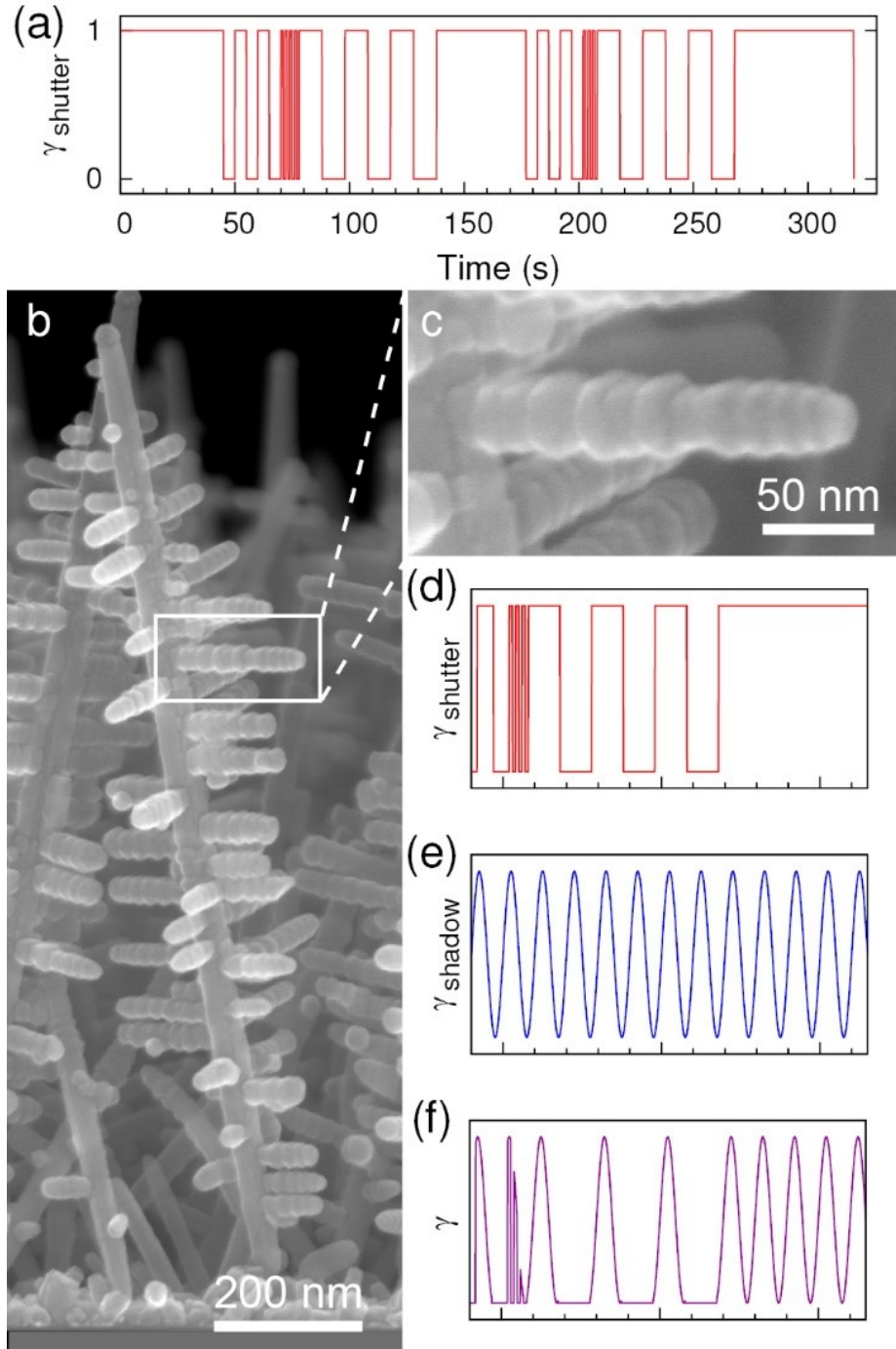


**Figure 4.5:** Complex VLS-GLAD ITO branch growth by shutter-modulated flux according to the pattern shown in (a), where 1 is shutter open and 0 is shutter closed; (b) SEM image of resulting NW with unique branching morphology; (c) magnified key branch region, with (d), (e), and (f) displaying the flux modulation due to shuttering, due to rotation-induced shadowing, and the combined shutter-rotation effect on the flux profile, respectively, for the magnified branch. Reproduced with permission from *Applied Physics Letters*.<sup>285</sup> Copyright 2012, AIP Publishing LLC.

We use the flux shutter profile shown in **Figure 4.5a**, with constant rotation, to produce the ITO NW shown in **Figure 4.5b**. The branch's features follow the shuttering events, controlling ripple amplitude and frequency. Figure 4c is a magnified image of a characteristic branch. **Figure 4.5 d and e** show the approximate shuttering ( $\gamma_{shutter}$ ) and rotational shadowing ( $\gamma_{rotation}$ ) functions, respectively, resulting in the total flux modulation function ( $\gamma$ , **Figure 4.5f**) contributing to the growth of the magnified branch. In both the shuttering and variable rotation cases, we demonstrate control over the rippling features according to the flux profile. Faster rotation rates result in smaller ripple spacing, and shuttered flux can result in long nodes between ripples. Both the variable rotation and shuttering methods demonstrate (through local shadowing and macroscopically modulated vapour pressure, respectively) direct control over supersaturation in the branch droplets.

## 4.4 Conclusions

We have demonstrated that flux starvation in VLS-GLAD enables controlled branch diameter modulation during ITO nanotree growth, consistent with a simple volume in/out model. Flux starvation can be induced through shadowing or by adjusting the flux rate directly, both general features of VLS-GLAD. The nanostructures made possible by the VLS-GLAD technique should be available to any material system compatible with branched VLS growth.

Droplet diameter is coupled to nanowire properties such as composition<sup>302,303</sup>, phase<sup>304</sup>, and crystallographic growth direction<sup>305,306</sup>. Thus, modulation of growth diameter with VLS-GLAD may provide a mechanism to modulate these properties during growth as well. Surface rippling may prove to be a valuable technique to enhance active surface area, create high energy surface defects, or induce phase changes in the material during growth. This technique also allows for the placement of “time stamps” during growth which may allow for improved investigation of time-related growth kinetics. Additional effects of flux shadowing will be investigated in the next chapter.

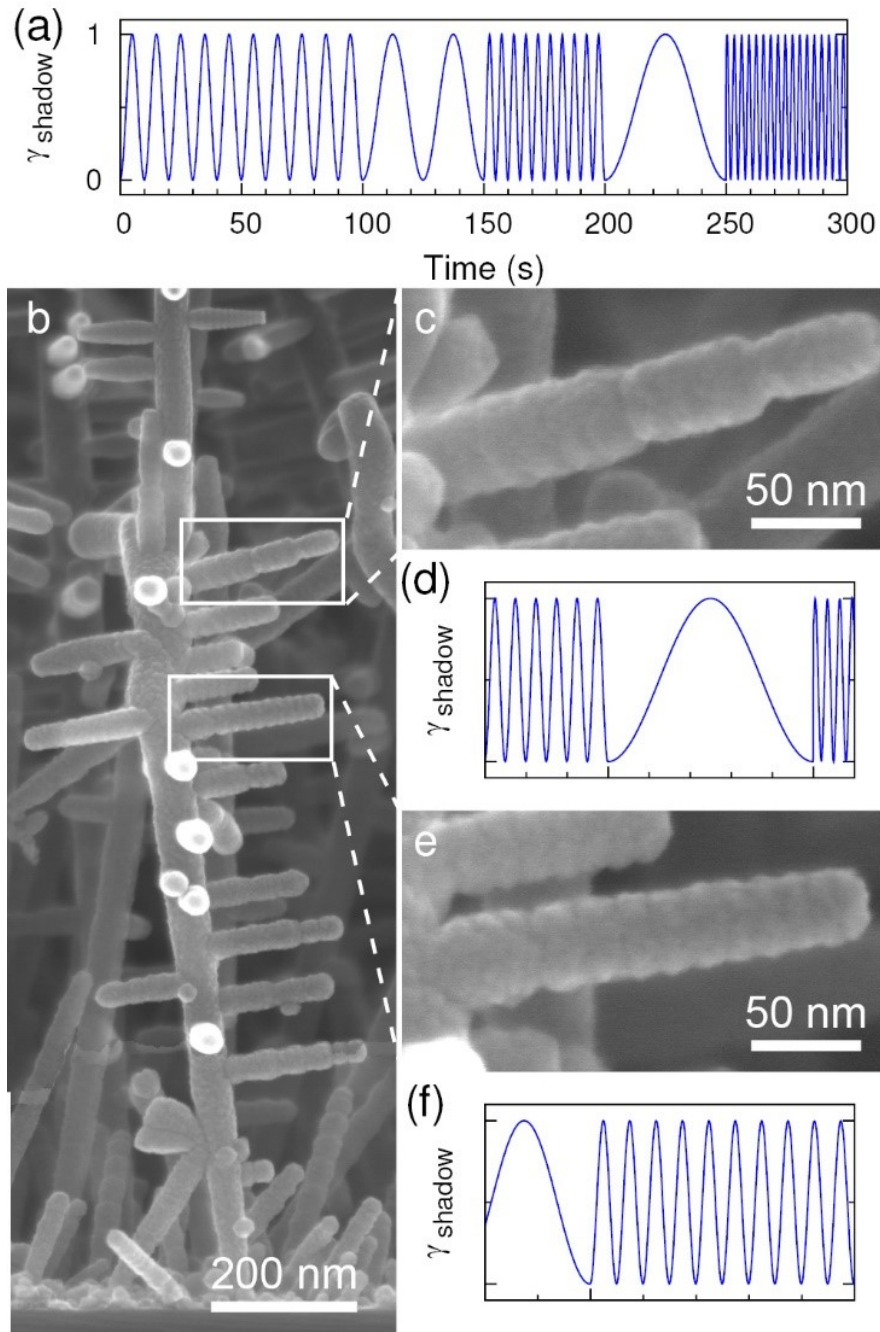


**Figure 4.6:** Complex VLS-GLAD ITO branch growth by changing the rotation rates according to the following program (rotations @  $\tau_{rot}$ ): 10 @ 10 s, 2 @ 25 s, 10 @ 5 s, 1 @ 50 s, ~17 @ 3 s, as shown in (a) as flux attenuation due to the rotational shadowing (1 is flux, 0 is shadowed); (b) SEM image of resulting NW morphology, and magnified branches (c, e) along with the approximate sections of rotational shadowing from (a) that contributed to each branch morphology (d, f, respectively). Reproduced with permission from *Applied Physics Letters*.<sup>285</sup> Copyright 2012, AIP Publishing LLC.

# 5. Branch Placement and Nanotree Alignment

---

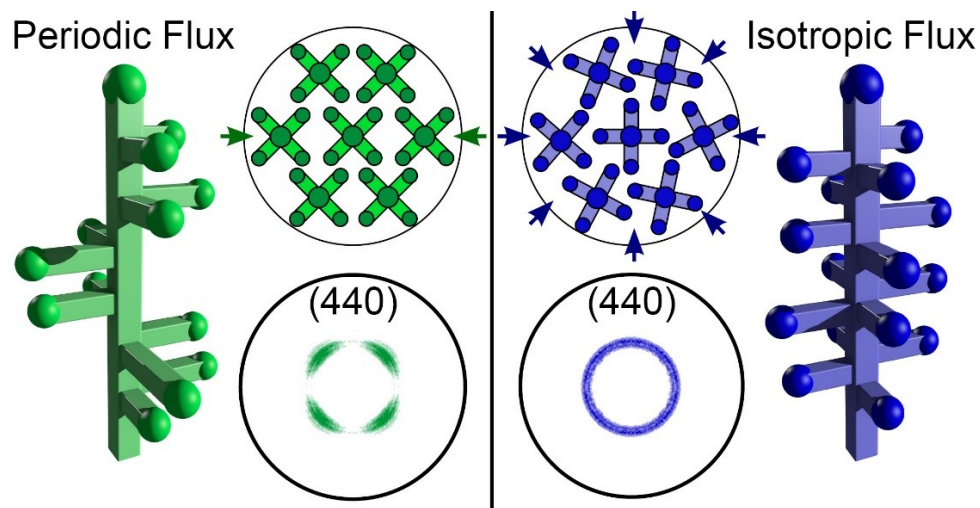


**Figure 5.1:** Table of Contents figure published in *Crystal Growth and Design*.<sup>307</sup> This figure schematically depicts in-plane nanotree alignment and height dependent branch placement using by engineering the azimuthal flux distribution as presented in this chapter. The arrows represent the azimuthal flux positions. Discretized flux position (left) result in aligned nanotrees, isotropic flux distribution (right) results in random nanotree alignment.

---

Portions of this chapter were reproduced with permission of American Chemical Society (ACS) from the following publication:

Beaudry, A. L., LaForge, J. M., Tucker, R. T., Li, P., Taschuk, M. T., and Brett, M. J. *Crystal Growth and Design* **2013**, *13*, 212.

## 5.1 Introduction

### *5.1.1 Introduction*

In this chapter, three unique capabilities of VLS-GLAD are demonstrated: (i) nanotrees are aligned without epitaxy, (ii) branches can be placed on select facets of the nanotree trunk, and (iii) branch orientation can be modified along the height of nanotrees. These new capabilities have the potential to significantly enhance the achievable structural complexity in 3D nanotree arrays. For instance, controlled anisotropic branch growth may enable the design of conductive pathways through NW networks, and the alignment of nanotrees on amorphous substrates may enhance the degree of interconnectivity throughout the arrays, which may be beneficial for charge transport between structures for OPV applications.

VLS-GLAD provides an asymmetric vapour flux which causes shadowing behind growing nanotrees, therefore, branch growth is preferred on the sides of nanotree trunks facing the flux. Dynamic control of the azimuthal orientation of the flux relative to the growing nanotrees enables the preferential orientation of branches to be modulated along the height of the nanotree array, which is demonstrated in this chapter with both continuous and discrete substrate rotation schemes. In addition, a competitive growth mechanism enables in-plane alignment of the nanotrees on amorphous substrates. Initially, nanotree alignment is random on the substrate, however, nanotrees oriented to capture the most flux outgrow other orientations, resulting in crystal texture evolution and nanotree alignment. The competitive selection mechanism is determined by the azimuthal flux distribution, and is absent for films grown with isotropic vapour distributions.

An electron diffraction investigation confirms that each nanotree is a single crystal, with continuity of the crystal structure across the trunk-branch interface. The degree of nanotree alignment and crystal texture is characterized by X-ray diffraction pole figure analysis and branch orientation measurements. By limiting the flux to discrete positions, the films develop both preferential vertical and azimuthal crystal alignment (biaxial texture). The preferential azimuthal alignment is the result of

competitive growth which leads to evolutionary selection of similarly oriented structures. Control over azimuthal nanotree crystal alignment and height dependent branch orientation should increase the achievable complexity in 3D NW architectures.

In this chapter, we show that a collimated obliquely incident flux produces preferentially oriented branch growth on ITO nanotrees. Branch growth is enhanced on the side of the nanotree facing the flux and inhibited on the shadowed regions of the trunk (**Figure 5.2**). The schematic in **Figure 5.2** shows a structure with two branches oriented  $\pm 45^\circ$  from the vapor flux; this is a representation of a typical nanotree orientation that would be selected during the proposed competitive growth mechanism, which will be discussed further below. The square cross-section of the trunk and branches in **Figure 5.2** reflects the square faceting of the single crystal nanotrees; observations of this effect will be shown. By modulating the azimuthal position of the substrate during growth, we show that preferential branch orientation can be changed along the height of the trunk. We demonstrate these effects in four classes of ITO nanotrees defined by their height dependent branching morphologies: unidirectional, periodic, chiral and isotropic. Additionally, we provide evidence to suggest that an observed preferential azimuthal (in-plane) branch alignment in nanotree films grown without epitaxy, accompanied by a biaxial crystal texture, may be primarily a result of an evolutionary selection mechanism seen in other GLAD work.<sup>159,166,170,308-311</sup>

### *5.1.2 Contributions*

The work presented in this chapter was the result of a collaborative effort. NW growth, morphological characterization, and interpretation of the results were led by Allan Beaudry. Joshua LaForge performed XRD, and analyzed pole figure data. Peng Li obtained HRTEM, SAED, and TEM tomography data. Ryan Tucker prepared schematic figures and helped interpret the results.

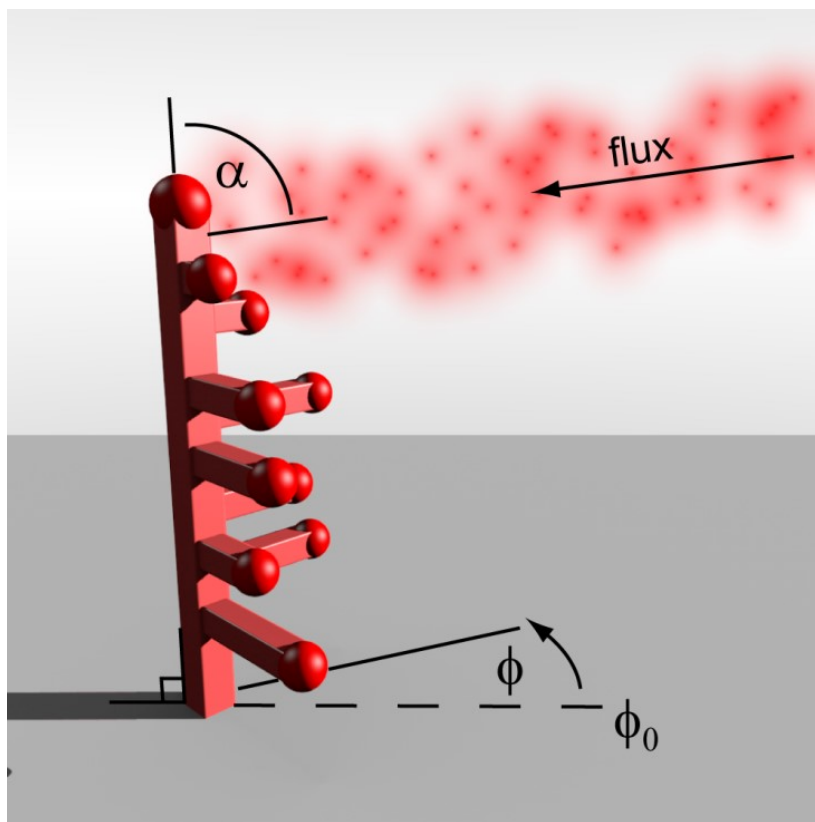


**Figure 5.2:** Illustration of VLS-GLAD growth of ITO nanotrees. Deposition angle ( $\alpha$ ) and angle of flux rotation ( $\phi$ ) are shown.  $\phi_0$  indicates the initial azimuthal position of the flux. Reproduced with permission from *Crystal Growth and Design*.<sup>307</sup> Copyright 2013, American Chemical Society.

## 5.2 Experimental

### 5.2.1 Film Fabrication

Films were grown at a nominal temperature of 240 °C, deposition angle of 85°, and nominal flux rates of 2 nm/s and 0.2 nm/s, using the same growth chamber as described in the previous chapter. Pitch is defined as the nominal thickness deposited per substrate rotation. Films grown at 2 nm/s were deposited with a nominal thickness of 1200 nm, and an infinite pitch  $p = \infty$  (no substrate rotation, unidirectional structure),  $p = 1200$  nm (1 continuous 360° rotation, chiral structure) and  $p = 10$  nm (120 continuous 360° rotations, isotropic structure). A periodically structured film was deposited using spin-pause deposition parameters (2 discrete 180° rotations, periodic structure). For the periodic film, the azimuthal angle was

periodically alternated, for a total nominal thickness of 1200 nm ( $\phi = 0^\circ$  for 0 nm - 400 nm;  $\phi = 180^\circ$  for 400 nm - 800 nm;  $\phi = 360^\circ$  for 800 nm - 1200 nm). The azimuthal modulation schemes used in this work are shown in **Figure 5.3**. Films with the same azimuthal modulation schemes were also grown at 0.2 nm/s to a nominal thickness of 300 nm measured at the CTM (except for the 0.2 nm/s periodic film, which was grown to a nominal thickness of 450 nm).

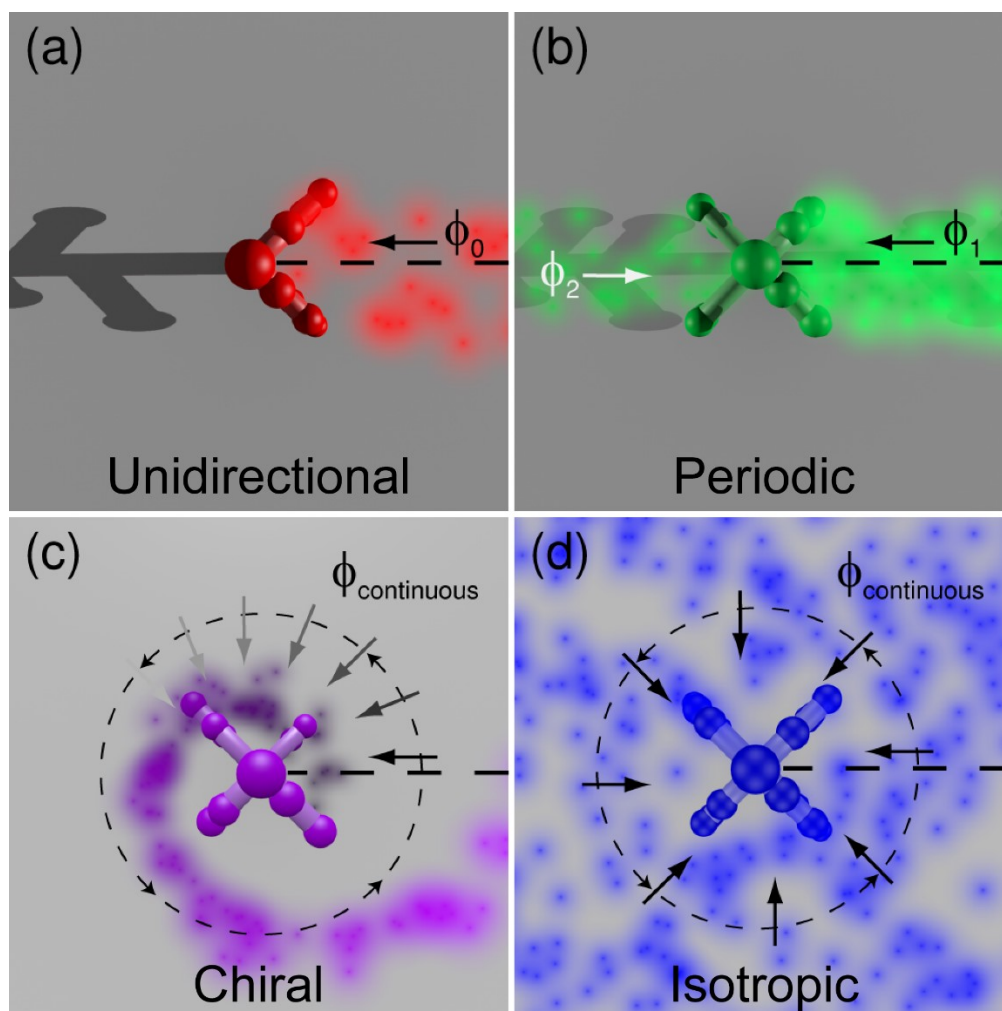


**Figure 5.3:** Top-down schematic of VLS-GLAD azimuthal modulation schemes for (a) unidirectional, (b) periodic, and (c) chiral (one continuous rotation) and isotropic ( $p = 10$  nm) ITO nanotree structures. Reproduced with permission from *Crystal Growth and Design*.<sup>307</sup> Copyright 2013, American Chemical Society.

### *5.2.2 Film characterization*

SEM, electron tomography, SAED, and XRD were used to characterize nanotree morphology, crystal texture, and their orientation relative to the flux directions. A Bruker D8 Discover with HiStar area detector acquired XRD line profiles and pole figures of the (400), (222), (440), and (622) diffraction peaks. A Cu  $K\alpha$  radiation source and 0.5 mm collimator was used for each acquisition, with the detector placed  $\sim 15$  cm from the focal point. Films grown at 2 nm/s exhibited stronger XRD signals than those at 0.2 nm/s and were used for the pole-figure study to reduce acquisition time. The pole-figure data was processed using GADDS software (Bruker). An absorption correction was applied by estimating the film's volume density from substrate mass measurements before and after deposition and accounting for film thickness and area. Radial integration of the pole-figure peaks was performed in GADDS to compare intensity variation in the azimuthal direction to branch orientation data collected from top-down SEM images of the sample taken with a Hitachi S-4800 at 10,000 times magnification. The trunks and branches of the nanotrees typically both grow along a [100] crystal direction, with the trunks tending towards growth along the substrate normal and the branches orthogonal to the trunk. All identifiable branches from four images of each sample were analyzed to compare the azimuthal branch orientations relative to the initial vapor flux direction ( $\phi_0$ ) with ImageJ.<sup>283</sup> Azimuthal orientation of each trunk in films grown at 2 nm/s was assessed by measuring the orientation of the most predominant branch on each trunk in 8 top-down SEM images (10,000x magnification). The trunk orientation is uniquely defined between  $0^\circ$  and  $90^\circ$  due to the 4-fold symmetry around the  $\langle 100 \rangle$  direction.

Electron tomography tilt series were acquired on a JEOL 2200 FS TEM/STEM, operated at an accelerating voltage of 200 kV with assistance from Peng Li. Bright field TEM (BF-TEM) images were collected from  $\pm 65^\circ$  with  $1^\circ$  steps with tilting axis along the trunk. Lacey carbon grids, which were coated with a 2 nm thick discontinuous gold film, were used as substrates. Reconstruction and visualization were performed using the TEMography<sup>TM</sup> software package from System In

Frontier Inc.<sup>312</sup> The Simultaneous Iterative Reconstruction Technique (SIRT) algorithm<sup>313</sup> was used to minimize the effect of gold particles overlapped with the sample. Electron diffraction analysis was performed on a Hitachi HF3300 TEM/STEM, operated at an accelerating voltage of 300 kV. Cross-section and individual nanotree TEM samples were prepared on a Hitachi NB5000 Focused Ion & Electron Beam System. Nanotrees were scratched off and loaded onto a silicon substrate, and then coated with a 100 nm thick carbon film as a protection layer during the subsequent FIB processing. Individual nanotree samples were plucked out and mounted onto a Hitachi 3D-observation holder by a standard micro-pillar sampling<sup>314</sup> with the tilt axis along the trunk, which enables diffraction analysis from a full 360 degrees.

## 5.3 Results and Discussion

### *5.3.1 Height dependent branch placement*

ITO nanotrees were grown via VLS-GLAD using the four substrate rotation configurations described in **Table 5.1** and shown schematically in **Figure 5.3**. Substrate rotation is used to control the azimuthal modulation of the flux from the perspective of the growing film. In this chapter,  $\phi$  is used to define the azimuthal position of the vapor flux with respect to the substrate. Cross-sectional SEM images of unidirectional, periodic, chiral, and isotropic nanotrees grown at a flux rates of 2 nm/s and 0.2 nm/s are shown in **Figure 5.4**. The azimuthal motion of the flux appears to control height dependent preferential branch orientation. The height dependent branch placement can be seen clearly in the closer view of nanotrees grown at 0.2 nm/s shown in **Figure 5.5**. In **Figure 5.5a**, the unidirectional nanotrees exhibit an asymmetric branch morphology, with average branch growth primarily directed toward the collimated flux. Periodic modulation between 0° and 180° during growth results in the nanotree structures shown in **Figure 5.5b**. It is clear that the branches grow on alternating sides of the trunk, depending on the relative azimuthal orientation of the flux during growth. Chiral nanotrees shown in **Figure 5.5c** were grown while the substrate completed a single rotation. The chirality of

the branch orientation is expected to follow flux rotation, but this is difficult to confirm with edge view SEM images. As the rotation rate is increased to a 10 nm pitch an isotropic nanotree is obtained as seen in **Figure 5.5d**. Branches grow uniformly on all four sides of the nanotree, with no observed preferential orientation.

Name	Pitch (nm)	$\phi$ (°)	Trunk Height ( $\mu\text{m}$ )	Trunk Density ( $\mu\text{m}^{-2}$ )
Unidirectional	$\infty$	0	$5.3 \pm 0.3$	$1.15 \pm 0.04$
Periodic	-	0, 180, 360	$4.3 \pm 0.1$	$1.32 \pm 0.04$
Chiral	1200	0 to 360	$3.3 \pm 0.2$	$1.20 \pm 0.04$
Isotropic	10	0 to 43200	$3.3 \pm 0.2$	$2.45 \pm 0.06$

**Table 5.1:** Deposition conditions and properties of nanotree films deposited at 2 nm/s to a nominal thickness of 1200 nm. Reproduced with permission from *Crystal Growth and Design*.<sup>307</sup> Copyright 2013, American Chemical Society.

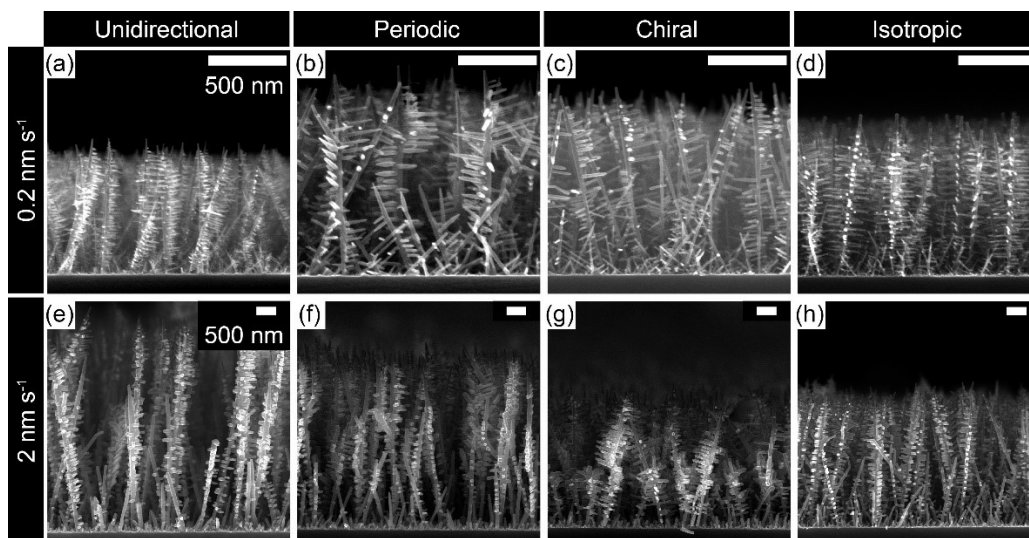


**Figure 5.4:** Cross-sectional SEM images of ITO nanotrees grown with  $\alpha = 85^\circ$ ,  $T = 240^\circ\text{C}$ , and flux rate =  $0.2\text{ nm/s}$  (top) or  $2\text{ nm/s}$  (bottom). Scale bars are all  $500\text{ nm}$  in length. The initial azimuthal vapour flux angle ( $\phi_0$ ) is oriented from the right to left in each image. The nominal thickness of the films are  $300\text{ nm}$  (top) and  $1200\text{ nm}$  (bottom). Reproduced with permission from *Crystal Growth and Design*.<sup>307</sup> Copyright 2013, American Chemical Society.

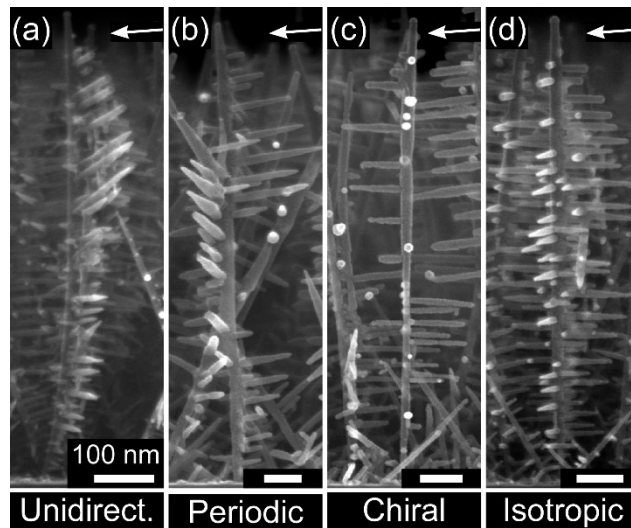


**Figure 5.5:** Cross-sectional SEM images of ITO nanotrees ( $\alpha = 85^\circ$ ,  $T = 240^\circ\text{C}$ , and flux rate =  $0.2\text{ nm/s}$ ). Scale bars are all  $100\text{ nm}$  in length. The ITO nanotrees are named: (a) unidirectional, (b) periodic, (c) chiral and (d) isotropic, based on the azimuthal modulation configuration used during growth, shown in **Figure 5.3**. The initial azimuthal vapor flux angle ( $\phi_0$ ) is oriented from the right to left as indicated by the arrow in each image. The nominal thicknesses (CTM) of the films were  $300\text{ nm}$  for (a), (b) and (c), and  $450\text{ nm}$  for (d). Reproduced with permission from *Crystal Growth and Design*.<sup>307</sup> Copyright 2013, American Chemical Society.

### 5.3.2 Azimuthal branch alignment

Branch orientation was measured with respect to the initial flux axis ( $\phi_0$ ) from plan-view SEM images (**Figure 5.6**) of the nanotree films grown at 2 nm/s. **Figure 5.7** shows sample measurements taken from top-down SEM images using ImageJ software.

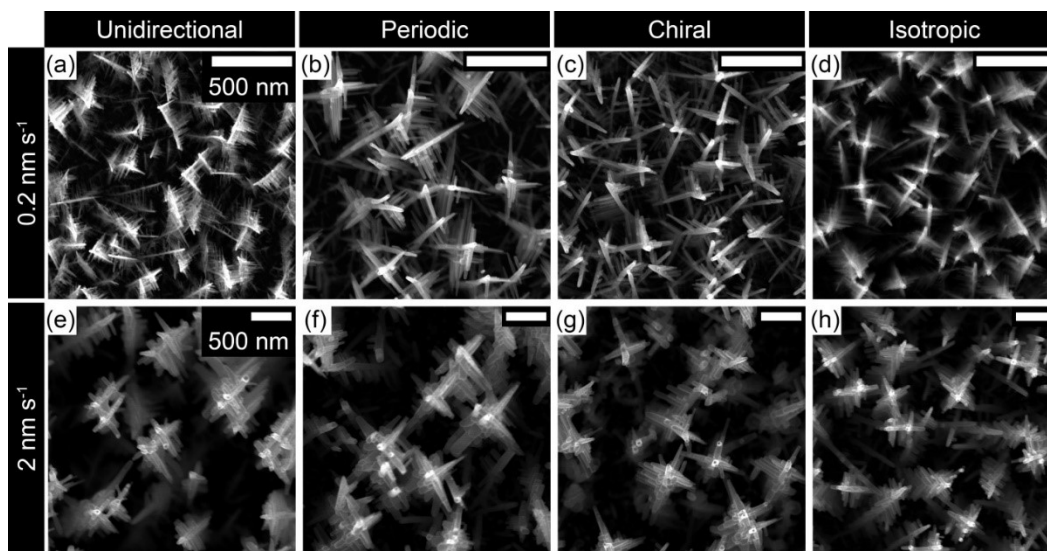


**Figure 5.6:** Top-SEMs of (a) unidirectional, (b) periodic, (c) chiral and (d) isotropic films. The top and bottom rows show structures grown at 0.2 nm/s and 2 nm/s, respectively. Initial flux position is from left to right in each case. Reproduced with permission from *Crystal Growth and Design*.<sup>307</sup> Copyright 2013, American Chemical Society.

Normalized radial histograms shown in **Figure 5.8** display the angular orientation of at least 1371 measured branches from 5 images in each film. **Figure 5.9** shows a color coded histogram plot, which indicates the number of branches measured with a certain length and orientation. The overlaid lines in **Figure 5.8** represent crystallographic data which will be discussed later in this work. Branches throughout the unidirectional and periodic films exhibit preferential growth at  $\pm 45^\circ$  and  $\pm 135^\circ$  relative to the flux axis (**Figure 5.8a,b** and **Figure 5.9a,b**). These directions are the result of in-plane crystal orientation of the nanotrees, discussed later. In the unidirectional film, branches oriented  $\pm 135^\circ$  from  $\phi_0$  grow on the shadowed side of the trunk, and as a result, are significantly shorter than branches oriented  $\pm 45^\circ$  from  $\phi_0$  (**Figure 5.9a**). The low number (**Figure 5.8a**) and short length of branches (**Figure 5.9a**) on the shadowed side of the trunk show the total

branch mass on the exposed side of the trunk is substantially greater. Note that in the periodic case, the low number of branches counted with orientations in the second and third quadrants (between  $90^\circ$  and  $270^\circ$ ) may be a result of their location midway up the trunk making them difficult to observe in plan-view images.

Preferential branch orientations are less pronounced in films grown with continuous substrate rotation (**Figure 5.8c,d** and **Figure 5.9c,d**). Films of chiral nanotrees appear to exhibit preferential branch orientation but it is far less pronounced than the unidirectional or periodic films. Isotropic films exhibit faint or no preferred orientation. As substrate rotation rate is increased, the vapor flux is effectively azimuthally isotropic, and as a result, preferential branch orientation is significantly reduced (**Figure 5.8d**).

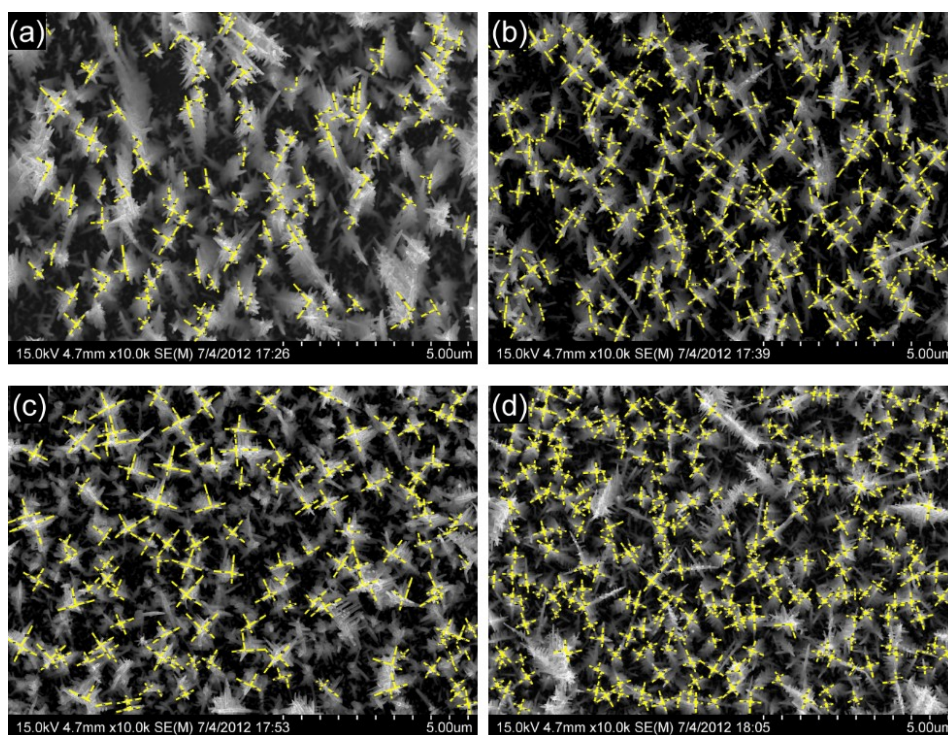


**Figure 5.7:** Sample measurements taken from top-down SEM images using ImageJ software for (a) unidirectional, (b) periodic, (c) chiral and (d) isotropic films. Five images (same as shown above) were measured for each array. One branch measured for each growth direction on a trunk, with a maximum of four measurements per trunk. Lines were drawn from trunk-branch interface to branch tip. Reproduced with permission from *Crystal Growth and Design*.<sup>307</sup> Copyright 2013, American Chemical Society.

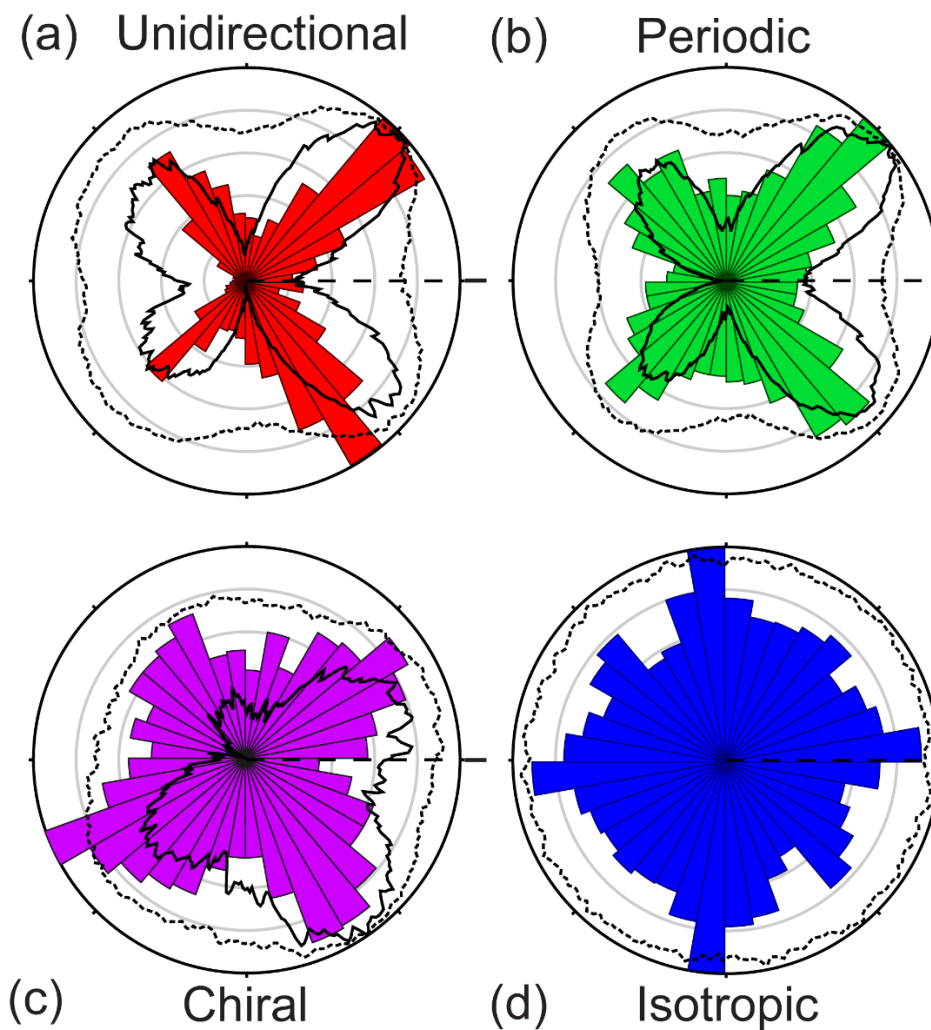


**Figure 5.8:** Normalized radial histograms illustrating the number of branches counted at azimuthal orientations from  $\phi_0$  are shown for (a) unidirectional, (b) periodic, (c) chiral, and (d) isotropic ITO nanotree films grown at 2 nm/s. Integrated intensity from (440) XRD pole figures are illustrated by dotted black lines in the histograms. Solid black lines illustrate the integrated intensity from (440) XRD pole figures with isotropic ITO nanotree background signal subtracted. The initial flux direction ( $\phi_0 = 0^\circ$ ) is oriented from right to left as indicated by the horizontal dashed black line and arrow in each figure. Rotation of the flux is counter clockwise in (c) and (d). Bin size is  $10^\circ$ , and the outer ring corresponds to a maximum of (a) 99, (b) 111, (c) 75, and (d) 154 counts for each histogram. Reproduced with permission from *Crystal Growth and Design*.<sup>307</sup> Copyright 2013, American Chemical Society.

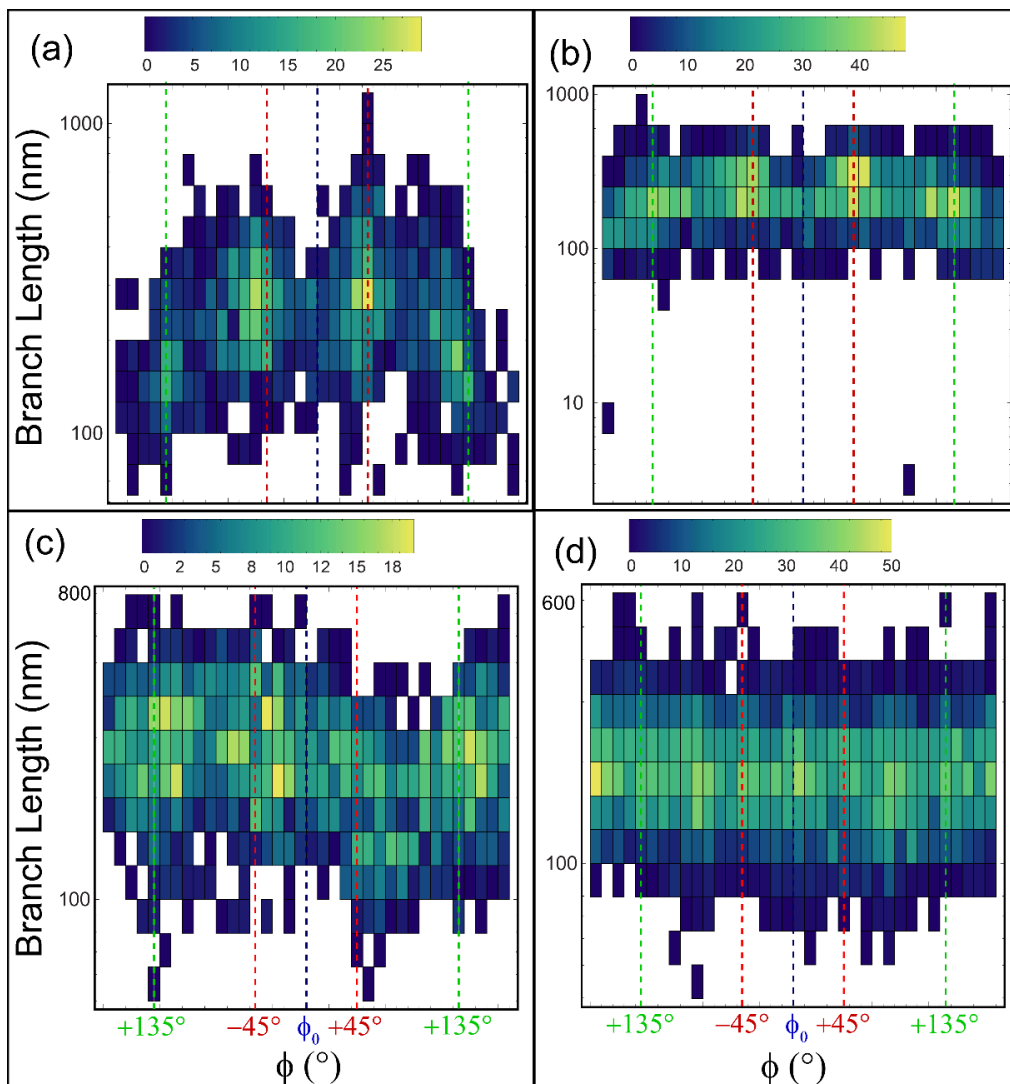


**Figure 5.9:** Histogram density plots of the branch orientation and length for (a) unidirectional, (b) periodic, (c) chiral, and (d) isotropic films. Bin color code indicates the number of counts at a particular orientation and length. Dotted blue lines indicate  $\phi_0$ , dotted red lines indicate  $\pm 45^\circ$  from  $\phi_0$ , and dotted green lines indicate  $\pm 135^\circ$  from  $\phi_0$ .

Overall, branches tend to grow on the region of trunks exposed to flux at the time of nucleation. This suggests branch nucleation occurs preferentially within a limited proximity to where the trunk is directly exposed to the collimated vapor flux. Branch nucleation due to surface diffusion vertically and azimuthally about the trunk appears to be limited as shown by the abrupt change in branch orientation midway up the periodic nanotrees (**Figure 5.5b**) and reduced branching on the shadowed surface in **Figure 5.8a**. However, branch growth is observed in several instances on regions of the trunk that were shadowed during the time of nucleation (left side of **Figure 5.8a**). This suggests that although branch nucleation is suppressed on shadowed surfaces due to flux starvation, a combination of surface diffusion around the trunk cross-section and re-evaporation from adjacent surfaces is sufficient to nucleate branches within the shadowed region. Once nucleated, these branches may grow by becoming directly exposed to the flux, or by collecting material from surface diffusion and re-evaporation. The branches on the shadowed side of unidirectional nanotree trunks are significantly shorter (**Figure 5.9a**), suggesting that branch growth rate is dominated by direct flux capture. Improved understanding of the surface diffusion limits, combined with the development of substrate motion configurations optimized to deliver flux near desired growth surfaces may allow further precision in branch placement.

### *5.3.3 Individual nanotree morphology*

Volumetric reconstructions of an isotropic nanotree grown at 2 nm/s were obtained using BF-TEM from a variety of angles (**Figure 5.10**) and an example is shown in **Figure 5.11a**. The relative orientation of the nanotree trunk and branches can be clearly seen: branches grow orthogonally on four sides of the trunk, and normal to the main trunk. The square faceting of the trunk cross-section is clearly visible in a cross sectional slice shown in **Figure 5.11b**, and can be confirmed with the TEM image of a cross sectional sample in **Figure 5.13a**. The presence of a corner likely reduces the probability of surface diffusion azimuthally about the trunk due to a 3D Schwoebel-Ehrlich barrier<sup>315</sup> agreeing with our observations of limited branch nucleation on shadowed surfaces.

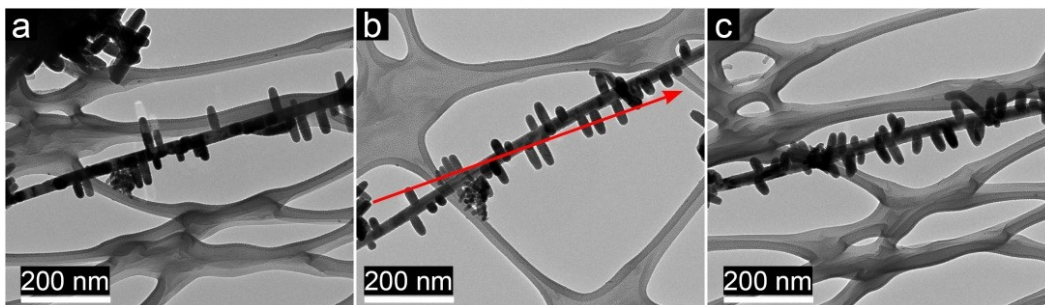


**Figure 5.10:** Typical BF-TEM images within a tilt series of an isotropic nanotree: (A) tilted at  $-65^\circ$ ; (B)  $0^\circ$  degree with red arrow indicating tilt axis; (C)  $+65^\circ$ . Reproduced with permission from *Crystal Growth and Design*.<sup>307</sup> Copyright 2013, American Chemical Society.

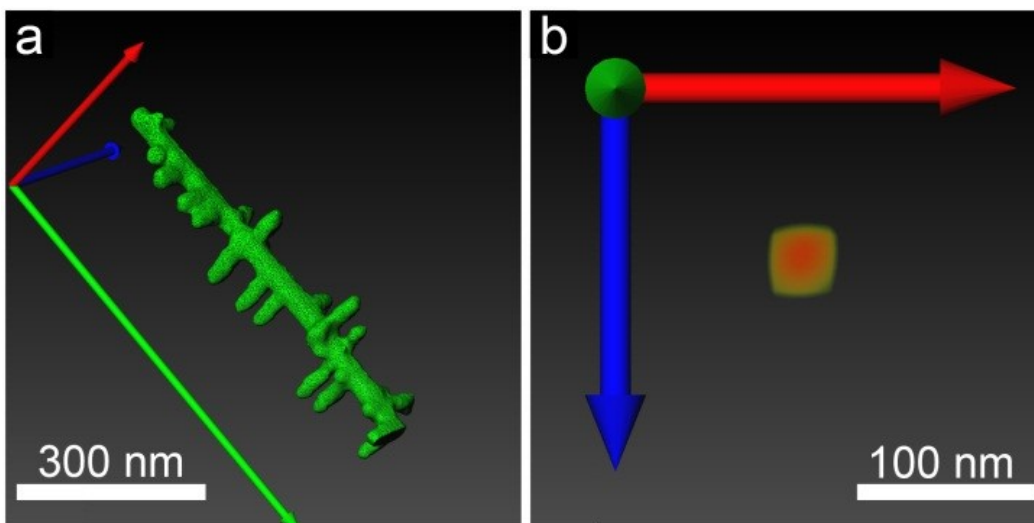


**Figure 5.11:** A volumetric rendering of an isotropic nanotree obtained from TEM tomography shown tilted at an arbitrary angle in (a), and sliced along its cross-section in (b). The red, blue and green arrows are used to identify axes between images. Reproduced with permission from *Crystal Growth and Design*.<sup>307</sup> Copyright 2013, American Chemical Society.

As the trunks grow vertically, in the substrate normal direction, it is expected that geometric shadowing gradually starves branches of flux deeper in the film.<sup>285</sup> Branches far beneath the nanotree tops are not expected to receive a significant amount of flux from re-evaporation because surrounding adatoms will have had time to thermalize and be incorporated into the solid state. Similarly, material from surface diffusion becomes increasingly limited as branches closer to the growth surface will act as sinks to captured flux. This effect places an upper limit on the time that a branch may continue to receive growth material and therefore limits branch length. The effect is apparent by the relatively uniform branch length with increasing trunk height observed in **Figure 5.5** and agrees with our previous observations of reduced growth rate as branches become occluded from the flux.<sup>285</sup>

#### *5.3.4 Crystal structure*

Electron and X-ray diffraction were used to examine the crystal structure of individual nanotrees and texture of the nanotree ensembles, respectively. Diffraction profiles of the four nanotree morphologies discussed here (see **Figure 5.12**) are consistent with the cubic crystal structure (space group  $Ia\bar{3}$ , 01-089-4597) previously observed. Identical electron diffraction patterns obtained from trunk, branch and their interface of a nanotree cross-section confirm that each nanotree is a single crystal and that branches exhibit epitaxial growth on the trunk, as shown in **Figure 5.13**. Electron diffraction patterns were taken along branch axes as well as at intermediate directions from a single nanotree sample with the electron beam normal to the trunk at all directions (**Figure 5.14**). A branch growth orientation of [001] can be derived from zone axes of diffraction patterns along the branch axes shown in **Figure 5.14b,e and h**. Trunk growth orientation is [100] (**Figure 5.13**), which is normal to the substrate and zone axes of all patterns in **Figure 5.14**.

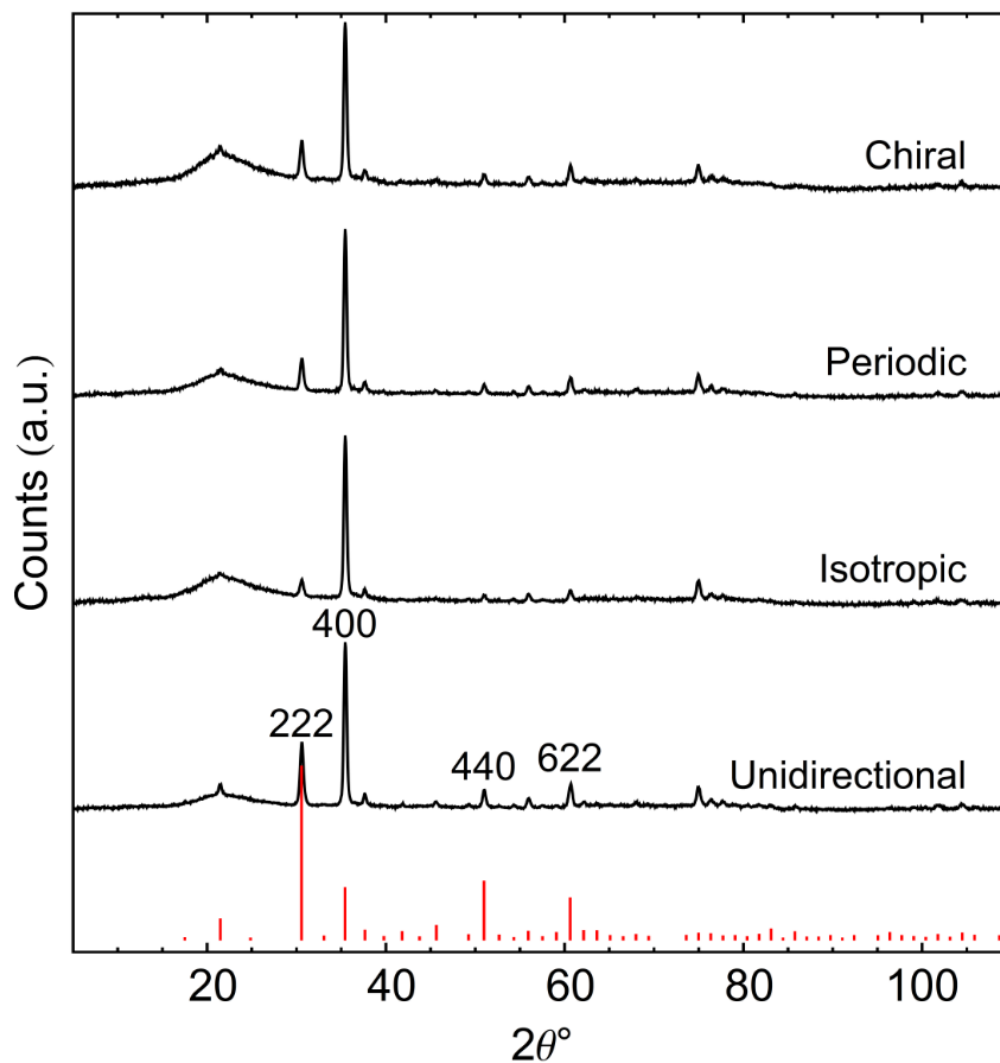


**Figure 5.12:** Diffraction line profiles for the 2.0 nm/s films that were used for pole-figures. Diffraction peaks in the profiles correspond to the expected peak positions for ITO (PDF: 01-089-4597) shown at the bottom of the figure. Reproduced with permission from *Crystal Growth and Design*.<sup>307</sup> Copyright 2013, American Chemical Society.

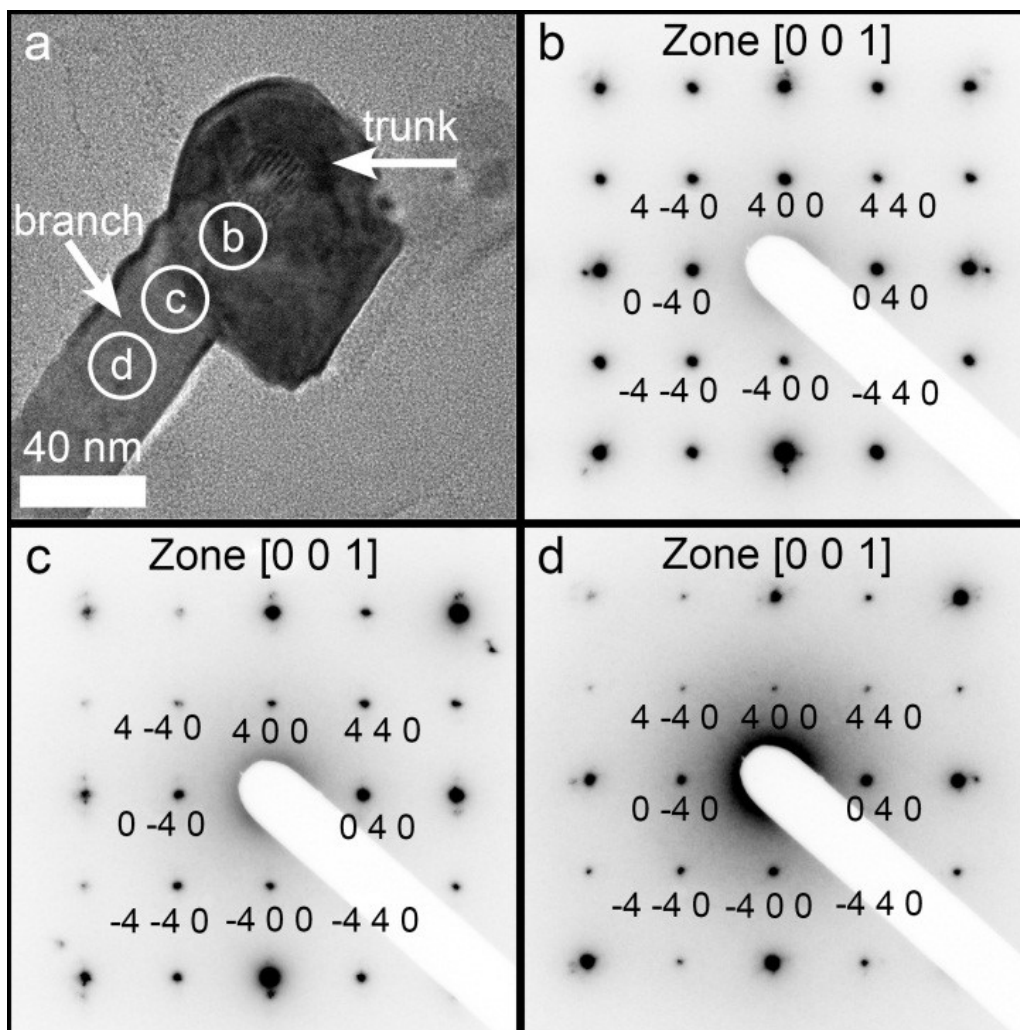


**Figure 5.13:** A TEM image of a nanotree cross-section at a branch-trunk interface is shown in (a). Electron diffraction patterns were taken at locations indicated by the white circles: (b) trunk, (c) trunk-branch interface and (d) branch. Reproduced with permission from *Crystal Growth and Design*.<sup>307</sup> Copyright 2013, American Chemical Society.

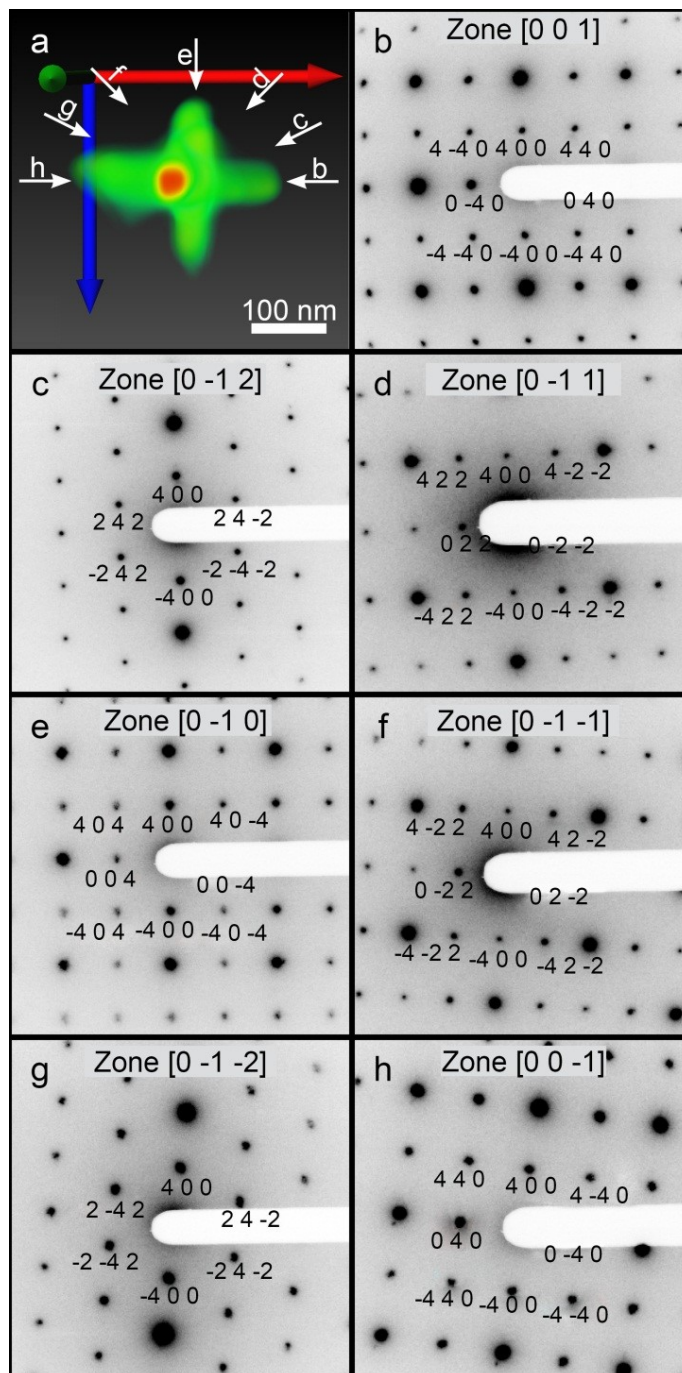


**Figure 5.14:** A projection view of a nanotree along its trunk obtained from a volumetric rendering is shown in (a). Diffraction analysis of a single nanotree with the electron beam perpendicular to the trunk was taken across a full 180°, at locations indicated by the white arrows, as shown from b to h. Diffraction patterns taken along branch axes (b, e, h) have a zone axis of [001], [0-10] and [00-1]. Reproduced with permission from *Crystal Growth and Design*.<sup>307</sup> Copyright 2013, American Chemical Society.

### *5.3.5 Crystal texture*

X-ray pole figures of the (400), (222), (440), and (622) diffraction peaks were taken to characterize the overall crystal texture and its relationship to the flux direction and branch orientation for each film (**Figure 5.15**). **Figure 5.16** shows the pole figures for the periodic nanotree film. All four morphologies have  $\langle 100 \rangle$  out-of-plane texture, preferring to grow with the  $\langle 100 \rangle$  direction/trunk axis aligned parallel to the growth direction/substrate normal. Schematics shown in **Figure 5.16e and f** demonstrates the expected orientation relationship between the  $\{100\}$ ,  $\{111\}$ ,  $\{110\}$  and  $\{311\}$  planes for a single crystal of ITO ( $m\bar{3}$  point symmetry) with  $\langle 100 \rangle$  out-of-plane texture. Agreement between the expected and observed radial positions of the (222), (440), and (622) peaks is observed. A slight tilt towards the flux direction exists in all of the pole-figures. It is possible that sample tilt within the goniometer could be responsible for this effect.

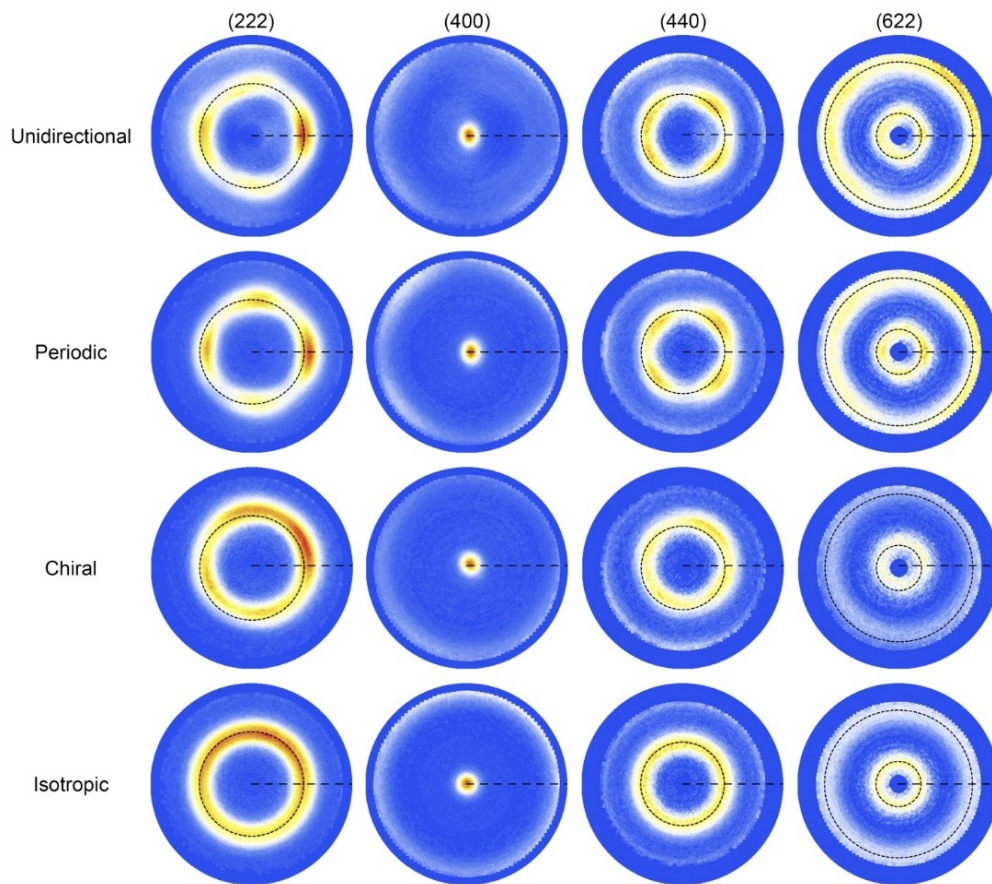


**Figure 5.15:** Pole figures for each films taken of the (222), (400), (440), and (622) diffraction peaks. The dashed circles indicate the expected radial positions for X-ray diffraction around a single crystal nanotree oriented [100] normal to the substrate and are located at  $54.7^\circ$  for (222),  $45^\circ$  for (440), and  $25.2^\circ$  (inner circle) and  $72.5^\circ$  for (622). The flat dashed line indicates the initial flux axis ( $\phi_0$ ), and the flux rotates counter clockwise in the chiral and isotropic films. Reproduced with permission from *Crystal Growth and Design*.<sup>307</sup> Copyright 2013, American Chemical Society.

Of the four morphologies, only the periodic and unidirectional structures have a clear biaxial texture, showing both in-plane and out-of-plane orientation. The four fold-symmetry and azimuthal positions of the (222), (440) and (622) peaks correspond to the expected positions for a  $\langle 100 \rangle$  out-of-plane oriented single crystal nanotree. For both periodic and unidirectional films, the (222) and (622) are oriented towards the flux, whereas the (440) peaks are offset by  $45^\circ$ . Thus, the vapor-incidence plane occurs parallel to (110) and the films exhibit [100](110) biaxial texture, following the notation of Abelmann and Lodder.<sup>137</sup>

The observed out-of-plane texture is due to the preferred growth direction of ITO nanotrees grown via VLS.<sup>33,197,316</sup> Biaxial texture is typically only observed in VLS systems when substrate epitaxy is used. However, development of biaxial texture in obliquely deposited films without substrate epitaxy has been observed in several other nanostructured material systems grown via ballistic transport instead of VLS.<sup>159,166,170,308–311</sup> Recently, the effect of substrate motion on the development of in-plane texture has been shown.<sup>170,308</sup> These studies report that in-plane texture can be developed only when the flux is deposited at directions that match the azimuthal symmetry of the crystalline growth. Continuous substrate rotation removes the in-plane texture but maintains the out-of-plane texture. We have observed a similar effect here: in-plane texture is observed for the unidirectional and periodic films, where the vapor-incidence plane is parallel to the (110) direction, and is reduced or lost when the substrate is continuously rotated for the chiral and isotropic films, respectively. Development of in-plane texture is often attributed to an evolutionary selection process in oblique deposition, and is discussed further below.

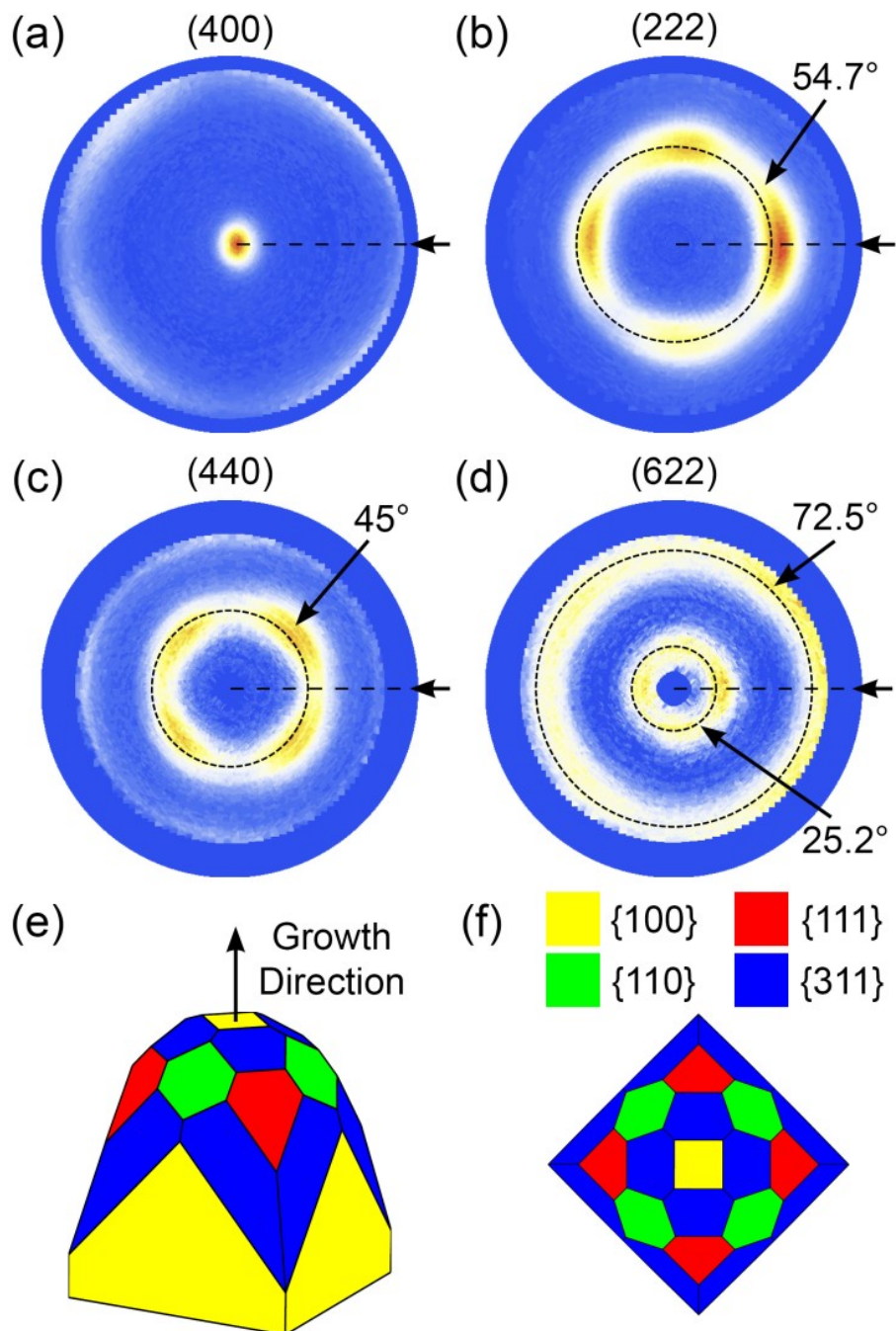


**Figure 5.16:** XRD pole figures obtained from a periodic ITO nanotree film are shown for (a) (400), (b) (222), (c) (440) and (d) (622) planes. The initial flux direction ( $\phi_0 = 0^\circ$ ) is oriented from right to left as indicated by the horizontal dashed black line and arrow for each pole figure. The dashed circles indicate the expected radial positions for X-ray diffraction around a single crystal nanotree oriented [100] normal to the substrate. A schematic illustrating the crystal structure and facets of a single crystal ITO nanotree trunk growing in the [100] direction are shown from (e) cross-sectional and (f) top-down perspectives. Branch growth occurs in the four {100} directions normal to the trunk. Reproduced with permission from *Crystal Growth and Design*.<sup>307</sup> Copyright 2013, American Chemical Society.

### *5.3.6 Branch alignment and crystal texture relationship*

The X-ray and electron diffraction data indicate that the nanotrees are single crystal with the trunks and branches growing in orthogonal [100] crystallographic directions. Thus, in-plane crystal orientation should be accompanied by a preferential branch orientation that is consistent with a [100] epitaxial relationship between a trunk and branches. To confirm this relationship, (440) pole figures were radially integrated to produce polar-plots, where the radial distance corresponds to the diffraction intensity, and overlaid onto the branch histograms (**Figure 5.8**). We used the (440) pole-figure because the relative azimuthal position of these diffraction peaks corresponds to the position of [100] oriented branches (**Figure 5.16f**). The results of this comparison show that for each film in **Figure 5.8**, the preferential branch orientation follows the diffracted intensity of the (440) pole figure consistent with branch growth in a [100] direction orthogonal to the trunk.

(440) pole figures exhibit peaks at  $\pm 45^\circ$  and  $\pm 135^\circ$  relative to the flux axis in the unidirectional and periodic films, establishing a link between the observed in-plane texture in these films and branch orientation. Although the periodic and unidirectional films have similar in-plane texture, the branch directions in the periodic film have a height dependence whereas the unidirectional films do not. This suggests that the in-plane texture can be maintained while changing the preferential branch orientation along the height of the trunks during growth as long as the flux directions reflect the crystal symmetry of the trunks. The reduced intensity seen in the chiral film between  $90^\circ$  and  $180^\circ$  (**Figure 5.8c**) is difficult to explain. The flux is in this region relatively early in the growth, and it may be the branching rate is suppressed in that period. In all cases, the diffraction intensity appears to reflect the branch count or total branch mass.

### 5.3.7 Competitive alignment

The preferential growth of nanotrees with a certain azimuthal orientation is likely due to a shadow mediated competitive growth mechanism. In GLAD, large features on the substrate capture the most flux, and increase in size. Therefore, smaller features become increasingly shadowed from the flux, and go extinct. Trunks capture the most growth material when oriented with the vertex of their square cross-section facing the in-plane projection of the oblique flux. Simply put, the diagonal is the longest line that can be drawn across a square, and therefore, square cross-sections oriented with their diagonal perpendicular to the in-plane flux projection cast the largest shadows. Therefore, other orientations eventually go extinct throughout growth as the preferred orientations increase in size and height, resulting in preferential azimuthal alignment of the trunks. The geometrical argument is depicted in **Figure 5.17**. Nanotree alignment can be observed morphologically due to the epitaxial growth of branches on the trunks' sidewalls.

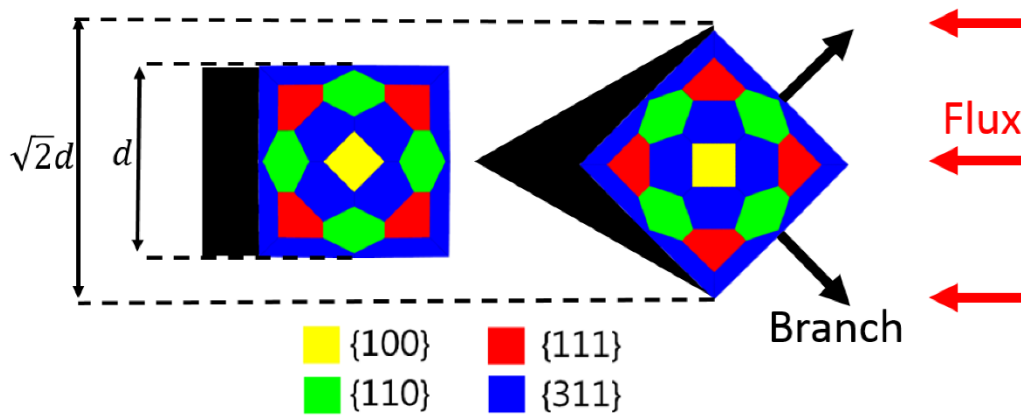


**Figure 5.17:** Plan view schematic of competitive growth mechanism. Shown are two different azimuthal trunk orientations that have flux capture cross-sections of  $d$  (left) and  $\sqrt{2}d$  (right).

Nanotrees with a  $\{100\}$  trunk face oriented  $45^\circ$  from the flux axis ( $\phi$ ) present the largest surface from the perspective of the collimated flux and therefore, capture more vapor from the flux that can diffuse to the trunk droplet and produce vertical growth. Therefore, nanotrees oriented with a vertex of their square trunk cross-section pointing towards the flux should exhibit the fastest vertical growth rate. The

faster growth rate will cause increased flux shadowing for neighboring trees that do not exhibit the preferred orientation, further suppressing their growth. Preferred branch nucleation and growth on the  $\{100\}$  faces of the trunk oriented  $\pm 45^\circ$  from  $\phi_0$  may increase the flux capture cross-section of these orientations at a higher rate than other orientations, further amplifying their competitive advantage. Thus, only nanotrees oriented favorably towards the flux are expected to avoid extinction, and continue to grow in the film.

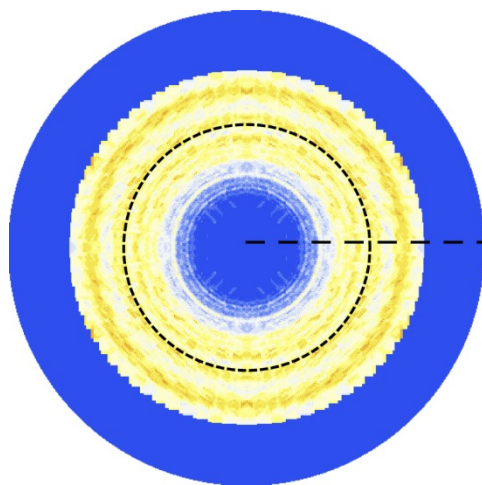


**Figure 5.18:** (222) pole figure for a unidirectional nanotree grown to a nominal thickness of 150 nm. The dashed circle indicates the expected radial position ( $54.7^\circ$ ) for X-ray diffraction around single crystal nanotrees oriented  $[100]$  normal to the substrate. The flat dashed line indicates the flux axis ( $\phi_0$ ). Reproduced with permission from *Crystal Growth and Design*.<sup>307</sup> Copyright 2013, American Chemical Society.

One consequence of the evolutionary selection process is that films consisting of relatively short nanotrees should not exhibit in-plane texture since trunks are randomly oriented in the early stages of growth prior to the extinction of less flux-favored orientations. Indeed, no in-plane texture is detected in a (222) pole figure of a unidirectional film grown under the same conditions but to less than one tenth the nominal thickness (**Figure 5.18**). A second consequence is that relaxation of the selection pressure should increase the number of nanotrees that survive, and this is observed in the high trunk density observed in the isotropic film seen in **Table 5.1**. A third consequence is that films with selection pressure should consist of taller nanotrees than those without, as the selected nanotrees should grow faster vertically due to increased flux capture distributed among fewer nanotrees. From **Table 5.1**,

we can see that both the unidirectional and periodic nanotrees are taller than chiral and isotropic nanotrees. However, this description does not capture any effects from varying branch density or differences in trunk/branch diameter, and must be considered a preliminary hypothesis at this time.

We measured the azimuthal crystal orientation of trunks with respect to  $\phi_0$  in order to investigate the competitive growth hypothesis. The 4-fold symmetry observed in the branch histograms provides evidence for biaxial texture in the unidirectional and chiral films (**Figure 5.8**), however, they do not quantify the extent of trunk alignment. Additionally, the radially integrated pole figure intensity in **Figure 5.8** was observed to depend on branch mass, therefore the extent of azimuthal trunk alignment remains uncertain. Measuring trunk orientation allows a direct morphological measurement of the preferential azimuthal alignment of nanotrees, providing additional confirmation of the evolutionary selection mechanism. We have shown that branches are an extension of the trunk's cubic crystal lattice (**Figure 5.13**), thus the orientation of a single branch uniquely identifies the azimuthal crystal orientation of a trunk. Therefore, the orientation of a single branch was measured for each trunk and assembled into radial histograms (unique between  $0^\circ$  and  $90^\circ$  due to cubic symmetry, sample measurements shown in **Figure 5.19**) shown in **Figure 5.20**. Symmetrized pole figures were radially integrated and plotted in polar coordinates over the trunk histograms, resulting in good agreement. **Figure 5.20** shows that nanotrees with  $\{100\}$  trunk faces oriented  $45^\circ$  from  $\phi_0$  are predominant in the unidirectional, periodic and chiral nanotree films, while the isotropic film exhibits a uniform distribution of trunk orientations. Consistent with the model for selection described above, the trunks that survive the competitive growth process are those that exhibit the largest flux capture cross-section from the perspective of the collimated vapor flux in the unidirectional and periodic films. The presence of favored trunk orientations in the chiral nanotree film suggests a slight selection pressure is applied early in growth due to slow rotation and is maintained as the nanotrees grow, agreeing with the relatively faint biaxial texture observed in the radially integrated pole figure data. As substrate rotation rate is

increased, the flux is not stationary a sufficient time to apply significant selection pressure, leading to an absence of clearly observable biaxial texture, and favorable trunk orientations (**Figure 5.20d**).

The quantification of the extent of trunk alignment supports the hypothesis that preferential alignment of branches results primarily through an evolutionary selection mechanism of favored trunk orientations, rather than occurring solely due to increased nucleation probability of branches on trunk faces that capture the most flux.

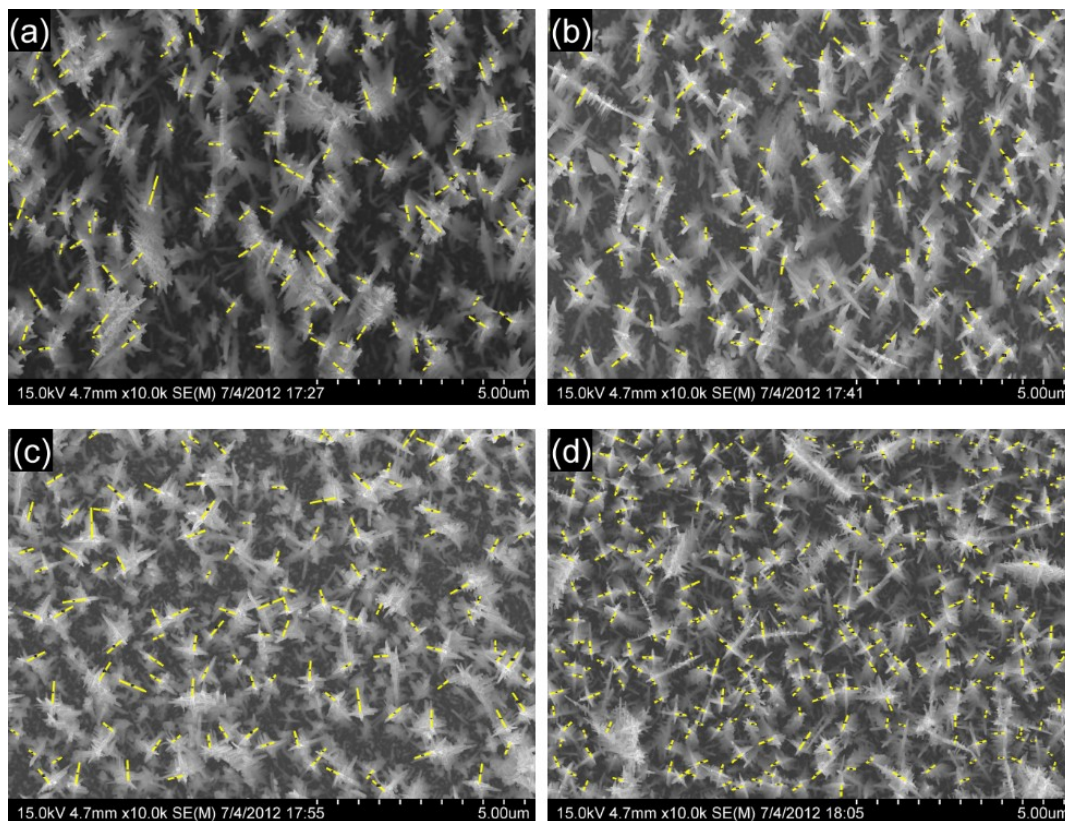


**Figure 5.19:** Sample measurements taken from top-down SEM images using ImageJ software for (a) unidirectional, (b) periodic, (c) chiral and (d) isotropic NW films. Five images (same as shown above) were measured for each array. One branch measured for per trunk. Lines were drawn from trunk-branch interface to branch tip.

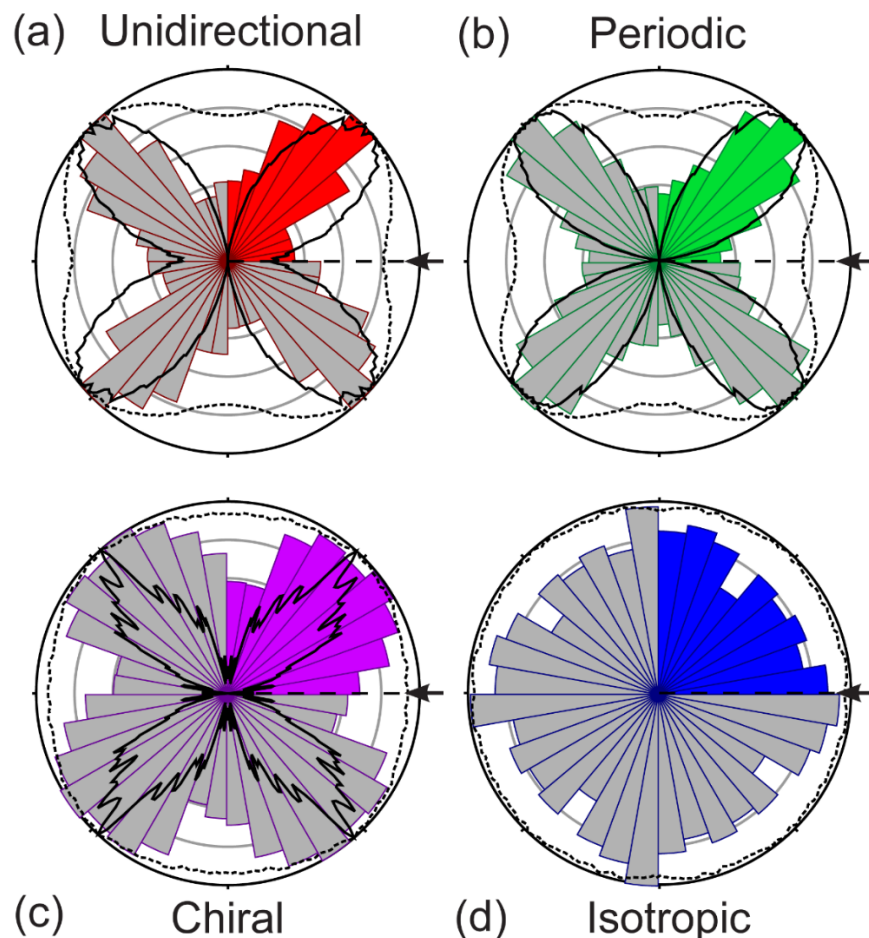


**Figure 5.20:** Normalized radial histograms illustrating the number of **trunks** oriented with a certain angle from  $\phi_0$  for (a) unidirectional, (b) periodic, (c) chiral and (d) isotropic ITO nanotree films grown at 2 nm/s. The colored regions between  $0^\circ$  and  $90^\circ$  provide all the unique trunk orientations due to the four fold symmetry of the square cross-section of an ITO nanotree trunk. The data was mirrored around the origin for clarity, indicated by the grey bars. Symmetrized pole figure data was radially integrated and plotted over the histograms, as shown by the solid black (isotropic background subtracted) and dotted black (with isotropic background) lines. The initial flux direction ( $\phi_0 = 0^\circ$ ) is oriented from right to left as indicated by the horizontal dashed black line and arrow in each figure. Bin size is  $10^\circ$ , and the outer ring corresponds to a maximum of (a) 186, (b) 219, (c) 144, and (d) 281 counts for each histogram. Reproduced with permission from *Crystal Growth and Design*.<sup>307</sup> Copyright 2013, American Chemical Society.

## 5.4 Conclusions

In this chapter, anisotropic branch placement throughout ITO nanotree arrays was demonstrated using VLS-GLAD. In addition, branches were placed with a preferred orientation at select heights by using substrate rotation to change the azimuthal position of the flux with respect to the growing NW trunks. The ability to place branches on select NW facets was largely underdeveloped prior to the work presented in this chapter, and enables a new level of structural control in 3D branched NW arrays. Although we have demonstrated this effect in a self-catalyzed VLS system, this technique should be applicable to all other VLS systems by having separate seed placement and NW growth steps.

Prior to VLS-GLAD, azimuthal alignment of nanotrees required epitaxial trunk growth at the substrate, but it has been demonstrated using an epitaxy-free approach on amorphous substrates here. Using VLS-GLAD, it should be possible to induce biaxial texture in other VLS systems, without requiring epitaxy, by matching the flux symmetry to the crystal symmetry around the growth axis. Epitaxy-free azimuthal alignment of NWs enables a much higher degree of 3D structural control on amorphous substrates such as glass.

However, the coupled branch placement and competitive alignment effects presented in this chapter place limitations on achievable structures. The ability to control these effects independently would significantly enhance structural control. In the next chapter, branch placement will be investigated further using VLS-GLAD by growing ITO nanotrees epitaxially on lattice matched substrates. Epitaxial trunk growth enforces nanotree alignment, and will allow branch placement and crystal alignment to be determined by independent processes. Such control is another step toward designed anisotropic interconnectivity in 3D NW arrays. In general, the use of a directed, collimated vapor flux used in VLS-GLAD as opposed to the more common isotropic flux has advantages that should be useful in fabricating complex, interconnected, 3D NW networks.

# 6. Epitaxially Aligned Nanotrees

---

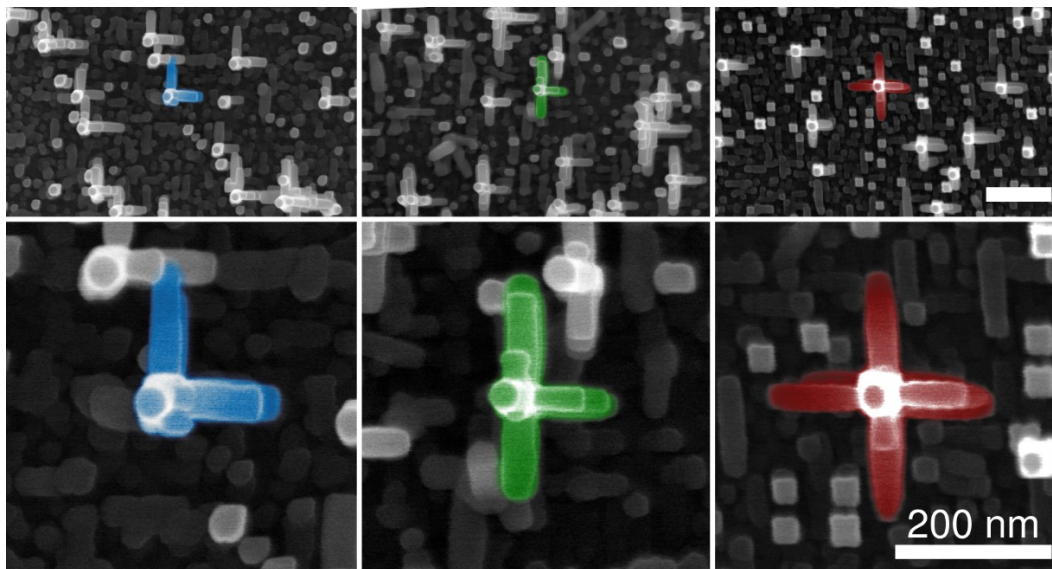


**Figure 6.1:** Table of Contents figure published in *Nano Letters*.<sup>317</sup> This figure schematically depicts directed branch growth in epitaxially aligned nanotree arrays, enabling the fabrication of self-similar L-, T-, and X-shaped ITO nanotrees.

---

Portions of this chapter were reproduced with permission of American Chemical Society (ACS) from the following publication:

Beaudry, A. L., LaForge, J. M., Tucker, R. T., Sorge J. B., Adamski, N. L., Li, P., Taschuk, M. T., and Brett, M. J. *Nano Letters* **2014**, *14*, 1797.

## 6.1 Introduction

### *6.1.1 Introduction*

The fabrication of nanotree arrays with controlled anisotropic interconnectivity will require significant advancements in branch placement capabilities. In the previous chapter, anisotropic branch growth in ITO nanotree arrays was demonstrated. However, branch placement was coupled to a competitive alignment effect, which produced a preferentially aligned nanotree ensemble, but not a truly self-similar and precisely aligned array of nanostructures required for controlled interconnectivity. In this chapter, precisely aligned nanotrees over large areas is obtained through epitaxial growth of trunks on a lattice matched substrate. Epitaxial trunk growth enables the collimated vapour flux to be directed onto select facets of the aligned NWs, improving branch placement control significantly. The directed branch growth demonstrated in this chapter enables the synthesis of aligned anisotropic building blocks that could be arranged through patterned growth to enable the bottom-up fabrication of complex 3D architectures.

In this chapter, branch growth is selectively directed along two, three, or four directions in epitaxially aligned nanowire arrays using VLS-GLAD flux engineering. The flux is positioned to grow branches on facets of the aligned NWs, enabling fabrication of aligned nanotree arrays with L-, T-, or X-branching. In addition, substrate motion algorithms are designed to selectively elongate branches along one axis of the substrate, which could lead to anisotropic interconnectivity and conductivity throughout the array. Nanotrees are found to be aligned across large areas by XRD pole figure analysis, and through manual branch length and orientation measurements collected over  $140 \mu\text{m}^2$  from SEM images for each array. The pathway to guided assembly of nanowire architectures with controlled interconnectivity in three-dimensions using VLS-GLAD is discussed.

Branch placement is decoupled from in-plane NW alignment through epitaxial VLS growth of branched ITO NWs on lattice matched yttria-stabilized zirconia (YSZ) substrates (lattice mismatch less than 2% between  $a_{\text{In}_2\text{O}_3} = 1.0118 \text{ nm}$  and  $2a_{\text{YSZ}} =$

1.026 nm).<sup>276,318–320</sup> Epitaxial growth of ITO NWs on YSZ enforces both in-plane and out-of-plane crystal alignment.<sup>102,247,321</sup> Therefore, the flux's azimuthal configuration can be engineered to grow branches on select facets of the cubic NWs without affecting in-plane NW alignment. The azimuthal flux position is controlled with respect to the YSZ substrate's in-plane [100] crystal direction ( $\phi$ ) (**Figure 6.2**).

### *6.1.2 Contributions*

As was the case throughout the entirety of the VLS-GLAD project, the work presented in this chapter was the result of a team effort. Allan Beaudry led the overall direction, experimental design, developed the epitaxial growth process, and designed the new heating assembly. Joshua LaForge assisted with experimental design, and performed XRD pole figure analysis. Ryan Tucker helped design the new heating assembly, designed schematics, and contributed to project design. Jason Sorge's knowledge of GLAD was utilized for flux motion algorithm design, and he assisted in installing and calibrating the new heating system. Nicholas Adamski grew countless NW arrays, and performed manual measurements of the branch orientations. Peng Li obtained SHIM and TEM images, and contributed greatly to their interpretation. Michael Taschuk used a model developed for another work to guide our understanding of the growth process.<sup>322</sup>

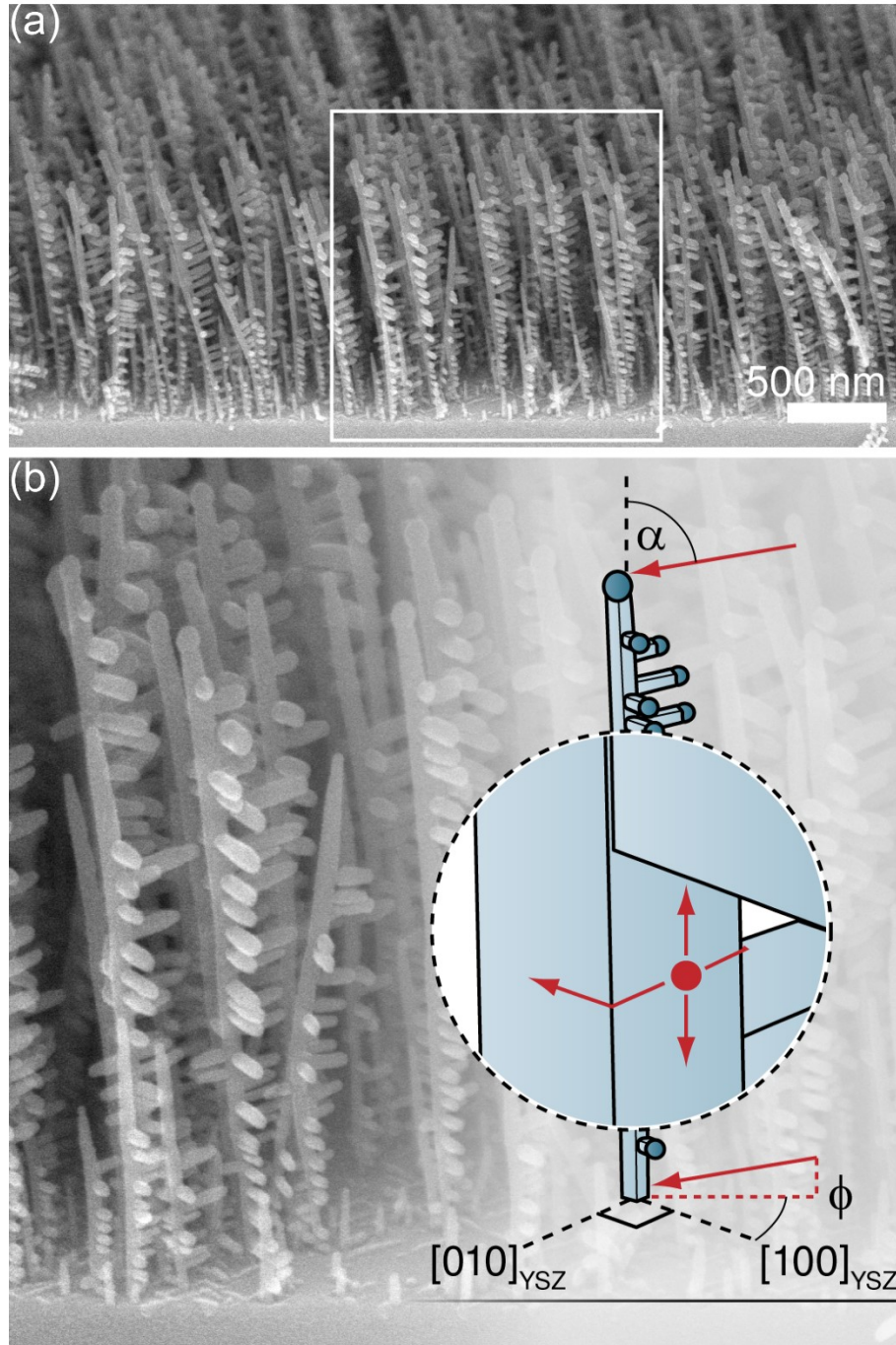


**Figure 6.2:** (a) Oblique view SEM of a nanotree film grown on YSZ. Region in the white box of (a) is shown magnified below in (b), with a schematic representation of epitaxial VLS-GLAD ITO nanotree growth. The vapor flux is deposited at oblique angles ( $\alpha$ ) relative to substrate normal, offset by an angle ( $\phi$ ) from the  $[100]$  direction of the single cubic crystal YSZ substrate. The inset depicts various surface diffusion processes that occur once the flux deposits material on the trunk sidewall. Growth conditions for nanotree array shown here are substrate temperature = 300 °C, flux rate = 0.1 nm/s,  $\alpha = 85^\circ$  and  $\phi = 45^\circ$ .

## 6.2 Experimental

### *6.2.1 Nanotree growth*

Electron beam evaporation of ITO source material (3 – 12 mm pieces of In<sub>2</sub>O<sub>3</sub>:SnO<sub>2</sub>, 91:9% mol; 99.99% purity; Materion Inc.) was performed at high vacuum (base pressure < 1 μTorr). Branched NW arrays were grown on silicon ((100), p-type, University Wafer) and yttria-stabilized zirconia (YSZ) substrates ((100), Semiconductor Wafer Inc.). YSZ substrates were submerged in a 36% aqueous solution of hydrochloric acid for 10 minutes, followed by sonication in acetone and isopropyl alcohol for 10 minutes each before drying with blown nitrogen. No solution cleaning was used for Si substrates. The distance between evaporation source and chuck center was ~42 cm. Nominal flux rate was measured by a quartz crystal monitor mounted near the chuck.

A new heating assembly was required to achieve the temperatures for epitaxial growth, and was installed in a different deposition system used in previous chapters. The other system was used because it was equipped with water cooling for the temperature sensitive ferrofluidic feedthrough. The new heating assembly is shown in **Figure 6.3**, wherein substrates were heated using four 300 W halogen bulbs directed at the center of the substrate chuck. A thermally insulative macor headpiece (**Figure 6.3d**) was used to mount the chuck to prevent damage to the motion controller. Temperature was monitored using a Type K TC elevated approximately 1 cm above the chuck center to enable substrate motion. A Type K TC was used to accommodate higher temperature measurements compared to previous work. The elevated TC was calibrated with respect to a TC mounted to a silicon substrate's surface, and was found to consistently report temperatures ~20 °C below the chuck surface temperature (**Figure 6.4**). The elevated TC temperature is reported throughout this work. Substrates were heated and held at growth temperature for 30 minutes prior to deposition. Silicon substrates were placed across the 4" chuck from edge to edge to test uniformity, and the results shown in **Figure 6.5** demonstrate high uniformity of structures across the chuck.

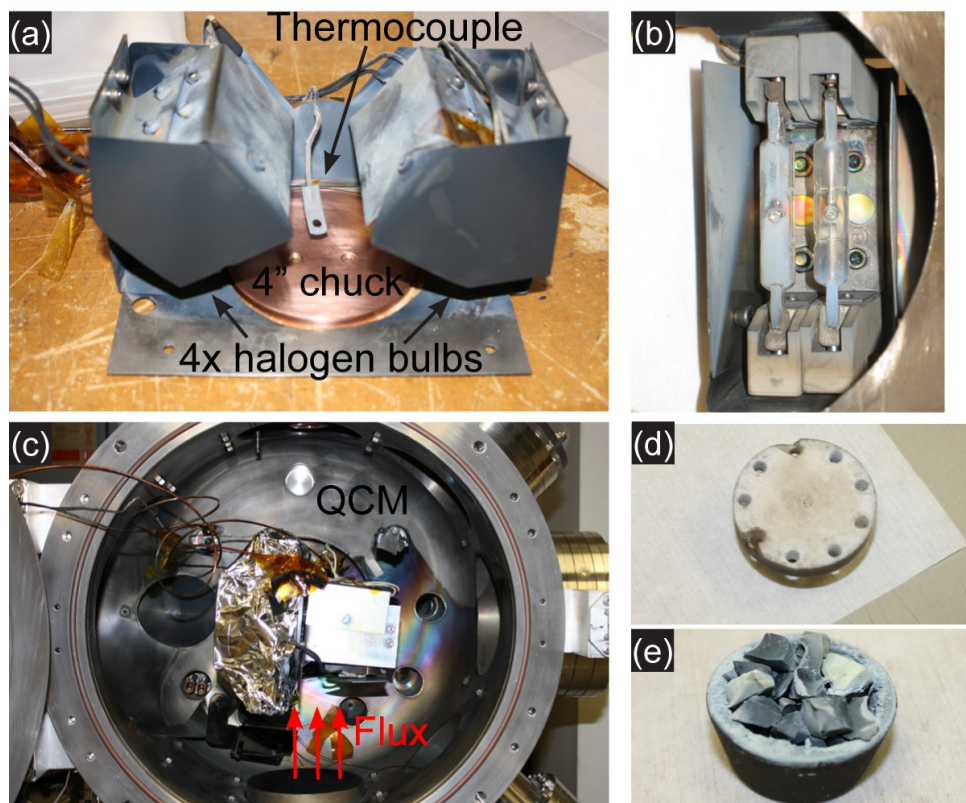


**Figure 6.3:** (a) New heating set-up used for epitaxial nanotree growth, with a reduced size 4'' chuck. (b) two 300 W halogen bulbs in each casing, four bulbs total. (c) Heating set-up installed in GLAD system, oriented with the flux  $85^\circ$  to substrate normal. QCM behind sample monitors deposition rate. (d) Macor head piece, and (e) ITO source material.

NW arrays in this work were grown to a nominal thickness of 300 nm, temperature of  $300^\circ\text{C}$ , deposition angle of  $85^\circ$ , and nominal flux rate of 1 nm/s unless otherwise stated.  $\phi$  was set by aligning flux with the sidewall of square YSZ substrates with [100] oriented sidewalls. Flux motion was either fixed position (constant  $\phi$ ), constant rotation (isotropic motion: 1 rotation per 10 nm of nominal material deposited), or serial bi-deposition (SBD). NW arrays grown with SBD motion required two stages: the first stage was grown at standard conditions with continuous substrate rotation to a nominal thickness of 300 nm, the second stage was grown to a nominal thickness of 150 nm at a reduced flux rate of 0.1 nm/s as the deposition angle was gradually reduced from  $85^\circ$  to  $70^\circ$ . During the second stage,  $\phi$  was alternated between two azimuthal positions separated by  $180^\circ$  (28 s at fixed  $\phi$ , 2 s transition).

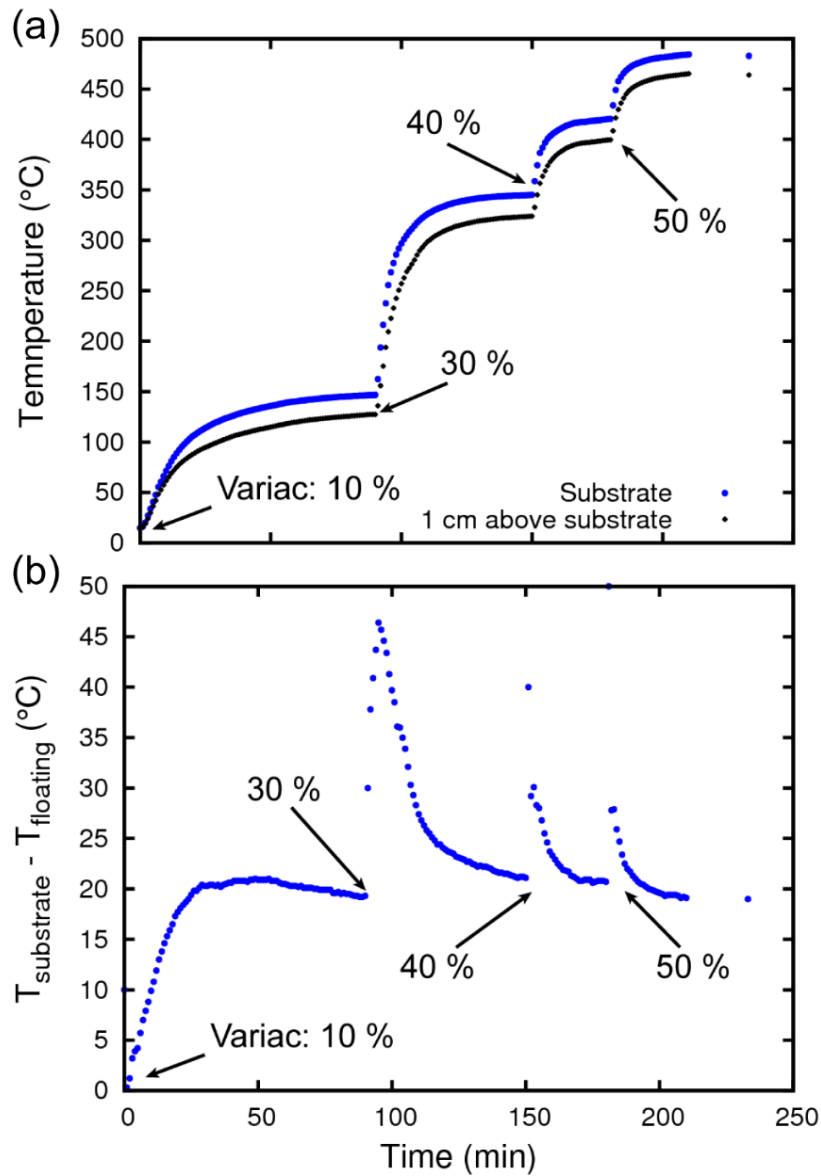


**Figure 6.4:** (a) Temperature measured by TC directly attached to Si substrate, and TC 1 cm above center of chuck as the variac controlling power to the lamps is incrementally increased. (b) Difference in temperature between the two TCs.

### 6.2.2 Characterization

The length and orientation of the longest branch per trunk sidewall was measured using ImageJ software<sup>283</sup> from five plan view SEM images taken with a Hitachi-S4800 at 20,000 times magnification (corresponding a total area of 140  $\mu\text{m}^2$  for each NW array), using the same methodology as in the previous chapter. At least ~

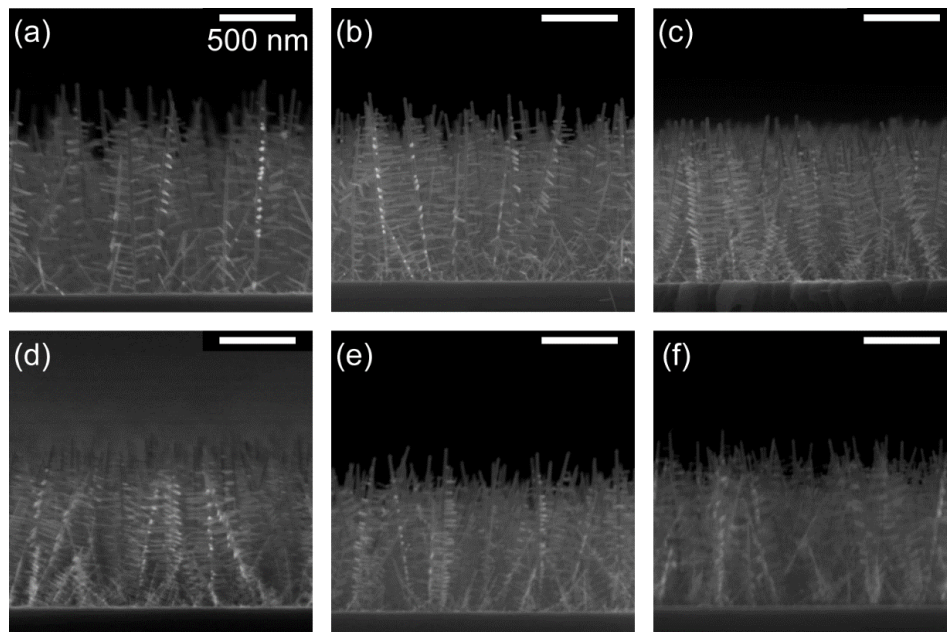


**Figure 6.5:** Cross-sectional SEM images of ITO NW films grown on Si substrates placed from one edge (a) to the other (f), through the center of the 4" chuck to test uniformity in the following order: (b), (c), (d) and (e).

1400 branches were measured in each array. A Bruker D8 Discover with HiStar area detector was used to acquire pole figures of the (400), (222), and (440) XRD peaks. GADDS (Bruker) software was used to process pole figure data. TEM analysis was performed on a JEOL JEM-ARM200F spherical aberration corrected STEM/TEM, equipped with a cold-field emission gun (c-FEG) and operated at 200 kV accelerating voltage. Cross-sectional TEM samples were prepared using a JEOL EM-09100IS Ion Slicer with 6 kV argon ion beam for initial polishing, and 1 kV for final polishing. SHIM (Zeiss ORION Plus) was used to obtain oblique images of nanotree arrays on YSZ substrates to overcome charging effects that obscure SEM images.

## 6.3 Results and Discussion

### 6.3.1 Nanotrees

SEMs of nanotrees grown at 0.1 nm/s at various temperatures and  $\phi$  are shown in **Figure 6.6**.  $\phi$  is defined as the angle between the [100] direction of the YSZ substrate and the azimuthal flux position (**Figure 6.2**). NW films grown at 300 °C are clearly aligned in-plane. With this temperature identified, subsequent nanotrees shown in **Figure 6.7** are grown at 300 °C and various deposition rates. Overall, 300 °C and 1 nm/s were selected as the optimal growth conditions due to clear branch alignment in the SEMs. These conditions were used for the rest of the work shown in this chapter.

SHIM images from multiple perspectives are shown for ITO nanotree arrays grown on YSZ at 1 nm/s and  $\alpha = 85^\circ$  in **Figure 6.8** with (a-d)  $\phi = 45^\circ$ , and (e-h)  $\phi = 0^\circ$ . The nanotrees appear to be vertically and azimuthally aligned. As expected, branches grow preferentially on the side of the trunks facing the flux. The resulting films are composed primarily of L-shaped nanotrees (**Figure 6.8b**) for  $\phi = 45^\circ$ , and T-shaped nanotrees for  $\phi = 0^\circ$ . Plan view images show a representative L-shaped nanotree for  $\phi = 45^\circ$  (**Figure 6.8c**), and a T-shaped nanotree for  $\phi = 0^\circ$  (**Figure 6.8g**). However, some nanotrees in the films do not adopt the representative shape. For example, under close inspection, a few L-shaped nanotrees can be observed in **Figure 6.8f**. These imperfections are likely a result of stochastic nucleation which may result in nearby nanotrees shadowing facets that would otherwise be exposed to flux. Variations in self-shadowing environments could potentially be alleviated by pre-patterning seeds to grow periodic arrays of nanotrees.<sup>143</sup> In addition, T-shaped nanotrees with short branches facing away from the flux are present in **Figure 6.8b**, which may be a result of adatom migration around the trunk catalyzing back facing growth. Due to the high depth of field afforded by helium microscopy, the nucleation layer resulting from the self-catalyzed VLS growth mechanism of ITO nanotrees can be clearly seen in **Figure 6.8 a and e** on the substrate surface between the nanotrees.

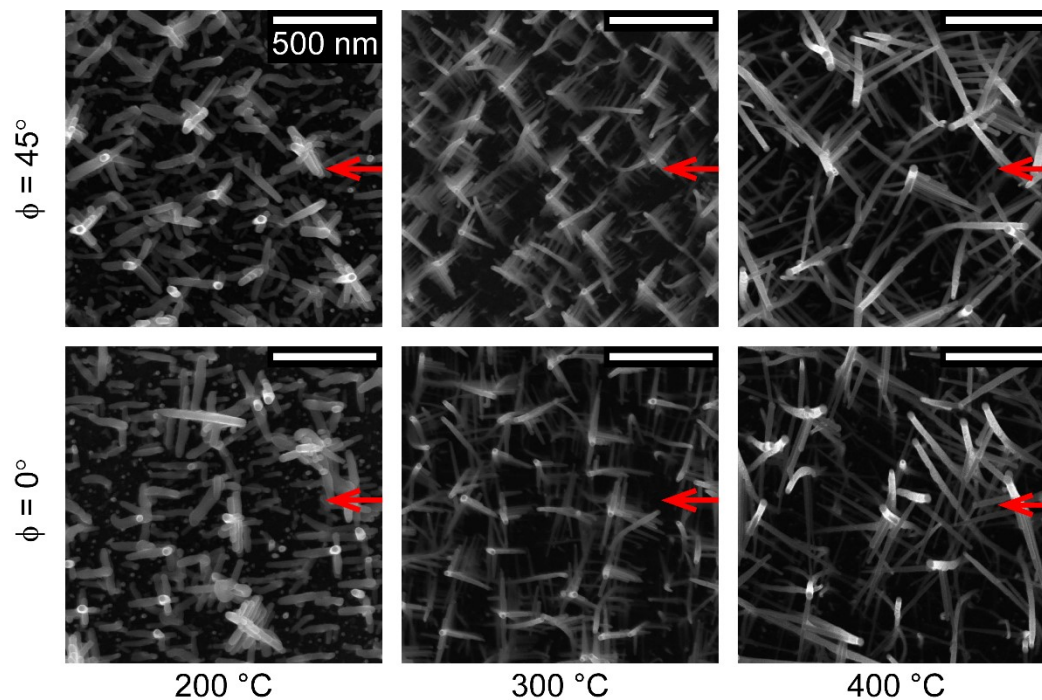


**Figure 6.6:** Nanotrees grown on YSZ substrates at a variety of temperatures at 1 nm/s and  $\alpha = 85^\circ$ . Red arrows indicate in-plane flux direction.

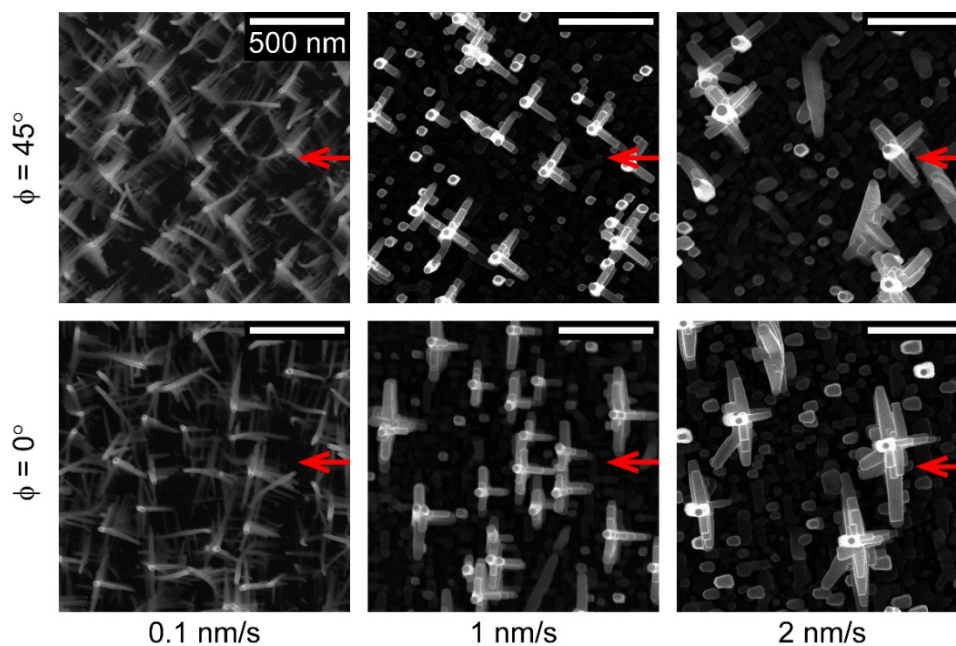


**Figure 6.7:** Nanotrees grown on YSZ substrates at a variety of deposition rates at 300 °C and  $\alpha = 85^\circ$ . Red arrows indicate in-plane flux direction.

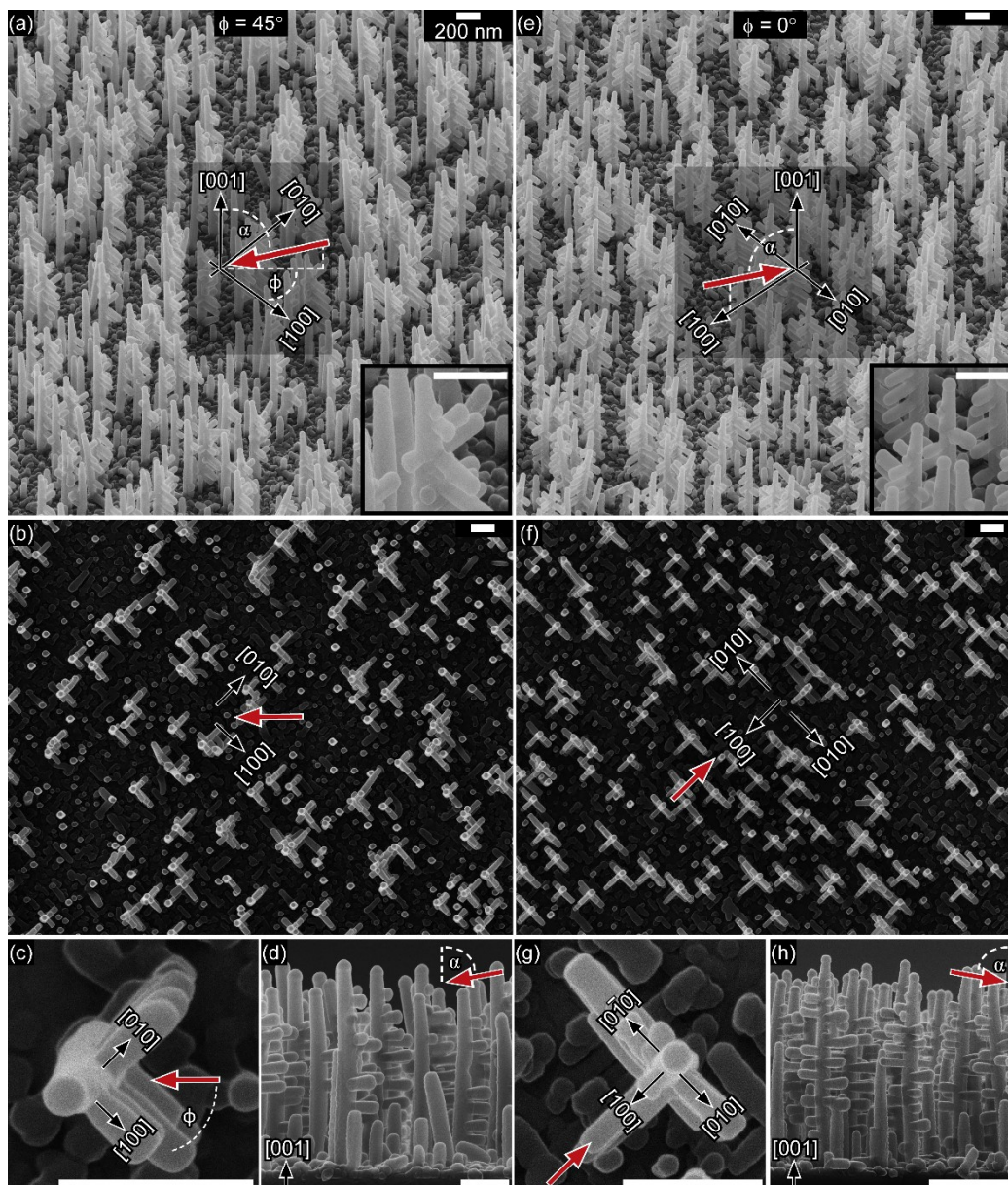


**Figure 6.8:** The vapor flux is deposited at oblique angles ( $\alpha$ ) relative to the substrate normal, offset by an angle ( $\phi$ ) from the [100] direction of the single cubic crystal YSZ substrate. SHIM images of ITZ nanotrees grown on YSZ with  $\alpha = 85^\circ$ , and (a-d)  $\phi = 45^\circ$  (resulting in L-shaped nanotrees), and (e-h)  $\phi = 0^\circ$  (resulting in T-shaped nanotrees). (a) and (e) are oblique images. (b), (c), (f) and (g) are plan view images. (d) and (h) are cross-sectional images. Red arrows depict vapor flux orientation, and black arrows indicate crystal directions of the YSZ substrate. All scale bars are 200 nm. Reproduced with permission from *Nano Letters*.<sup>317</sup> Copyright 2014, American Chemical Society.

### *6.3.2 Nanotree alignment*

XRD was used to analyze alignment of the crystalline nanotrees. **Figure 6.9** shows XRD line scans taken from a variety of positions above the sample and overlaid onto a single  $2\theta$  plot. The green and red boundary lines in **Figure 6.9** indicate the  $2\theta$  range used to generate the pole figures for the (400), (222), (440), and (622) ITO diffraction planes shown in **Figure 6.10**. The second set of peaks for the (622) plane were not measured in the process (the outer radial ring for expected peaks). The pole figures confirm vertical and azimuthal alignment over large areas ( $\sim 1 \text{ mm}^2$ ) of nanotrees epitaxially grown along the [001] substrate normal direction. Pole figures spatially map XRD intensity from select crystal planes projected on the surface of a hemisphere above the sample. The sharpness of the peaks indicates a high degree of alignment. In each case, mirror diffraction peaks from the YSZ substrate were partially overlapped with the diffraction peaks from the ITO nanotree array as expected for YSZ-ITO epitaxy.

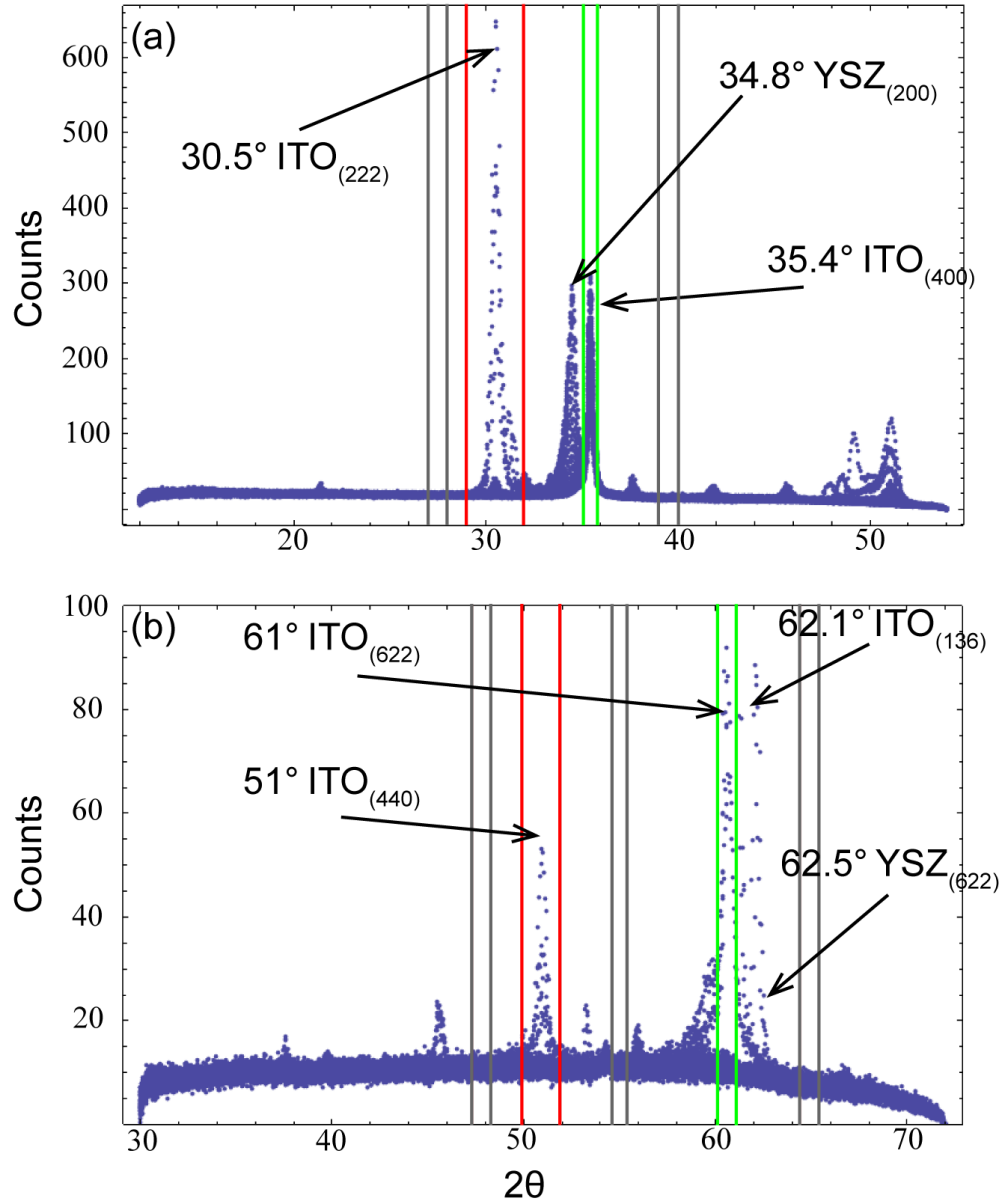


**Figure 6.9:** Overlain XRD  $2\theta$  plots taken detected from a variety of positions above the sample. Red and green lines in (a) and (b) indicate boundaries for ITO peaks used in pole figure generation. Grey lines indicate background regions used for pole figure analysis.

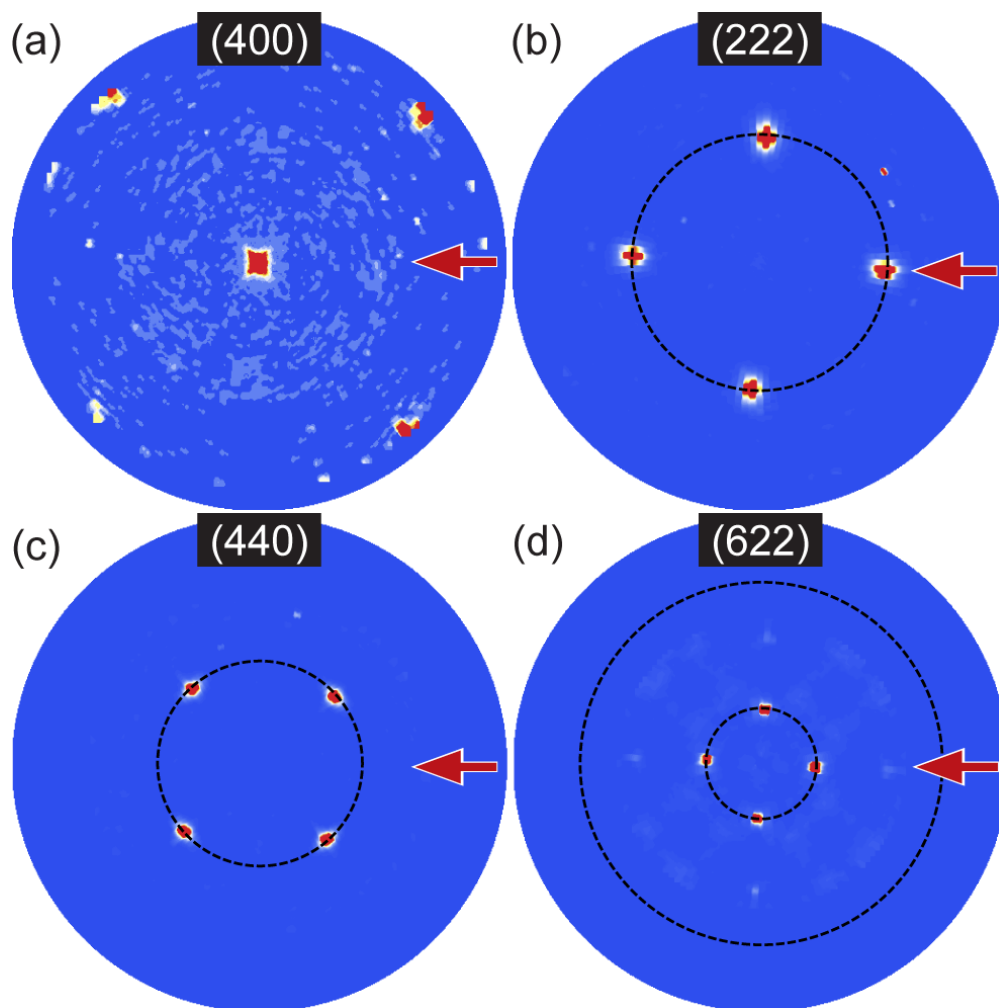


**Figure 6.10:** XRD pole figures for (a) (400), (b) (222), (c) (440), and (d) (622) planes for an ITO nanotree array grown epitaxially on a YSZ substrate with 1 nm/s,  $\phi = 45^\circ$  and  $\alpha = 85^\circ$ . The red arrows correspond to the flux direction, and the black dotted lines in (b), (c) and (d) correspond to the expected radial positions for the diffraction peaks. The region with missing peaks at the outer radial ring in (d) was not measured. Reproduced with permission from *Nano Letters*.<sup>317</sup> Copyright 2014, American Chemical Society.

### *6.3.3 Epitaxy*

HRTEM imaging of the trunk-substrate interface is shown in **Figure 6.11a and b**. The HRTEM images confirm epitaxial growth of the trunk on the YSZ substrate, and a vertical growth direction of [004], agreeing with pole figure data. An atomic-resolution high-angle annular dark-field scanning-TEM (HAADF-STEM) image of a substrate-trunk interface (**Figure 6.11 c and d**) shows that rows of atomic columns continue at regular spacing from the substrate into the NW, further confirming epitaxial growth. An edge dislocation can be seen at the trunk-substrate interface (in the circled region in **Figure 6.11d**). Under close inspection, the YSZ substrate's horizontal atomic column rows are not perfectly straight near the surface (see green lines in **Figure 6.11d**), however, the horizontal rows of atomic columns in ITO are stacked in straight lines. In addition, the stacking direction in ITO appears to be  $2^\circ$  from the stacking direction in the YSZ substrate.

A more detailed analysis of the HAADF-STEM data is shown in **Figure 6.12a**. The image was taken with an electron beam oriented along the [110] direction of an ITO NW trunk. Only Sn or In atomic columns are observable in the HAADF-STEM images, and they are indistinguishable here. The hexagonal arrangement of atomic columns is due to viewing the cubic lattice along the [110] direction or zone-axis, as indicated by the arrangement of atoms in the schematic shown in **Figure 6.12b**. HAADF-STEM directly images the position of atomic columns using incoherent scattering of an electron beam rastered across the sample, allowing for straightforward interpretation. Conversely, HRTEM relies on phase contrast due to interference of coherent Bragg scattered electrons, and therefore, precise atomic arrangement is more difficult to determine. Schematics of a cubic bixbyite  $\text{In}_2\text{O}_3$  unit cell from different viewing directions are shown in **Figure 6.12c and d**. The horizontal rows of atomic columns are separated by 0.26 nm, corresponding to the spacing between (004) planes in ITO, confirming trunks are growing vertically along the [004] direction. In addition, rows of atomic columns slanted at  $\sim 57^\circ$  with respect to the [004] direction are spaced out by 0.29 nm, agreeing with the spacing between (002) planes. The measured angle of  $57^\circ$  between the [004] and [222]

directions is close to the expected value of  $55^\circ$ ; the discrepancy may be due to imperfect alignment of the electron beam.

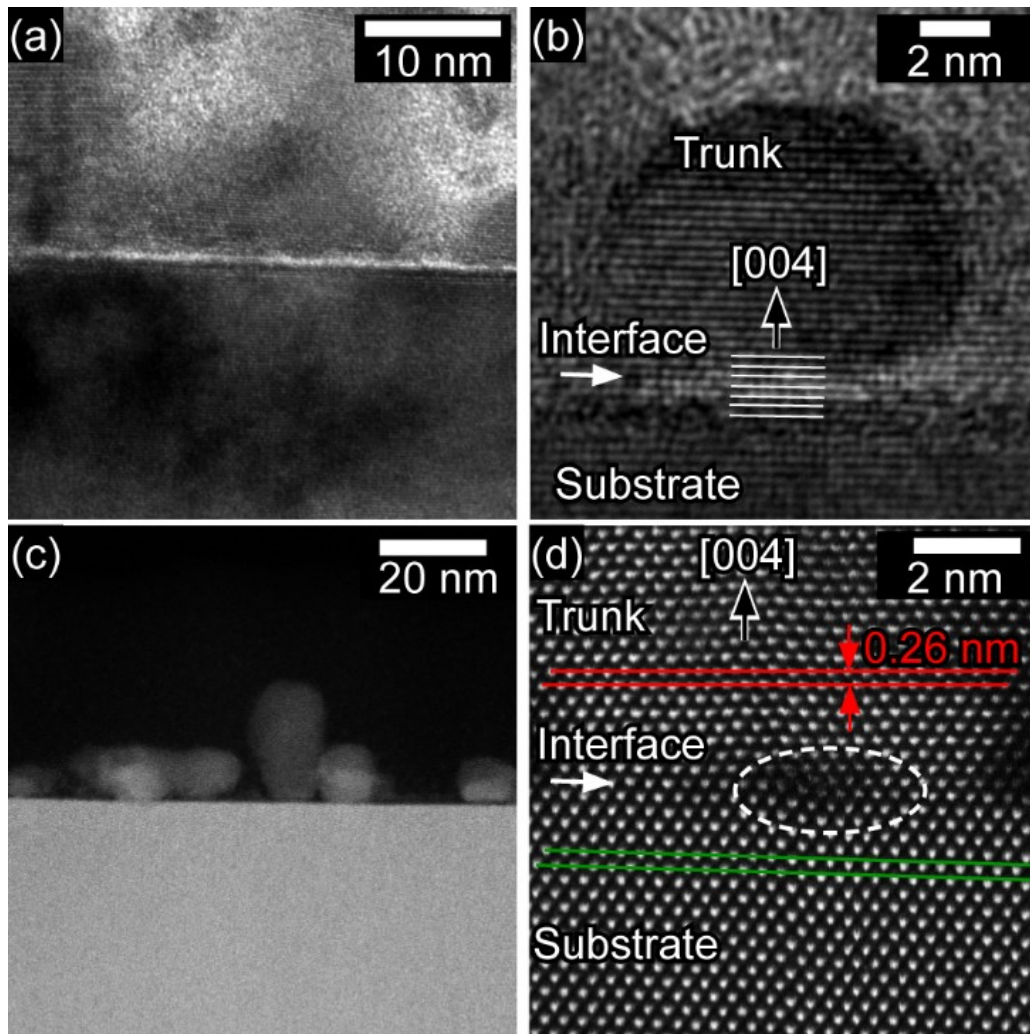


**Figure 6.11:** (a, b) HRTEM images of ITO NW-YSZ substrate interface. (b) white lines indicate stacking of lattice planes from substrate into NW trunk. (c, d) STEM images of the interface between the YSZ substrate and an ITO nanotree early in the growth process. Red lines in (d) indicate 0.26 nm measured in ITO trunk. Dashed white circle indicates edge dislocation at interface. Green lines indicate imperfect stacking of horizontal atomic columns in YSZ substrate. Reproduced with permission from *Nano Letters*.<sup>317</sup> Copyright 2014, American Chemical Society.

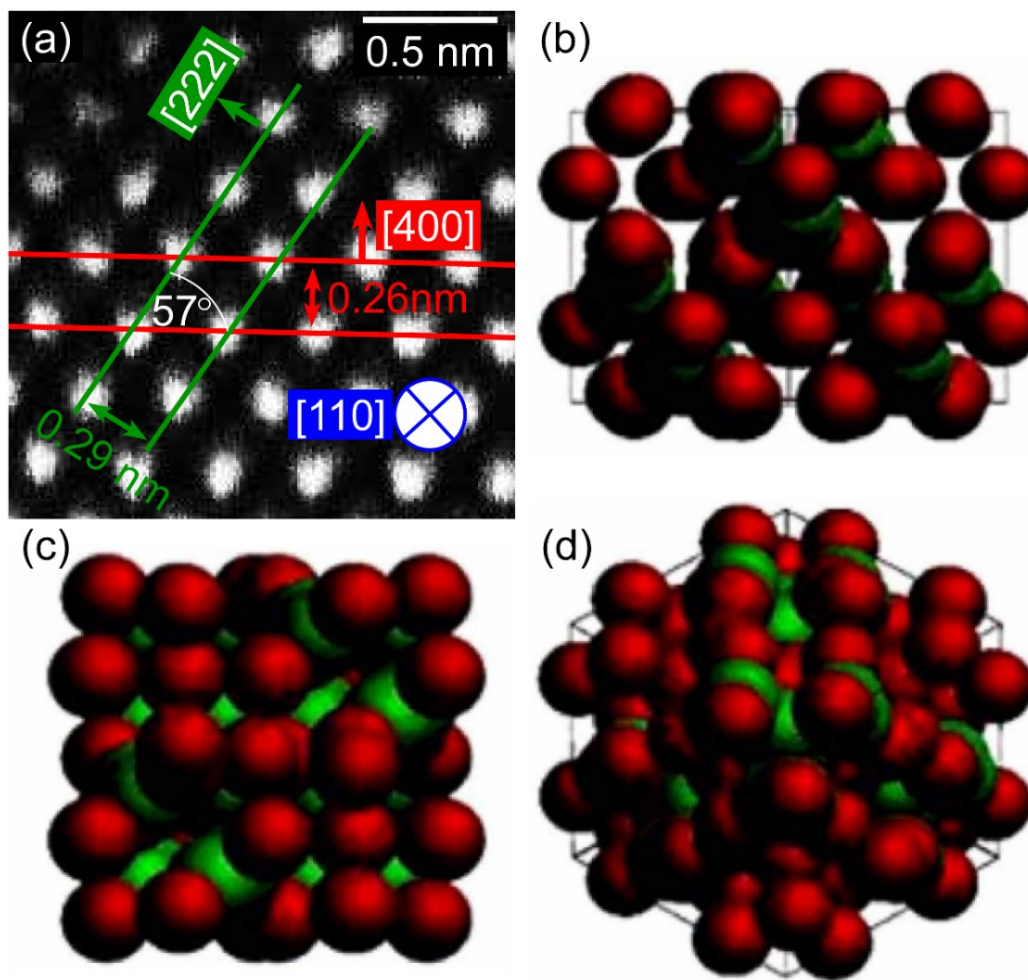


**Figure 6.12:** (a) HAADF-STEM image with electron beam oriented along [110] direction of ITO NW trunk. Bright spots indicate In or Sn atomic columns. Schematics of In<sub>2</sub>O<sub>3</sub> unit cells viewed along (b) [110], (c) [100], and (d) [111] directions. Red and blue balls correspond to In and O atoms, respectively. (b), (c), and (d) were reproduced with permission from Rauf, I. A. *Appl. Phys. Lett.* **2008**, *93*, 143101.<sup>323</sup> Copyright 2008, AIP Publishing LLC.

### 6.3.4 L-, T-, and X-shaped nanotrees

L-shaped nanotrees grow when  $\phi = 45^\circ$ . In this configuration, the azimuthal position of the flux is aligned along the [110] direction of the substrate, and along a vertex of each cubic trunk's square cross-section. The resulting nanotree array is composed of L-shaped NWs with branches directed along the two orthogonal in-plane [100] and [010] directions of the substrate. Branch length and orientation measurements were taken from plan view SEM images (across a total area of  $140 \mu\text{m}^2$ , see **Figure 6.13**) and are presented in a radial density scatter plot shown in **Figure 6.14b**. Long range alignment of L-shaped nanotrees is further confirmed, agreeing with XRD pole figure data.

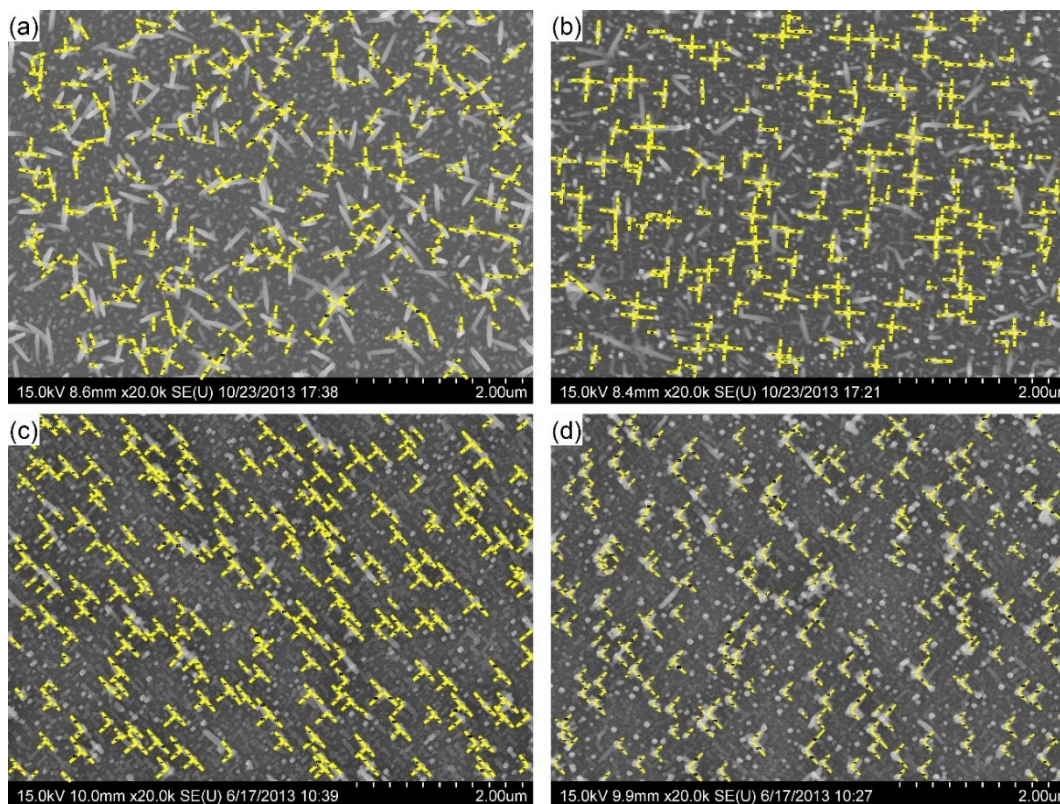


**Figure 6.13:** One fifth of total branch orientation and length measurements taken from top-down SEM images for each of (a)  $\phi$  continuously rotated on Si, and (b)  $\phi$  continuously rotated, (c)  $\phi = 0^\circ$ , and (d)  $\phi = 45^\circ$  on YSZ. Reproduced with permission from *Nano Letters*.<sup>317</sup> Copyright 2014, American Chemical Society.

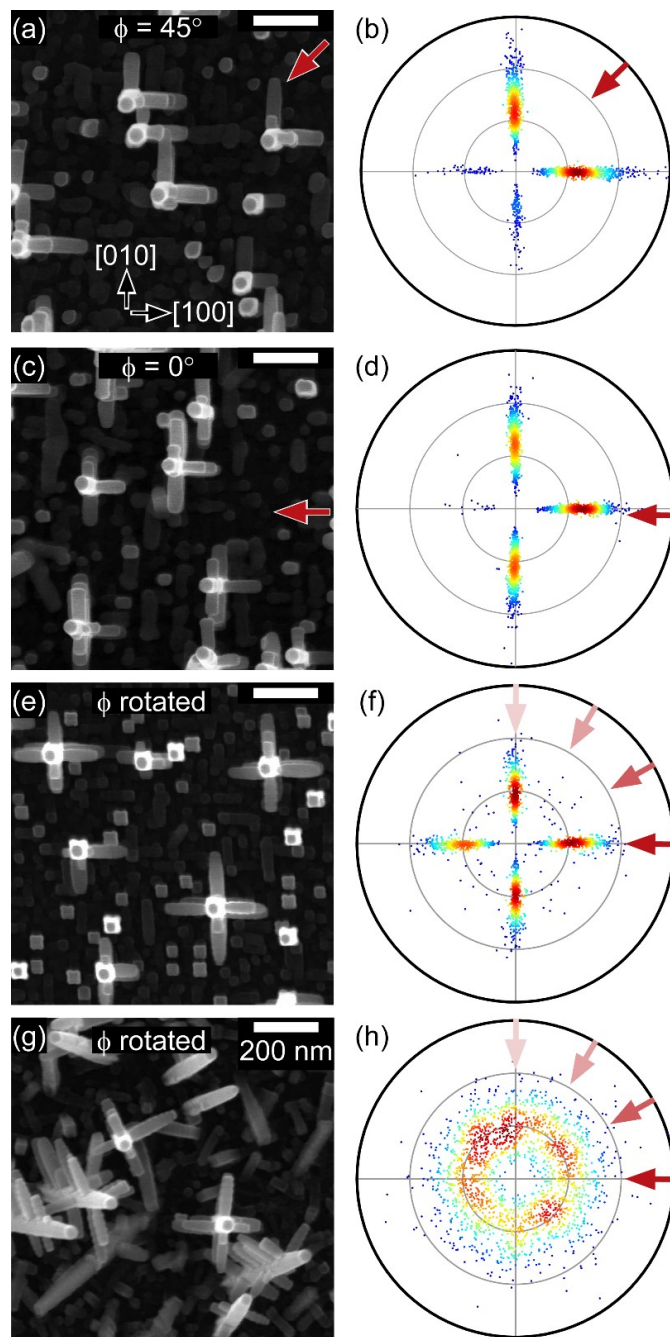


**Figure 6.14:** Plan view SEM images of nanotrees grown on YSZ substrates with (a)  $\phi = 45^\circ$ , (c)  $\phi = 0^\circ$ , and (e)  $\phi$  rotated. (g) Plan view SEM image of nanotrees grown on a Si substrate with  $\phi$  rotated. Radial density scatter plots shown in (b), (d), (f), and (h) depict 1892, 2552, 1866, and 1919 branch length and orientation measurements taken across  $140 \mu\text{m}^2$  of plan view SEM images of nanotree arrays in (a), (c), (e), and (g), respectively. Radial rings represent 100 nm length increments. Red arrows indicate flux direction. The in-plane [100] and [010] directions shown in (a) are the same for (a-f). All data in figure corresponds to growth conditions of rate = 1 nm/s,  $T = 300^\circ\text{C}$  and  $\alpha = 85^\circ$ . Reproduced with permission from *Nano Letters*.<sup>317</sup> Copyright 2014, American Chemical Society.

T-shaped nanotrees grow when  $\phi = 0^\circ$  as shown in **Figure 6.14c**. In this configuration, flux is directed along the [100] substrate direction, and normal to a sidewall of each growing trunk's square cross-section. Branch growth is promoted along three orthogonal in-plane directions of the YSZ substrate ([100], [010], and  $[0\bar{1}0]$ ) and inhibited along the direction opposite the flux ( $[\bar{1}00]$ ) as shown in the radial density scatter plot depicting branch orientation and length measurements (measurements in **Figure 6.13c**) in **Figure 6.14d**.

X-shaped nanotrees grown on YSZ using continuous substrate rotation are shown in **Figure 6.14e**. There are four branch growth directions per ITO nanotree due to epitaxial branch growth on the cubic trunks' sidewalls, resulting in X-shaped nanotrees. Epitaxial trunk alignment further restricts branch growth to four in-plane directions ([100],  $[\bar{1}00]$ , [010], and  $[0\bar{1}0]$ ) of the YSZ substrate, resulting in azimuthal alignment of the X-shaped nanotrees as confirmed by the radial density plot in **Figure 6.14f**. To contrast with nanotree arrays grown epitaxially on YSZ, we also grew nanotrees on Si (**Figure 6.14g**). As shown in the previous chapter, no preferential in-plane branch orientation arises for nanotrees grown on Si with isotropic flux (**Figure 6.14h**).

### *6.3.5 Mechanism*

A plan view schematic depicting and explaining the growth of individual L-, T-, and X-shaped nanotrees is shown in **Figure 6.15**. L-shaped nanotrees (**Figure 6.15a**) result when the flux is oriented toward the vertex of the trunk's square cross-section, promoting branch growth on two sidewalls directly exposed to flux. T-shaped nanotrees (**Figure 6.15b**) result when flux is incident normal to a sidewall. Growth material migrates onto trunk sidewalls oriented parallel to the flux, catalyzing branch growth orthogonal to the flux. X-shaped nanotrees (**Figure 6.15c**) result when material is equally distributed around the NW surface via continuous substrate rotation, promoting branch growth on all four sidewalls of the trunk.

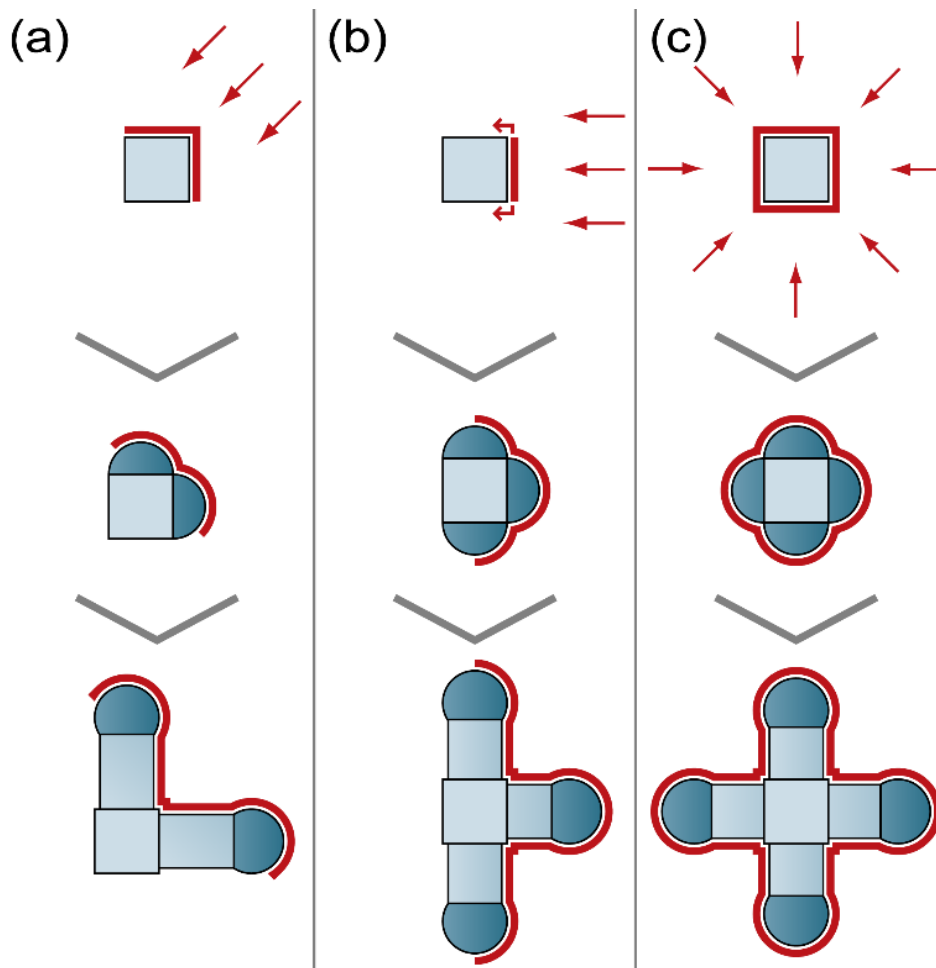


**Figure 6.15:** Plan view schematic of direct branch growth on select NW facets. (a)  $\phi = 45^\circ$  leads to L-shaped nanotrees, (b)  $\phi = 0^\circ$  leads to T-shaped nanotrees, and (c)  $\phi$  rotated leads to X-shaped nanotrees. Red arrows illustrate flux direction and the red lines along the surface indicate where the nanotree's cross-section is directly exposed to flux. Reproduced with permission from *Nano Letters*.<sup>317</sup> Copyright 2014, American Chemical Society.

### 6.3.6 Non-idealities

In an ideal VLS-GLAD situation, it is expected that I-shaped (single-branched) rather than T-shaped nanotrees would grow when  $\phi = 0^\circ$ . However, branches oriented orthogonal to the vapor flux are observed to be of approximately equal length and frequency compared to branches growing directly toward the vapor flux for T-shaped nanotrees when viewed from above (**Figure 6.14d** and **Figure 6.15b**). While trunk sidewalls oriented parallel to the flux should not directly capture material in an ideal VLS-GLAD process, three mechanisms might allow adatom

particles to migrate to sidewalls that are not directly exposed to flux: imperfect flux collimation, surface diffusion from the substrate and/or around trunk corners, and re-evaporation and reflection of incident adatoms. A branch growing on a sidewall parallel to the flux will become directly exposed to flux after even a small amount of growth. Conversely, even if catalysts form on the trunk sidewall facing away from the flux, insufficient flux would be directly captured by the catalysts to achieve substantial growth. The combination of these effects results in T-shaped nanotrees. Similarly, surface diffusion around the trunk may result in catalyst formation on shadowed sidewalls in L-shaped nanotrees; however, branch growth is inhibited on these sides due to limited direct flux capture.

To grow such I-shaped nanotrees a two-material VLS system may be required where the catalyst and NW growth material are different and deposited separately. In that case, catalysts could be deposited on the sidewall of previously grown NWs under conditions to limit adatom migration (i.e. low temperature), and with a much larger distance to the vapor source to improve flux collimation. Branches would then be grown from the selectively deposited catalysts. In addition, the separation of catalyst placement and NW growth would enable flux engineering directed branching to be used for material systems that require chemical vapor deposition, molecular beam epitaxy, or vapor phase epitaxy for NW growth.

### *6.3.7 Uniaxial branch elongation*

Improved understanding of adatom migration in VLS-GLAD processes enabled the growth of nanotree structures with branches preferentially elongated along one axis of the YSZ substrate. A GLAD motion algorithm known as serial bi-deposition<sup>110</sup> was used to elongate branches along the axis oriented orthogonal to the flux. In SBD, the flux's azimuthal position is periodically alternated between  $\phi = 0^\circ$  and  $\phi = 180^\circ$ , as illustrated in **Figure 6.16a**. Branches that grow along the  $[010]$  and  $[0\bar{1}0]$  directions are orthogonal to the flux and will capture flux throughout the entire SBD process. However, branches growing along the  $[100]$  and  $[\bar{1}00]$  directions are periodically starved from flux due to shadowing from the trunk. Therefore,

branches orthogonal to the flux will capture more flux and grow longer than branches oriented along the flux axis, resulting in preferential branch growth along one axis as shown in the plan view SEM image in **Figure 6.16b**. During the SBD process,  $\alpha$  was gradually reduced from  $85^\circ$  to  $70^\circ$  so the flux could reach and elongate branches that become shadowed as surrounding trunks increase in height.

A nanotree with branches elongated along the axis oriented orthogonal to the flux during the SBD process is shown in an oblique SHIM image in **Figure 6.16c**. The preferential elongation of branches along the  $[010]$  and  $[0\bar{1}0]$  directions of the YSZ substrate is confirmed in the radial density scatter plot shown in **Figure 6.16d**. This asymmetric branch growth may increase the likelihood for interconnectivity between nanotrees along the  $[010]$  and  $[0\bar{1}0]$  directions, as indicated by the potential overlap between branches in the circled region in **Figure 6.16b**.

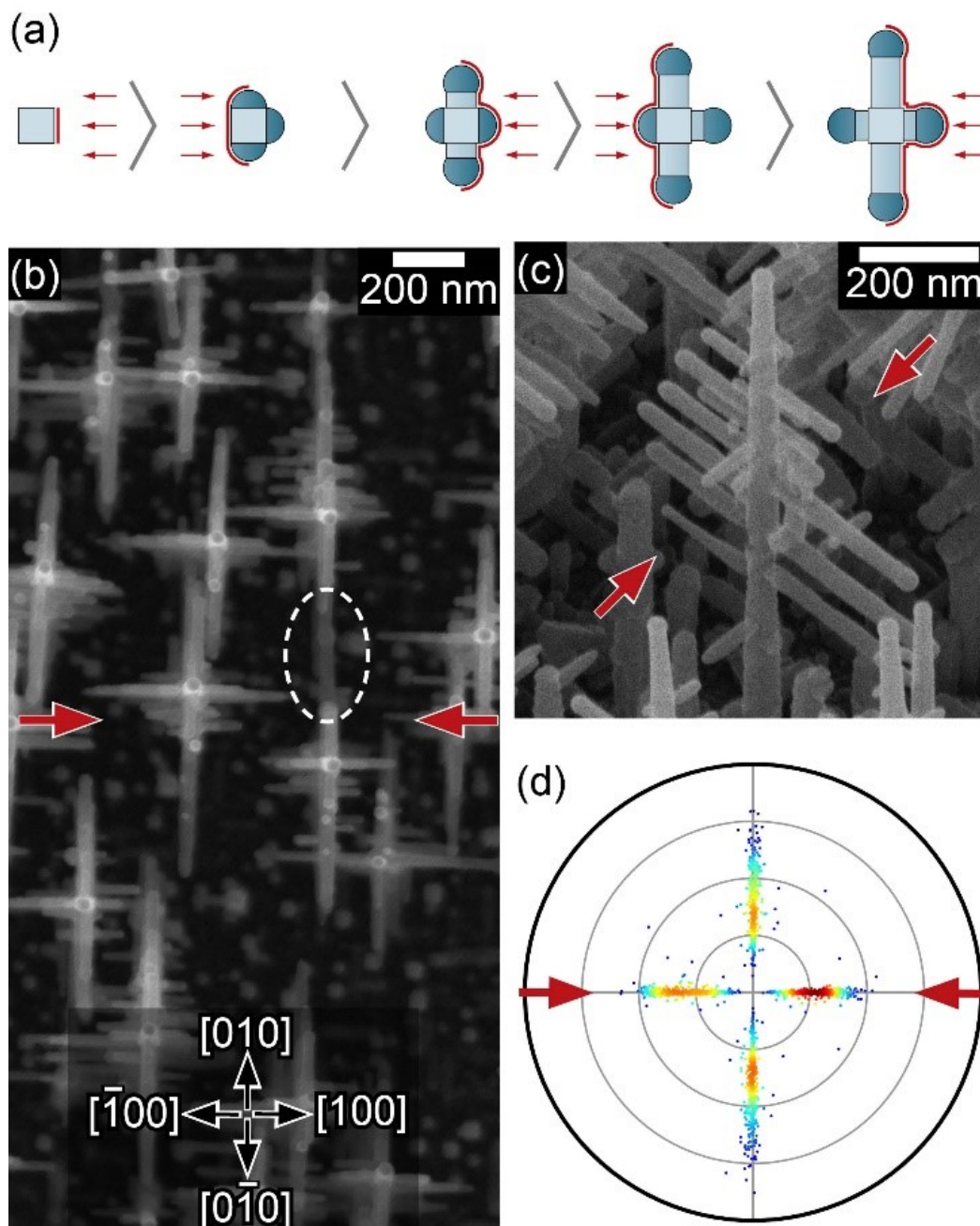


**Figure 6.16:** (a) Plan view schematic of a nanotree grown with serial bi-deposition motion where the azimuthal flux position is periodically alternated between two positions separated by  $180^\circ$ . (b) Plan view SEM image, and (c) oblique SHIM image showing nanotrees grown using a SBD process, the alternated flux positions are indicated by the red arrows. The white dotted line circle in (b) indicates a possible interconnection between two nanotrees. (d) Radial density scatter plot of 1437 branch length and orientation measurements taken across an area of  $140 \mu\text{m}^2$  where each ring corresponds to 200 nm length. Reproduced with permission from *Nano Letters*.<sup>317</sup> Copyright 2014, American Chemical Society.

## 6.4 Conclusions

Aligned ITO nanotree arrays consisting of NWs with two, three, or four orthogonal branch directions were produced using VLS-GLAD. The flux was engineered to starve branches along select directions of the substrate, enabling the growth of aligned arrays of L-, T-, or X-shaped nanotrees. The alignment of these structures over large areas was confirmed using XRD pole figures, and by manually measuring the length and azimuthal orientation of branches across large areas. In addition, branches were preferentially grown along one axis of the substrate using a SBD flux motion algorithm. The work presented in this chapter represents a new level of control over branching anisotropy in NW arrays.

Patterning of catalysts prior to growth rather than relying on stochastic nucleation would enable nanotrees to be arranged into a square grid pattern on the substrate and would ensure that branches grow directly towards neighboring nanotrees. With improved height dependent branch placement, catalyst patterning, and the directed branching demonstrated in this work, 3D nanowire networks with directional and height dependent interconnectivity could be fabricated.

VLS-GLAD and flux engineering may be a part of the solution to achieving a higher degree of 3D control in NW architectures, a capability that the NW community is currently lacking.<sup>81,90,106</sup> VLS-GLAD significantly enhances structural control, however, the functional properties of 3D architectures also need to be optimized for device applications. The focus will now turn to optimization of conductivity and optical transmittance of the branched ITO NW arrays for transparent electrode applications.

# 7. Transparent Electrode Optimization

---

## 7.1 Introduction

### *7.1.1 Introduction*

Branched ITO NW networks are promising candidates for nanostructured transparent electrode applications (see Chapter 2). For example, ITO nanostructured electrodes can be used to extract charge from photoactive polymers in OPV devices.<sup>33,95,123,201</sup> In addition, ITO nanostructures, including branched nanowires<sup>324</sup>, and nanoparticles<sup>325</sup>, have been shown to enable the fabrication of mechanically resilient transparent electrodes on flexible substrates. VLS-GLAD's powerful control over branched ITO NW architectures may be used to optimize their structure for a variety of transparent electrode applications.

---

Portions of this chapter were reproduced with permission of The Institute of Physics (IOP) from the following publications:

(1) Beaudry, A. L., Tucker, R. T., LaForge, J. M., Taschuk, M. T., and Brett M. J. *Nanotechnology* **2012**, *23*, 105608.

(2) LaForge, J. M., Cocker, T. L., Beaudry, A. L., Cui, K., Tucker, R. T., Taschuk, M. T., Hegmann, F. A., and Brett, M. J. *Nanotechnology* **2014**, *25*, 035701.

In this chapter, VLS-GLAD's structural control will be used to fabricate nanostructured ITO transparent electrodes with simultaneously high transmittance and conductivity. Doping and crystallinity in ITO electrodes need to be optimized to balance carrier concentration, mobility and optical transmittance. The effects of architecture, deposition conditions and post-growth annealing processes on the sheet resistance and optical transmittance of VLS-GLAD grown ITO NW electrodes will be presented. These studies will be supported by results from a follow-up work performed in our group by LaForge et al.<sup>326</sup>

### *7.1.2 ITO transparent electrode optimization*

ITO is a complex material system with highly tunable electrical and optical properties that depend on the morphology, degree of crystallinity, oxidation, stoichiometry, and doping.<sup>177</sup> As discussed in Chapter 2, ITO's conductivity arises from degenerate n-type doping from both Sn, and oxygen vacancies. Optimizing the conductivity relies on achieving simultaneously high mobility and high carrier concentration. However, the introduction of dopants introduces defects which results in increased scattering of free carriers and reduced mobility.

In addition, the electrical and optical properties of ITO are tightly linked.<sup>177</sup> For instance, high carrier concentrations can lead to increased free carrier absorption, decreasing infrared transmittance. In addition, high carrier concentrations shift the transmittance "window" to smaller wavelengths in ITO by increasing the plasma frequency resulting in a reduced onset reflectance wavelength, and increasing the bandgap through the Moss-Burstein effect.<sup>173</sup> Therefore, it can be challenging to achieve simultaneously high transmittance and high carrier concentrations.

In the case of nanostructured ITO, the degree of interconnectivity between adjacent structures strongly impacts long range electrical transport. Thus, structural considerations must also be made for transparent electrode applications. Simultaneous optimization of optical transmission, mobility, carrier concentration, and architecture of nanostructured ITO transparent electrodes is required; such a task is not trivial.

In this chapter, NW films are first annealed in air to remove defects and enhance crystallinity, resulting in improved mobility and transmittance.<sup>185,327–329</sup> However, the air anneal also oxidizes ITO, resulting in reduced carrier concentration. In this chapter, the films are subsequently annealed in H<sub>2</sub> to provide a reducing environment to reintroduce oxygen vacancies into the healed lattice. It is well known that annealing ITO films in H<sub>2</sub> results in increased carrier concentrations, and leads to enhanced conductivity.<sup>185,327,330–334</sup> The two-stage annealing process allows high carrier concentrations to be recovered following the air anneal by using an H<sub>2</sub> anneal to reintroduce oxygen vacancies without significantly diminishing the improved optical transmittance.

## 7.2 Experimental

### *7.2.1 Annealing procedure*

ITO NW films were grown on quartz substrates using VLS-GLAD as discussed in previous chapters. A nominal thickness for each film was about 1 μm. A two-stage annealing process, developed in previous work by our group to optimize GLAD ITO electrodes<sup>122</sup>, was performed following growth. The first stage air anneal was initiated with a ramp rate of 10 °C per minute from room temperature to 500 °C in atmosphere and then held for 90 minutes. The heating is turned off and the samples were removed after passively cooling to 90 °C. The second stage anneal was performed in a three-zone tube furnace. Forming gas consisting of 5% H<sub>2</sub> (balance Ar) was flowed over the samples at a rate of 100 sccm during the anneal. The temperature of the samples was ramped linearly to 375 °C in 90 minutes, held at 375 °C for 60 minutes, and then turned off and allowed to passively cool to below 90 °C before removing the samples from the furnace.

### *7.2.2 Characterization*

Transmission spectra of films on quartz substrates were measured from 185 nm to 3300 nm using a spectrophotometer (Perkin-Elmer NIR-UV). Film sheet resistance (quartz substrate) was measured using a four point probe. Transmission and sheet

resistance measurements were conducted before and after each annealing stage. The sheet resistance is calculated as:

$$R_S = \frac{V}{I} \frac{\pi}{\ln 2} \quad (7.1)$$

Which is the widely used calculation assuming four-point-probe on an infinite sheet.<sup>335</sup>

Achieving optimal sheet resistance and optical transmittance is a challenging balancing act. This compromise exemplifies the complicated relationship between electrical, optical and structural properties observed in nanostructured ITO films. To achieve such a balance of sheet resistance and optical transmittance, several figure of merits have been proposed.<sup>184,336–338</sup>

In 1976, in a paper by Haacke, a figure of merit was introduced to quantify and compare the quality of transparent electrodes based on their sheet resistance ( $R_S$ ) and transmissivity ( $T_0$ ).<sup>338</sup>

$$F_H = \frac{T_0^x}{R_S} \quad (7.2)$$

where  $R_S$  is sheet resistance,  $T_0$  is optical transparency (averaged over  $400 \text{ nm} < \lambda < 780 \text{ nm}$ ) and  $x = 10$ , typically.<sup>338</sup> The value of  $x$  is chosen to vary the importance of transmission. Typical device grade planar ITO films have  $2 \times 10^{-3} \Omega^{-1} < F_H < 22 \times 10^{-3} \Omega^{-1}$ . Haacke's figure of merit will be used to compare electrodes here.

## 7.3 Results

### 7.3.1 Sheet resistance – four-point-probe

In bulk-like films, transmission spectra and in-plane conductivity measured via four-point probe can readily assess the optical and electrical performance. Four-point-probe can be used to measure changes in conductivity throughout NW arrays, however, it is difficult to distinguish whether changes in conductivity are due to

intrinsic properties of the material, or the structure of the electrode. The conductivity of ITO NW architectures will depend on the degree of interconnectivity between structures; however, regardless of these limitations four-point-probe is routinely used to measure conductivity in nanostructured ITO arrays.<sup>33,98,202,242,325</sup> Interestingly, four-point-probe measurements provide insight into the structure and its evolution and behaviour with changing process parameters. In a follow-up work by our group performed by LaForge et al., terahertz time domain spectroscopy (THz-TDS) was coupled with EDX and X-ray photoelectron spectroscopy (XPS) to gain deeper insight into the mechanism driving conductivity changes within the ITO NWs. Results from LaForge et al's work will be used to support the findings in this chapter.

### *7.3.2 Sheet resistance – $\alpha$*

Sheet resistance increases rapidly with increasing  $\alpha$  in NW arrays (**Figure 7.1** and **Table 7.1**), likely due to increased spacing leading to poor charge transport between adjacent NWs in films (as seen in Chapter 3). Films grown at high  $\alpha$  are thus not suitable for transparent electrode applications without a conductive base layer, as separated structures are not capable of efficiently transporting charge to adjacent structures. It is likely the small conductivity measured through the NW arrays grown at high  $\alpha$  is primarily due to the thin planar nucleation layer at the base of the film (**Figure 7.3**). A proper balance between the required spacing and sheet resistance must be reached for the desired application.

Separated nanostructures could be deposited onto a pre-deposited planar ITO film to enable good conductivity. Planar ITO films have a nominal sheet resistance of 5  $\Omega$ /sq following the annealing procedure used in our lab. Charge transport between well separated structures can also be achieved by fabricating a density graded film, as shown in Chapter 3 (see **Figure 3.19e**). The film was grown by increasing  $\alpha$  from 30° to 85° midway through deposition. This architecture exhibited a low sheet resistance of 147  $\Omega$ /sq prior to annealing, and 81  $\Omega$ /sq following the two-stage anneal process. The dense base of the film would serve as a conductive layer to

transport the collected charges from the protruding structures embedded in the photoactive polymer of OPV devices. VLS-GLAD allows the dense base layer and protruding NW layer to be grown in a single deposition step. Substrate motion could be engineered to fabricate designed density gradients along the height of the film to reach an optimal compromise between structural spacing and electrical interconnectivity.

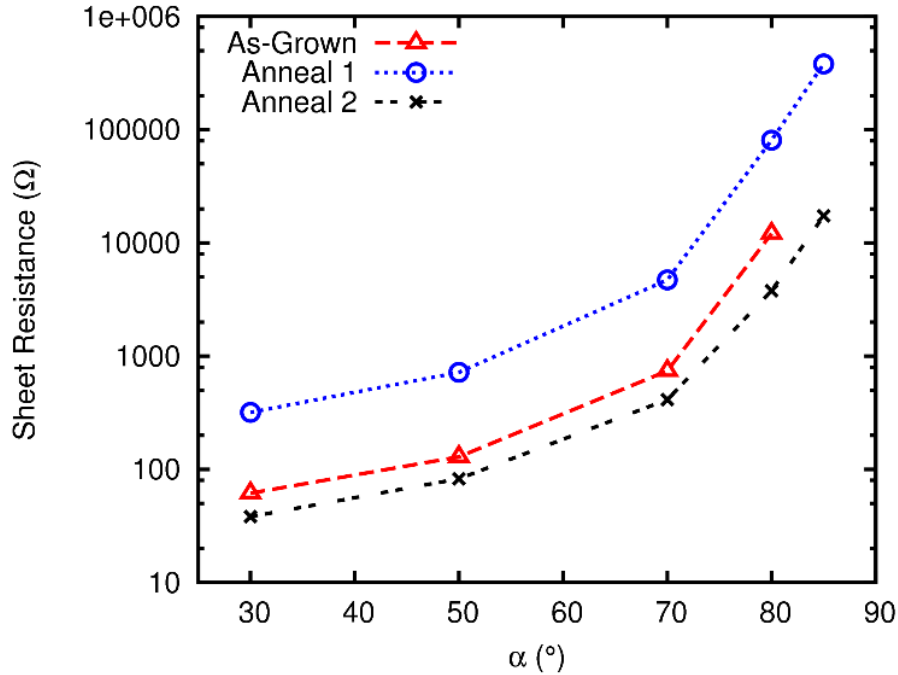


**Figure 7.1:** Sheet resistance for ITO NW films grown at different deposition angles ( $\alpha$ ), measured for as-grown, after annealing in air (anneal 1), and after H<sub>2</sub> anneal (anneal 2).

### 7.3.3 Sheet resistance – deposition rate

Sheet resistance was found to be lower in NW films grown at high deposition rates (**Figure 7.2** and **Table 7.2**). For  $\alpha = 50^\circ$ , the sheet resistance decreased from 230  $\Omega$ /sq to 51  $\Omega$ /sq (119  $\Omega$ /sq to 37  $\Omega$ /sq after annealing) as the deposition rate was increased from 0.05 nm/s to 2 nm/s. The effect is the same for as-grown NW films grown at  $\alpha = 85^\circ$ , where the sheet resistance decreases from 6.1 M $\Omega$ /sq to 15.7 k $\Omega$ /sq (50.7 k $\Omega$ /sq to 820  $\Omega$ /sq after annealing) as the deposition rate is increased from 0.1 nm/s to 2 nm/s.

$\alpha$ (°)	Sheet Resistance			$T_{\text{avg}}$ ( $400 < \lambda < 780$ nm)			Haacke's Figure of Merit ( $F_H$ )		
	Pre-anneal ( $\Omega/\text{sq}$ )	Anneal 1 ( $\Omega/\text{sq}$ )	Anneal 2 ( $\Omega/\text{sq}$ )	Pre-anneal (%)	Anneal 1 (%)	Anneal 2 (%)	Pre-anneal ( $10^{-3}/\Omega$ )	Anneal 1 ( $10^{-3}/\Omega$ )	Anneal 2 ( $10^{-3}/\Omega$ )
30	$61.6 \pm 0.7$	$319 \pm 2$	$38.2 \pm 0.3$	$53.2 \pm 0.2$	$76.1 \pm 0.2$	$77.5 \pm 0.2$	$0.029 \pm 0.001$	$0.204 \pm 0.006$	$2.05 \pm 0.05$
50	$128.8 \pm 0.2$	$719 \pm 2$	$82.6 \pm 0.7$	$84.1 \pm 0.2$	$88.5 \pm 0.2$	$88.4 \pm 0.2$	$1.37 \pm 0.03$	$0.408 \pm 0.009$	$3.51 \pm 0.08$
70	$740 \pm 15$	$4710 \pm 40$	$412 \pm 2$	$89.0 \pm 0.2$	$91.7 \pm 0.2$	$91.2 \pm 0.2$	$0.42 \pm 0.01$	$0.089 \pm 0.002$	$0.97 \pm 0.02$
80	$12100 \pm 300$	$81000 \pm 2000$	$3780 \pm 40$	$92.0 \pm 0.2$	$92.9 \pm 0.2$	$92.7 \pm 0.2$	$0.036 \pm 0.001$	$0.0059 \pm 0.0001$	$0.124 \pm 0.003$
85		$3.81 \pm 0.1 \times 10^5$	$17300 \pm 700$	$92.7 \pm 0.2$	$93.0 \pm 0.2$	$93.1 \pm 0.2$	$3.24 \pm 0.07 \times 10^{-4}$	$1.27 \pm 0.05 \times 10^{-3}$	$0.028 \pm 0.001$

**Table 7.1:** Sheet resistance, average visible transmission ( $400 < \lambda < 780$  nm) and Haacke's figure of merit measured before and after each annealing stage for ITO NW films grown at a temperature of 240 °C, rate of 0.2 nm/s, and at various  $\alpha$ .

$\alpha$ (°)	Rate (nm/s)	Sheet Resistance			$T_{avg}$ (400 < $\lambda$ < 780 nm)			Haacke's Figure of Merit ( $F_H$ )		
		Pre-anneal ( $\Omega$ /sq)	Anneal 1 ( $\Omega$ /sq)	Anneal 2 ( $\Omega$ /sq)	Pre-anneal (%)	Anneal 1 (%)	Anneal 2 (%)	Pre-anneal ( $10^{-3}/\Omega$ )	Anneal 1 ( $10^{-3}/\Omega$ )	Anneal 2 ( $10^{-3}/\Omega$ )
50	0.05	231.6 ± 0.7	1970 ± 20	117.7 ± 0.7	84.3 ± 0.2	91.5 ± 0.2	91.2 ± 0.2	0.79 ± 0.02	0.209 ± 0.005	3.39 ± 0.08
50	0.1	213.5 ± 0.8	1920 ± 10	119.0 ± 0.2	84.4 ± 0.2	91.6 ± 0.2	91.2 ± 0.2	0.86 ± 0.02	0.216 ± 0.005	3.36 ± 0.07
50	0.2	128.8 ± 0.2	720 ± 2	82.6 ± 0.7	84.1 ± 0.2	88.5 ± 0.2	88.3 ± 0.2	1.37 ± 0.03	0.408 ± 0.009	3.51 ± 0.08
50	0.5	137.8 ± 0.2	870 ± 20	72.0 ± 0.3	78.1 ± 0.2	86.0 ± 0.2	86.2 ± 0.2	0.61 ± 0.02	0.255 ± 0.008	3.13 ± 0.07
50	1	87.1 ± 0.2	618 ± 4	48.0 ± 0.1	70.4 ± 0.2	80.8 ± 0.2	81.8 ± 0.2	0.34 ± 0.01	0.191 ± 0.005	2.78 ± 0.07
50	2	51.0 ± 0.5	447 ± 2	37.1 ± 0.1	35.2 ± 0.2	62.2 ± 0.2	63.9 ± 0.2	5.7 ± 0.3x10 <sup>-4</sup>	0.0194 ± 0.0006	0.305 ± 0.009
85	0.05			5.1 ± 2x10 <sup>4</sup>	92.1 ± 0.2	92.7 ± 0.2	92.3 ± 0.2			0.0088 ± 0.0004
85	0.1	6.0 ± 0.1x10 <sup>6</sup>	1.64 ± 0.05x10 <sup>6</sup>	3.9 ± 2x10 <sup>4</sup>	92.4 ± 0.2	93.2 ± 0.2	92.9 ± 0.2	7.5 ± 0.2x10 <sup>-5</sup>	3.0 ± 0.1x10 <sup>-4</sup>	0.0122 ± 0.0005
85	0.2		3.8 ± 0.1 x10 <sup>5</sup>	17300 ± 600	92.7 ± 0.2	93.0 ± 0.2	93.0 ± 0.2		1.27 ± 0.05x10 <sup>-3</sup>	0.028 ± 0.001
85	0.5	24800 ± 300	65400 ± 200	6610 ± 30	93.2 ± 0.2	93.1 ± 0.2	93.0 ± 0.2	0.020 ± 0.001	7.5 ± 0.2x10 <sup>-3</sup>	0.073 ± 0.002
85	1	9 ± 1x10 <sup>5</sup>	79000 ± 4000	5600 ± 200	83.1 ± 0.2	86.3 ± 0.2	86.8 ± 0.2	1.8 ± 0.2x10 <sup>-4</sup>	2.9 ± 0.2x10 <sup>-3</sup>	0.043 ± 0.002
85	2	15700 ± 400	11200 ± 200	820 ± 3	79.1 ± 0.2	81.8 ± 0.2	84.2 ± 0.2	6.1 ± 0.2x10 <sup>-3</sup>	0.0119 ± 0.0004	0.217 ± 0.005

**Table 7.2** Sheet resistance, average visible transmission (400 <  $\lambda$  < 780 nm) and Haacke's figure of merit measured before and after each annealing stage for ITO NW films grown at a temperature of 240 °C.

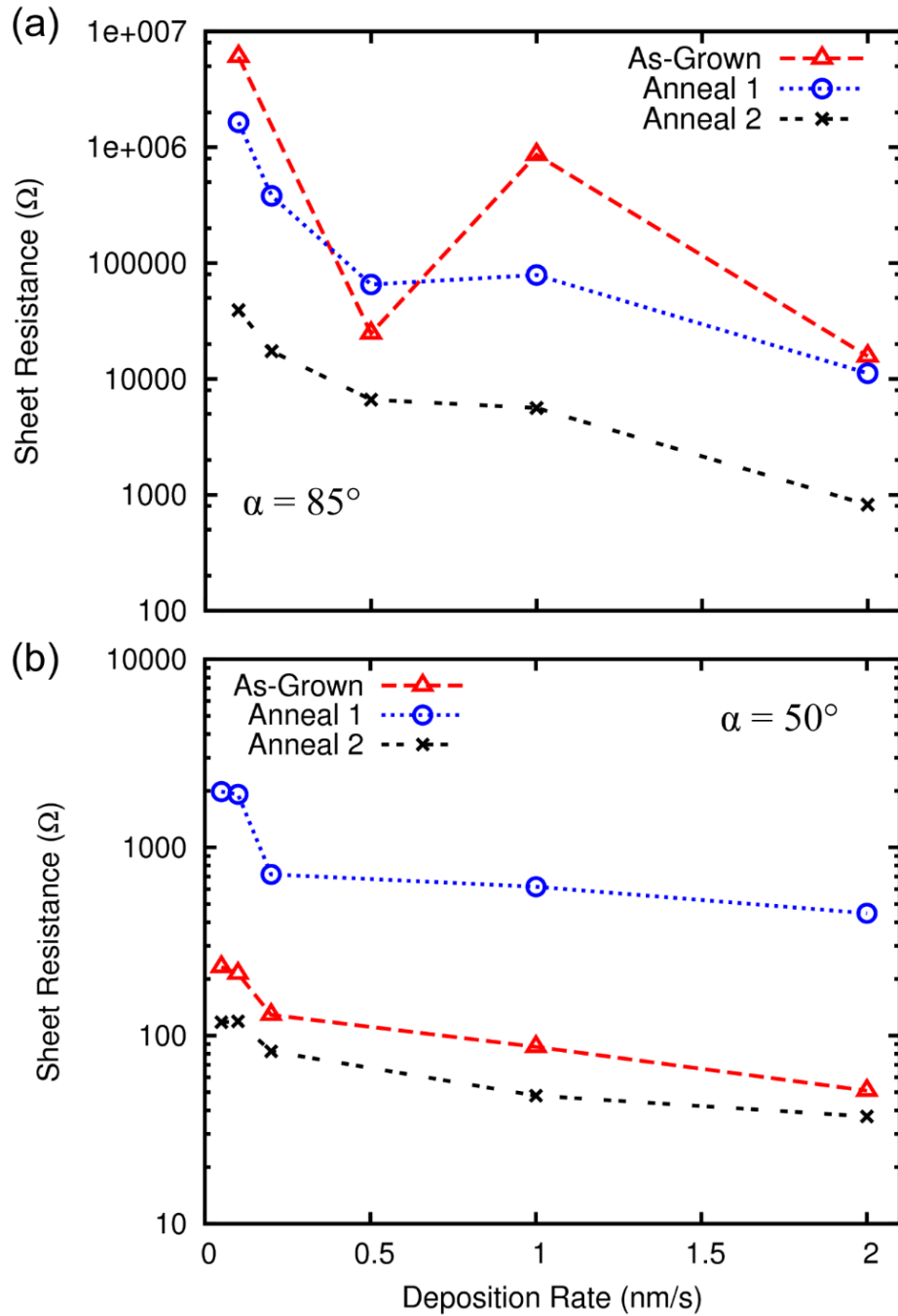


**Figure 7.2:** Sheet resistance for ITO NW films grown at (a)  $\alpha = 85^\circ$  and (b)  $\alpha = 50^\circ$ , and different deposition rates. Measured for as-grown, after annealing in air (anneal 1), and after  $H_2$  anneal (anneal 2).

Structural changes may be partially responsible for the variance in conductivity observed in films grown at different deposition rates, such as a thicker planar nucleation layer at high deposition rates contributing to increased lateral conductivity (**Figure 7.3**). However, it is challenging to decipher whether conductivity changes are due to intrinsic material property changes, such as stoichiometry or crystallinity, or structural changes, such as degree of interconnectivity or nucleation layer thickness, using four-point-probe measurements.

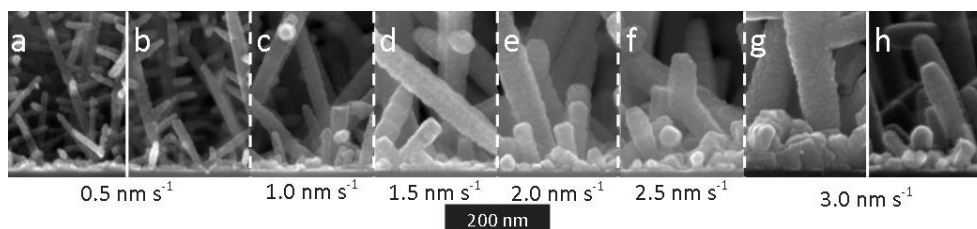


**Figure 7.3:** Comparison of the nucleation layer of NW arrays grown at various deposition rates. Figure reproduced with permission from *Nanotechnology*.<sup>326</sup> Copyright 2014, Institute of Physics.

In a follow up work by our group (LaForge et al.)<sup>326</sup>, we were able to use a contact THz-TDS, coupled with EDX and XPS, to gain deeper insight into conductivity changes at different deposition rates. In LaForge's work, a four-fold increase in carrier concentration (from  $1.5 \pm 0.2 \times 10^{20} \text{ cm}^{-3}$  to  $5.8 \pm 0.7 \times 10^{20} \text{ cm}^{-3}$ ) was measured as deposition rate was increased from 0.5 nm/s to 3 nm/s. The relative In and Sn concentrations were found to be independent of deposition rate using both EDX and XPS (**Figure 7.4**). It was therefore postulated that the dramatic increase in carrier concentration was a result of increased oxygen deficiency during higher rate depositions leading to increased oxygen vacancy concentration in the structures. This result agrees with the observed decreased sheet resistance in high rate films in this chapter.

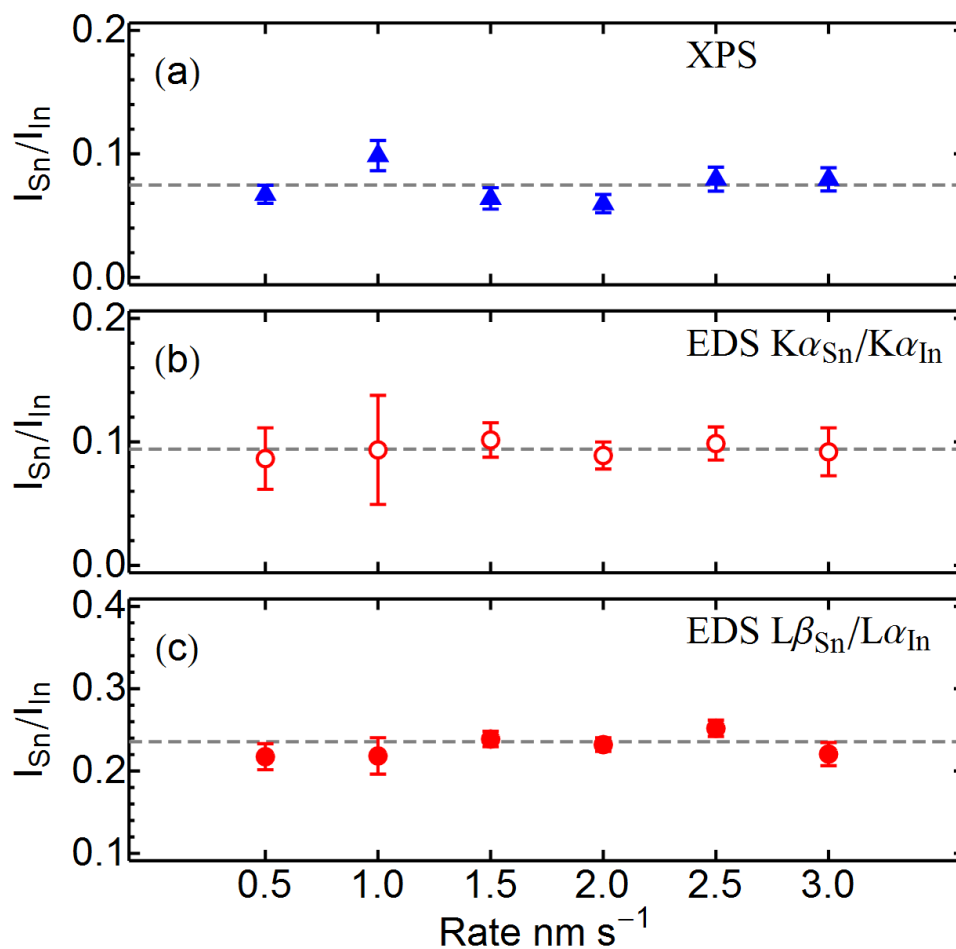


**Figure 7.4:** The Sn/In ratio of the nanowires as a function of flux rate. Composition was estimated by (a) XPS and by EDS through comparison of the (b) K- $\alpha$  lines of Sn and In and (c) the L- $\beta$  Sn lines to the L- $\alpha$  In lines. The dashed horizontal lines represent the average value for each set of data. Figure reproduced with permission from *Nanotechnology*.<sup>326</sup> Copyright 2014, Institute of Physics.

### 7.3.4 Sheet resistance – temperature

The sheet resistance in as-deposited NW films grown at  $\alpha = 50^\circ$  increases from 24  $\Omega/\text{sq}$  to 129  $\Omega/\text{sq}$  (41  $\Omega/\text{sq}$  to 83  $\Omega/\text{sq}$  after annealing) as the deposition temperature is increased from 130  $^\circ\text{C}$  to 240  $^\circ\text{C}$  as shown in **Figure 7.5**. The increase in sheet resistance may be due to the onset of VLS growth above 130  $^\circ\text{C}$ , resulting in a transition from planar films to disconnected NWs. In order to properly design an electrode architecture, the deposition conditions need to be optimized

both for structural interconnectivity and desirable intrinsic material properties to optimize long range conductivity throughout the film.

In this study, the sheet resistance of NW films typically increase by an order of magnitude following annealing in air, as seen in **Figure 7.1**, **Figure 7.2**, and **Figure 7.5**. No significant changes to morphology were observed following either annealing stage, which suggests the observed decrease in sheet resistance was due to changes in intrinsic properties of the material, such as oxygen vacancy concentration and degree of disorder in the crystal, rather than morphological effects, such as the degree of interconnectivity between structures. The transmission spectra also provides insight into charge carriers in the film.

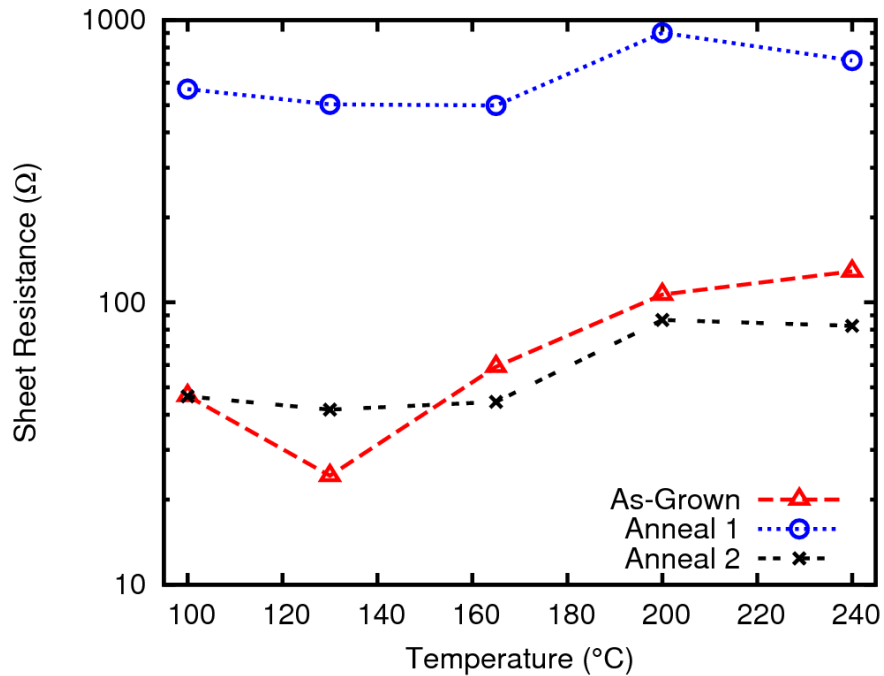


**Figure 7.5:** Sheet resistance for ITO NW films grown at  $\alpha = 50^\circ$ , 0.2 nm/s, different deposition temperatures. Measured for as-grown, after annealing in air (anneal 1), and after H<sub>2</sub> anneal (anneal 2).

### *7.3.5 Optical transmittance – annealing*

Following the first stage air anneal, NW arrays become much more transmissive as shown in the photographs in **Figure 7.6a** and **b**. Low transmissivity in ITO films grown in oxygen deficient environments has been attributed to the presence of free indium in the lattice, which is removed upon annealing in air.<sup>177,187</sup> A characteristic spectrum illustrating the effects on transmittance due to the two annealing stages is shown in **Figure 7.6c**.

It is well known that annealing ITO in air results in improved transmission due to improved crystallinity, and reduced free carrier densities.<sup>327</sup> Prior to annealing, reflection at the plasma wavelength ( $\sim 1100$  nm) is observed (**Figure 7.6c**). The absence of reflectance at the plasma wavelength ( $\sim 1000$  nm) observed in the spectra following annealing in air (**Figure 7.6c**) suggests that carrier density decreases significantly, agreeing with the increase in sheet resistance following air anneals. The reflectance at the plasma wavelength ( $\sim 1200$  nm) is observed following the second stage H<sub>2</sub> anneal (**Figure 7.6c**), suggesting a dramatic increase in free carrier concentration, but the relatively unaffected transmission in the visible spectrum suggests the improved crystallinity achieved from annealing in air remains intact. Therefore, the H<sub>2</sub> stage anneal can be performed to increase carrier density with negligible effect on the visible transmittance. This suggests the H<sub>2</sub> anneal introduces oxygen vacancies without overly disrupting order in the crystal, allowing for higher mobility and optical transmission. The infrared region becomes more opaque following the H<sub>2</sub> anneal, which is expected due to the increased free carrier absorption.

### *7.3.6 Optical transmittance - $\alpha$*

Higher optical transmissivity was observed for films grown at elevated  $\alpha$  (**Figure 7.7a**). For as-grown films, the average visible transmissivity increases from 84% to 93% as the deposition angle is increased from 50° to 90° (**Figure 7.7b**). Following the two-stage anneal process, the visible transmissivity increases to 88% for the  $\alpha$

= 50°, while the  $\alpha = 90^\circ$  film remains at 93%. Increased transmissivity in high  $\alpha$  films is likely primarily due to decreased mass density on the substrate.

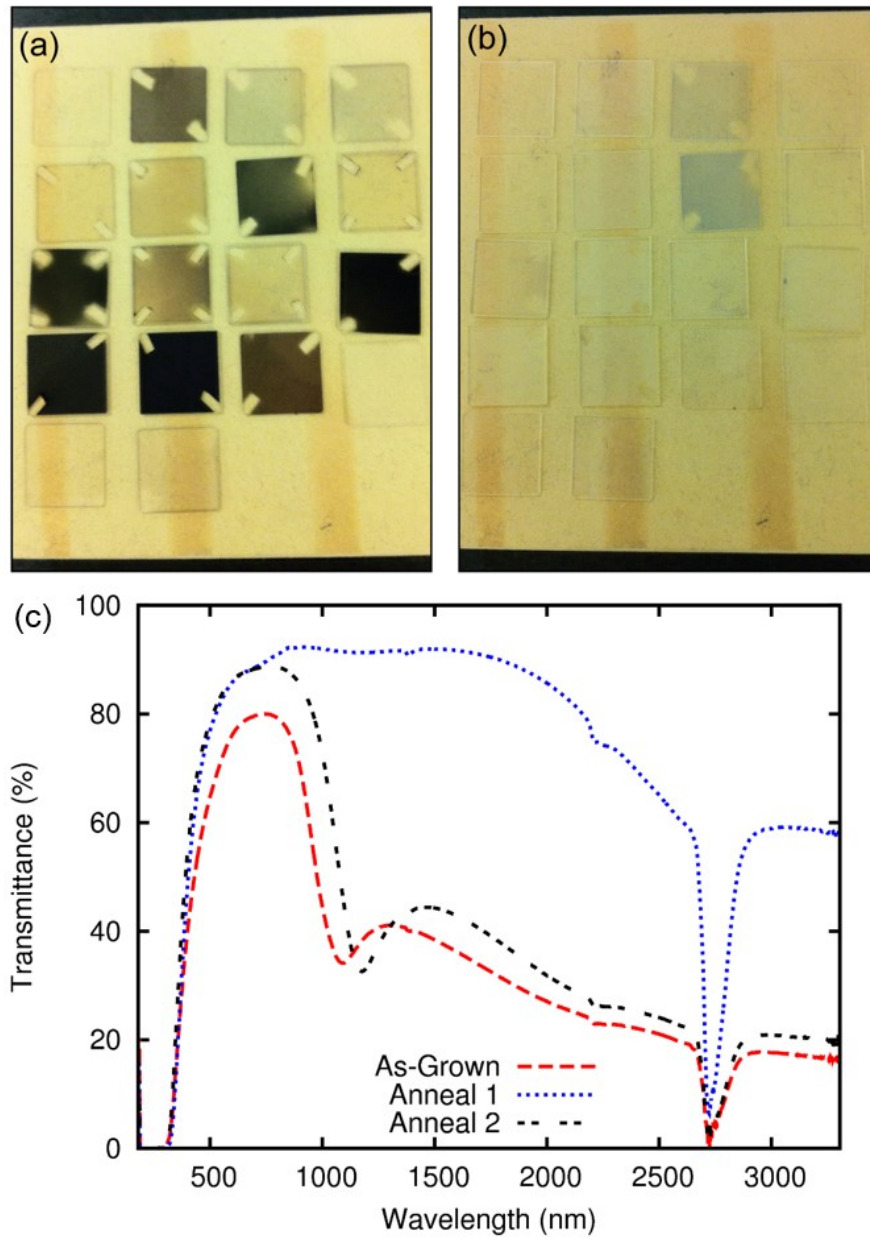


**Figure 7.6:** Photograph of various ITO NW films (a) as-grown, and (b) after first stage air anneal. (c) Transmission spectra for an ITO NW film grown at 1 nm/s,  $\alpha = 50^\circ$ , and 240 °C, as-grown, after annealing in air, and after H<sub>2</sub> anneal.

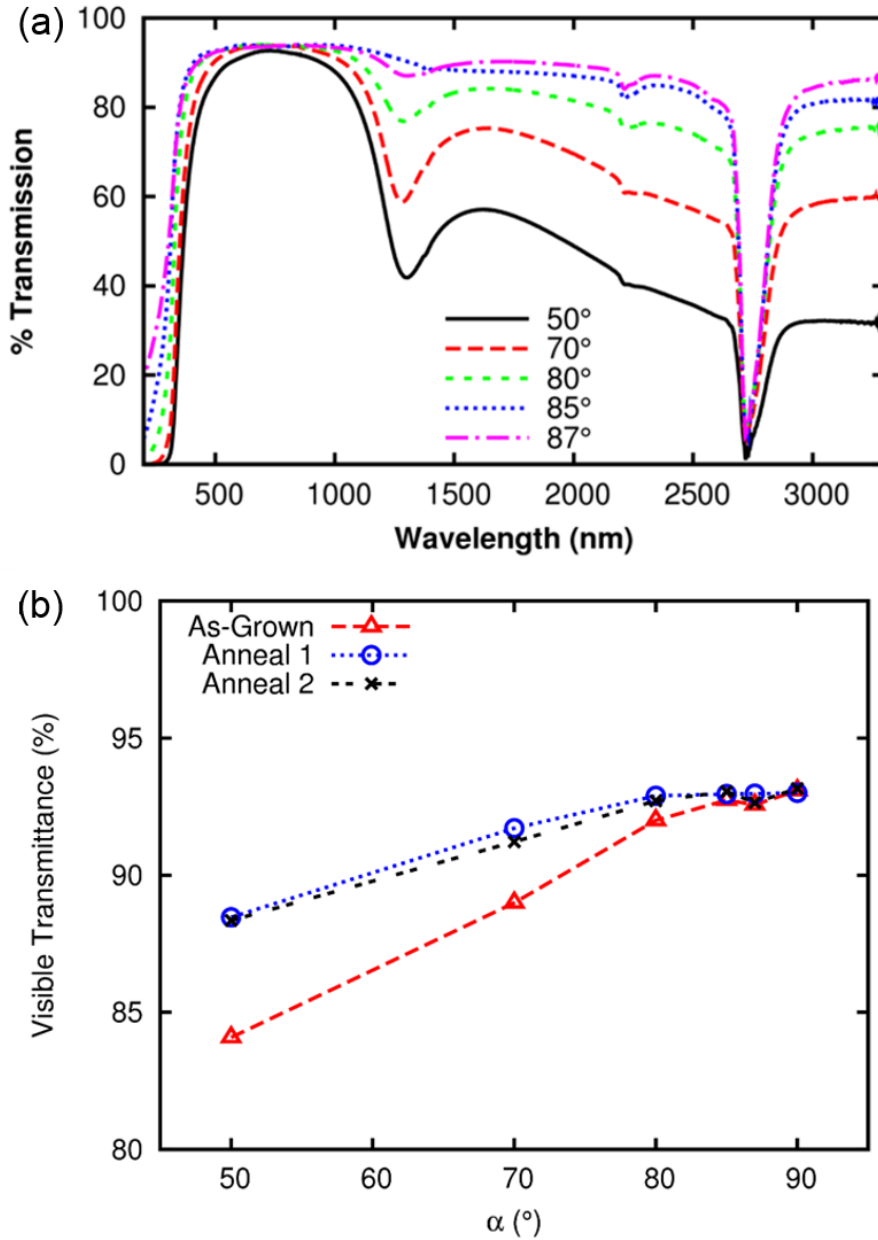


**Figure 7.7:** (a) Transmission spectra for ITO NW films grown at 0.2 nm/s, 240 °C and different  $\alpha$ , after annealing. (b) Average visible transmittance ( $400 < \lambda < 780$  nm) for ITO NW films grown at 0.2 nm/s, 240 °C and different  $\alpha$ . Measured for as-grown, after annealing in air (Anneal 1), and after H<sub>2</sub> anneal (Anneal 2). (a) Reproduced with permission from *Nanotechnology*.<sup>271</sup> Copyright 2012 Institute of Physics.

### *7.3.7 Optical transmittance – deposition rate*

NW arrays grown at higher deposition rates have reduced transmission compared to films grown at low rates (**Figure 7.8a**). For as-grown  $\alpha = 50^\circ$  films, the average visible transmission decreases from 84 % to 38 % (92 % to 64 % after annealing) as the deposition rate is increased from 0.05 nm/s to 2 nm/s. The plasma wavelength shifts from  $\sim 1400$  nm to  $\sim 1200$  nm (shrinking the transmission window) as the deposition rate is increased, suggesting an increase in carrier concentration. This result agrees with observations by LaForge<sup>326</sup>, where it was found the growth environment likely became increasingly oxygen deficient at higher deposition rates leading to increased carrier concentrations. In LaForge's work, carrier localization was also observed in films grown at high rates, suggesting increased disorder and increased impurity concentration, which may cause the reduced visible transmittance observed for high rate films seen in **Figure 7.8b**.

### *7.3.8 Optical transmittance - temperature*

As-grown NW films are typically more transmissive at higher deposition temperatures (**Figure 7.9**), which is likely due to reduced disorder in the lattice. The average visible transmissivity increases from 40% to 92% as the deposition temperature is increased from 100 °C to 200 °C for as-grown  $\alpha = 85^\circ$  films. In addition, for as-grown  $\alpha = 50^\circ$  films, the films go from being opaque to having  $> 80\%$  visible transmission as the temperature is increased from 100 °C to 240 °C. Following the two-stage anneal process, the transmission of low temperature films increases substantially, suggesting structural disorder and impurity concentration may be reduced upon annealing. As previously discussed, the H<sub>2</sub> anneal has negligible effect on visible transmission.

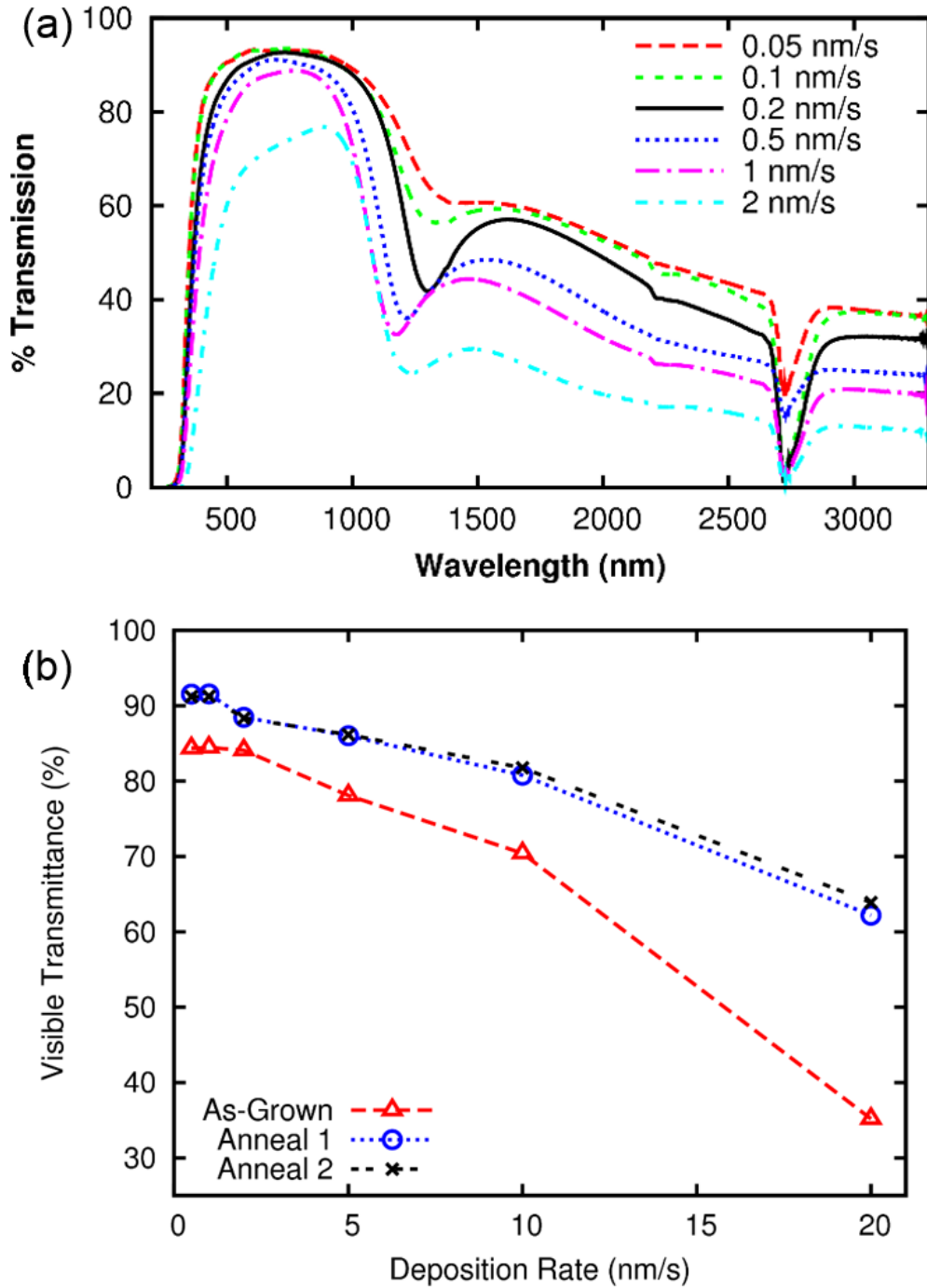


**Figure 7.8:** (a) Optical transmission of ITO NW films deposited at  $\alpha = 50^\circ$ ,  $240^\circ\text{C}$  and various flux rates, after annealing. (b) Average visible transmittance ( $400 < \lambda < 780 \text{ nm}$ ) for ITO NW films grown at  $\alpha = 50^\circ$ ,  $240^\circ\text{C}$  and various deposition rates. Measured for as-grown, after annealing in air (anneal 1), and after  $\text{H}_2$  anneal (anneal 2). (a) Reproduced with permission from *Nanotechnology*.<sup>271</sup> Copyright 2012 Institute of Physics.

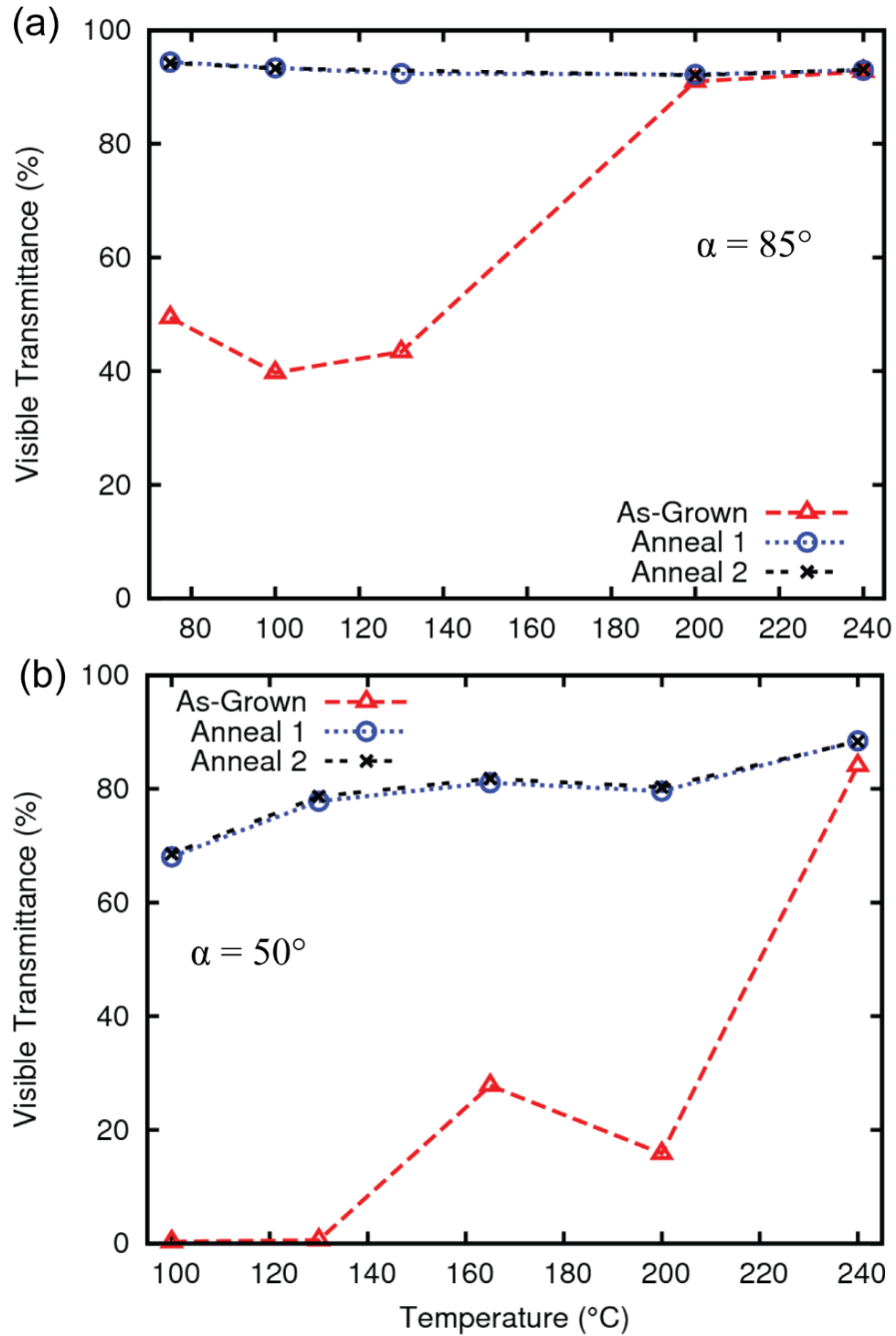


**Figure 7.9:** Average visible transmission for ITO NW films grown at 0.2 nm/s, and various deposition temperatures, for (a)  $\alpha = 85^\circ$  and (b)  $\alpha = 50^\circ$ . Measured for as-grown, after annealing in air (anneal 1), and after  $H_2$  anneal (anneal 2).

### *7.3.9 Haacke's Figure of Merit*

Haacke's FOM is defined in Equation 7.2. The first anneal increased the transmission of the films and the second anneal decreased the sheet resistance of the films, collectively improving  $F_H$  by 1 to 2 orders of magnitude (**Figure 7.2**, **Table 7.1**, and **Table 7.2**). As  $\alpha$  is increased, the sharp increase in sheet resistance significantly reduces  $F_H$  (**Figure 7.10a**). However, by using a low  $\alpha$  base layer, and a high  $\alpha$  interfacial layer (as previously described), a high  $F_H$  ( $\sim 4.6 \times 10^{-3} \Omega^{-1}$ ) can be reached, while still having the desired protruding surface for enhanced charge extraction in OPV devices (recall **Figure 3.19e**). Interestingly,  $F_H$  decreases with deposition rate for  $\alpha = 50^\circ$  films despite conductivity enhancements at high rates (**Figure 7.10b**). Therefore, the significantly degraded transmittance at elevated deposition rates in  $\alpha = 50^\circ$  films outweighs the improved film conductivity. In summary, low  $\alpha$  films grown at low deposition rates exhibit the largest  $F_H$ . If high  $\alpha$  films are to be applied as an electrode, they must be grown on a planar ITO film, or use substrate motion to fabricate density graded films.

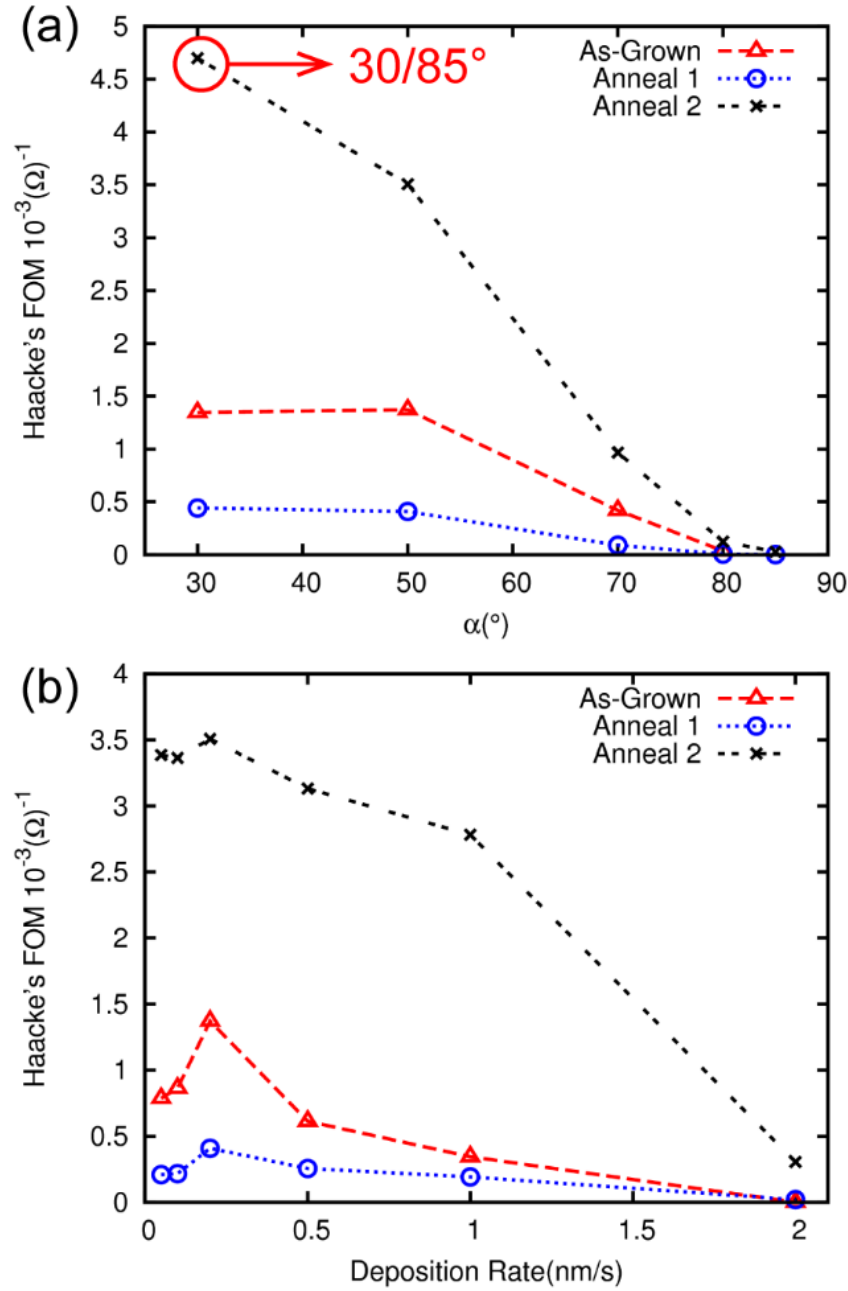


**Figure 7.10:** Haacke's FOM ( $F_H$ ) for ITO NW films grown at (a) 0.2 nm/s, and 240 °C, at various  $\alpha$ , and (b)  $\alpha = 50^\circ$ , and 240 °C, at various deposition rates. 30/85° label in (a) refers to NW film grown with  $\alpha$  changed midway through growth as shown in **Figure 3.19e**.

## 7.4 Conclusions

Nanostructured ITO electrodes are promising candidates for a variety of applications, including charge extractors in OPV devices, and flexible transparent electrodes. VLS-GLAD has enabled powerful control over the electrode structure, however, optimizing the conductivity and optical transmittance had been left uninvestigated prior to this chapter. Insight into the complex relationship between electrical and optical properties was achieved, and the two stage annealing process was shown to be highly effective in optimizing both visible transmittance and sheet resistance for transparent electrode applications. In addition, it was found that the deposition parameters can be set to achieve the desired electrode architecture, and post-growth annealing can be performed to optimize intrinsic properties of the material without impacting the electrode's structure.

The use of a four-point-probe proved to be limited as only interstructure conductivity can be assessed, and more sophisticated techniques are required to understand the intrinsic conductivity within the individual NWs. However, the four-point-probe technique provided excellent insight into the evolving structure of the electrodes with changing deposition parameters, including the nucleation layer, and degree of interconnectivity between structures. Further work using THz-TDS will help elucidate the mechanisms resulting in enhanced conductivity in annealed ITO NW films.

VLS-GLAD is a powerful nanostructuring technique capable of fabricating a variety of branched ITO NW networks. This chapter presented the first step to optimization of the functional properties of VLS-GLAD grown architectures for device purposes, and much more investigation will be required. However, the results in this chapter show immense promise for VLS-GLAD as an electrode fabrication technique. New device architectures for other applications including transistors or solar cells may be possible as VLS-GLAD is extended to more material systems.

# 8. Conclusions

---

## 8.1 Summary of Thesis Results

### *8.1.1 Summary*

This thesis outlined the development of a technique named VLS-GLAD that uses glancing angle deposition to guide the self-assembly of NWs through vapour-liquid-solid growth. VLS-GLAD was shown to have powerful 3D structural control in branched ITO NW arrays. The anisotropic branching demonstrated in this work may enable the fabrication of 3D interconnected NW networks with directional interconnectivity, leading to new device architectures. In addition, optimization of the structural, electrical and optical properties of branched ITO NW transparent electrodes was performed. With further development, VLS-GLAD could be a powerful technique in achieving controlled bottom-up synthesis of functional 3D nanoscale architectures.

### 8.1.2 VLS-GLAD capabilities

Several capabilities were achieved in this thesis using VLS-GLAD as summarized in **Figure 8.1**, including:

1. Height dependent morphology
2. Branch diameter oscillation control
3. Height dependent anisotropic branch growth
4. Epitaxy-free azimuthal alignment of nanotrees
5. L-, T-, and X-branched nanotrees
6. Optimization of 3D nanostructured transparent electrodes

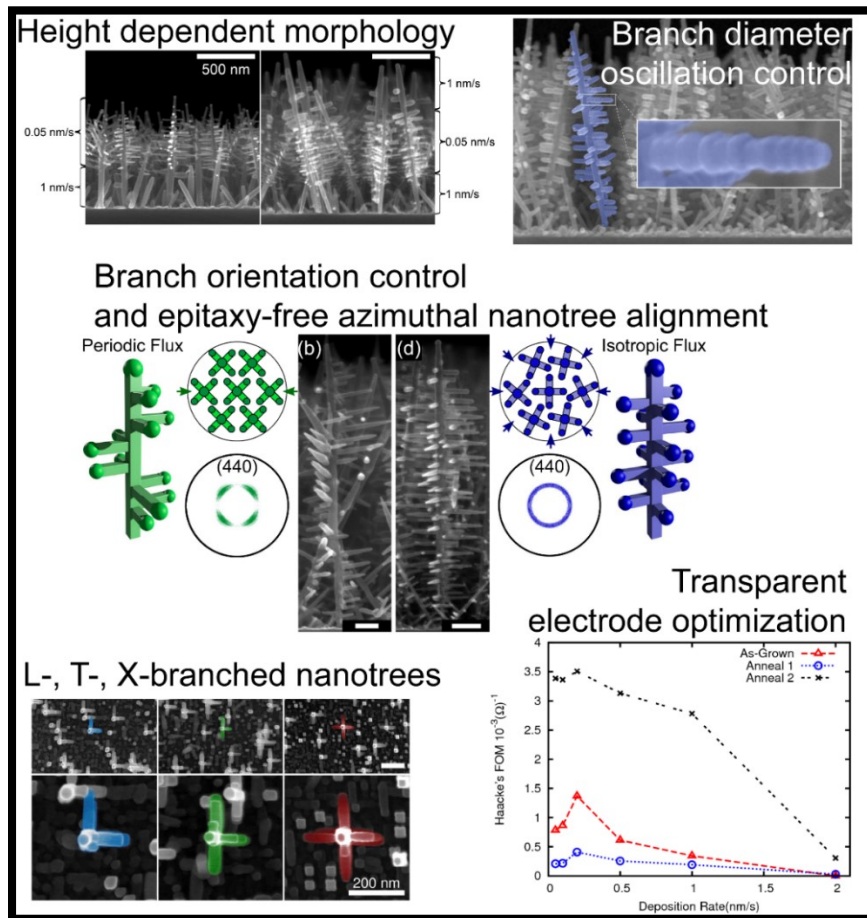


**Figure 8.1:** Summary of notable achievements in this thesis using VLS-GLAD.

### *8.1.3 Morphological control*

In Chapter 3, control over NW spacing, branching, and feature sizes simply by changing deposition parameters was demonstrated. By changing deposition parameters during growth, these features could be controlled with high precision along the height of the NW film. NWs with height dependent diameters and branching densities can now be readily fabricated using VLS-GLAD.

### *8.1.4 Engineered branch oscillations*

Chapter 4 discussed the dynamic control over branch diameter. Periodic oscillations were repeatedly observed in the diameter of branches on NWs grown with continuous substrate rotation. It was postulated that the oscillations were due to self-shadowing as the vapour flux rotated about the trunk, periodically starving a branch's catalytic droplet of material. The droplet therefore oscillates in size and leads to oscillation in the amount of material precipitated at the liquid-interface. The effect was found to be reproducible using a simple model. In addition, aperiodic oscillations could be encoded in the oscillations using dynamic substrate rotation schemes and macroscopic shuttering of the flux. The mechanism enables time-stamping during VLS-GLAD growth, leading to deeper insight into adatom migration and burying of features in the film.

### *8.1.5 Height dependent branch orientation control*

In Chapter 5, asymmetric flux deposition was found to cause anisotropic branching in ITO NWs. Branches preferentially grew on sidewalls of the trunks facing the flux. In addition, the azimuthal branch orientations were changed along the height of a NW by changing the azimuthal orientation between the collimated flux and growing trunks. The height dependent branch orientation control demonstrated in this thesis may allow improved control over interconnectivity in NW arrays.

### *8.1.6 Epitaxy-free competitive nanotree alignment*

Interestingly, nanotree crystals, and resultantly, branches, were preferentially aligned in-plane in a configuration dependent on the azimuthal alignment of the

flux on any substrate. This effect exemplifies the significance of the intersection between ballistic vapour deposition, and kinetic crystal growth processes. The branch alignment effect is due to a combination of the cubic shape of the crystalline NWs, and shadowing of the obliquely incident vapour flux. Initially, the azimuthal orientation of the nuclei is random, however, the directional flux induces a competitive growth process. Trunks oriented with the largest flux capture cross-section capture more growth material, and trunks oriented with smaller flux capture cross-sections become increasingly shadowed from the flux as the preferred trunks increase in height, resulting in extinction. The trunk crystals become preferentially aligned azimuthally, and due to the epitaxial growth of branches on the trunk sidewall, the branches adopt a morphologically measurable alignment. The crystal alignment can also be measured throughout the nanotree ensemble using XRD pole figures. Agreement between XRD pole figure data and morphological observations is an elegant consequence of the crystalline nature of the branched structures. The alignment of crystalline branched NWs without requiring epitaxial growth at the substrate is a unique capability offered by VLS-GLAD, and allows for more ordered architectures to be fabricated on amorphous substrates, such as glass.

### *8.1.7 L-, T-, and X-branched nanotrees*

In Chapter 6, directed branch growth in aligned nanotrees was presented. The in-plane alignment of nanotrees can be fixed by epitaxial growth on a lattice matched substrate. By fixing the in-plane alignment of nanotrees, the azimuthal position of the flux to be decoupled from alignment of the structures. The flux can then be directed solely to place growth material on select NW facets without impacting the alignment of the structures. Using this control, aligned arrays of self-similar L-, T-, and X-branched nanotrees were grown over large substrate areas. The ability to grow branches along select directions may enable directional interconnectivity between adjacent NWs, as well as morphological anisotropy, which is a significant contribution to the achievable complexity in 3D NW networks.

### *8.1.8 Transparent electrodes*

In addition to improving structural control over 3D NW architectures, the feasibility of applying the branched ITO NW networks as nanostructured electrodes in OPV devices was assessed. The performance of the ITO NW films as TCOs was determined by characterizing sheet resistance and transmittance. While measuring the sheet resistance was useful in gaining an understanding into changes in film conductivity, it was impossible to distinguish between conductivity changes due to structural features and intrinsic material properties, such as stoichiometry or crystallinity. To address this issue, LaForge et al. performed THz-TDS to assess the intrinsic conductivity of ITO independently of structural effects on long-range conductivity, enabling optimization of the growth parameters.<sup>326</sup> Determining optimal deposition parameters and post-growth annealing procedures to achieve ideal stoichiometry, crystallinity, and structure for OPV devices will require further work. However, the results in this thesis provide a foundation for future electrode optimization.

## 8.2 Future Work

### *8.2.1 Looking forward*

The use of GLAD to provide a controlled directional vapour source during VLS growth began as an exploratory project that rapidly expanded as new capabilities were discovered, and it was unfortunately not possible to explore every possible direction. VLS-GLAD has promising capabilities that may be useful for fundamental materials science studies, fabrication of 3D nanoelectronics devices, and for OPV device applications.

### *8.2.2 Directional branch interconnectivity*

Throughout this thesis, branch placement capabilities were continuously improved. In-plane branch alignment was demonstrated for both non-epitaxial and epitaxial growth at the substrate. Utilizing epitaxial alignment of branched ITO NWs to intentionally interconnect NWs using branches is the natural next step. Epitaxial

alignment restricts branch growth to four possible in-plane directions due to the cubic crystal geometry of ITO. Interconnects could be formed between adjacent NWs along select directions by growing anisotropic branched NWs using VLS-GLAD growth on pre-patterned seeds.

### *8.2.3 Enhanced branch placement – new material systems*

Using a separate catalyst and NW growth material would allow catalyst placement to be performed independently of branch and trunk growth. Catalysts could then be deposited on select NW facets at lower temperatures, and at precise locations along the height of the NW.

### *8.2.4 Further transparent electrode optimization*

This thesis presented preliminary efforts to optimize VLS-GLAD ITO NW films for transparent electrode applications. Further work using THz-TDS to optimize the intrinsic material properties using post-growth annealing and deposition conditions would be beneficial. Further understanding of how to best optimize the architecture, stoichiometry, and crystallinity of the structures would be invaluable to fabricating high performance devices. VLS-GLAD significantly enhances control over the film structure and architecture, while post-processing annealing optimization should enable enhanced control over intrinsic material properties. In addition, preliminary work towards flexible electrodes has begun using VLS-GLAD grown branched ITO NWs. VLS-GLAD's powerful structural control should enable architectural optimization for flexibility and conductivity.

## 8.3 Reflection

Material selection was of the utmost importance in ensuring the success of this project. As discussed in Chapter 3, other groups had attempted VLS-GLAD, however, limited control morphological control was demonstrated. In this thesis, ITO was an ideal material system to investigate VLS-GLAD due to the relatively low temperature required to achieve self-catalyzed VLS growth. As a result, a GLAD deposition system could readily be outfitted with a simple heating apparatus capable of reaching growth temperature. The self-catalyzed VLS mechanism also removed a catalyst deposition step, allowing for higher throughput experiments. In addition, branching readily provided insight into the impact of asymmetric vapour source on the morphology of individual structures and the ensemble as a whole. Branch orientation measurements provided deep insight into the texture evolution throughout the nanotree ensemble, which resulted in the evolution of aligned self-similar crystalline structures through a competitive growth process.

Investigations linking crystal properties to the morphology of individual structures via TEM tomography enabled another link to be formed between XRD pole figure data, and branch orientation data. Although it is postulated that this technique would be generally applicable to all VLS material systems, the aforementioned reasons made ITO an excellent material to demonstrate the control VLS-GLAD offers over 3D NW architectures, and to investigate the intersection between ballistic flux deposition and crystal growth.

# References

---

- (1) Lieber, C. *Mrs Bull.* **2003**, 486–491.
- (2) Whitesides, G. M.; Grzybowski, B. *Science* **2002**, *295*, 2418–2421.
- (3) Schmidt, V.; Wittemann, J. V.; Gösele, U. *Chem. Rev.* **2010**, *110*, 361–388.
- (4) Rao, C. N. R.; Deepak, F. L.; Gundiah, G.; Govindaraj, A. *Prog. Solid State Chem.* **2003**, *31*, 5–147.
- (5) Hu, J.; Odom, T. W.; Lieber, C. M. *Acc. Chem. Res.* **1999**, *32*, 435–445.
- (6) Wang, N.; Cai, Y.; Zhang, R. Q. *Mater. Sci. Eng. R Reports* **2008**, *60*, 1–51.
- (7) Law, M.; Goldberger, J.; Yang, P. *Annu. Rev. Mater. Res.* **2004**, *34*, 83–122.
- (8) Schmidt, V.; Gösele, U. *Science* **2007**, *316*, 698–699.
- (9) Schmidt, V.; Wittemann, J. V.; Senz, S.; Gösele, U. *Adv. Mater.* **2009**, *21*, 2681–2702.
- (10) Lu, W.; Lieber, C. M. *J. Phys. D. Appl. Phys.* **2006**, *39*, R387–R406.
- (11) Dasgupta, N. P.; Sun, J.; Liu, C.; Brittman, S.; Andrews, S. C.; Lim, J.; Gao, H.; Yan, R.; Yang, P. *Adv. Mater.* **2014**, n/a–n/a.
- (12) Levitt, A. P. *Whisker Technology*; John Wiley & Sons Inc: New York, 1971.
- (13) Wagner, R.; Ellis, W. *Appl. Phys. Lett.* **1964**, *4*, 89–90.
- (14) Wagner, R.; Ellis, W. *Trans. Met. Soc. AIME* **1965**, 233.
- (15) Morales, A. M. A.; Lieber, C. C. M. *Science* **1998**, *279*, 208–211.
- (16) Garnett, E.; Yang, P. *Nano Lett.* **2010**, *10*, 1082–1087.
- (17) Seo, K.; Wober, M.; Steinvurzel, P.; Schonbrun, E.; Dan, Y.; Ellenbogen, T.; Crozier, K. B. *Nano Lett.* **2011**, *11*, 1851–1856.
- (18) Park, W. Il; Zheng, G.; Jiang, X.; Tian, B.; Lieber, C. M. *Nano Lett.* **2008**, *8*, 3004–3009.

- (19) Tsivion, D.; Schwartzman, M.; Popovitz-Biro, R. *Science* **2011**, *333*, 1003–1007.
- (20) Lu, W.; Xie, P.; Lieber, C. M. *IEEE Trans. Electron Devices* **2008**, *55*, 2859–2876.
- (21) Cui, Y.; Zhong, Z.; Wang, D.; Wang, W. U.; Lieber, C. M. *Nano Lett.* **2003**, *3*, 149–152.
- (22) Nguyen, P.; Ng, H.; Yamada, T.; Smith, M.; Li, J. *Nano Lett.* **2004**, *4*, 651–657.
- (23) Ng, H. T.; Han, J.; Yamada, T.; Nguyen, P.; Chen, Y. P.; Meyyappan, M. *Nano Lett.* **2004**, *4*, 1247–1252.
- (24) Koo, S.; Fujiwara, A.; Han, J.; Vogel, E. *Nano Lett.* **2004**, *4*, 2197–2201.
- (25) Xiang, J.; Lu, W.; Hu, Y.; Wu, Y.; Yan, H.; Lieber, C. M. *Nature* **2006**, *441*, 489–493.
- (26) Motayed, A.; Vaudin, M.; Davydov, A. V.; Melngailis, J.; He, M.; Mohammad, S. N. *Appl. Phys. Lett.* **2007**, *90*, 043104.
- (27) Ferain, I.; Colinge, C. A.; Colinge, J.-P. *Nature* **2011**, *479*, 310–316.
- (28) Tomioka, K.; Yoshimura, M.; Fukui, T. *Nature* **2012**, *488*, 189–192.
- (29) Chuang, S.; Gao, Q.; Kapadia, R.; Ford, A. C.; Guo, J.; Javey, A. *Nano Lett.* **2013**, *13*, 555–558.
- (30) Larrieu, G.; Han, X.-L. *Nanoscale* **2013**, *5*, 2437–2441.
- (31) Baxter, J. B.; Aydil, E. S. *Appl. Phys. Lett.* **2005**, *86*, 053114.
- (32) Bierman, M. J.; Jin, S. *Energy Environ. Sci.* **2009**, *2*, 1050.
- (33) Fung, M. K.; Sun, Y. C.; Ng, A.; Ng, A. M. C.; Djurisić, A. B.; Chan, H. T.; Chan, W. K. *ACS Appl. Mater. Interfaces* **2011**, *3*, 522–527.
- (34) Garnett, E. C.; Brongersma, M. L.; Cui, Y.; McGehee, M. D. *Annu. Rev. Mater. Res.* **2011**, *41*, 269–295.
- (35) Garnett, E. C.; Yang, P. *J. Am. Chem. Soc.* **2008**, *130*, 9224–9225.
- (36) Kelzenberg, M. D.; Turner-Evans, D. B.; Putnam, M. C.; Boettcher, S. W.; Briggs, R. M.; Baek, J. Y.; Lewis, N. S.; Atwater, H. A. *Energy Environ. Sci.* **2011**, *4*, 866.
- (37) Law, M.; Greene, L. E.; Johnson, J. C.; Saykally, R.; Yang, P. *Nat. Mater.* **2005**, *4*, 455–459.
- (38) Li, Y.; Qian, F.; Xiang, J.; Lieber, C. *Mater. Today* **2006**, *9*, 18–27.
- (39) Peng, K.-Q.; Lee, S.-T. *Adv. Mater.* **2011**, *23*, 198–215.
- (40) Tian, B.; Zheng, X.; Kempa, T. J.; Fang, Y.; Yu, N.; Yu, G.; Huang, J.; Lieber, C. M. *Nature* **2007**, *449*, 885–889.
- (41) Wallentin, J.; Anttu, N.; Asoli, D.; Huffman, M.; Aberg, I.; Magnusson, M. H.; Siefer, G.; Fuss-Kailuweit, P.; Dimroth, F.; Witzigmann, B.; Xu, H. Q.; Samuelson, L.; Deppert, K.; Borgström, M. T. *Science* **2013**, *339*, 1057–1060.
- (42) Hochbaum, A. I.; Yang, P. *Chem. Rev.* **2010**, *110*, 527–546.
- (43) Hahm, J.; Lieber, C. M. *Nano Lett.* **2004**, *4*, 51–54.
- (44) Timko, B. P.; Cohen-Karni, T.; Yu, G.; Qing, Q.; Tian, B.; Lieber, C. M. *Nano Lett.* **2009**, *9*, 914–918.
- (45) Cohen-Karni, T.; Casanova, D.; Cahoon, J. F.; Qing, Q.; Bell, D. C.; Lieber, C. M. *Nano Lett.* **2012**, *12*, 2639–2644.
- (46) Jiang, Z.; Qing, Q.; Xie, P.; Gao, R.; Lieber, C. M. *Nano Lett.* **2012**, *12*, 1711–1716.

- (47) Xu, L.; Jiang, Z.; Qing, Q.; Mai, L.; Zhang, Q.; Lieber, C. M. *Nano Lett.* **2013**, *13*, 746–751.
- (48) Suyatin, D. B.; Wallman, L.; Thelin, J.; Prinz, C. N.; Jörntell, H.; Samuelson, L.; Montelius, L.; Schouenborg, J. *PLoS One* **2013**, *8*, e56673.
- (49) Patolsky, F.; Timko, B. P.; Yu, G.; Fang, Y.; Greytak, A. B.; Zheng, G.; Lieber, C. M. *Science* **2006**, *313*, 1100–1104.
- (50) Patolsky, F.; Zheng, G.; Lieber, C. *Anal. Chem.* **2006**.
- (51) Cui, Y.; Wei, Q.; Park, H.; Lieber, C. *Science* **2001**, *293*, 1289–1292.
- (52) Zheng, G.; Patolsky, F.; Cui, Y.; Wang, W. U.; Lieber, C. M. *Nat. Biotechnol.* **2005**, *23*, 1294–1301.
- (53) Musin, R.; Wang, X.-Q. *Phys. Rev. B* **2005**, *71*, 155318.
- (54) Lauhon, L. J.; Gudiksen, M. S.; Wang, D.; Lieber, C. M. *Nature* **2002**, *420*, 57–61.
- (55) Lu, W.; Xiang, J.; Timko, B. B. P.; Wu, Y.; Lieber, C. M. *PNAS* **2005**, *102*, 10046–10051.
- (56) Gudiksen, M. S.; Lauhon, L. J.; Wang, J.; Smith, D. C.; Lieber, C. M. *Nature* **2002**, *415*, 617–620.
- (57) Kempa, T. J.; Tian, B.; Kim, D. R.; Hu, J.; Zheng, X.; Lieber, C. M. *Nano Lett.* **2008**, *8*, 3456–3460.
- (58) Ertekin, E.; Greaney, P. A.; Chrzan, D. C.; Sands, T. D. *J. Appl. Phys.* **2005**, *97*, 114325.
- (59) Glas, F. *Phys. Rev. B* **2006**, *74*, 121302.
- (60) Chuang, L. C.; Moewe, M.; Chase, C.; Kobayashi, N. P.; Chang-Hasnain, C.; Crankshaw, S. *Appl. Phys. Lett.* **2007**, *90*, 043115.
- (61) Wei, W.; Bao, X.-Y.; Soci, C.; Ding, Y.; Wang, Z.-L.; Wang, D. *Nano Lett.* **2009**, *9*, 2926–2934.
- (62) Wang, Y.; Schmidt, V.; Senz, S.; Gösele, U. *Nat. Nanotechnol.* **2006**, *1*, 186–189.
- (63) Kayes, B. M.; Filler, M. A.; Putnam, M. C.; Kelzenberg, M. D.; Lewis, N. S.; Atwater, H. A. *Appl. Phys. Lett.* **2007**, *91*, 103110.
- (64) Markov, I. V. *Crystal Growth for Beginners: Fundamentals of Nucleation, Crystal Growth, and Epitaxy*; World Scientific Publishing Co: New Jersey, 1941.
- (65) Frank, F. C. *Discuss. Faraday Soc.* **1949**, *5*, 48–54.
- (66) Burton, W. K.; Cabrera, N.; Frank, F. C. *Nature* **1949**.
- (67) Burton, W. K.; Cabrera, N.; Frank, F. C. *Philosophical Trans. R. Soc. A* **1951**.
- (68) Sears, G. W. *Acta Metall.* **1955**, 1–3.
- (69) Dragsdorf, R. D.; Webb, W. W. *J. Appl. Phys.* **1958**, *29*, 817.
- (70) Webb, W. W. *J. Appl. Phys.* **1965**, *36*, 214.
- (71) Jin, S.; Bierman, M. J.; Morin, S. A. *J. Phys. Chem. Lett.* **2010**, *1*, 1472–1480.
- (72) Kim, B.; Tersoff, J.; Wen, C.-Y.; Reuter, M.; Stach, E.; Ross, F. *Phys. Rev. Lett.* **2009**, *103*, 155701.
- (73) Kim, B. J.; Tersoff, J.; Kodambaka, S.; Reuter, M. C.; Stach, E. a; Ross, F. M. *Science* **2008**, *322*, 1070–1073.
- (74) Wen, C.-Y.; Reuter, M. C.; Bruley, J.; Tersoff, J.; Kodambaka, S.; Stach, E. a; Ross, F. M. *Science* **2009**, *326*, 1247–1250.

- (75) Bryllert, T.; Wernersson, L.-E.; Löwgren, T.; Samuelson, L. *Nanotechnology* **2006**, *17*, S227–S230.
- (76) Colinge, J.-P.; Lee, C.-W.; Afzal, A.; Akhavan, N. D.; Yan, R.; Ferain, I.; Razavi, P.; O'Neill, B.; Blake, A.; White, M.; Kelleher, A.-M.; McCarthy, B.; Murphy, R. *Nat. Nanotechnol.* **2010**, *5*, 225–229.
- (77) Ansari, L.; Feldman, B.; Fagas, G.; Colinge, J.-P.; Greer, J. C. *Appl. Phys. Lett.* **2010**, *97*, 062105.
- (78) Yao, J.; Yan, H.; Das, S.; Klemic, J. F.; Ellenbogen, J. C.; Lieber, C. M. *PNAS* **2014**, 20–24.
- (79) Kempa, T. J.; Day, R. W.; Kim, S.-K.; Park, H.-G.; Lieber, C. M. *Energy Environ. Sci.* **2013**, *6*, 719.
- (80) Polman, A.; Atwater, H. A. *Nat. Mater.* **2012**, *11*, 174–177.
- (81) Wang, D.; Lieber, C. M. *Nat. Mater.* **2003**, *2*, 355–356.
- (82) Wang, D.; Qian, F.; Yang, C.; Zhong, Z.; Lieber, C. M. *Nano Lett.* **2004**, *4*, 871–874.
- (83) Dick, K. A.; Deppert, K.; Larsson, M. W.; Mårtensson, T.; Seifert, W.; Wallenberg, L. R.; Samuelson, L. *Nat. Mater.* **2004**, *3*, 380–384.
- (84) Dick, K. A.; Deppert, K.; Karlsson, L. S.; Seifert, W.; Wallenberg, L. R.; Samuelson, L. *Nano Lett.* **2006**, *6*, 2842–2847.
- (85) Dick, K. A.; Deppert, K.; Larsson, M. W.; Seifert, W.; Reine Wallenberg, L.; Samuelson, L. *Nanotechnology* **2007**, *18*, 035601.
- (86) Dick, K. A.; Geretovszky, Z.; Mikkelsen, A.; Karlsson, L. S.; Lundgren, E.; Malm, J.-O.; Andersen, J. N.; Samuelson, L.; Seifert, W.; Wacaser, B. A.; Deppert, K. *Nanotechnology* **2006**, *17*, 1344–1350.
- (87) Dick, K.; Deppert, K.; Karlsson, L. *MRS Bull.* **2007**, *32*, 127–133.
- (88) Bierman, M. J.; Lau, Y. K. A.; Jin, S. *Nano Lett.* **2007**, *7*, 2907–2912.
- (89) Bierman, M. J.; Lau, Y. K. A.; Kvit, A. V.; Schmitt, A. L.; Jin, S. *Science* **2008**, *320*, 1060–1063.
- (90) Jun, K.; Jacobson, J. M. *Nano Lett.* **2010**, *10*, 2777–2782.
- (91) Jiang, X.; Tian, B.; Xiang, J.; Qian, F. *PNAS* **2011**, *108*, 12212–12216.
- (92) Cheng, C.; Fan, H. J. *Nano Today* **2012**, *7*, 327–343.
- (93) Joshi, R. K.; Schneider, J. J. *Chem. Soc. Rev.* **2012**, *41*, 5285–5312.
- (94) Suyatin, D.; Sun, J.; Fuhrer, A.; Wallin, D. *Nano Lett.* **2008**, 0–4.
- (95) Yu, H.; Dong, W.; Jung, G.; Lee, J. *ACS Nano* **2011**, *5*, 8026–8032.
- (96) Doerk, G. S.; Ferralis, N.; Carraro, C.; Maboudian, R. *J. Mater. Chem.* **2008**, *18*, 5376.
- (97) Castañeda, S. I.; Rueda, F.; Díaz, R.; Ripalda, J. M.; Montero, I. *J. Appl. Phys.* **1998**, *83*, 1995.
- (98) Takaki, S.; Aoshima, Y.; Satoh, R. *Jpn. J. Appl. Phys.* **2006**, *45*, 2714–2721.
- (99) Takaki, S.; Aoshima, Y.; Satoh, R. *Jpn. J. Appl. Phys.* **2007**, *46*, 3537–3544.
- (100) Zhu, J.; Peng, H.; Chan, C. K.; Jarausch, K.; Zhang, X. F.; Cui, Y. *Nano Lett.* **2007**, *7*, 1095–1099.
- (101) Lugstein, A.; Andrews, A. M.; Steinmair, M.; Hyun, Y.-J.; Bertagnolli, E.; Weil, M.; Pongratz, P.; Schramböck, M.; Roch, T.; Strasser, G. *Nanotechnology* **2007**, *18*, 355306.

- (102) Wan, Q.; Wei, M.; Zhi, D.; MacManus-Driscoll, J. L.; Blamire, M. G. *Adv. Mater.* **2006**, *18*, 234–238.
- (103) Zhou, J.; Ding, Y.; Deng, S. Z.; Gong, L.; Xu, N. S.; Wang, Z. L. *Adv. Mater.* **2005**, *17*, 2107–2110.
- (104) Gu, Z.; Liu, F.; Howe, J.; Paranthaman, M. P.; Pan, Z. *Cryst. Growth Des.* **2009**, *9*, 35 – 39.
- (105) Rauber, M.; Alber, I.; Müller, S.; Neumann, R.; Picht, O.; Roth, C.; Schökel, A.; Toimil-Molares, M. E.; Ensinger, W. *Nano Lett.* **2011**, *11*, 2304–2310.
- (106) Dalacu, D.; Kam, A.; Austing, D. G.; Poole, P. J. *Nano Lett.* **2013**, *13*, 2676–2681.
- (107) Brett, M. J.; Hawkeye, M. M. *Science* **2008**, *319*, 1192–1193.
- (108) Hawkeye, M. M.; Brett, M. J. *J. Vac. Sci. Technol., A* **2007**, *25*, 1317.
- (109) Robbie, K.; Brett, M.; Lakhtakia, A. *Nature* **1996**.
- (110) Taschuk, M. T.; Hawkeye, M. M.; Brett, M. J. In *Handbook of Deposition Technologies for Films and Coatings*; Elsevier, 2010.
- (111) Robbie, K.; Brett, M. J. *J. Vac. Sci. Technol., A* **1997**, *15*, 1460–1465.
- (112) Robbie, K.; Sit, J. C.; Brett, M. J. *J. Vac. Sci. Technol., B* **1998**, *16*, 1115.
- (113) Robbie, K.; Brett, M. J. Method of depositing shadow sculpted thin film. 5 866 204, 1999.
- (114) Harris, K.; Huizinga, A.; Brett, M. *Electrochem. Solid-State Lett.* **2002**, *5*, H27–H29.
- (115) Steele, J. J.; van Popta, A. C.; Hawkeye, M. M.; Sit, J. C.; Brett, M. J. *Sensors Actuators B Chem.* **2006**, *120*, 213–219.
- (116) Smetaniuk, D. P.; Taschuk, M. T.; Brett, M. J. *IEEE Sens. J.* **2011**, *11*, 1713–1719.
- (117) Xie, Z.; Henry, B. M.; Kirov, K. R.; Smith, H. E.; Barkhouse, A.; Grovenor, C. R. M. *Thin Solid Films* **2006**, *512*, 523 – 528.
- (118) Van Dijken, J. G.; Fleischauer, M. D.; Brett, M. J. *Org. Electron.* **2011**, *12*, 2111–2119.
- (119) Van Dijken, J. G.; Fleischauer, M. D.; Brett, M. J. *J. Mater. Chem.* **2011**, *21*, 1013.
- (120) Thomas, M.; Worfolk, B. J.; Rider, D. A.; Taschuk, M. T.; Buriak, J. M.; Brett, M. J. *ACS Appl. Mater. Interfaces* **2011**, *3*, 1887–1894.
- (121) Thomas, M.; Li, W.; Bo, Z. S.; Brett, M. J. *Org. Electron.* **2012**, *13*, 2647–2652.
- (122) Rider, D. A.; Tucker, R. T.; Worfolk, B. J.; Krause, K. M.; Lalany, A.; Brett, M. J.; Buriak, J. M.; Harris, K. D. *Nanotechnology* **2011**, *22*, 085706.
- (123) Kwon, H.; Ham, J.; Kim, D. Y.; Oh, S. J.; Lee, S.; Oh, S. H.; Schubert, E. F.; Lim, K.-G.; Lee, T.-W.; Kim, S.; Lee, J.-L.; Kim, J. K. *Adv. Energy Mater.* **2014**, 1301566.
- (124) Zhou, Y.; Taima, T.; Miyadera, T.; Yamanari, T.; Kitamura, M.; Nakatsu, K.; Yoshida, Y. **2012**.
- (125) Wannemacher, J.; Jim, S. R.; Taschuk, M. T.; Brett, M. J.; Morlock, G. E. *J. Chromatogr. A* **2013**, *1318*, 234–243.
- (126) Jim, S. R.; Foroughi-Abari, A.; Krause, K. M.; Li, P.; Kupsta, M.; Taschuk, M. T.; Cadien, K. C.; Brett, M. J. *J. Chromatogr. A* **2013**, *1299*, 118–125.
- (127) Hall, J. Z.; Taschuk, M. T.; Brett, M. J. *J. Chromatogr. A* **2012**, *1266*, 168–174.
- (128) Oko, A. J.; Jim, S. R.; Taschuk, M. T.; Brett, M. J. *J. Chromatogr. A* **2012**, *1249*, 226–232.
- (129) Jim, S. R.; Oko, A. J.; Taschuk, M. T.; Brett, M. J. *J. Chromatogr. A* **2011**, *1218*, 7203–7210.

- (130) Oko, A. J.; Jim, S. R.; Taschuk, M. T.; Brett, M. J. *J. Chromatogr. A* **2011**, *1218*, 2661–2667.
- (131) Jim, S. R.; Taschuk, M. T.; Morlock, G. E.; Bezuidenhout, L. W.; Schwack, W.; Brett, M. *J. Anal. Chem.* **2010**, *82*, 5349–5356.
- (132) Bezuidenhout, L. W.; Brett, M. J. *J. Chromatogr. A* **2008**, *1183*, 179–185.
- (133) Sit, J. C.; Broer, D. J.; Brett, M. J. *Liq. Cryst.* **2000**, *27*, 387–391.
- (134) Robbie, K.; Broer, D.; Brett, M. *Nature* **1999**, *399*, 764–766.
- (135) Kennedy, S. R.; Sit, J. C.; Broer, D. J.; Brett, M. J. *Liq. Cryst.* **2001**, *28*, 1799–1803.
- (136) Elias, A. L.; Brett, M. J.; Sousa, M. E.; Woltman, S. J.; Crawford, G. P.; Bastiaansen, C. W. M.; Broer, D. J. *J. Appl. Phys.* **2006**, *99*, 116105.
- (137) Abelmann, L.; Lodder, C. *Thin Solid Films* **1997**, *305*, 1–21.
- (138) Taschuk, M. T.; Hawkeye, M. M.; Brett, M. J. In *Handbook of Deposition Technologies for Films and Coatings*; Elsevier, 2010.
- (139) Gish, D.; Summers, M.; Brett, M. J. *Phot. Nano. Fund. Appl* **2006**, *4*, 23–29.
- (140) Jensen, M. O.; Brett, M. J. *Appl. Phys. A* **2005**, *80*, 763–768.
- (141) Steele, J. J.; Brett, M. J. *J. Mater. Sci. Mater. Electron.* **2006**, *18*, 367–379.
- (142) Taschuk, M. T.; Chai, J.; Buriak, J. M.; Brett, M. J. *Phys. Status Solidi* **2009**, *6*, S127–S130.
- (143) Kennedy, S. R.; Brett, M. J.; Toader, O.; John, S. *Nano Lett.* **2002**, *2*, 59–62.
- (144) Jensen, M.; Brett, M. *IEEE Trans. Nanotechnol.* **2005**, *4*, 269–277.
- (145) Gish, D. A.; Summers, M. A.; Brett, M. J. *Phot. Nano. Fund. Appl* **2006**, *4*, 23–29.
- (146) Ye, D.-X.; Karabacak, T.; Picu, R. C.; Wang, G.-C.; Lu, T.-M. *Nanotechnology* **2005**, *16*, 1717–1723.
- (147) Dick, B.; Brett, M. J.; Smy, T. J.; Freeman, M. R.; Malac, M.; Egerton, R. F. *J. Vac. Sci. Technol., A* **2000**, *18*, 1838.
- (148) Malac, M.; Egerton, R. F. *J. Vac. Sci. Technol., A* **2001**, *19*, 158.
- (149) Dick, B.; Brett, M. J.; Smy, T. *J. Vac. Sci. Technol., B* **2003**, *21*, 2569.
- (150) Karabacak, T.; Mallikarjunan, A.; Singh, J. P.; Ye, D.; Wang, G.-C.; Lu, T.-M. *Appl. Phys. Lett.* **2003**, *83*, 3096.
- (151) Singh, J. P.; Tang, F.; Karabacak, T.; Lu, T.-M.; Wang, G.-C. *J. Vac. Sci. Technol., B* **2004**, *22*, 1048.
- (152) Alouach, H.; Mankey, G. J. *J. Vac. Sci. Technol., A* **2004**, *22*, 1379.
- (153) Tang, F.; Gaire, C.; Ye, D.-X.; Karabacak, T.; Lu, T.-M.; Wang, G.-C. *Phys. Rev. B* **2005**, *72*, 035430.
- (154) Tang, F.; Karabacak, T.; Morrow, P.; Gaire, C.; Wang, G.-C.; Lu, T.-M. *Phys. Rev. B* **2005**, *72*, 1–6.
- (155) Alouach, H.; Mankey, G. J. *Appl. Phys. Lett.* **2005**, *86*, 123114.
- (156) Wang, J.; Huang, H.; Kesapragada, S. V; Gall, D. *Nano Lett.* **2005**, *5*, 2505–2508.
- (157) Frederick, J. R.; Gall, D. *J. Appl. Phys.* **2005**, *98*, 054906.
- (158) Morrow, P.; Tang, F.; Karabacak, T.; Wang, P.-I.; Ye, D.-X.; Wang, G.-C.; Lu, T.-M. *J. Vac. Sci. Technol., A* **2006**, *24*, 235.

- (159) Mahieu, S.; Ghekiere, P.; Depla, D.; De Gryse, R.; Lebedev, O. I.; Van Tendeloo, G. *J. Cryst. Growth* **2006**, *290*, 272–279.
- (160) Choi, W. K.; Li, L.; Chew, H. G.; Zheng, F. *Nanotechnology* **2007**, *18*, 385302.
- (161) Li, H.-F.; Parker, T.; Tang, F.; Wang, G.-C.; Lu, T.-M.; Lee, S. *J. Cryst. Growth* **2008**, *310*, 3610–3614.
- (162) Li, L.; Fang, X.; Chew, H. G.; Zheng, F.; Liew, T. H.; Xu, X.; Zhang, Y.; Pan, S.; Li, G.; Zhang, L. *Adv. Funct. Mater.* **2008**, *18*, 1080–1088.
- (163) Teki, R.; Parker, T.; Li, H.; Koratkar, N.; Lu, T.; Lee, S. *Thin Solid Films* **2008**, *516*, 4993–4996.
- (164) He, Y.; Zhang, Z.; Hoffmann, C.; Zhao, Y. *Adv. Funct. Mater.* **2008**, *18*, 1676–1684.
- (165) He, Y.; Zhao, Y.; Wu, J. *Appl. Phys. Lett.* **2008**, *92*, 063107.
- (166) Krishnan, R.; Parker, T.; Lee, S.; Lu, T.-M. *Nanotechnology* **2009**, *20*, 465609.
- (167) Li, H.; Snow, P.; He, M.; Wang, P.; Wang, G.; Lu, T. *ACS Nano* **2010**, *4*, 5627–5632.
- (168) He, Y.; Zhao, Y. *Cryst. Growth Des.* **2010**, *10*, 440–448.
- (169) LaForge, J. M.; Taschuk, M. T.; Brett, M. J. *Thin Solid Films* **2011**, *519*, 3530–3537.
- (170) LaForge, J. M.; Ingram, G. L.; Taschuk, M. T.; Brett, M. J. *Cryst. Growth Des.* **2012**, *12*, 3661–3667.
- (171) Chen, L.; Andrea, L.; Timalina, Y. P.; Wang, G.-C.; Lu, T.-M. *Cryst. Growth Des.* **2013**, *13*, 2075–2080.
- (172) Birkholz, M. *Thin Film Analysis by X-Ray Scattering*; Wiley: Weinheim, 2005.
- (173) Exarhos, G. J.; Zhou, X.-D. *Thin Solid Films* **2007**, *515*, 7025–7052.
- (174) Wu, W.-F.; Chiou, B.-S. *Thin Solid Films* **1994**, *247*, 201–207.
- (175) Molzen, W. W. *J. Vac. Sci. Technol.* **1975**, *12*, 99.
- (176) Ishibashi, S. *J. Vac. Sci. Technol., A* **1990**, *8*, 1403.
- (177) Bel Hadj Tahar, R.; Ban, T.; Ohya, Y.; Takahashi, Y. *J. Appl. Phys.* **1998**, *83*, 2631.
- (178) Vossen, J. L. *RCA Rev.* **1971**, *32*, 289.
- (179) Manificier, J. *Thin Solid Films* **1982**, *90*, 297–308.
- (180) Gordon, R. G. G. *MRS Bull.* **2000**, *25*, 52–57.
- (181) Haacke, G. *Annu. Rev. Mater. Sci.* **1977**, *7*, 73–93.
- (182) Vossen, J. L.; Poliniak, E. S. *Thin Solid Films* **1972**, *13*, 281–284.
- (183) Wu, C. C.; Wu, C. I.; Sturm, J. C.; Kahn, a. *Appl. Phys. Lett.* **1997**, *70*, 1348.
- (184) Fraser, D. B.; Cook, H. D. *J. Electrochem. Soc.* **1972**, *119*, 1368.
- (185) Frank, G.; Kostlin, H. *Appl. Phys. A Solids Surfaces* **1982**, *27*, 197–206.
- (186) Chopra, K.; Major, S.; Pandya, D. K. *Thin Solid Films* **1983**, *102*, 1–46.
- (187) Ishida, T.; Kobayashi, H.; Nakato, Y. *J. Appl. Phys.* **1993**, *73*, 4344.
- (188) Haines, W. G.; Bube, R. H. *J. Appl. Phys.* **1978**, *49*, 304.
- (189) Mizuhashi, M. *Thin Solid Films* **1980**, *70*, 91–100.
- (190) Ray, S.; Banerjee, R.; Basu, N.; Batabyal, A. K.; Barua, A. K. *J. Appl. Phys.* **1983**, *54*, 3497.

- (191) Bender, M.; Seelig, W.; Daube, C.; Frankenberger, H.; Ocker, B.; Stollenwerk, J. *Thin Solid Films* **1998**, *326*, 72–77.
- (192) Köstlin, H.; Jost, R.; Lems, W. *Phys. Status Solidi* **1975**, *29*, 87–93.
- (193) Harvey, S. P.; Mason, T. O.; Gassenbauer, Y.; Schafraneck, R.; Klein, A. *J. Phys. D. Appl. Phys.* **2006**, *39*, 3959–3968.
- (194) Yumoto, H.; Hatano, J.; Watanabe, T.; Fujikawa, K.; Sato, H. *Jpn. J. Appl. Phys.* **1993**, *32*, 1204–1209.
- (195) Yumoto, H.; Onozumi, S.; Kato, Y.; Ishihara, M.; Kishi, K. *Cryst. Res. Technol.* **1996**, *31*, 159–164.
- (196) Yumoto, H.; Sako, T.; Gotoh, Y.; Nishiyama, K.; Kaneko, T. *J. Cryst. Growth* **1999**, *203*, 136–140.
- (197) Peng, X. S.; Meng, G. W.; Wang, X. F.; Wang, Y. W.; Zhang, J.; Liu, X.; Zhang, L. D. *Chem. Mater.* **2002**, *14*, 4490–4493.
- (198) Wan, Q.; Song, Z. T.; Feng, S. L.; Wang, T. H. *Appl. Phys. Lett.* **2004**, *85*, 4759.
- (199) Chen, Y. Q.; Jiang, J.; Wang, B.; Hou, J. G. *J. Phys. D. Appl. Phys.* **2004**, *37*, 3319–3322.
- (200) Chiu, C. H.; Yu, P.; Chang, C. H.; Yang, C. S.; Hsu, M. H.; Kuo, H. C.; Tsai, M. a. *Opt. Express* **2009**, *17*, 21250–21256.
- (201) Yu, P.; Chang, C.-H.; Su, M.-S.; Hsu, M.-H.; Wei, K.-H. *Appl. Phys. Lett.* **2010**, *96*, 153307.
- (202) Fung, M. K.; Sun, Y. C.; Ng, a. M. C.; Chen, X. Y.; Wong, K. K.; Djurišić, A. B.; Chan, W. K. *Appl. Phys. A* **2011**, *104*, 1075–1080.
- (203) Chamberlain, G. *Sol. Cells* **1983**, *8*, 47–83.
- (204) Tang, C. W. *Appl. Phys. Lett.* **1986**, *48*, 183.
- (205) Tang, C. W.; VanSlyke, S. a. *Appl. Phys. Lett.* **1987**, *51*, 913.
- (206) Kugler, T.; Salaneck, W.; Rost, H. *Chem. Phys. Lett.* **1999**, 391–396.
- (207) Kim, H.; Piqué, a.; Horwitz, J. S.; Mattoussi, H.; Murata, H.; Kafafi, Z. H.; Chrisey, D. B. *Appl. Phys. Lett.* **1999**, *74*, 3444.
- (208) Schulze, K.; Maennig, B.; Leo, K.; Tomita, Y.; May, C.; Hüpkes, J.; Brier, E.; Reinold, E.; Bäuerle, P. *Appl. Phys. Lett.* **2007**, *91*, 073521.
- (209) Günes, S.; Neugebauer, H.; Sariciftci, N. S. *Chem. Rev.* **2007**, *107*, 1324–1338.
- (210) Armstrong, N. R.; Veneman, P. A.; Ratcliff, E.; Placencia, D.; Brumbach, M. *Acc. Chem. Res.* **2009**, *42*, 1748–1757.
- (211) Hoppe, H.; Sariciftci, N. S. *J. Mater. Res.* **2011**, *19*, 1924–1945.
- (212) Hotchkiss, P.; Jones, S. *Acc. Chem. Res.* **2011**, *45*, 337–346.
- (213) Wu, Q.-H. *Crit. Rev. Solid State Mater. Sci.* **2013**, *38*, 318–352.
- (214) Burstein, E. *Phys. Rev.* **1954**, 2–3.
- (215) Rosen, J.; Warschkow, O. *Phys. Rev. B* **2009**, *80*, 115215.
- (216) Bashar, S. A. **1998**.
- (217) Granqvist, C. G. *Sol. Energy Mater. Sol. Cells* **2007**, *91*, 1529–1598.
- (218) Terzini, E.; Thilakan, P.; Minarini, C. *Mater. Sci. Eng. B* **2000**, *77*, 110–114.
- (219) Wu, W.; Chiou, B.; Hsieh, S. *Semicond. Sci. Technol.* **1994**, *9*, 1242 – 1249.

- (220) Shewchun, J.; Dubow, J.; Wilmsen, C. W.; Singh, R.; Burk, D.; Wager, J. F. *J. Appl. Phys.* **1979**, *50*, 2832.
- (221) Park, Y.; Choong, V.; Gao, Y.; Hsieh, B. R.; Tang, C. W. *Appl. Phys. Lett.* **1996**, *68*, 2699.
- (222) Parker, I. D. *J. Appl. Phys.* **1994**, *75*, 1656.
- (223) Inerbaev, T. M.; Sahara, R.; Mizuseki, H.; Kawazoe, Y.; Nakamura, T. *Mater. Trans.* **2007**, *48*, 666–669.
- (224) Walsh, A.; Catlow, C. R. A. *J. Mater. Chem.* **2010**, *20*, 10438.
- (225) Zhang, K. H. L.; Walsh, A.; Catlow, C. R. A.; Lazarov, V. K.; Egdell, R. G. *Nano Lett.* **2010**, *10*, 3740–3746.
- (226) Kim, J.-H.; Lee, J.-H.; Heo, Y.-W.; Kim, J.-J.; Park, J.-O. *J. Electroceramics* **2007**, *23*, 169–174.
- (227) Jung, Y. S.; Lee, S. S. *J. Cryst. Growth* **2003**, *259*, 343–351.
- (228) Ba, J.; Rohlfing, D. F.; Feldhoff, A.; Brezesinski, T.; Djerdj, I.; Wark, M.; Niederberger, M.; V, D.-H.; March, R. V.; Re, V.; Recci, M.; April, V. **2006**, 2848–2854.
- (229) Gao, J.; Chen, R.; Li, D. H.; Jiang, L.; Ye, J. C.; Ma, X. C.; Chen, X. D.; Xiong, Q. H.; Sun, H. D.; Wu, T. *Nanotechnology* **2011**, *22*, 195706.
- (230) Neri, G.; Bonavita, a.; Micali, G.; Rizzo, G.; Pinna, N.; Niederberger, M.; Ba, J. *Thin Solid Films* **2007**, *515*, 8637–8640.
- (231) González, G. B.; Cohen, J. B.; Hwang, J.-H.; Mason, T. O.; Hodges, J. P.; Jorgensen, J. D. *J. Appl. Phys.* **2001**, *89*, 2550.
- (232) Nadaud, N.; Lequeux, N.; Nanot, M.; Jové, J.; Roisnel, T. *J. Solid State Chem.* **1998**, *135*, 140–148.
- (233) Yang, C.-S.; Chang, C.-H.; Lin, M.-H.; Yu, P.; Wada, O.; Pan, C.-L. *Opt. Express* **2012**, *20*, A441.
- (234) Savu, R.; Joanni, E. *Scr. Mater.* **2006**, *55*, 979–981.
- (235) Savu, R.; Joanni, E. *J. Mater. Sci.* **2007**, *43*, 609–613.
- (236) Chang, C.; Hsu, M.; Chang, W.; Sun, W.; Wu, C.; Yu, P. In *Photovoltaic Specialists Conference (PVSC), 2010 35th IEEE*; IEEE, 2010; Vol. 1, pp. 003109–003111.
- (237) Chang, C. H.; Hsu, M.-H.; Yu, P.; Kuo, H. C.; Chang, W. L.; Sun, W. C. *2009 34th IEEE Photovolt. Spec. Conf.* **2009**, 000540–000543.
- (238) Chang, C. H.; Yu, P.; Yang, C. S. *Appl. Phys. Lett.* **2009**, *94*, 051114.
- (239) Park, J. H.; Park, H. K.; Jeong, J.; Kim, W.; Min, B. K.; Do, Y. R. *J. Electrochem. Soc.* **2011**, *158*, K131.
- (240) Wan, N.; Xu, J.; Sun, L.; Lin, T. *CrystEngComm* **2013**, *15*, 3925.
- (241) Wan, N.; Xu, J.; Chen, G.; Gan, X.; Guo, S.; Xu, L.; Chen, K. *Acta Mater.* **2010**, *58*, 3068–3072.
- (242) O’Dwyer, C.; Szachowicz, M.; Visimberga, G.; Lavayen, V.; Newcomb, S. B.; Torres, C. M. S. *Nat. Nanotechnol.* **2009**, *4*.
- (243) Okamoto, H. *J. Phase Equilibria Diffus.* **2006**, *27*, 313–313.
- (244) Frank, G. *J. Cryst. Growth* **1976**, *36*, 179–180.
- (245) Park, K.-S.; Choi, Y.-J.; Kang, J.-G.; Sung, Y.-M.; Park, J.-G. *Nanotechnology* **2011**, *22*, 285712.

- (246) Chen, C.-J.; Xu, W.-L.; Chern, M.-Y. *Adv. Mater.* **2007**, *19*, 3012–3015.
- (247) Wan, Q.; Feng, P.; Wang, T. H. *Appl. Phys. Lett.* **2006**, *89*, 123102.
- (248) Gao, J.; Lebedev, O. I.; Turner, S.; Li, Y. F.; Lu, Y. H.; Feng, Y. P.; Boullay, P.; Prellier, W.; van Tendeloo, G.; Wu, T. *Nano Lett.* **2012**, *12*, 275–280.
- (249) Pan, K.-Y.; Lin, L.-D.; Chang, L.-W.; Shih, H. C. *Appl. Surf. Sci.* **2013**, *273*, 12–18.
- (250) Chang, W.-C.; Kuo, C.-H.; Lee, P.-J.; Chueh, Y.-L.; Lin, S.-J. *Phys. Chem. Chem. Phys.* **2012**, *14*, 13041–13045.
- (251) Meng, G.; Yanagida, T.; Nagashima, K.; Yoshida, H.; Kanai, M.; Klamchuen, A.; Zhuge, F.; He, Y.; Rahong, S.; Fang, X.; Takeda, S.; Kawai, T. *J. Am. Chem. Soc.* **2013**, *135*, 7033–7038.
- (252) Nguyen, P.; Ng, H. T.; Kong, J.; Cassell, A. M.; Quinn, R.; Li, J.; Han, J.; McNeil, M.; Meyyappan, M. *Nano Lett.* **2003**, *3*, 925–928.
- (253) Chiu, S.-P.; Chung, H.-F.; Lin, Y.-H.; Kai, J.-J.; Chen, F.-R.; Lin, J.-J. *Nanotechnology* **2009**, *20*, 105203.
- (254) Li, S. Y.; Lee, C. Y.; Lin, P.; Tseng, T. Y. *Nanotechnology* **2005**, *16*, 451–457.
- (255) Vomiero, A.; Bianchi, S.; Comini, E.; Faglia, G.; Ferroni, M.; Sberveglieri, G. *Cryst. Growth Des.* **2007**, *7*, 2500–2504.
- (256) Spanggaard, H.; Krebs, F. C. *Sol. Energy Mater. Sol. Cells* **2004**, *83*, 125–146.
- (257) Blom, P. W. M.; Mihailetchi, V. D.; Koster, L. J. A.; Markov, D. E. *Adv. Mater.* **2007**, *19*, 1551–1566.
- (258) Thompson, B. C.; Fréchet, J. M. J. *Angew. Chem. Int. Ed. Engl.* **2008**, *47*, 58–77.
- (259) Brabec, C. J.; Gowrisanker, S.; Halls, J. J. M.; Laird, D.; Jia, S.; Williams, S. P. *Adv. Mater.* **2010**, *22*, 3839–3856.
- (260) Clarke, T. M.; Durrant, J. R. *Chem. Rev.* **2010**, *110*, 6736–6767.
- (261) Rider, D. A.; Tucker, R. T.; Worfolk, B. J.; Krause, K. M.; Lalany, A.; Brett, M. J.; Buriak, J. M.; Harris, K. D. *Nanotechnology* **2011**, *22*, 085706.
- (262) Goldstein, J.; Newbury, D.; Joy, D.; Lyman, C.; Echlin, P.; Lifshin, E.; Sawyer, L.; Michael, J. *Scanning Electron Microscopy and X-ray Microanalysis*; 3rd ed.; Springer, 2003.
- (263) Ward, B. W.; Notte, J. A.; Economou, N. P. *J. Vac. Sci. Technol., B* **2006**, *24*, 2871.
- (264) Morgan, J.; Notte, J.; Hill, R.; Ward, B. *Microsc. Today* **2006**.
- (265) Bell, D. *Microsc. Microanal.* **2009**, 147–153.
- (266) Williams, D.; Carter, C. *Transmission electron microscopy: a textbook for materials science*; Springer: New York, 1997.
- (267) Horiuchi, S. *Fundamentals of high-resolution transmission electron microscopy*; North-Holland: Madison, 1994.
- (268) Bals, S.; Kabius, B.; Haider, M.; Radmilovic, V.; Kisielowski, C. *Solid State Commun.* **2004**, *130*, 675–680.
- (269) Pennycook, S.; Jesson, D. *Phys. Rev. Lett.* **1990**, *64*.
- (270) James, E. M.; Browning, N. D.; Nicholls, a. W.; Kawasaki, M.; Xin, Y.; Stemmer, S. *J. Electron Microsc. (Tokyo)*. **1998**, *47*, 561–574.
- (271) Beaudry, A. L.; Tucker, R. T.; LaForge, J. M.; Taschuk, M. T.; Brett, M. J. *Nanotechnology* **2012**, *23*, 105608.

- (272) Alagoz, A. S.; Karabacak, T. *MRS Proc.* **2011**, 1350.
- (273) Suzuki, M.; Hamachi, K.; Hara, H.; Nakajima, K.; Kimura, K.; Hsu, C.-W.; Chou, L.-J. *Appl. Phys. Lett.* **2011**, 99, 223107.
- (274) Suzuki, M.; Hamachi, K.; Nagai, K.; Kita, R.; Nakajima, K.; Kimura, K. *ECS Trans.* **2010**, 33, 41–48.
- (275) Suzuki, M.; Nagai, K.; Kinoshita, S.; Nakajima, K.; Kimura, K.; Okano, T.; Sasakawa, K. *Appl. Phys. Lett.* **2006**, 89, 133103.
- (276) Sugata, H.; Ohshio, S.; Saitoh, H. *Jpn. J. Appl. Phys.* **2003**, 42, 2786–2790.
- (277) Jang, H.; Kim, D.; Lee, H.; Lee, S. *Mater. Lett.* **2005**, 59, 1526–1529.
- (278) Xin-Yu, X.; Song-Lin, S.; Zhi-Xian, L.; Ke-Lu, Z.; Yong-Ai, Z.; Tai-Liang, G.; Tai-Hong, W. *Chinese Phys. Lett.* **2007**, 24, 3492.
- (279) Vomiero, A.; Ferroni, M.; Comini, E.; Faglia, G.; Sberveglieri, G. *Cryst. Growth Des.* **2010**, 10, 140–145.
- (280) Chen, C.-J.; Chern, M.-Y.; Wu, C.-T.; Chen, C.-H. *Mater. Res. Bull.* **2010**, 45, 230–234.
- (281) *Manual on the Use of Thermocouples in Temperature Measurement, Fourth Edition, Sponsored by ASTM Committee E20 on Temperature Measurement*; Park, R.; Carroll, R.; Bliss, P.; Burns, G.; Desmaris, R.; Hall, F.; Herzkovitz, M.; MacKenzie, D.; McGuire, E.; Reed, R.; Sparks, L.; Wang, T., Eds.; ASTM International: 100 Barr Harbor Drive, PO Box C700, West Conshohocken, PA 19428-2959, 1993.
- (282) Hunt, G. A. **2013**.
- (283) Rasband, W. S. ImageJ.
- (284) Wacaser, B. A.; Dick, K. A.; Johansson, J.; Borgström, M. T.; Deppert, K.; Samuelson, L. *Adv. Mater.* **2009**, 21, 153–165.
- (285) Tucker, R. T.; Beaudry, A. L.; LaForge, J. M.; Taschuk, M. T.; Brett, M. J. *Appl. Phys. Lett.* **2012**, 101, 193101.
- (286) Wang, J. X.; Xie, S. S.; Gao, Y.; Yan, X. Q.; Liu, D. F.; Yuan, H. J.; Zhou, Z. P.; Song, L.; Liu, L. F.; Zhou, W. Y.; Wang, G. J. *Cryst. Growth* **2004**, 267, 177–183.
- (287) Cai, X. M.; Djurišić, A. B.; Xie, M. H.; Chiu, C. S.; Gwo, S. *Appl. Phys. Lett.* **2005**, 87, 183103.
- (288) Cao, L.; Garipcan, B.; Atchison, J. S.; Ni, C.; Nabet, B.; Spanier, J. E. *Nano Lett.* **2006**, 6, 1852–1857.
- (289) Givargizov, E. I. *J. Cryst. Growth* **1973**, 20, 217–226.
- (290) Hannon, J. B.; Kodambaka, S.; Ross, F. M.; Tromp, R. M. *Nature* **2006**, 440, 69–71.
- (291) Kohno, H.; Takeda, S. *J. Cryst. Growth* **2000**, 216, 185–191.
- (292) Kolíbal, M.; Kalousek, R.; Vystavěl, T.; Novák, L.; Šikola, T. *Appl. Phys. Lett.* **2012**, 100, 203102.
- (293) Lilach, Y.; Zhang, J.-P.; Moskovits, M.; Kolmakov, A. *Nano Lett.* **2005**, 5, 2019–2022.
- (294) Yan, Y.; Zhou, L.; Zou, J.; Zhang, Y. *Appl. Phys. A* **2008**, 94, 559–565.
- (295) Yuan, Y.; Pan, J. *J. Mater. Sci.* **1998**, 3, 5773–5780.
- (296) Zhang, Y.; Yan, Y.; Zhu, F. *Nanoscale Res. Lett.* **2007**, 2, 492–495.
- (297) Kohno, H.; Yoshida, H. *Solid State Commun.* **2004**, 132, 59–62.
- (298) Mohammad, S. *Nano Lett.* **2008**, 8, 1532–1538.

- (299) Johansson, J.; Wacaser, B. A.; Dick, K. A.; Seifert, W. *Nanotechnology* **2006**, *17*, S355–S361.
- (300) Dubrovskii, V. G.; Sibirev, N. V. *J. Cryst. Growth* **2007**, *304*, 504–513.
- (301) Kashchiev, D. *Cryst. Growth Des.* **2006**, *6*, 1154–1156.
- (302) Schwalbach, E. J.; Voorhees, P. W. *Nano Lett.* **2008**, *8*, 3739–3745.
- (303) Zhang, X.; Lew, K.-K.; Nimmatoori, P.; Redwing, J. M.; Dickey, E. C. *Nano Lett.* **2007**, *7*, 3241–3245.
- (304) Caroff, P.; Dick, K. A.; Johansson, J.; Messing, M. E.; Deppert, K.; Samuelson, L. *Nat. Nanotechnol.* **2009**, *4*, 50–55.
- (305) Schmidt, V.; Senz, S.; Gösele, U. *Nano Lett.* **2005**, *5*, 931–935.
- (306) Wang, Z. W.; Li, Z. Y. *Nano Lett.* **2009**, *9*, 1467–1471.
- (307) Beaudry, A. L.; LaForge, J. M.; Tucker, R. T.; Li, P.; Taschuk, M. T.; Brett, M. J. *Cryst. Growth Des.* **2013**, *13*, 212–219.
- (308) Chen, L.; Lu, T.-M.; Wang, G.-C. *Nanotechnology* **2011**, *22*, 505701.
- (309) Lu, T.-M.; Tang, F.; Wang, G.-C. *Proc. SPIE* **2008**, *7041*, 704107–704107–7.
- (310) Ma, B.; Li, M.; Koritala, R. E.; Fisher, B. L.; Markowitz, A. R.; Erck, R. A.; Dorris, S. E.; Miller, D. J.; Balachandran, U. *IEEE Trans. Applied Supercond.* **2003**, *13*, 2695–2698.
- (311) Mahieu, S.; Ghekiere, P.; Depla, D.; Degryse, R. *Thin Solid Films* **2006**, *515*, 1229–1249.
- (312) TEMography.
- (313) Frank, J. *Electron Tomography: Methods for Three-Dimensional Visualization of Structures in the Cell*; Second.; Springer: New York, 2006.
- (314) Kamino, T.; Yaguchi, T.; Ohnishi, T.; Ishitani, T.; Osumi, M. O. *J. Electron Microsc. (Tokyo)*. **2004**, *53*, 563–566.
- (315) Liu, S. J.; Huang, H.; Woo, C. H. *Appl. Phys. Lett.* **2002**, *80*, 3295.
- (316) Wan, N.; Xu, J.; Chen, G.; Gan, X.; Guo, S.; Xu, L.; Chen, K. *Acta Mater.* **2010**, *58*, 3068–3072.
- (317) Beaudry, A. L.; Laforge, J. M.; Tucker, R. T.; Sorge, J. B.; Adamski, N. L.; Li, P.; Taschuk, M. T.; Brett, M. J. *Nano Lett.* **2014**, *14*, 1797–1803.
- (318) Kamei, M.; Yagami, T.; Takaki, S.; Shigesato, Y. *Appl. Phys. Lett.* **1994**, *64*, 2712–2714.
- (319) Ohta, H.; Orita, M.; Hirano, M.; Tanji, H.; Kawazoe, H.; Hosono, H. *Appl. Phys. Lett.* **2000**, *76*, 2740.
- (320) Taga, N.; Odaka, H.; Shigesato, Y.; Yasui, I.; Kamei, M.; Haynes, T. E. *J. Appl. Phys.* **1996**, *80*, 978.
- (321) Wan, Q.; Dattoli, E. N.; Fung, W. Y.; Guo, W.; Chen, Y.; Pan, X.; Lu, W. *Nano Lett.* **2006**, *6*, 2909–2915.
- (322) Taschuk, M. T.; Tucker, R. T.; LaForge, J. M.; Beaudry, A. L.; Kupsta, M. R.; Brett, M. J. *J. Appl. Phys.* **2013**, *114*, 244304.
- (323) Rauf, I. A. *Appl. Phys. Lett.* **2008**, *93*, 143101.
- (324) Yu, H. K.; Kim, S.; Koo, B.; Jung, G. H.; Lee, B.; Ham, J.; Lee, J.-L. *Nanoscale* **2012**, *3*, 2–5.
- (325) Yun, J.; Park, Y. H.; Bae, T.-S.; Lee, S.; Lee, G.-H. *ACS Appl. Mater. Interfaces* **2013**, *5*, 164–172.

- (326) LaForge, J. M.; Cocker, T. L.; Beaudry, A. L.; Cui, K.; Tucker, R. T.; Taschuk, M. T.; Hegmann, F. A.; Brett, M. J. *Nanotechnology* **2014**, *25*, 035701.
- (327) Lee, J.; Lim, D.-G.; Song, W.; Yi, J. *J. Korean Phys. Soc.* **2007**, *51*, 1143.
- (328) Jung, Y. S.; Choi, Y. W.; Lee, H. C.; Lee, D. W. **2003**, *440*, 278–284.
- (329) Morgan, D. V.; Aliyu, Y. H.; Bunce, R. W.; Salehi, a. *Thin Solid Films* **1998**, *312*, 268–272.
- (330) Chang, S.-C. *Microelectronics J.* **2007**, *38*, 1220–1225.
- (331) Lee, S.; Noh, J.; Bae, S.; Cho, I. *Korean Phys. Soc.* **2009**, *113*, 7443–7447.
- (332) Lin, T.-C.; Chang, S.-C.; Chiu, C.-F. *Mater. Sci. Eng. B* **2006**, *129*, 39–42.
- (333) Zhang, K.; Zhu, F.; Huan, C. H. .; Wee, A. T. . *Thin Solid Films* **2000**, *376*, 255–263.
- (334) Morgan, D. V.; Aliyu, Y. H.; Bunce, R. W.; Salehi, a. *Thin Solid Films* **1998**, *312*, 268–272.
- (335) Smits, F. *Bell Syst. Tech. J* **1958**.
- (336) Jain, V.; Kulshreshtha, a. *Sol. Energy Mater.* **1981**, *4*, 151–158.
- (337) Knickerbocker, S. a. *J. Vac. Sci. Technol., A* **1995**, *13*, 1048.
- (338) Haacke, G. *J. Appl. Phys.* **1976**, *47*, 4086.